Technische Universität München
Institut für Energietechnik

Lehrstuhl für Thermodynamik

Combustion Noise Prediction with Linearized Navier-Stokes Equations and Spectral Sound Sources

Wolfram Christoph Ullrich

Vorwort

Die vorliegende Arbeit entstand im Rahmen meiner Tätigkeit als wissenschaftlicher Mitarbeiter am Lehrstuhl für Thermodynamik der Technischen Universität München.

Mein besonderer Dank gilt meinem Doktorvater Prof. Dr.-Ing. Thomas Sattelmayer für die Betreuung der Arbeit und das in mich gesetzte Vertrauen. Ihm habe ich während der Zeit als Doktorand viele wichtige Impulse und eine intensive Unterstützung bei der Veröffentlichungen von Forschungsergebnissen zu verdanken. Außerdem bedanke ich mich bei Herrn Prof. Dr. rer. nat. Lars Enghardt für die Übernahme des Koreferats und Herrn Prof. Dr.-Ing. habil. Boris Lohmann für die Übernahme des Prüfungsvorsitzes.

Mein Dank geht an alle Mitarbeiter des Lehrstuhls für die Zusammenarbeit und die äußerst hilfreichen fachlichen Diskussionen in einer freundschaftlichen Arbeitsatmosphäre. Ebenso danke ich Dr.-Ing. Christoph Hirsch, der für Fragen und Diskussionen immer zur Verfügung stand und mir wichtige Impulse während der Zeit am Lehrstuhl gegeben hat. Außerdem möchte ich mich bei Helga Bassett und Sigrid Schulz-Reichwald für die fortwährende Unterstützung in den administrativen und organisatorischen Angelegenheiten bedanken.

Die vorliegende Arbeit entstand im Rahmen des EU-geförderten RECORD (Research On Core Noise Reduction) Projektes. In diesem Zusammenhang möchte ich auch die erfolgreiche und intensive Zusammenarbeit mit allen Projektpartnern nicht unerwähnt lassen. Dabei werden mir besonders die vielen freundlichen und hilfreichen Gespräche, Telefonate und Meetings mit Dr.-Ing. Friedrich Bake, Ph. D. Yasser Mahmoudi, Dr.-Ing. André Fischer und Kilian Lackhove in Erinnerung bleiben.

Abschließend gilt mein herzlicher Dank meiner Familie für die große Unterstützung während meiner gesamten Ausbildungszeit und Promotionszeit. Ohne euch hätte ich das alles nicht geschafft.

Neustadt an der Weinstraße, im Dezember 2019   Wolfram Ullrich

Kurzfassung

Bei der Entwicklung zukünftiger Fluggasturbinen steht zunehmend die Reduktion des Verbrennungslärms im Vordergrund. Daher kommt der Verbesserung und Weiterentwicklung von numerischen Vorhersagemethoden von Verbrennungslärm eine entscheidende Rolle zu. Beim Verbrennungslärm wird zwischen dem direkten und indirekten Entstehungsmechanismus unterschieden. Während der direkte Anteil durch Schwankungen der Wärmefreisetzung in der Flamme entsteht, ist der indirekte Lärm an die Beschleunigung von konvektiv transportierten Temperatur- und Wirbelstörungen in der Turbine gekoppelt.

Die vorliegende Arbeit leistet einen Beitrag zur numerischen Vorhersage von direktem und indirektem Verbrennungslärm von turbulenten Flammen. Dazu wird ein bestehender hybrider Ansatz um Quellterme für turbulenten Verbrennungslärm erweitert. Bei dem hybriden Ansatz wird zunächst die stationäre Grundströmung in der Brennkammer durch Reynolds-Averaged Navier-Stokes (RANS) Simulationen ermittelt. Dann wird die Ausbreitung von akustischen Wellen und von Temperatur- und Wirbelstörungen in der Grundströmung berechnet. Dazu werden die linearisierten Navier-Stokes Gleichungen (LNSE) im Frequenzbereich gelöst. Die LNSE werden durch spektrale Quellterme angeregt, deren Spektrum wiederum durch bestehende statistische Lärmmodelle erzeugt wird. Bei statistischen Lärmmodellen wird ein Quellspektrum aus der stationären Grundströmung ermittelt, wodurch der Einsatz von zeitlich aufwändigen instationären RANS Simulationen oder Large Eddy Simulationen (LES) vermieden wird. Außerdem wird ein semi-analytisches Quellterm-Modell für die Unterscheidung von perfekt-vorgemischten und nicht-vorgemischten Flammen vorgeschlagen, um die Entstehung von Temperaturstörungen bei unterschiedlichen Flammentypen korrekt abzubilden.

Im Rahmen dieser Arbeit wird der Ansatz anhand von zwei Prüfstandsbrennkammern validiert. Bei der vorgemischten druckbeaufschlagten Propanflamme der CESAM-HP Brennkammer ergeben sich gute Übereinstimmungen bezüglich Amplitude und Peakfrequenz für zwei von drei Betriebspunkten unter Verwendung des statistischen Lärmmodells von Hirsch et al. [2006, 2007]. Das Lärmspektrum wird wesentlich durch das zugrundeliegende Wärmefreisetzungs-Quellspektrum bestimmt, während die räumliche Verteilung und Phase des Quellterms nur geringen Einfluss haben. Durch Verwendung des Quelltermansatzes für perfekt-vorgemischte Flammen werden qualitativ korrekte Vorhersagen für den indirekten Lärmanteil erzielt. Aufgrund der vorgemischten Flamme ist der indirekte Lärm gering im Vergleich zum direkten Anteil. Beim zweiten Testfall wird das Lärmmodell von Jörg [2015] für nicht-vorgemischte Flammen auf eine atmosphärisch-betriebene Kerosin-Flamme angewendet. Für das Lärmspektrum ergibt sich eine gute Übereinstimmung zwischen Experiment und Simulation. Die von der Flamme erzeugten Temperaturstörungen werden bereits vor Erreichen des Brennkammer-Austritts durch Scherungen in der Strömung dissipiert. Damit ergibt sich auch hier ein vernachlässigbar kleiner indirekter Lärmanteil.

Abstract

The reduction of combustion noise is of increasing importance for the development of low-emission aero-engines. Within this process the improvement and further development of numerical tools for predicting combustion noise plays a key role. In the field of combustion noise it is distinguished between the direct and indirect generation mechanism. While direct noise is caused by heat release oscillations of the flame, indirect noise generation is associated with the acceleration of convectively transported temperature and vortical inhomogeneities into the turbine.

The present thesis provides a contribution to the numerical prediction of direct and indirect combustion noise. For this purpose an existing hybrid approach is extended to incorporate stochastic sound sources due to turbulent combustion. In the hybrid approach first the combustor mean flow field is computed using Reynolds-averaged Navier-Stokes (RANS) simulations. Then the propagation of acoustic waves as well as temperature and vortical disturbances in presence of the mean flow is computed by solving linearized Navier-Stokes equations (LNSE) in frequency domain. The LNSE are excited by spectral sound sources, whose spectra are in turn determined from statistical noise models. When using statistical models the source spectrum is deduced from the steady mean flow, making the application of time-consuming unsteady RANS simulations or even large eddy simulations (LES) obsolete. A semi-analytical source model is proposed which discriminates between perfectly-premixed and non-premixed flames. Like this the generation of temperature disturbances in different flame types can be correctly reproduced.

In this thesis the hybrid approach is validated with data from two different combustion chamber test rigs. Good agreement concerning amplitude and peak frequency is obtained for two out of three operating points when applying the statistical noise model by Hirsch et al. [2006, 2007] to the premixed pressurized propane flame confined in the CESAM-HP combustor. The noise spectrum is controlled by the underlying heat release source spectrum, whereas the spatial distribution and phase of the source terms only marginally influence the noise spectrum. Using the source term for perfectly-premixed flames the indirect noise is qualitatively correctly predicted. For the premixed flame the indirect noise contribution is small in comparison to the direct noise. In the second test case the noise model by Jörg [2015] for non-premixed flames is applied to an atmospheric kerosene flame. Good agreement between experiment and simulation is obtained for the resulting noise spectrum. Temperature disturbances created by the flame are dissipated before reaching the combustor outlet due to flow shearing effects. This results in a negligible indirect noise contribution.

Contents

Nomenclature

General definitions

Symbol	Unit	Meaning
a	$[\frac{\mathrm{m}^2}{\mathrm{s}}]$	Thermal diffusivity
b	$[\mathrm{m}]$	Lateral combustion chamber length
$b_i^{(e)}, \boldsymbol{b}^{(e)}$		Element load vector (FEM)
c	$[\text{-}]$	Reaction progress variable
c	$[\frac{\mathrm{m}}{\mathrm{s}}]$	Speed of sound
c_d, c_g, c_s	$[\text{-}]$	Modeling constants of the statistical noise model
c_l	$[\text{-}]$	Constant for turbulent length scale
c_q	$[\text{-}]$	Scaling constant for mean heat release evaluation in non-premixed flames
c_p	$[\frac{\mathrm{J}}{\mathrm{kgK}}]$	Specific isobaric heat capacity
$c_{p,k}$	$[\frac{\mathrm{J}}{\mathrm{kgK}}]$	Specific isobaric heat capacity of the k-th species
c_v	$[\frac{\mathrm{J}}{\mathrm{kgK}}]$	Specific isochoric heat capacity
c_w	$[\text{-}]$	Modeling constant for Damköhler number in Schmidt model
$c_{\epsilon 1}, c_{\epsilon 2}$	$[\text{-}]$	Modeling constants of $k-\epsilon$ turbulence model
c_μ	$[\text{-}]$	Modeling constant of eddy-viscosity-models
c_τ	$[\text{-}]$	Constant for chemical time scale
$\widetilde{c''^2}$	$[\text{-}]$	Mean variance of the reaction progress variable
d	$[\mathrm{m}]$	Diameter
$d_i^{(e)}, \boldsymbol{d}^{(e)}$		Vector of discrete nodal values (FEM)
f	$[\mathrm{Hz}]$	Frequency
f_p	$[\mathrm{Hz}]$	Peak frequency
$f_i, \boldsymbol{f}$	$[\frac{\mathrm{m}}{\mathrm{s}^2}]$	Specific body force vector
$f_i, \boldsymbol{f}$		Momentum and energy source vector (FEM)
$g_i^{(e)}, \boldsymbol{g}^{(e)}$	$[\text{-}]$	Vector of constant multiplicators (FEM)
h	$[\frac{\mathrm{J}}{\mathrm{kg}}]$	Specific enthalpy
$h^{(e)}$	$[\mathrm{m}]$	Characteristic element length
$h_{f,k}^0$	$[\frac{\mathrm{J}}{\mathrm{kg}}]$	Enthalpy of formation of the k-th species
h_s	$[\frac{\mathrm{J}}{\mathrm{kg}}]$	Sensible enthalpy
h_t	$[\frac{\mathrm{J}}{\mathrm{kg}}]$	Total specific enthalpy
k	$[\frac{\mathrm{J}}{\mathrm{kg}}]$	Turbulent kinetic energy
k	$[\frac{1}{\mathrm{m}}]$	Wave number
k_p	$[\frac{1}{\mathrm{m}}]$	Plank absorption coefficient
$k_{ij}^{(e)}, \mathbf{k}^{(e)}$	$[\text{-}]$	Element stiffness matrix (FEM)

l	[m]	Length
l_c	[m]	Corrsin length scale
l_g	[m]	Gibson length scale
l_t	[m]	Turbulent length scale
$\dot{m}$	$[\frac{\text{kg}}{\text{s}}]$	Mass flow
$m_{ij}^{(e)}, \mathbf{m}^{(e)}$	[-]	Element mass matrix (FEM)
n	[-]	Total number of species
n	[-]	Circumferential mode number
n_p	[-]	Number of nodes on each element (FEM)
$ndof$	[-]	Total number of degrees of freedom (FEM)
nel	[-]	Total number of elements (FEM)
n_{mon}	[-]	Number of monitor planes for wave extraction
$n_i, \boldsymbol{n}$	[-]	Surface normal vector
p	$[\frac{\text{N}}{\text{m}^2}]$	Pressure
$p(z)$	[-]	Probability density function
$\hat{p}^+, \hat{p}^-$	$[\frac{\text{N}}{\text{m}^2}]$	Complex valued right (+) and left (-) traveling waves
$\dot{q}_V$	$[\frac{\text{W}}{\text{m}^3}]$	Heat release rate due to electrical sources
$\dot{q}_i, \dot{\boldsymbol{q}}$	$[\frac{\text{W}}{\text{m}^2}]$	Specific heat flux vector
r	[m]	Radius, cylindrical (polar) coordinate
s	$[\frac{\text{J}}{\text{kgK}}]$	Specific entropy
s_l	$[\frac{\text{m}}{\text{s}}]$	Laminar flame speed
s_t	$[\frac{\text{m}}{\text{s}}]$	Turbulent flame speed
s_V	$[\frac{1}{\text{s}}]$	Volume source term
t	[s]	Time
t_p	[s]	Pulse duration
$u_i, \boldsymbol{u}$	$[\frac{\text{m}}{\text{s}}]$	Velocity vector
u_t	$[\frac{\text{m}}{\text{s}}]$	Velocity of integral turbulent length scales
$w_i, \boldsymbol{w}$	$[\frac{\text{m}}{\text{s}}]$	Vector of weighting functions (FEM)
$x_i, \boldsymbol{x}$	[m]	Cartesian position vector in real space
x, y, z	[m]	Cartesian coordinates
z	[m]	Axial coordinate in cylindrical (polar) coordinates
z	[-]	Mixture fraction
$\widetilde{z''^2}$	[-]	Mean variance of the mixture fraction
A	[m^2]	Area
$\mathbf{A}_x, \mathbf{A}_y, \mathbf{A}_z$		Convection matrices (FEM)
$\boldsymbol{B}$		Global load vector
$\mathbf{C}$		Coupling matrix (FEM)
D	$[\frac{\text{m}^2}{\text{s}}]$	Diffusion coefficient
D	$[\frac{\text{W}}{\text{m}^3}]$	Energy source term
$\boldsymbol{D}$		Global vector of discrete nodal values (FEM)
Da	[-]	Damköhler number

E	$[\frac{J}{m^3}]$	Energy density
E_q	$[\frac{W}{m^2}]$	Eulerian spectrum of the heat release (premixed flame)
E_ω	$[\frac{W}{m^2}]$	Eulerian spectrum of the heat release (non-premixed flame)
F	[-]	Forcing function
F_i	$[\frac{W}{m^2}]$	Energy flux vector
H_l	$[\frac{J}{kg}]$	Lower heating value
$\mathbf{J}$	[-]	Jacobian matrix (FEM)
K	$[\frac{1}{s}]$	Model constant of boundary condition
$\mathbf{K}$		Global stiffness matrix (FEM)
$\mathbf{K}_{ij}$	[-]	Diffusion matrices (FEM)
Le	[-]	Lewis number
M	[-]	Mach number
M_k	$[\frac{kg}{mol}]$	Molar weight of the k-th species
$\mathbf{M}$		Global mass matrix (FEM)
$\mathbf{N}$	[-]	Matrix of shape functions (FEM)
P_a	[W]	Acoustic power released by the turbulent flame
P_k	$[\frac{kg}{ms^3}]$	Production term of turbulence
P_{th}	[W]	Thermal power released by the flame
Pr	[-]	Prandtl number
P^+, P^-	$[\frac{N}{m^2}]$	Complex amplitudes of right (+) and left (-) traveling waves
$\dot{\mathcal{Q}}_c$	$[\frac{W}{Hz}]$	Integral heat release spectrum of a premixed flame
$\dot{\mathcal{Q}}_z$	$[\frac{W}{Hz}]$	Integral heat release spectrum of a non-premixed flame
R	$[\frac{J}{kgK}]$	Specific gas constant
R	[-]	Reflection coefficient
R_m	$[\frac{J}{molK}]$	Universal gas constant
$R_{\rho u}^*$	[-]	Correlation function between turbulent density and velocity fluctuations
S	$[\frac{J}{kgK}]$	Complex amplitude of entropy wave
S	$[-]$	Swirl number
S_p	$[\frac{N}{m^2}]$	Entropy source in pressure formulation
$\mathcal{S}_V$	$[\frac{kg}{sHz}]$	Integral volume source spectrum of a premixed flame
$\mathbf{S}_a$	[-]	Scattering matrix
T	[K]	Temperature
T	[-]	Transmission coefficient
T_{ad}	[K]	Adiabatic flame temperature
$\mathcal{T}$	[K]	Temperature spectrum
$\widetilde{T''^2}$	[-]	Mean variance of the temperature
$\mathbf{T}$	[-]	Transfer matrix in p, u-notation
Tu	$[-]$	Turbulence intensity
V	$[m^3]$	Volume
V_{coh}	$[m^3]$	Coherence volume
V_f	$[m^3]$	Flame volume
X_k	[-]	Molar fraction of the k-th species
Y_k	[-]	Mass fraction of the k-th species

| Z | [-] | Reduced impedance |
| Z_a | [-] | Acoustic impedance |

Greek letters

Symbol	Unit	Meaning
α	$[\frac{1}{K}]$	Volumetric expansion coefficient
α	[-]	Constant of velocity spectrum
α_τ	[-]	Constant for stabilization parameter
β	[-]	Constant of velocity spectrum
δ_f	[m]	Flame thickness
δ_t	[m]	Turbulent flame thickness
ϵ	$[\frac{W}{kg}]$	Turbulent dissipation rate
ζ	[-]	Noise ratio
η	$[\frac{kg}{ms}]$	Dynamic viscosity
η_c	[m]	Spectral cut-off length scale
η_k	[m]	Characteristic length of Kolmogorov sub-scales
η_t	$[\frac{kg}{ms}]$	Turbulent dynamic viscosity
θ	[rad]	Cylindrical (polar) coordinate
θ	[-]	Non-dimensional temperature
$\widetilde{\theta''^2}$	[-]	Non-dimensional temperature variance
κ	[-]	Isentropic exponent
κ	$[\frac{1}{m}]$	Wave number in spectral models
λ	[-]	Air ratio
λ	$[\frac{W}{mK}]$	Heat conductivity
λ	[m]	Wave length
μ_k	$[\frac{J}{mol}]$	Chemical potential of the k-th species
ν	$[\frac{m^2}{s}]$	Kinematic viscosity
ν_t	$[\frac{m^2}{s}]$	Turbulent kinematic viscosity (eddy viscosity)
$\xi_i, \boldsymbol{\xi}$	[m]	Cartesian position vector in parameter space (FEM)
π	[-]	Circle number pi
ρ	$[\frac{kg}{m^3}]$	Density
ρ_e	$[\frac{kg}{m^3}]$	Excess density
σ	[-]	Standard deviation
σ	$[\frac{W}{m^2K^4}]$	Stefan-Boltzmann constant
σ	[-]	Scaling coefficient in boundary condition
$\sigma_k, \sigma_\epsilon$	[-]	Modeling constants of $k-\epsilon$ turbulence model
τ	[-]	Heat release parameter of Bray Moss Libby (BML) model
τ	[s]	Time delay
τ_c	[s]	Characteristic chemical time scale
τ_s	[s]	Retarded time

τ_t	[s]	Characteristic turbulent time of integral scales
$\boldsymbol{\tau}$	$[\frac{1}{s}]$	Stabilization matrix
$\tau_{ij}, \boldsymbol{\tau}$	$[\frac{N}{m^2}]$	Shear stress tensor
$\tau_{ij,L}, \boldsymbol{\tau}_L$	$[\frac{N}{m^2}]$	Lighthill stress tensor
ϕ		Arbitrary quantity
ϕ	[-]	Equivalence ratio
$\hat{\boldsymbol{\phi}}$		Vector of unknowns (FEM)
χ	$[\frac{1}{s}]$	Scalar dissipation rate
χ_q	$[\frac{W}{m^3 Hz}]$	Lagrangian frequency spectrum of the heat release rate
$\chi_{\widetilde{c''2}}$	$[\frac{1}{Hz}]$	Auto-spectrum (Power spectral density) of the reaction progress variable
$\chi_{\widetilde{T''2}}$	$[\frac{K^2}{Hz}]$	Auto-spectrum (Power spectral density) of the temperature
$\chi_{\widetilde{z''2}}$	$[\frac{1}{Hz}]$	Auto-spectrum (Power spectral density) of the mixture fraction
$\chi_{\rho u}$	$[\frac{kg}{m^2 sHz}]$	Cross-spectrum of the velocity density covariance
ω	$[\frac{1}{s}]$	Circular frequency
$\dot{\omega}_c$	$[\frac{kg}{m^3 s}]$	Source term of the reaction progress variable
$\dot{\omega}_k$	$[\frac{kg}{m^3 s}]$	Reaction term of k-th species
$\dot{\omega}_z$	$[\frac{W}{m^3}]$	Source term of non-premixed flame
$\dot{\omega}_T$	$[\frac{W}{m^3}]$	Heat of combustion (energy eq. in enthalpy formulation)
Γ	$[m^2]$	Boundary
Δh_R	$[\frac{J}{kg}]$	Enthalpy of reaction
Φ	$[\frac{W}{m^3}]$	Dissipation function
Ω	$[m^3]$	Domain
$\Omega_i, \boldsymbol{\Omega}$	$[\frac{1}{s}]$	Vorticity vector

Sub- and Superscripts

INDEX	MEANING
$\bar{\ldots}$	Stationary/ Time-averaged quantity
$\ldots'$	Coherent linear fluctuating quantity
$\ldots''$	Stochastic turbulent quantity
$\hat{\ldots}$	Complex amplitude
$\langle\ldots\rangle$	Ensemble / phase-averaged quantity
$\widetilde{\ldots}$	Favre-averaged quantity
$\ldots^*$	Conjugate complex quantity
0	Initial conditions / Reference state
1	Combustion chamber inlet plane
2	Combustion chamber outlet plane
3	Exhaust nozzle exit plane

i, j, k, l	Einstein's summation indices
a	Fluctuating quantity related to acoustic wave
c	Quantity related to premixed flame
$conv$	Convergent nozzle part
d	Downstream
d	Direct noise
div	Divergent nozzle part
(e)	Element
exp	Experimental quantity
i	Indirect noise
k	Species index
min	Nozzle throat
ref	Reference value
rms	rms value
s	Fluctuating quantity related to entropy wave
st	Value at stoichiometric conditions
t	Turbulent quantity
u	Upstream
v	Fluctuating quantity related to vorticity wave
z	Quantity related to non-premixed flame
D	Dirichlet boundary
F	Fuel
GLS	GLS-stabilized
N	Neumann boundary
O	Oxidizer
P	Products
R	Reactants
T	Transpose of a vector

Mathematical Operators and Symbols

SYMBOL	MEANING
d	Differential operator
det	Determinant
$e/\exp$	Exponential / Euler function
i	Imaginary unit
log	Logarithm function
max	Maximum function
min	Minimum function
$\mathbb{C}$	Set of complex values
D	Material differential operator

$\mathcal{F}$	Fast Fourier transformation (FFT)
$\mathcal{L}$	Linear differential operator vector
$\mathcal{O}$	Landau symbol
$\mathbb{R}$	Set of real values
$\Re$	Real part of complex quantity
$\mathcal{R}$	Residual vector
δ_{ij}	Kronecker delta
ϵ_{ijk}	Permutation matrix in index notation
$\rho(\dots)$	Spectral radius
Δ	Difference
∂	Partial differential operator

Abbreviations

SYMBOL	MEANING
ACARE	Advisory Council for Aviation Research and Innovation in Europe
APE	Acoustic perturbation equations
BML	Bray Moss Libby
CAA	Computational aeroacoustics
CESAM-HP	Combustion étagée swirlée acoustiquement maîtrisée-high pressure
CFD	Computational fluid dynamics
CNRS	Centre National de la Recherche Scientifique
DLR	German Aerospace Center
DNS	Direct numerical simulation
EDM	Eddy dissipation model
EWG	Entropy Wave Generator
FEM	Finite element method
FFT	Fast Fourier transformation
FGM	Flamelet Generated Manifold
FRPM-CN	Fast random particle-mesh methods for combustion noise
GLS	Galerkin/least-squares method
HAT	Hot Acoustic Testrig
ICS	Impedance control system
LEE	Linearized Euler equations
LES	Large eddy simulation
LNSE	Linearized Navier-Stokes equations
LOTAN	Low-Order Thermo-Acoustic Network Model
LPP	lean premixed prevaporized
NGV	Turbine nozzle guide vane
OP	Operating point

PDE	Partial differential equation
PDF	Probability density function
PERM	Partially evaporating and rapid mixing
PIV	Particle-image velocimetry
PWL	Sound power level
RANS	Reynolds averaged Navier-Stokes equations
RECORD	Research on Core Noise Reduction
RMS	Root mean square
RQL	Rich-burn quick-quench lean-burn
RSM	Reynolds stress turbulence model
SPL	Sound pressure level
TUM	Technische Universität München
UCAM	University of Cambridge
UDF	User defined functions
URANS	Unsteady Reynolds averaged Navier-Stokes equations
VWG	Vorticity Wave Generator

1   Introduction

In the near future the air traffic is expected to increase significantly, which makes a further reduction of aircraft noise indispensable. This must address all aircraft components, but particularly the engine, in order to meet strict political requirements such as the ACARE[1] goal prescribing a noise reduction of 50% by 2020. The earlier development of reduction technologies has been mainly focused on the aero engine fan, compressor and jet noise leading to the invention of forced mixers, chevrons and acoustic linings in the intake, among others, cf. fig. 1.1. Beyond this the successive increase of the aero engine bypass-ratio results in low jet noise emissions and high propulsion efficiencies. Altogether this highlights the increasing relevance of core noise in modern aero engines, representing an additional contribution to jet noise. This additional noise component was initially reported by Cumpsty and Marble [1977a] and termed excess noise. It is closely related to the unsteady turbulent combustion process, which represents a natural source of combustion noise. The operation of modern premixing low-NOx combustors even intensifies combustion noise as compared to conventional Rich-burn quick-quench lean-burn (RQL) combustors [Dowling and Mahmoudi, 2015, Dowling and Stow, 2003, Lieuwen, 2003]. Additionally, lean burning technologies such as the lean premixed prevaporized (LPP) combustion are more likely to promote combustion instabilities [Dowling, 1995]. These resonance phenomena evolve from the feedback of acoustics on the combustion process: Under certain circumstances the unsteady combustion is enhanced by the acoustics, which in turn leads to an amplification of the acoustics and so forth. As a result combustion instabilities appear as tonal peaks at distinct frequencies in the noise spectrum which constitutes a major difference to broadband combustion noise, which is the central topic of this thesis.

1.1 Motivation

In general combustion noise of turbulent flames originates from two different mechanisms [Crighton et al., 1992, Howe, 2010], which are illustrated in fig. 1.2: The first mechanism is called direct combustion noise. It is caused by unsteady combustion due to interactions between the turbulent flow and the flame. These interactions create locally coherent fluctuations of heat release and combustion gas expansion on the scales of turbulence. These act as monopole sound sources and in sum produce acoustic waves, which are termed direct combustion noise. The second relevant mechanism is the indirect combustion noise. It originates from the acceleration of convected temperature inhomogeneities (hot and cold-spots)

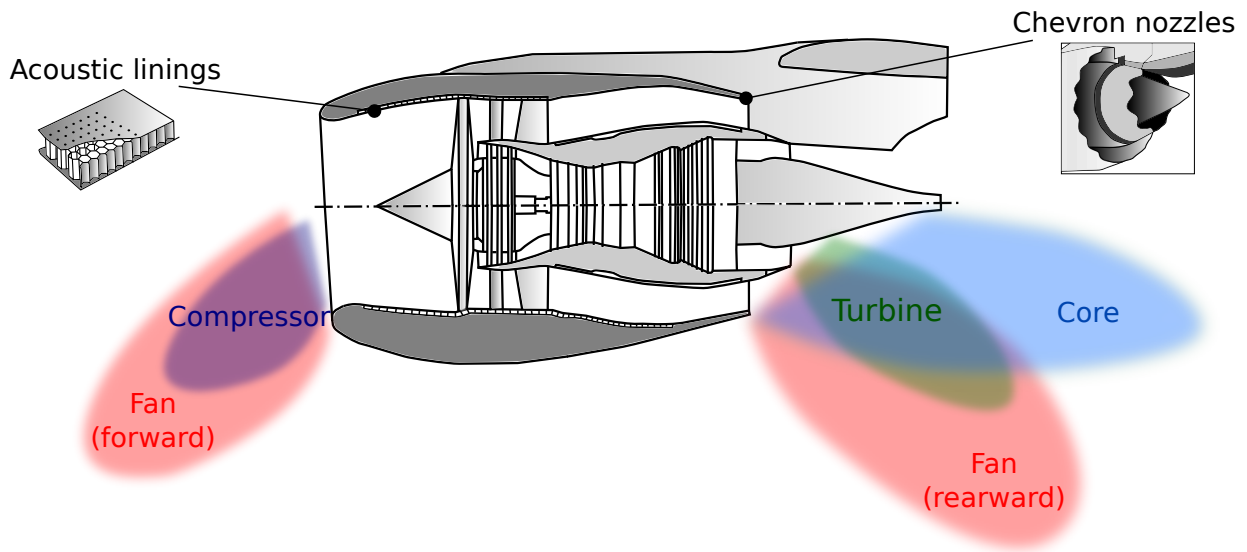[1]Advisory Council for Aviation Research and Innovation in Europe, `www.acare4europe.com`

Figure 1.1: Noise characteristics of a modern high bypass-ratio aero engine at departure and approach operating conditions. Adapted from Bräunling [2009].

and vortical fluctuations into the turbine, which are created by the unsteady combustion process of the flame, [Cumpsty, 1979, Cumpsty and Marble, 1977a,b]. Both mechanisms are treated in more detail in the following paragraphs.

Direct combustion noise shows broadband characteristics as it is created by flame-turbulence interactions involving a wide range of length and time scales [Dowling and Mahmoudi, 2015]. A representative combustion noise spectrum of a turbulent premixed flame without enclosure as measured by Rajaram and Lieuwen [2009] is sketched in fig. 1.3. The spectrum is characterized by a distinct maximum amplitude, which occurs around the so called peak frequency f_p. It separates the spectrum into a low frequency region where amplitudes grow towards the peak frequency with f^β and the high frequency region where amplitudes fall with $f^{-\alpha}$. In general the shape of the combustion noise spectrum depends on various parameters such as the thermal power, the burner geometry, the incoming turbulence intensity, the swirl number and the equivalence ratio [Kotake and Takamoto, 1987, 1990, Winkler et al., 2005]. Several scaling laws were developed to estimate the different influencing parameters, some of which were collected by Crighton et al. [1992] and Candel et al. [2009]. Recent overviews about the topic of combustion noise are given by Candel et al. [2009] or Dowling and Mahmoudi [2015].

Indirect combustion noise is associated with the acceleration of temperature and vortical inhomogeneities downstream of the combustor [Cumpsty, 1979, Cumpsty and Marble, 1977a,b]. These temperature and vortical disturbances are also known as entropy and vorticity waves. They are created in the mixing regions of the combustion chamber and are convected with the mean flow into the turbine. There the turbine nozzle guide vane
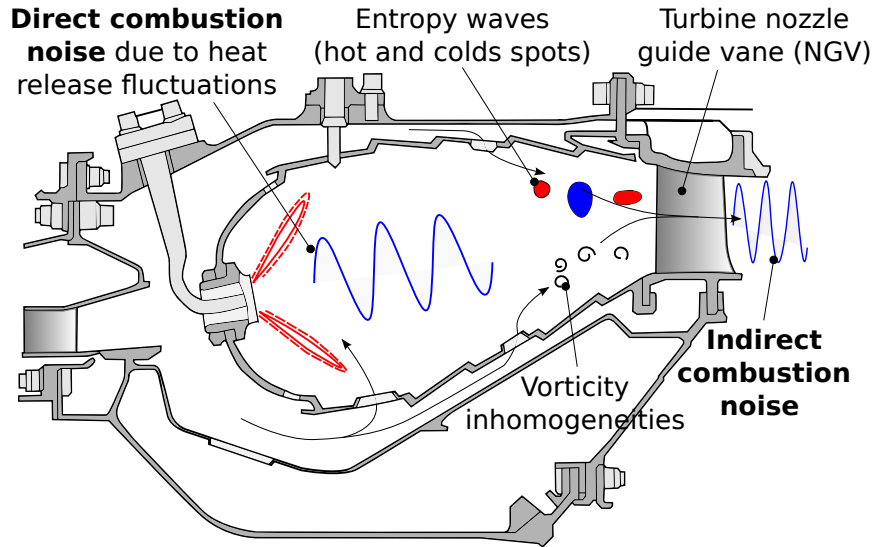
Figure 1.2: Sketch of a conventional RQL aero engine combustor and its two main combustion noise sources. Adapted from Bräunling [2009].

(NGV) provides strong flow acceleration up to transsonic conditions which results in the release of indirect combustion noise, cf. fig. 1.2. Entropy waves are created as a consequence of mixture fraction fluctuations caused by incomplete premixing of fuel and air or through secondary air mixing from dilution jets and liner cooling. They are less intense in premixed systems and even vanish in the limiting case of perfectly premixed systems. For this reason the indirect noise generation is expected to be more relevant in conventional RQL combustors. Another important aspect to be considered in the context of indirect noise generation is the shear dispersion effect of entropy waves. Entropy waves are exposed to strong flow shearing effects in the combustion chamber which causes their attenuation before reaching the turbine NGV [Sattelmayer, 2003]. The damping effect due to shear dispersion depends on the mean flow characteristics and significantly increases with frequency.

Contradictory findings are reported in numerous studies about the magnitude of the contributions of direct and indirect noise to the overall combustion noise. Possibly this is because the separation of both noise contributions on full scale engine level is a challenging task. Cross-correlation techniques based on measurements of interior and exterior pressure signals were applied. Early studies of a single can-type combustor by Muthukrishnan et al. [1977] revealed a dominating influence of the indirect noise in the low frequency regime for a choked exhaust nozzle. Direct noise contributions were found to dominate the noise signature in case of low exit Mach numbers. The experimental studies by Miles [2010, 2011] of a full-scale turbofan engine provided further support of the importance of indirect noise in the low frequency range below 100 Hz. In recent experimental studies by Kings et al. [2016] and Mazur [2017] of a generic premixed and pressurized combustor the indirect noise was found to play a minor role as compared to direct noise emissions. These studies give
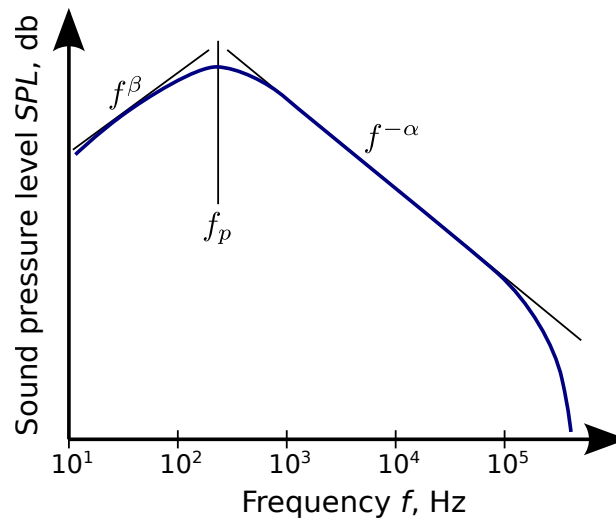
Figure 1.3: Typical combustion noise spectrum. Adapted from Rajaram and Lieuwen [2009].

strong support for the dependence of the indirect noise on the flame type. The influence of the entropy shear dispersion on the acoustic stability of a generic combustion chamber was investigated by Sattelmayer [2003] and Goh and Morgans [2011]. Even at low frequencies only weak coupling between the combustor acoustics and the indirect noise release was encountered. The study by Sattelmayer [2003] was confirmed by the experimental studies by Eckstein et al. [2006] and Eckstein and Sattelmayer [2006] who found a minor contribution of the feedback mechanism from indirect noise on the low-frequency stability of a liquid fueled RQL combustor. The generation of indirect noise was also investigated by Leyko et al. [2009] and Duran and Moreau [2013] using analytical and semi-analytical modeling tools, which were applied on simplified model combustors connected to a quasi one-dimensional nozzle. The major outcome of these studies is the dominance of indirect noise in case of high nozzle Mach numbers and low frequencies. In conclusion none of these studies ultimately settle the question of the contribution of indirect noise to the overall noise. They rather reveal some common qualitative tendencies such as the predominating low-frequency content of indirect noise whereas the quantitative result always depends on the particular case.

The findings above highlight the complexity of combustion generated noise, where interactions between fluid dynamics, thermodynamics and acoustics need to be taken into account. Important questions such as the contribution of indirect noise to the overall emitted noise have not been answered yet. The development of effective methods for the reduction of combustion noise emissions requires the further development of accurate predictive tools for combustion noise generation and propagation. Reliable predictions in terms of amplitudes and frequency content are of vital importance for the combustor development in all design stages in order to avoid additional development iterations. In particular subsequent

4

changes of the final design are extremely expensive and time-consuming. For this reason accurate predictions should be available as early as possible within the design process.

The **Re**search on **C**ore **N**oise **R**eduction (RECORD)[2] project, funded by the European Commission within the Seventh Framework Program FP7[3], aims to provide deeper understanding of the noise source mechanisms mentioned above. In this project state-of-the art methods covering the broad range from analytical models and experiments to high fidelity simulations were assessed and validated with respect to their ability for predicting core noise. The present thesis was developed in the frame of the RECORD project. Its main purpose is to make a contribution to the development of numerical methods for the prediction of combustion noise. The most important approaches towards this goal are in the next section.

1.2 Combustion Noise Prediction

In order to determine combustion noise emitted from turbulent flames, analytical methods, hybrid CFD/CAA-methods (computational fluid dynamics/ computational aeroacoustics) and compressible large eddy simulations (LES) were applied [Nicoud and Wieczorek, 2009]. Analytical methods are very inexpensive with respect to time and cost, but their applicability is usually limited to the specific combustors for which they were calibrated. The next more general stage of modeling are network models, which may approximate more complex geometries by a series of analytical elements. An example for such a network tool is the Low-Order Thermo-Acoustic Network Model (LOTAN) solver, developed by Stow and Dowling [2001] and Dowling and Mahmoudi [2015]. Network tools represent the industrial standard due to their broad applicability, robustness and low computational effort. However their validity and accuracy for complex combustor geometries and flows is questionable unless the network model was calibrated for the application. Compressible LES are computationally extremely expensive but have shown to deliver very accurate combustion noise predictions on laboratory scale [Huet et al., 2016, Kings et al., 2016] as well as on full scale engine level [Livebardon et al., 2015, 2016]. Hybrid CFD/CAA-methods were developed to significantly reduce the computational effort as compared with compressible LES while maintaining good prediction quality in complex geometries and flows. Hybrid models separate the involved phenomena into the mean reacting turbulent flow field described by reactive RANS and the acoustic field. CAA methods are most commonly based on a linearization procedure where small amplitude fluctuations are solved around a stationary mean flow field. Different levels of complexity are established by solving either the linear wave equation, the linearized Euler equations (LEE), the linearized Navier-Stokes equations (LNSE) or acoustic perturbation equations (APE) [Bui et al., 2007b, Ewert and Schröder, 2003]. These equations are excited by combustion noise source terms, which are either directly obtained from incompressible LES [Bui et al., 2006, 2007a] or calculated

---

[2]http://cordis.europa.eu/project/rcn/104865_en.html
[3]https://ec.europa.eu/research/fp7/index_en.cfm

using statistical models. There are two promising statistical combustion noise models, namely the Fast Random Particle-Mesh Methods for combustion noise (FRPM-CN) and the statistical spectral noise model developed by Hirsch et al. [2006, 2007]. The FRPM was initially invented by Ewert [2008] for aerodynamic and airframe noise predictions. Later it was extended to combustion noise by Mühlbauer et al. [2010] and Grimm et al. [2014]. The statistical noise model by Hirsch et al. [2007] derived for premixed flames was successfully applied on unconfined swirling flames [Wäsle, 2007, Winkler, 2007] and on a heater system [Weyermann, 2010]. The model was recently extended and validated for the prediction of non-premixed swirl flames by Jörg [2015]. Liu et al. [2014] applied a modified version of the model by Hirsch et al. [2007] to a network model of a demonstrator combustor and obtained good agreement with experimental data.

A difficulty of the hybrid CFD/CAA methods is the consistent derivation of the combustion noise source terms in the governing linearized equations. Based on the classical Lighthill equation [Lighthill and Newman, 1952], Dowling derived an extended wave equation for reacting flows, where combustion noise sources are expressed in terms of the excess density [Crighton et al., 1992]. This approach is followed by several authors: In the APE for reacting flows for instance the source term is determined by the total time derivative of the density [Bui et al., 2007a]. The FRPM-CN methods introduce sound sources by the evaluation of the total time derivative of the temperature [Mühlbauer et al., 2010]. Little attention has been payed to the different physics of entropy wave generation in perfectly premixed and non-premixed flames. While in perfectly premixed flames no propagating entropy waves are generated, the unmixedness of non-premixed flames leads to the formation of propagating entropy waves. This issue needs further clarification in particular because the combustion noise source model crucially impacts the indirect noise contribution. In recently published theoretical studies by Strobio Chen et al. [2014, 2016] the consideration of the flame surface movement is shown to be essential to correctly predict entropy wave generation. However the implementation of her findings in linearized equations such as LEE or LNSE remains unclear. Therefore hybrid approaches could not yet take advantage of them. In the present thesis a semi-analytical model of stochastic combustion noise source terms for hybrid approaches is proposed, which accounts for the different physics of the entropy wave generation in different flames. In this way a contribution to the further development of these predictive tools is made.

1.3 Goals and Structure

In this thesis a unified and comprehensive methodology for the numerical prediction of direct and indirect combustion noise of confined premixed and non-premixed flames is established. The core of the approach are frequency domain simulations of linear acoustic, entropy and vortical fluctuations described by the LNSE, which are solved around a stationary mean flow field obtained from reactive RANS simulations. The hybrid RANS/LNSE approach is based on the work by Gikadi et al. [2014]. It was successfully validated for

acoustic scattering problems with increasing complexity [Gikadi et al., 2012b, 2013] as well as for stability analyses in context of annular aero engine combustors [Gikadi et al., 2012a, 2014]. In the frame of the present thesis stochastic sound sources were incorporated in the LNSE using a triple-decomposition approach. A semi-analytical source model is proposed to account for the characteristics of entropy wave generation in perfectly-premixed and non-premixed flames. The stochastic sound and entropy sources are derived from heat release source spectra, which are obtained from a statistical noise model postprocessor. Depending on the flame type, the mean flow, turbulence and reaction rate fields from RANS are postprocessed using either the model for premixed flames by Hirsch et al. [2007] or the extension to non-premixed flames by Jörg [2015]. Finally, the LNSE combustor simulations are coupled to one-dimensional network models representing the components downstream of the combustor to compute the ratio between the indirect and direct noise at the nozzle exit. A validation strategy is presented to quantify the accuracy of the predictions of each separate step within the entire simulation chain above.

- Chapter 2 introduces the fundamental equations regarding reactive flows in the laminar and turbulent case. This includes a brief review of the RANS equations and related closure-models for premixed and non-premixed flames.

- The governing equations of non-reacting linear acoustics along with the most important analytical solutions and supplementing boundary conditions are presented in chapter 3. Scattering and transfer matrices are shortly introduced in the context of acoustic network models.

- After briefly reviewing the relevant literature on the general physics of combustion noise in chapter 4, a model for stochastic sound sources arising from turbulent reactive flows is embedded in the LNSE using a triple-decomposition approach. Semi-analytical submodels for perfectly-premixed and non-premixed flames are deduced based on physical reasoning in order to account for the different effects of entropy wave generation. This is followed by the review of the statistical noise models for premixed flames by Hirsch et al. [2007] and Liu et al. [2014], and the extension to non-premixed flames by Jörg [2015].

- Chapter 5 gives an overview about the entire methodology for the prediction of direct and indirect combustion noise, which includes the presentation of the entire simulation strategy and the different submodels.

- In chapter 6 the basic mechanisms of direct noise propagation and transmission in a convergent-divergent nozzle are investigated in the frame of the Entropy Wave Generator (EWG) and Hot Acoustic Testrig (HAT) test cases.

- Chapter 7 is focused on the examination of indirect noise generation by entropy waves and vorticity waves by applying the hybrid RANS/LNSE approach to the EWG and Vorticity Wave Generator (VWG) test cases.

- Three different combustors with successively increasing complexity are investigated in chapter 8. This includes the validation of the LNSE simulations applied in conjunction with different spectral noise models and the stochastic source term model proposed in this thesis.

- Finally in chapter 9 the main findings of this thesis are summarized and recommendations for further investigations on combustion noise are given.

2   Reacting Flows

Combustion noise of turbulent flames originates from unsteady flame-turbulence interactions which are responsible for local heat release fluctuations. These in turn lead to an unsteady gas expansion and finally to combustion noise. In this chapter the governing equations of reacting flows are given. This is followed by a sketch of the averaged and modeled set of equations used in all reactive mean flow simulations of the turbulent cases, which are referred to as RANS (Reynolds-averaged Navier-Stokes) equations. The RANS equations represent the basis for all combustor mean flow and turbulence simulations conducted in this thesis.

2.1 Governing Equations

The starting point for all mean flow and acoustic simulations in this thesis are the Navier-Stokes equations for reacting, compressible and viscous flows of n species. They are obtained by inserting the constitutive relations of an ideal gas into the conservation laws for mass (2.1), species (2.2), momentum (2.3) and energy (2.4) [Poinsot and Veynante, 2005]

$$\frac{\mathrm{D}\rho}{\mathrm{D}t} = -\rho\frac{\partial u_k}{\partial x_k}, \tag{2.1}$$

$$\rho\frac{\mathrm{D}Y_k}{\mathrm{D}t} = \frac{\partial}{\partial x_i}\left(\rho D_k\frac{\partial Y_k}{\partial x_i}\right) + \dot{\omega}_k, \tag{2.2}$$

$$\rho\frac{\mathrm{D}u_i}{\mathrm{D}t} = -\frac{\partial p}{\partial x_i} + \frac{\partial \tau_{ji}}{\partial x_j} = -\frac{\partial p}{\partial x_i} + \eta\frac{\partial}{\partial x_j}\left[\frac{\partial u_j}{\partial x_i} + \frac{\partial u_i}{\partial x_j} - \frac{2}{3}\delta_{ij}\frac{\partial u_k}{\partial x_k}\right], \tag{2.3}$$

$$\rho\frac{\mathrm{D}h}{\mathrm{D}t} = \frac{\mathrm{D}p}{\mathrm{D}t} + \Phi + \frac{\partial}{\partial x_i}\left(\lambda\frac{\partial T}{\partial x_i}\right) + \dot{q}_V. \tag{2.4}$$

The Navier-Stokes equations represent a system of five partial differential equations for the density ρ, velocity u_i and enthalpy h, along with n species equations for the n components of the mixture. The mixture composition is expressed in terms of the mass fractions Y_k. The pressure p, density ρ and temperature T are coupled through the equation of state

$$p = \rho RT, \tag{2.5}$$

where R defines the specific gas constant of the mixture. It represents the sum of mass-weighted gas constants of each mixture component R_k, i.e. $R = \sum_{k=1}^{n} Y_k R_k = R_m \sum_{k=1}^{n} Y_k/M_k$

with the universal gas constant R_m and molar weight M_k. In the energy eq. (2.4) the enthalpy h of the mixture is defined by the caloric equation of state

$$h = \sum_{k=1}^{n} h_k Y_k = \sum_{k=1}^{n} (h_{f,k}^0 + h_{s,k}) Y_k = \sum_{k=1}^{n} h_{f,k}^0 Y_k + h_s = \sum_{k=1}^{n} h_{f,k}^0 Y_k + \int_{T_0}^{T} c_p(T)\, \mathrm{d}T. \quad (2.6)$$

The enthalpy of the mixture h is determined by the sum of the mass-weighted enthalpies of the species h_k. The enthalpy of each species h_k is linked to the enthalpy of formation $h_{f,k}^0$ and the sensible enthalpy $h_{s,k}$, i.e. $h_k = h_{f,k}^0 + h_{s,k}$. The former one represents the chemical energy bounded in the molecules while the latter one stands for the thermal energy due to the statistical microscopic movement of the molecules. For ideal gases the sensible enthalpy only depends on the temperature but not on the pressure: $h_{s,k} = \int_{T_0}^{T} c_{p,k}(T)\mathrm{d}T$. Then the sensible enthalpy of the mixture h_s is the mass-weighted sum of the individual sensible enthalpies, so that $h_s = \sum_{k=1}^{n} h_{s,k} Y_k = \int_{T_0}^{T} \sum_{k=1}^{n} c_{p,k}(T) Y_k \mathrm{d}T = \int_{T_0}^{T} c_p(T) \mathrm{d}T$, with $c_p = \sum_{k=1}^{n} c_{p,k}(T) Y_k$ being the isobaric heat capacity of the mixture. Therefore the sensible enthalpy h_s is a measure for the temperature of the mixture.

As stated by the species eq. (2.2), changes of the mixture composition are a result of species diffusion with the diffusion coefficient D_k and the species formation rate $\dot{\omega}_k$ due to chemical reactions. The sum of all species formation rates $\dot{\omega}_k$ is zero to fulfill the global mass conservation as described by the continuity eq. (2.1). Eq. (2.3) expresses that momentum changes of the fluid are caused by pressure gradients and viscous shear stresses τ_{ij}, which are defined by the Cauchy-Poisson law [Spurk and Aksel, 2007]

$$\tau_{ij} = \eta \left(\frac{\partial u_i}{\partial x_j} + \frac{\partial u_j}{\partial x_i} \right) - \frac{2}{3} \eta \delta_{ij} \frac{\partial u_k}{\partial x_k}. \quad (2.7)$$

As stated by eq. (2.4), the enthalpy of the mixture is changed along the streamlines by material pressure changes, viscous dissipation, thermal heat conduction with the thermal conductivity λ and external energy sources $\dot{q}_V$ like electrical heating. Viscous dissipation is quantified by the dissipation function Φ, which describes the irreversible and isotropic conversion of kinetic energy into sensible enthalpy h_s by viscous shear stresses τ_{ij}, i.e.

$$\Phi := \tau_{ij} \frac{\partial u_i}{\partial x_j} = \eta \frac{\partial u_i}{\partial x_j} \left[\frac{\partial u_j}{\partial x_i} + \frac{\partial u_i}{\partial x_j} - \frac{2}{3} \delta_{ij} \frac{\partial u_k}{\partial x_k} \right]. \quad (2.8)$$

The enthalpy eq. (2.4) does not contain source terms due to chemical reactions like combustion. In absence of viscous and thermal diffusion ($\tau_{ij} = \lambda = 0$) the enthalpy eq. (2.4) for low Mach number flames ($\mathrm{D}p/\mathrm{D}t = 0$) simplifies to $\mathrm{D}h/\mathrm{D}t = 0$. In this case the enthalpy is conserved across the flame, i.e. $h = \mathrm{const}$.

In the following alternative formulations of the energy eq. (2.4) are presented. The pressure formulation is in particular relevant for the implementation of the acoustic propagation models. The sensible enthalpy and entropy formulation are of vital importance for the development and analysis of the combustion noise source terms embedded in the acoustic equations.

Energy Equation in Sensible Enthalpy Formulation

The equation for the sensible enthalpy of the mixture is obtained by inserting the caloric equation of state (2.6) into the energy eq. (2.4) [Poinsot and Veynante, 2005]

$$\rho\frac{\mathrm{D}h_s}{\mathrm{D}t} = \frac{\mathrm{D}p}{\mathrm{D}t} + \Phi + \frac{\partial}{\partial x_i}\Big(\lambda\frac{\partial T}{\partial x_i}\Big) + \dot{q}_V + \frac{\partial}{\partial x_i}\Big(\rho\sum_{k=1}^{n} h_{s,k}D_k\frac{\partial Y_k}{\partial x_i}\Big) + \dot{\omega}_T. \qquad (2.9)$$

Unlike the enthalpy eq. (2.4), the source term $\dot{\omega}_T$ due to chemical reactions is contained in eq. (2.9). The heat rate of combustion $\dot{\omega}_T$ connects the energy eq. (2.9) to the species eq. (2.2) through the species formation rate $\dot{\omega}_k$, i.e.

$$\dot{\omega}_T = -\sum_{k=1}^{n} h_{f,k}^0 \dot{\omega}_k. \qquad (2.10)$$

The change of the mixture composition due to combustion leads to a change of the chemical energy contained in the molecules. For exothermic reactions the sum of the formation enthalpies of the products is lower than the sum of the formation enthalpies of the reactants. Therefore the release of chemical energy due to combustion is reflected in an increase of the sensible enthalpy and temperature across the flame while the enthalpy stays constant. This process of the partial conversion of chemically bounded energy into sensible enthalpy is described by the heat rate of combustion $\dot{\omega}_T$.

Energy Equation in Pressure Formulation

The energy equation (2.9) may be expressed alternatively in terms of the pressure as demonstrated by Poinsot and Veynante [2005]. The derivation is based on the continuity eq. (2.1) and the sum of the species in eq. (2.2), each of which are multiplied by $h_{s,k}$ in order to deliver a relation between the material derivative of the sensible enthalpy and temperature. This relation is used to replace the sensible enthalpy in eq. (2.9), so that an exclusive equation for the material derivative of the temperature is obtained. Inserting the equation of state (2.5) in differential form along with the assumption of equal heat capacities for all species ($c_{p,k} = c_p$ implying $h_{s,k} = h_s$) yields the energy equation in pressure formulation:

$$\frac{\mathrm{D}p}{\mathrm{D}t} = -p\kappa\frac{\partial u_k}{\partial x_k} + \kappa p\frac{1}{R}\frac{\mathrm{D}R}{\mathrm{D}t} + (\kappa - 1)\Big\{\Phi + \frac{\partial}{\partial x_i}\Big(\lambda\frac{\partial T}{\partial x_i}\Big) + \dot{q}_V + \rho\sum_{k=1}^{n}\Big(c_{p,k}D_k\frac{\partial Y_k}{\partial x_i}\Big)\frac{\partial T}{\partial x_i} + \dot{\omega}_T\Big\}.$$
$$(2.11)$$

Here the ratio between the specific isobaric heat capacity c_p and the isochoric heat capacity c_v is termed isentropic exponent $\kappa := c_p/c_v$. The pressure of a certain fluid particle mainly changes due to compressibility effects as it travels along the streamline. This is represented by the first term in eq. (2.11). In reactive flows the change of the ideal gas constant (second term) is usually negligible for the material derivative of the pressure [Poinsot and

Veynante, 2005]. All remaining terms in eq. (2.11) related to viscous dissipation, thermal heat conduction, electrical heating, species diffusion and combustion already appeared in the sensible enthalpy formulation. The energy equation in pressure formulation (2.11) is the basis for all acoustic simulations in the present thesis.

Energy Equation in Entropy Formulation

The energy eq. (2.11) is subsequently reformulated in terms of the specific entropy s to provide the basis for a thorough analysis of the generation mechanisms of entropy waves given later in sec. 3.2. This is of vital importance for this thesis because of its goal to develop combustion noise source terms and to accurately predict indirect noise. The energy equation in entropy form reads [Crighton et al., 1992, Lieuwen, 2012]:

$$\rho T \frac{\mathrm{D}s}{\mathrm{D}t} = \tau_{ij}\frac{\partial u_i}{\partial x_j} - \frac{\partial \dot{q}_i}{\partial x_i} + \dot{q}_V - \rho \sum_{k=1}^{n} \frac{\mu_k}{M_k}\frac{\mathrm{D}Y_k}{\mathrm{D}t}. \tag{2.12}$$

The last term on the right of eq. (2.12) is related to the combustion, where μ_k represents the chemical potential of the k-th species. The energy flux vector $\dot{q}_i$ is associated with heat conduction and diffusive mass transport [Poinsot and Veynante, 2005]. Eq. (2.12) states that entropy sources arise from viscous dissipation, heat transfer, combustion and species diffusion [Lieuwen, 2012]. Crighton et al. [1992] initially derived the material derivative of the entropy as a function of pressure and density, which yields

$$\left(\frac{\partial p}{\partial s}\right)_{\rho,Y_k}\frac{\mathrm{D}s}{\mathrm{D}t} = \left[\frac{\mathrm{D}p}{\mathrm{D}t} - c^2\frac{\mathrm{D}\rho}{\mathrm{D}t} - \sum_{k=1}^{n}\left(\frac{\partial p}{\partial Y_k}\right)_{\rho,s,Y_{m\neq k}}\frac{\mathrm{D}Y_k}{\mathrm{D}t}\right]. \tag{2.13}$$

They further eliminated the entropy derivative to obtain the pressure-density relation for reactive flows in differential form

$$\frac{\mathrm{D}\rho}{\mathrm{D}t} = \frac{1}{c^2}\frac{\mathrm{D}p}{\mathrm{D}t} + \frac{\alpha}{c_p}\left[\rho\sum_{k=1}^{n}\left(\frac{\partial h}{\partial Y_k}\right)_{\rho,p,Y_{m\neq k}}\frac{\mathrm{D}Y_k}{\mathrm{D}t} - \frac{\partial}{\partial x_i}\left(\lambda\frac{\partial T}{\partial x_i}\right) - \Phi - \dot{q}_V\right], \tag{2.14}$$

with the speed of sound c and the volumetric expansion coefficient $\alpha = -1/\rho(\partial\rho/\partial T)_p$, which equals $\alpha = 1/T$ for ideal gases. The speed of sound c of an ideal gas is defined by the isentropic pressure-density-gradient of the mean flow [Sattelmayer, 2008]:

$$c^2 := \left(\frac{\partial p}{\partial \rho}\right)_s = \kappa\frac{p}{\rho} = \kappa RT. \tag{2.15}$$

In the pressure-density relation (2.14), the derivative of the enthalpy with respect to the k-th mass fraction $(\partial h/\partial Y_k)_{\rho,p,Y_m} = h_{f,k}^0$ is equal to the enthalpy of formation when assuming isomolar combustion [Dowling and Mahmoudi, 2015]. This can be shown by taking the derivative of eq. (2.6) with respect to the mass fraction Y_k while keeping the density, pressure and all other mass fractions $Y_{m\neq k}$ constant. Taking this result into account together

with the species eq. (2.2) with negligible mass diffusion ($\rho DY_k/Dt = \dot{\omega}_k$), the second term on the right hand side of (2.14) turns out to be the heat rate of combustion as defined by eq. (2.10), i.e. $\dot{\omega}_T = -\sum_{k=1}^{n}(\partial h/\partial Y_k)_{\rho,p,Y_m}\rho DY_k/Dt$.

The pressure-density relation (2.14) is of particular importance for the derivation of a relation between the source terms in the continuity and energy equation of the LNSE including stochastic sources. This will be demonstrated and discussed in detail in subsec. 4.2.1. The LNSE implementation presented in this thesis utilizes the density, velocities and pressure as primary solver variables, whereas the entropy is not explicitly solved. Instead the entropy generation and propagation is implicitly encoded in the continuity and energy equation in pressure formulation as defined by the entropy differential in eq. (2.13). This equation is evaluated in subsec. 4.2.3 to reveal the impact of the different source models on the entropy production.

2.2 RANS Simulation

For realistic applications computational resources and time are too limited to fully resolve the compressible turbulent reactive flow in time and space. This explains why turbulent flows are often described in a stochastic sense involving a certain degree of turbulence modeling. The most prominent representative of the stochastic turbulence description are the Reynolds-Averaged Navier-Stokes-Equations (RANS).

Reynolds- and Favre Decomposition

The standard reactive RANS equation set is based on Favre averages. The instantaneous variable ϕ is decomposed into a density weighted mean $\widetilde{\phi}$ and a fluctuating variable ϕ''. For a statistically steady flow this becomes as if an unsteady ensemble average is sought:

$$\phi\left(\boldsymbol{x},t\right) = \widetilde{\phi}\left(\boldsymbol{x}\right) + \phi''\left(\boldsymbol{x},t\right), \qquad \text{where} \qquad \widetilde{\phi} = \frac{\langle\rho\phi\rangle}{\langle\rho\rangle}. \qquad (2.16)$$

Averaged Conservation Equations and Closure Models

The RANS equations for a reactive compressible flow are obtained by substituting the Favre decomposition (2.16) into the Navier-Stokes eqs. (2.1)-(2.4). This is followed by ensemble-averaging for statistically unsteady flows or time-averaging for statistically stationary flows. The complete set of equations is derived and explained in detail by Poinsot and Veynante [2005]. It should be noted that the particular form of the energy equation, e.g. (2.4) or (2.9), depends on the CFD solver. The formulations of the energy equation applied in this thesis are specified below.

The RANS equations contain various unclosed terms, which need to be modeled as a function of the average primitive variables. Turbulent shear stresses of the form $\langle\rho\rangle\widetilde{u_i'' u_j''}$

are modeled using the *Boussinesq-hypothesis*, which belongs to the *eddy-viscosity-models* [Adams, 2008]. It postulates a linear relation between the turbulent shear stresses and the anisotropic part of the mean velocity gradient

$$\langle \rho u_i' u_j' \rangle = \langle \rho \rangle \widetilde{u_i'' u_j''} = \frac{2}{3} \delta_{ij} \langle \rho \rangle k - \eta_t \left(\frac{\partial \widetilde{u}_i}{\partial x_j} + \frac{\partial \widetilde{u}_j}{\partial x_i} - \frac{2}{3} \delta_{ij} \frac{\partial \widetilde{u}_k}{\partial x_k} \right). \tag{2.17}$$

The dynamic turbulent or so-called eddy viscosity η_t is not a material property but a property of the turbulent flow field. It may be also given in terms of the kinematic viscosity, so that $\nu_t = \mu_t / \langle \rho \rangle$. The turbulent kinetic energy is defined as $k := \frac{1}{2} \widetilde{u_i'' u_i''}$. In the k-ϵ model mainly used in this thesis the turbulent viscosity ν_t is determined by the turbulent kinetic energy k and the turbulent dissipation rate ϵ

$$\nu_t = c_\mu \frac{k^2}{\epsilon}, \tag{2.18}$$

where $c_\mu = 0.09$ is a constant of proportionality. Turbulent fluxes of species and enthalpy are usually approximated by means of the gradient assumption [Ferziger and Peric, 2008]:

$$\langle \rho \rangle \widetilde{u_i'' \phi''} = -\langle \rho \rangle \frac{\nu_t}{\sigma_\phi} \frac{\partial \widetilde{\phi}}{\partial x_i}, \qquad \text{where} \qquad \phi = Y_k, h_s. \tag{2.19}$$

The two equation based k-ϵ turbulence model is one well known approach for estimating the turbulent viscosity in eq. (2.18). While the transport equation for the turbulent kinetic energy k may be derived analytically from the RANS, the corresponding transport equation for ϵ is modeled in accordance to k, which finally yields [Adams, 2008, Pope, 2000]

$$\frac{\partial}{\partial t} (\langle \rho \rangle k) + \frac{\partial}{\partial x_i} (\langle \rho \rangle \widetilde{u}_i k) = \frac{\partial}{\partial x_i} \left[\left(\nu + \frac{\nu_t}{\sigma_k} \right) \frac{\partial k}{\partial x_i} \right] + P_k - \langle \rho \rangle \epsilon, \tag{2.20}$$

$$\frac{\partial}{\partial t} (\langle \rho \rangle \epsilon) + \frac{\partial}{\partial x_i} (\langle \rho \rangle \widetilde{u}_i \epsilon) = \frac{\partial}{\partial x_i} \left[\left(\nu + \frac{\nu_t}{\sigma_\epsilon} \right) \frac{\partial \epsilon}{\partial x_i} \right] + c_{\epsilon 1} \frac{\epsilon}{k} P_k - c_{\epsilon 2} \langle \rho \rangle \frac{\epsilon^2}{k}. \tag{2.21}$$

The term $P_k = -\langle \rho \rangle \widetilde{u_i'' u_j''} \partial \widetilde{u}_i / \partial x_j$ is responsible for the production of turbulence. The model constants are: $c_{\epsilon 1} = 1.44$, $c_{\epsilon 2} = 1.92$, $\sigma_k = 1.0$ and $\sigma_\epsilon = 1.3$.

The RANS equations contain the averaged source terms $\langle \dot{\omega}_k \rangle$ due to combustion in the averaged form of the species eq. (2.2). The averaged heat of combustion $\langle \dot{\omega}_T \rangle$, defined by eq. (2.10), appears in the RANS equations as an additional source term if the energy equation is implemented in terms of the sensible enthalpy. When simplifying the chemical reactions of a premixed flame to an irreversible one-step chemistry, the energy eq. (2.9) and species eqs. (2.2) can be reduced to a single equation for the reaction progress variable. Even in this case of a drastically simplified reaction model the RANS still contain an averaged source term in the equation for the progress variable. In the RANS equations these averaged combustion source terms like the reaction rates of the k-th species $\langle \dot{\omega}_k \rangle$ are closed by appropriate combustion models, which account for the particular flame type and

combustion regime [Poinsot and Veynante, 2005].

The reactive mean flow RANS simulations were performed with ANSYS FLUENT RE-LEASE 14.0 [ANSYS, 2011a]. The standard k-ϵ model with Boussinesq approach was chosen for the turbulence closure [ANSYS, 2011a, chapter 4.3.1, page 49]. The models of the particular flame types applied in this thesis will be shortly described below in the corresponding subsections for premixed and non-premixed flames.

Premixed Flames

Premixed flames were calculated with the finite-rate/Eddy-dissipation combustion model implemented in the code ANSYS FLUENT RELEASE 14.0 [ANSYS, 2011a, chapter 7.1.2.3., page 204]. In this case the energy equation is implemented in form of the total internal energy, defined by $e_t = e_s + u^2/2 = h_s - p/\rho + u^2/2$. The equation is explicitly given by [ANSYS, 2011a, chapter 5.2.1.1., page 140].

Diffusion Flames

Non-premixed flames [ANSYS, 2011a, chapter 8.2, page 226] were simulated using the flamelet model [ANSYS, 2011a, chapter 8.4, page 248] and the build in flamelet table generator [ANSYS, 2011b, chapter 17.6., page 927]. In case of non-premixed combustion the energy equation is implemented in form of the enthalpy eq. (2.4) [ANSYS, 2011a, chapter 5.2.1.3, page 141].

As explained in detail in sec. 2.1, the enthalpy equation eq. (2.4) does not contain a heat release source term due to combustion. However in context of the statistical noise modeling of non-premixed flames the mean flow heat release rate is needed. According to Poinsot and Veynante [2005] the mean heat rate of combustion is retrieved by evaluating

$$\langle\dot{\omega}_z^*\rangle(\widetilde{z''^2}) = \frac{Y_F^0 H_l}{2(1-z_{st})}(\langle\rho\rangle\widetilde{\chi})p(z_{st}) = \frac{Y_F^0 H_l}{2(1-z_{st})}c_d\langle\rho\rangle\frac{\epsilon}{k}\widetilde{z''^2}p(z_{st}), \tag{2.22}$$

where $p(z_{st})$ is the assumed probability-density function (PDF) evaluated at the stoichiometric mixture fraction z_{st}. The mean scalar dissipation rate $\widetilde{\chi} = 2D(\nabla\widetilde{z})^2$ depends on the mean mixture fraction gradient. Comparing the field integral of (2.22) with the integral balance some inconsistency due to finite numerical resolution is found. This is corrected by the scaling factor c_q, which is introduced in eq. (2.22)

$$c_q := \frac{\dot{m}_F H_l}{\int_V \langle\dot{\omega}_z^*\rangle \mathrm{d}V}, \tag{2.23}$$

where $\dot{m}_F$ denotes the total fuel mass flow and H_l the lower heating value. Then the mean heat release distribution of a non-premixed flame is determined by $\langle\dot{\omega}_z\rangle = c_q\langle\dot{\omega}_z^*\rangle$.

3 Aeroacoustic Models

The purpose of this chapter is to introduce the most prominent aeroacoustic propagation models without considering the different noise sources. These are the linearized Navier-Stokes equations (LNSE), the linearized Euler equations (LEE) and the inhomogeneous wave equation. Important features of the LNSE such as the interactions of acoustic, entropy and vorticity waves are outlined as they are sources of indirect noise. Analytical solutions for acoustic and entropy waves are reviewed along with the appropriate boundary conditions for the LNSE simulations. As they are later used acoustic network models derived from the LEE including the scattering and transfer matrices are briefly introduced.

This chapter represents the basis for the more complex combustion noise source modeling, which is the topic of the subsequent chapter. As combustion noise is not considered in this chapter, all equations presented in the following are limited to non-reacting flows.

3.1 Linearization

In the linear acoustic theory any unsteady quantity of the flow field $\phi(\boldsymbol{x}, t)$ is decomposed into its statistically stationary mean part $\bar{\phi}(\boldsymbol{x})$ and small periodic fluctuations $\phi'(\boldsymbol{x}, t)$ in time. The unsteady fluctuating contribution is assumed to be small compared to the mean part such that products of fluctuating quantities are negligible, i.e. $\phi'\phi' \approx 0$:

$$
\begin{aligned}
\rho\left(\boldsymbol{x}, t\right) &= \bar{\rho}\left(\boldsymbol{x}\right) + \rho'\left(\boldsymbol{x}, t\right), & \rho' &\ll \bar{\rho}, \\
u_i\left(\boldsymbol{x}, t\right) &= \bar{u}_i\left(\boldsymbol{x}\right) + u_i'\left(\boldsymbol{x}, t\right), & u_i' &\ll \bar{c}, \\
p\left(\boldsymbol{x}, t\right) &= \bar{p}\left(\boldsymbol{x}\right) + p'\left(\boldsymbol{x}, t\right), & p' &\ll \bar{p}.
\end{aligned}
\tag{3.1}
$$

Eq. (3.1) appears to be similar to the Reynolds-decomposition [Adams, 2008], but the phase-averaging subsequently applied to the decomposed equations eliminates the stochastic turbulent part $\langle \phi'' \rangle = 0$, whereas the linear periodic fluctuations are maintained, i.e. $\langle \phi' \rangle = \phi'$. It will be demonstrated later that the fluctuating part ϕ' is associated with three types of fundamental waves, which are the acoustic, entropy and vorticity waves.

3.2 Linearized Navier-Stokes Equations (LNSE)

The procedure to derive the LNSE can be stated as follows: In a first step the Navier-Stokes eqs. (2.1), (2.3) and (2.11) are simplified to non-reactive conditions ($Y_k = 1$, $DY_k/Dt = 0$), so that the species eq. (2.2) is omitted. Then the decomposition approach (3.1) is inserted

into the non-reacting form of the conservation equations of mass (2.1), momentum (2.3) and energy (2.11). Products of the fluctuating quantities ρ', u' and p' are neglected due to the linear assumption. In a final step the averaged conservation equations, describing the mean flow field, are subtracted from the linearized equations in order to deliver a system of linear partial differential equations for the fluctuating density ρ', velocities u_i' and pressure p':

$$\frac{\mathrm{D}\rho'}{\mathrm{D}t} = \frac{\partial \rho'}{\partial t} + \bar{u}_i \frac{\partial \rho'}{\partial x_i} = -u_i' \frac{\partial \bar{\rho}}{\partial x_i} - \bar{\rho} \frac{\partial u_i'}{\partial x_i} - \rho' \frac{\partial \bar{u}_i}{\partial x_i}, \tag{3.2}$$

$$\bar{\rho} \frac{\mathrm{D}u_i'}{\mathrm{D}t} = \bar{\rho} \frac{\partial u_i'}{\partial t} + \bar{\rho}\bar{u}_j \frac{\partial u_i'}{\partial x_j} = -\bar{\rho} u_j' \frac{\partial \bar{u}_i}{\partial x_j} - \rho' \bar{u}_j \frac{\partial \bar{u}_i}{\partial x_j} - \frac{\partial p'}{\partial x_i} + \eta \left[\frac{\partial^2 u_i'}{\partial x_k \partial x_k} + \frac{1}{3} \frac{\partial}{\partial x_i} \left(\frac{\partial u_k'}{\partial x_k} \right) \right] + \bar{\rho} f_i', \tag{3.3}$$

$$\frac{\mathrm{D}p'}{\mathrm{D}t} = \frac{\partial p'}{\partial t} + \bar{u}_i \frac{\partial p'}{\partial x_i} = -u_i' \frac{\partial \bar{p}}{\partial x_i} - \kappa \bar{p} \frac{\partial u_k'}{\partial x_k} - \kappa p' \frac{\partial \bar{u}_k}{\partial x_k} + (\kappa - 1) \left\{ \Phi' + \lambda \frac{\partial^2 T'}{\partial x_i \partial x_i} + \dot{q}_V' \right\}. \tag{3.4}$$

Early studies by Chu and Kovásznay [1958] and Kovásznay [1953] have demonstrated that the linearized Navier-Stokes eqs. (3.2)-(3.4) feature three different linear transport processes in presence of a stationary mean flow: Acoustic waves propagate with local speed of sound in the relative frame of the mean flow in the upstream and downstream flow directions. Entropy and vorticity waves are convected with the mean velocity in flow direction. Therefore these waves appear as "frozen patterns" to an observer moving in the relative frame of the mean flow. Throughout this thesis quantities related to the acoustic, vorticity and entropy waves will be indicated by the subscripts a, v and s. In the postprocessing the vorticity wave Ω_i' can be retrieved from the velocity fluctuations evaluating

$$\Omega_i' = \epsilon_{ijk} \frac{\partial u_k'}{\partial x_j}, \qquad \epsilon_{ijk} = \begin{cases} 1, & ijk = 123, 231, 312 \\ -1, & ijk = 321, 213, 132 \\ 0, & \text{else} \end{cases} \tag{3.5}$$

where ϵ_{ijk} is the permutation matrix in index notation [Spurk and Aksel, 2007]. Entropy waves are mainly linked to temperature and density fluctuations, which are calculated by means of the linearized equation of state of the ideal gas [Nicoud and Wieczorek, 2009]

$$\frac{p'}{\bar{p}} - \frac{\rho'}{\bar{\rho}} - \frac{T'}{\bar{T}} = 0, \tag{3.6}$$

$$s' = c_v \frac{p'}{\bar{p}} - c_p \frac{\rho'}{\bar{\rho}}. \tag{3.7}$$

A thorough analysis of the generation and interaction mechanisms of vorticity and entropy waves is given in following subsections, where the linearized energy equation in entropy form and linearized vorticity equation are discussed in detail.

Linearized Entropy Equation

The propagation of entropy waves is implicitly described with the linearized continuity eq. (3.2) and energy eq. (3.4) in pressure formulation. An explicit formulation of the linearized entropy equation is obtained from the linearization of the non-reactive form of eq. (2.12)

$$
\bar{\rho}\bar{T}\frac{\mathrm{D}s'}{\mathrm{D}t} = \bar{\rho}\bar{T}\left(\frac{\partial s'}{\partial t} + \bar{u}_i\frac{\partial s'}{\partial x_i}\right) = -\left(\underbrace{u_i'\bar{\rho}\bar{T}}_{\text{I}} + \underbrace{\bar{u}_i\bar{\rho}T'}_{\text{II}} + \underbrace{\bar{u}_i\rho'\bar{T}}_{\text{III}}\right)\frac{\partial \bar{s}}{\partial x_i} + \underbrace{\Phi'}_{\text{IV}} + \underbrace{\lambda\frac{\partial^2 T'}{\partial x_k \partial x_k}}_{\text{V}} + \underbrace{\dot{q}_V'}_{\text{VI}}.
$$

(3.8)

Since the left hand side of eq. (3.8) represents the material derivative of the entropy, all terms on the right hand side can be understood as interaction terms of entropy waves with other modes and the mean flow as they travel along their stream-path. Entropy waves are influenced by or arise from the following mechanisms:

- Interactions of acoustics and vorticity (I) with non-isentropic mean flow.

- Interactions of entropy (II and III) with non-isentropic mean flow as density and temperature fluctuations are mainly caused by entropy waves.

- Dissipation of acoustics and vorticity into entropy (IV), described by the linearized dissipation function Φ':

$$
\Phi' := \tau_{ji}'\frac{\partial \bar{u}_i}{\partial x_j} + \bar{\tau}_{ji}\frac{\partial u_i'}{\partial x_j} = 2\eta\left[\frac{\partial \bar{u}_i}{\partial x_j}\frac{\partial u_j'}{\partial x_i} + \frac{\partial u_i'}{\partial x_j}\frac{\partial \bar{u}_i}{\partial x_j} - \frac{2}{3}\frac{\partial \bar{u}_k}{\partial x_k}\frac{\partial u_l'}{\partial x_l}\right].
$$

(3.9)

- Diffusion and dissipation due to heat conduction (V).

- Fluctuating heat sources (VI).

- Mean flow dispersion due to different propagation speeds in shear flows (convection term $\bar{u}_i\partial s'/\partial x_i$).

Since the entropy eq. (3.8) is derived from the non-reactive form the frequently applied re-introduction of combustion heat release fluctuations via $\dot{q}_V'$ will lead to inconsistencies. In the subsequent chapter 4.1 a semi-analytical and consistent combustion noise source model is proposed which accounts for the different physics of entropy wave generation in premixed and non-premixed flames.

Linearized Vorticity Equation

The propagation of vorticity waves is inherent to the linearized momentum eq. (3.3) which is the starting point for the derivation of the linearized vorticity equation. Taking the curl

of eq. (3.3) finally gives [Lieuwen, 2012]

$$\frac{\mathrm{D}\Omega_i'}{\mathrm{D}t} = \underbrace{-u_j'\frac{\partial\bar{\Omega}_i}{\partial x_j}}_{\text{I}} + \underbrace{\bar{\Omega}_j\frac{\partial u_i'}{\partial x_j}}_{\text{II}} + \underbrace{\Omega_j'\frac{\partial\bar{u}_i}{\partial x_j}}_{\text{III}} - \underbrace{\bar{\Omega}_i\frac{\partial u_k'}{\partial x_k}}_{\text{IV}} - \underbrace{\Omega_i'\frac{\partial\bar{u}_k}{\partial x_k}}_{\text{V}} + \underbrace{\frac{1}{\bar{\rho}^2}\epsilon_{ijk}\frac{\partial\rho'}{\partial x_j}\frac{\partial\bar{p}}{\partial x_k}}_{\text{VI}} +$$

$$+ \underbrace{\frac{1}{\bar{\rho}^2}\epsilon_{ijk}\frac{\partial\bar{\rho}}{\partial x_j}\frac{\partial p'}{\partial x_k}}_{\text{VII}} - \underbrace{2\frac{\rho'}{\bar{\rho}^3}\epsilon_{ijk}\frac{\partial\bar{\rho}}{\partial x_j}\frac{\partial\bar{p}}{\partial x_k}}_{\text{VIII}} + \underbrace{\nu\frac{\partial^2\Omega_i'}{\partial x_k\partial x_k}}_{\text{IX}} + \underbrace{\epsilon_{ijk}\frac{\partial f_k'}{\partial x_j}}_{\text{X}}. \quad (3.10)$$

Again all terms of the right hand side can be interpreted as interaction terms of vorticity with acoustic and entropy modes and the mean flow. Vorticity waves are influenced or arise from the following mechanisms:

- Interactions of acoustic and vortical disturbances with shear and boundary layers with $\bar{\Omega}_i = \epsilon_{ijk}\partial\bar{u}_k/\partial x_j$ (I and II).

- Stretching and bending of vorticity tubes by mean flow gradients (III).

- Transformation of acoustics into vorticity in strong rotational mean flow (IV).

- Strong dilatation/ compressible mean flow effects, e.g. shock-induced or amplified vorticity (V).

- Baroclinic effects due to acoustic (VII) and entropy waves (VI and VIII).

- Viscous dissipation into heat (IX).

- Non-conservative/ rotational body forces (X).

Later in subsec. 6.1.4 the linearized vorticity eq. (3.10) is applied on the Entropy Wave Generator (EWG) test case to analyze and to explain the different acoustic reflection behavior with respect to upstream and downstream excitation.

Transformation Into Frequency Domain

The solution of the LNSE in frequency domain has several considerable advantages concerning the implementation of boundary conditions, the numerical stability and the post-processing effort, among others. Further details are discussed by Rao and Morris [2006]. The transformation of the LNSE into frequency domain relies on the assumption of fluctuations with time harmonic character, such that ρ', u' and p' are harmonic functions in time, i.e.

$$\begin{aligned}
\rho'\left(\boldsymbol{x}, t\right) &= \hat{\rho}\left(\boldsymbol{x}\right)e^{\mathrm{i}\omega t}, \\
u_i'\left(\boldsymbol{x}, t\right) &= \hat{u}_i\left(\boldsymbol{x}\right)e^{\mathrm{i}\omega t}, \\
p'\left(\boldsymbol{x}, t\right) &= \hat{p}\left(\boldsymbol{x}\right)e^{\mathrm{i}\omega t}.
\end{aligned} \quad (3.11)$$

In this way the time and spatial dependency of the variables is separated and the complex valued amplitudes of density $\hat{\rho}$, velocity $\hat{u}_i$ and pressure fluctuations $\hat{p}$ are exclusive functions of space. When postprocessing the LNSE results only the real part of these complex variables $\Re\{\hat{\phi}\}$ is of physical relevance in time domain.

Substituting approach (3.11) into the LNSE (3.2)-(3.4) leads to their frequency-transformed counterpart for the fluctuating density $\hat{\rho}$, velocities $\hat{u}_i$ and pressure $\hat{p}$ propagating at circular frequency $\omega = 2\pi f$ in a moving fluid

$$\mathrm{i}\omega\hat{\rho} + \bar{u}_i \frac{\partial\hat{\rho}}{\partial x_i} = -\hat{u}_i \frac{\partial\bar{\rho}}{\partial x_i} - \bar{\rho}\frac{\partial\hat{u}_i}{\partial x_i} - \hat{\rho}\frac{\partial\bar{u}_i}{\partial x_i}, \tag{3.12}$$

$$\mathrm{i}\omega\bar{\rho}\hat{u}_i + \bar{\rho}\bar{u}_j \frac{\partial\hat{u}_i}{\partial x_j} = -\bar{\rho}\hat{u}_j \frac{\partial\bar{u}_i}{\partial x_j} - \hat{\rho}\bar{u}_j\frac{\partial\bar{u}_i}{\partial x_j} - \frac{\partial\hat{p}}{\partial x_i} + \eta\left[\frac{\partial^2\hat{u}_i}{\partial x_k\partial x_k} + \frac{1}{3}\frac{\partial}{\partial x_i}\left(\frac{\partial\hat{u}_k}{\partial x_k}\right)\right] + \bar{\rho}\hat{f}_i, \tag{3.13}$$

$$\mathrm{i}\omega\hat{p} + \bar{u}_i\frac{\partial\hat{p}}{\partial x_i} = -\hat{u}_i\frac{\partial\bar{p}}{\partial x_i} - \kappa\bar{p}\frac{\partial\hat{u}_k}{\partial x_k} - \kappa\hat{p}\frac{\partial\bar{u}_k}{\partial x_k} + (\kappa - 1)\left\{\hat{\Phi} + \lambda\frac{\partial^2\hat{T}}{\partial x_k\partial x_k} + \hat{q}_V\right\}. \tag{3.14}$$

For given boundary conditions (BCs) and mean flow the system of partial differential eqs. (3.12)-(3.14) is solved for the unknown fluctuations with the frequency ω as a given parameter. Alternatively it is recast into an eigenvalue problem and solved for the related complex-valued eigenfrequencies and eigenmodes [Nicoud and Wieczorek, 2009]. Neither initial conditions nor time-dependent boundary conditions need to be imposed [Adams, 2007]. Temperature and entropy fluctuations can be calculated in a postprocessing step by evaluating the linearized equation of state (3.6) and (3.7), defined in frequency domain:

$$\hat{T} = \bar{T}\left(\frac{\hat{p}}{\bar{p}} - \frac{\hat{\rho}}{\bar{\rho}}\right), \tag{3.15}$$

$$\hat{s} = c_v\frac{\hat{p}}{\bar{p}} - c_p\frac{\hat{\rho}}{\bar{\rho}}. \tag{3.16}$$

Vorticity fluctuations are postprocessed using the frequency transformed version of eq. (3.5) to give $\hat{\Omega}_i = \epsilon_{ijk}\partial\hat{u}_k/\partial x_j$.

3.3 Linearized Euler Equations (LEE)

The linearized Euler equations (LEE) are obtained from the LNSE (3.2)-(3.4) by setting $\eta = 0$ and $\lambda = 0$

$$\frac{\mathrm{D}\rho'}{\mathrm{D}t} = \frac{\partial\rho'}{\partial t} + \bar{u}_i\frac{\partial\rho'}{\partial x_i} = -u_i'\frac{\partial\bar{\rho}}{\partial x_i} - \bar{\rho}\frac{\partial u_i'}{\partial x_i} - \rho'\frac{\partial\bar{u}_i}{\partial x_i}, \tag{3.17}$$

$$\bar{\rho}\frac{\mathrm{D}u_i'}{\mathrm{D}t} = \bar{\rho}\frac{\partial u_i'}{\partial t} + \bar{\rho}\bar{u}_j\frac{\partial u_i'}{\partial x_j} = -\bar{\rho}u_j'\frac{\partial\bar{u}_i}{\partial x_j} - \rho'\bar{u}_j\frac{\partial\bar{u}_i}{\partial x_j} - \frac{\partial p'}{\partial x_i} + \bar{\rho}f_i', \tag{3.18}$$

$$\frac{\mathrm{D}p'}{\mathrm{D}t} = \frac{\partial p'}{\partial t} + \bar{u}_i\frac{\partial p'}{\partial x_i} = -u_i'\frac{\partial\bar{p}}{\partial x_i} - \kappa\bar{p}\frac{\partial u_k'}{\partial x_k} - \kappa p'\frac{\partial\bar{u}_k}{\partial x_k} + (\kappa - 1)\dot{q}_V'. \tag{3.19}$$

As before the frequency-transformed LEE then result from inserting the time-harmonic approach (3.11) into eqs. (3.17)-(3.19).

3.4 Isentropic Wave Propagation

In the case of isentropic wave propagation the amplitude of any entropy disturbance is not altered when traveling along its streampath. The material derivative of the entropy vanishes, i.e.

$$\bar{\rho}\bar{T}\frac{\mathrm{D}s'}{\mathrm{D}t} = 0. \tag{3.20}$$

A comparison of this requirement and the linearized entropy eq. (3.8) reveals that isentropic wave propagation can only be realized in presence of an isentropic mean flow ($\partial \bar{s}/\partial x_i = 0$) without heat sources ($\dot{q}'_V = 0$) and thermal and viscous diffusion ($\eta = \lambda = 0$).

Linearized Isentropic Pressure-Density Relation

A more restrictive definition of isentropic wave propagation, sometimes called *homentropic condition* [Adams, 2010], is obtained when entropy waves are assumed to be absent. This presumption leads to a significant simplification of the linearized equation of state for the entropy (3.7), which in general links the pressure, density and entropy fluctuations to each other. Inserting $s' = 0$ in conjunction with the definition of the speed of sound (2.15) into eq. (3.7) yields the well-known *linearized pressure-density relation*

$$p' = \bar{c}^2 \rho'. \tag{3.21}$$

It states that pressure and density disturbances are dependent variables whenever entropy waves are absent, i.e. $s' = 0$. In this case the number of dependent variables in the LNSE (3.2)-(3.4) or LEE (3.17)-(3.19) is reduced by one so that either the linearized continuity or the energy equation can be omitted. Therefore this assumption is of great advantage with respect to the computational effort and costs.

In general the investigation of the indirect noise generation excludes the isentropic assumption (3.21). If only direct noise is regarded the assumption of isentropic conditions is sufficient to capture the acoustic wave propagation. Also the computation of scattering matrices describing the acoustic transmission and reflection properties of certain components may justify isentropic wave propagation. In chapter 6 for instance the transmission and reflection properties of two different nozzle test cases are determined. The acoustic models of these two cases are mainly based on isentropic conditions to reduce the computational efforts. Whenever isentropic conditions are assumed in this thesis, the pressure is substituted by eq. (3.21). Then the linearized energy eq. (3.4) is dropped in the LNSE or LEE, which are solved for the four unknown variables ρ' and u'_i.

3.5 Inhomogeneous Wave and Helmholtz Equation

The inhomogeneous wave equation is deduced from the LEE (3.17)- (3.19) under the assumption of a mean flow at rest ($\bar{u}_i = 0$, $\partial \bar{u}_i/\partial x_j = 0$, $\partial \bar{\rho}/\partial x_i = \partial \bar{p}/\partial x_i = 0$) and the absence of body forces ($f_i' = 0$) [Poinsot and Veynante, 2005]:

$$-\frac{1}{\bar{\rho}\bar{c}^2}\frac{\partial^2 p'}{\partial t^2} + \frac{\partial}{\partial x_i}\Big(\frac{1}{\bar{\rho}}\frac{\partial p'}{\partial x_i}\Big) = -\frac{\kappa - 1}{\bar{\rho}\bar{c}^2}\frac{\partial \dot{q}_V'}{\partial t}. \tag{3.22}$$

This equation represents the acoustic sound propagation in absence of a mean flow but accounts for energy sources $\dot{q}_V'$ and density gradients $\partial \bar{\rho}/\partial x_i$. Only a single equation is solved to obtain the acoustic pressure field p', while the acoustic velocities u_i' are retrieved from the simplified momentum eq. (3.18), i.e. $\bar{\rho}\partial u_i'/\partial t = -\partial p'/\partial x_i$. Density disturbances ρ' may be recovered using the linearized pressure-density relation (3.21). The wave equation can be transformed into frequency domain, which is then called inhomogeneous Helmholtz equation

$$\frac{1}{\bar{\rho}}k^2\hat{p} + \frac{\partial}{\partial x_i}\Big(\frac{1}{\bar{\rho}}\frac{\partial \hat{p}}{\partial x_i}\Big) = -\mathrm{i}\omega\frac{\kappa - 1}{\bar{\rho}\bar{c}^2}\hat{q}_V, \tag{3.23}$$

where $k = \omega/\bar{c}$ denotes the acoustic wave number.

3.6 Analytical Solutions

The analytical solution of the LEE (3.17)-(3.19) for time-harmonic waves propagating in an infinitely long and quasi one-dimensional duct with constant area and homogeneous mean flow $\bar{u}$ in axial x-direction is given by [Ehrenfried, 2002, Nicoud and Wieczorek, 2009]

$$p'(x,t) = \Re\{P^+ e^{-\mathrm{i}k\frac{x}{1+\mathrm{M}}+\mathrm{i}\omega t} + P^- e^{+\mathrm{i}k\frac{x}{1-\mathrm{M}}+\mathrm{i}\omega t}\}, \tag{3.24}$$

$$u'(x,t) = \Re\Big\{\frac{1}{\bar{\rho}\bar{c}}\big(P^+ e^{-\mathrm{i}k\frac{x}{1+\mathrm{M}}+\mathrm{i}\omega t} - P^- e^{+\mathrm{i}k\frac{x}{1-\mathrm{M}}+\mathrm{i}\omega t}\big)\Big\}, \tag{3.25}$$

$$s'(x,t) = \Re\{S e^{-\mathrm{i}k_s x+\mathrm{i}\omega t}\}. \tag{3.26}$$

The solution for the pressure (3.24) and velocity (3.25) represents a superposition of two acoustic waves propagating at the same time in opposite directions. The wave $\hat{p}^+ = P^+\exp\{-\mathrm{i}k\frac{x}{1+\mathrm{M}}\}$ with complex pressure amplitude P^+ and phase $-kx/(1+\bar{\mathrm{M}})$ propagates in positive x-direction with the speed $\bar{u} + \bar{c}$. The other wave $\hat{p}^- = P^-\exp\{+\mathrm{i}k\frac{x}{1-\mathrm{M}}\}$ with complex amplitude P^- and phase $kx/(1-\bar{\mathrm{M}})$ travels with the speed $\bar{u} - \bar{c}$ in the negative x-direction. Each of these two single acoustic waves is determined by the superposition of pressure and velocity disturbances, i.e.

$$p^{+'}(x,t) = \frac{1}{2}\left(p' + \bar{\rho}\bar{c}u'\right), \tag{3.27}$$

$$p^{-'}(x,t) = \frac{1}{2}\left(p' - \bar{\rho}\bar{c}u'\right). \tag{3.28}$$

As described by eq. (3.26), in addition to the propagation of acoustic waves an entropy wave with complex amplitude S and phase $-k_s x$ is convectively transported with the mean flow velocity $\bar{u}$. The different propagation speed of the entropy wave is reflected in the entropy wave number $k_s = \omega/\bar{u}$. In an one-dimensional homogeneous mean flow the solution of the entropy wave (3.26) is perfectly decoupled from the acoustic waves, i.e. they are traveling independent from each other. Finally it should be noted that no vorticity waves may propagate in an one-dimensional model. Analytical solutions for vorticity waves propagating in a duct with homogeneous axial mean flow are given for instance by Stow et al. [2002] and by Dowling and Mahmoudi [2015].

3.7 Boundary Conditions

Before introducing the most important boundary conditions applied in the frame of the LNSE simulations, the definitions of the reflection coefficient and impedance are presented. These are helpful quantities to characterize the acoustic boundary properties.

Reflection Coefficient

The reflection coefficient of a boundary defines, which part of an incoming wave is reflected by it. Depending on the propagation direction, the reflection coefficient with respect to a left and a right traveling wave can be distinguished:

$$R = \frac{\hat{p}^+}{\hat{p}^-} = \frac{P^+ e^{-\mathrm{i}kx}}{P^- e^{+\mathrm{i}kx}}, \qquad \text{(left)} \qquad (3.29)$$

$$R = \frac{\hat{p}^-}{\hat{p}^+} = \frac{P^- e^{+\mathrm{i}kx}}{P^+ e^{-\mathrm{i}kx}}. \qquad \text{(right)} \qquad (3.30)$$

The reflection coefficient depends on the frequency and is in general a complex quantity.

Reduced Impedance

The acoustic impedance on a boundary with surface normal n_i is defined as the ratio of complex pressure and velocity amplitudes

$$Z_a = \frac{\hat{p}}{\hat{u}_i n_i}. \qquad (3.31)$$

The acoustic impedance is divided by $\bar{\rho}\bar{c}$ in order to obtain a non-dimensional quantity, called the *reduced impedance*. Using the eqs. (3.27), (3.28), (3.29) and (3.30) the reduced impedance and the reflection coefficient are connected by

$$Z = \frac{\hat{p}}{\hat{u}_i n_i \bar{\rho}\bar{c}} = \frac{1+R}{1-R}. \qquad (3.32)$$

Like the reflection coefficient, the reduced impedance is a complex quantity [Ehrenfried, 2002, Poinsot and Veynante, 2005]. Based on these definitions the most important boundary conditions applied in the current thesis are introduced.

Impedance Boundaries

Impedance BCs are the most general form of the boundary conditions for the LNSE and LEE. Rearranging the definition of the reduced impedance (3.32) yields the corresponding impedance boundary condition

$$\hat{u}_i n_i Z \bar{\rho} \bar{c} - \hat{p} = 0. \tag{3.33}$$

This condition only holds for boundaries, which are not exposed to a mean flow. In presence of a mean flow the boundary condition is given for instance by Rienstra and Hirschberg [2012]. In the case of isentropic wave propagation the pressure $\hat{p}$ in eq. (3.33) is replaced by the density $\hat{\rho}$ using eq. (3.21) to give

$$\hat{u}_i n_i Z \bar{\rho} - \bar{c} \hat{\rho} = 0. \tag{3.34}$$

When solving the Helmholtz eq. (3.23), the simplified linearized momentum eq. (3.18) (i.e. $\mathrm{i}\omega\bar{\rho}\hat{u}_i = -\partial\hat{p}/\partial x_i$) is exploited to exclusively express the impedance boundary condition (3.33) as a function of pressure:

$$\frac{\partial \hat{p}}{\partial x_i} n_i Z \bar{c} + \mathrm{i}\omega\hat{p} = 0. \tag{3.35}$$

Rigid Walls

When considering viscous fluids the relative motion between acoustic oscillations and a wall vanishes at the interface. For rigid walls this yields

$$\hat{u}_i = 0. \tag{3.36}$$

As explained by Rienstra and Hirschberg [2012] the effects of viscous dissipation and boundary layers on the acoustic propagation are negligible in most situations, so that condition (3.36) can be usually relaxed to a purely kinematic requirement even when solving the LNSE:

$$\hat{u}_i n_i = 0. \tag{3.37}$$

This condition is strictly valid for isentropic wave propagation without the formation of an acoustic boundary layer. It is also obtained by imposing $Z \to \infty$ in the impedance boundary condition (3.33). The corresponding boundary condition for the Helmholtz eq. (3.23) is derived by inserting eq. (3.37) in the simplified momentum eq. (3.18) [Nicoud and Wieczorek, 2009], so that

$$\frac{\partial \hat{p}}{\partial x_i} n_i = 0. \tag{3.38}$$

Non-Reflecting Boundaries

Non-reflecting boundary conditions are prescribed through a reduced impedance of $Z = 1$ in the impedance boundary condition (3.33). This corresponds to $R = 0$, which follows from eq. (3.32), i.e. $R = (Z - 1)/(Z + 1)$. Non-reflecting boundaries at isentropic conditions are obtained in the same way by imposing $Z = 1$ in eq. (3.34).

Inlet Boundaries

The impedance BC (3.33) controls the ratio of incoming and outgoing waves. If a certain acoustic flux is desired, the acoustic impedance and a Dirichlet condition for one of the variables is needed or both $\hat{p}$ and $\hat{u}$ need to be prescribed. When dealing with the LNSE or LEE an additional condition for the convective incoming entropy wave must be provided at the inlet. This condition can be stated as

$$\hat{p} - \bar{c}^2 \hat{\rho} = S_p. \tag{3.39}$$

The source of entropy S_p is formulated in terms of the pressure $S_p = \bar{p}S/c_v$, where S is the complex amplitude of the entropy wave as defined by eq. (3.26). The pressure and density fluctuations in the BC (3.39) are part of the solution, while the entropy amplitude S is a given and fixed source quantity. No entropy waves are entering the domain when setting $S_p = 0$, which represents the most natural choice.

Pressure Boundaries

At the ending of ducts, which are connected to a large atmosphere, the ambient pressure is imposed on the fluid. There the fluctuating pressure must obey

$$\hat{p} = 0. \tag{3.40}$$

This is equivalent to a fully-reflecting boundary condition with a reflection coefficient of $R = 1$ or a reduced impedance of $Z = 0$. When solving the LNSE or LEE along with the isentropic assumption, eq. (3.40) is stated in terms of the fluctuating density to give

$$\hat{\rho} = 0. \tag{3.41}$$

It should be noted that the validity of this condition is limited to the low frequency range. The experimental studies by Munt [1977, 1990] and the numerical study by Jörg et al. [2013] show that the reflection coefficient monotonically falls with increasing frequencies.

Choked Nozzle

As derived by Marble and Candel [1977] a choked and acoustically compact nozzle may be replaced by the following boundary condition

$$2\frac{\hat{u}}{\bar{u}} + \frac{\hat{\rho}}{\bar{\rho}} - \frac{\hat{p}}{\bar{p}} = 0. \tag{3.42}$$

If isentropic wave propagation is assumed then either the pressure or the density may be replaced in eq. (3.42) to obtain

$$2\frac{\hat{u}}{\bar{u}} - \frac{\hat{\rho}}{\bar{\rho}}(\kappa - 1) = 0, \qquad\qquad 2\frac{\hat{u}}{\bar{u}} - \frac{\hat{p}}{\bar{p}}\left(\frac{\kappa - 1}{\kappa}\right) = 0. \qquad (3.43)$$

This condition is identical to impose $Z = 2/[(\kappa - 1)\bar{\mathrm{M}}]$ in eq. (3.33) or (3.34).

3.8 Acoustic Network Models

The numerical effort of LNSE can be greatly reduced if in parts of the domain the acoustical wave propagation can be described sufficiently in one space coordinate such that network models can be used for these subdomains. E.g. Schulze [2016] has shown this approach to describe the 1D dynamics of the multitude of rocket combustor injectors in a 3D LNSE FEM simulation.

For network modeling the subdomain is split up along the propagation direction into a set of canonical elements representing the acoustic behavior of the subdomain. In these canonical elements the incoming and outgoing acoustic waves of acoustic nodes are linked to each other by a set of linear relations [Polifke, 2004]. The coefficients of these linear relations form the *scattering matrix* or the *transfer matrix*, which connect $\hat{p}$ and $\hat{u}$ at the inlet and outlet node of each element. Concatenating the series of single network elements, e.g. by multiplying the element transfer matrices, the acoustical behavior of the subdomain can be computed. These network models are coupled to complex 3D LNSE simulations as done in this thesis or by Schulze [2016].

3.8.1 Acoustic Scattering and Transfer Matrices
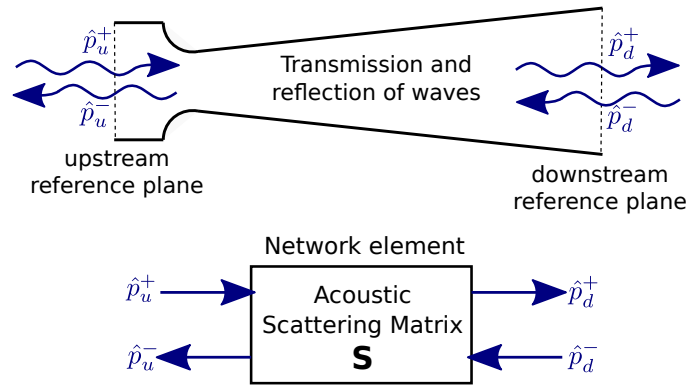
Figure 3.1: Acoustic network element and scattering matrix.

As shown in fig. 3.1 in the top graph, two waves are defined at the reference plane at either side of a 1D acoustical element. They have the index u referring to the upstream

reference plane and index d for the downstream side. While in the special case upstream and downstream relate to the positive flow direction, in the general case they indicate the 1D coordinate direction where upstream is at a lower coordinate value then downstream. Formalizing the network element below the two sets of waves upstream and downstream are connected through a 2×2 matrix. Depending on the particular definition, the matrix is called the scattering matrix with

$$
\left(\begin{array}{c} \hat{p}_d^+ \\ \hat{p}_u^- \end{array} \right) = \underbrace{\left[\begin{array}{cc} T_u & R_d \\ R_u & T_d \end{array} \right]}_{\mathbf{S}_a} \left(\begin{array}{c} \hat{p}_u^+ \\ \hat{p}_d^- \end{array} \right).
\tag{3.44}
$$

or the transfer matrix

$$
\left(\begin{array}{c} \hat{p}^+ \\ \hat{p}^- \end{array} \right)_d = \underbrace{\left[\begin{array}{cc} T_{11} & T_{12} \\ T_{21} & T_{22} \end{array} \right]}_{\mathbf{T}} \left(\begin{array}{c} \hat{p}^+ \\ \hat{p}^- \end{array} \right)_u.
\tag{3.45}
$$

As shown by Fischer [2004] the scattering and transfer matrix can be transformed into each other using linear relations.

3.8.2 Transfer Matrices for Indirect Noise Generation
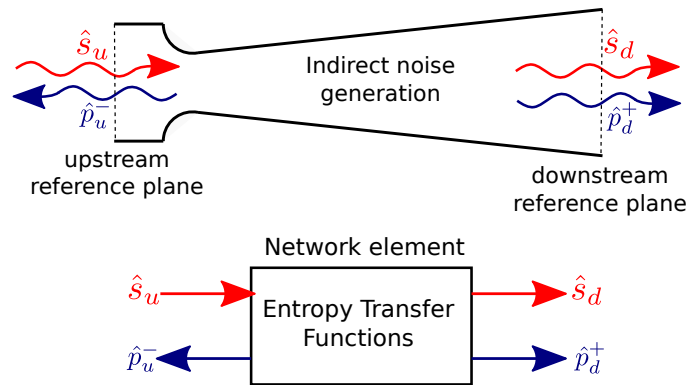
Figure 3.2: Indirect noise generation in a network element and entropy transfer functions.

So far, the network elements were limited to acoustic wave propagation. The indirect noise generation due to entropy and vorticity waves can be also included in the network elements, which is presented in the following. As shown in fig. 3.2 the entropy wave $\hat{s}_u$, accelerated in the convergent-divergent nozzle, leads to the upstream and downstream propagating acoustic waves $\hat{p}_u^-$ and $\hat{p}_d^+$, respectively. Then the equations (3.44) in matrix-vector form are extended to the indirect noise generation by introducing the entropy transmission

coefficient $T_s = \hat{p}_{d,s}^{+}/\hat{s}_u$ and reflection coefficient $R_s = \hat{p}_{u,s}^{-}/\hat{s}_u$ to obtain

$$\hat{p}_d^{+} = T_u \hat{p}_u^{+} + R_d \hat{p}_d^{-} + T_s \hat{s}_u, \tag{3.46}$$

$$\hat{p}_u^{-} = R_u \hat{p}_u^{+} + T_d \hat{p}_d^{-} + R_s \hat{s}_u. \tag{3.47}$$

$$\hat{s}_d = S_{33} \hat{s}_u. \tag{3.48}$$

Note that the matrix coefficient S_{33} describes the amplification or damping of entropy waves as they travel from the upstream to the downstream side. For isentropic wave propagation the coefficient is $S_{33} = 1$. This set of equations (3.46) - (3.48) can be recast into matrix-vector form to yield

$$\begin{pmatrix} \hat{p}_d^{+} \\ \hat{p}_u^{-} \\ \hat{s}_d \end{pmatrix} = \underbrace{\begin{bmatrix} T_u & R_d & T_s \\ R_u & T_d & R_s \\ 0 & 0 & S_{33} \end{bmatrix}}_{\mathbf{S}} \begin{pmatrix} \hat{p}_u^{+} \\ \hat{p}_d^{-} \\ \hat{s}_u \end{pmatrix}. \tag{3.49}$$

In principle the indirect noise generation by vorticity waves can be included in the same manner as it was done in case of the entropy waves. This results in an additional vorticity transmission coefficient $T_{\Omega_i} = \hat{p}_{d,\Omega_i}^{+}/\hat{\Omega}_{i,u}$ and reflection coefficient $R_{\Omega_i} = \hat{p}_{u,\Omega_i}^{-}/\hat{\Omega}_{i,u}$.

3.8.3 Determination of Acoustic Elements with the Two-Source Location Method

The determination of the scattering and transfer matrices is based on the *two-source location method* [Munjal and Doige, 1990a,b]. The acoustic scattering matrix in eq. (3.44) contains four unknown matrix coefficients T_u, T_d, R_u and R_d, so a set of four linear independent equations must be formulated and solved. This is achieved by the successive excitation of acoustic waves from the upstream and downstream side of the examined system. Acoustic variables related to the upstream excitation are indicated by subscript I, while the downstream excitation is subscripted by II. In each case the resulting pressure signal is recorded at the system's inlet and outlet planes to retrieve the acoustic waves entering and leaving the system. This is done in the postprocessing of the LNSE simulation by the definition of several monitor planes in the direction of the elements coordinate, in which the pressure and mean flow quantities are sampled. Area averaging of the acoustic and mean flow variables yields quasi one-dimensional quantities in each monitor plane x_m. The upstream and downstream propagating acoustic waves $\hat{p}^{+}$ and $\hat{p}^{-}$ are recovered from the discrete pressure values $\hat{p}(x_m)$ by applying a non-linear Gauß-Newton regression algorithm based on the analytical solution eq. (3.24)

$$\min_{P^{+},P^{-}} \left\{ \sum_{m=1}^{n_{mon}} \left(\hat{p}(x_m) - P^{+} e^{-\mathrm{i}k\frac{1}{1+\mathrm{M}}x_m} - P^{-} e^{\mathrm{i}k\frac{1}{1-\mathrm{M}}x_m} \right)^2 \right\} = \min_{P^{+},P^{-}} \left\{ \sum_{m=1}^{n_{mon}} \left(\hat{p}(x_m) - \hat{p}^{+} + \hat{p}^{-} \right)^2 \right\}. \tag{3.50}$$

The first acoustic state provides the waves $\hat{p}_{u,I}^{+}$, $\hat{p}_{u,I}^{-}$, $\hat{p}_{d,I}^{+}$ and $\hat{p}_{d,I}^{-}$, while the second acoustic state yields $\hat{p}_{u,II}^{+}$, $\hat{p}_{u,II}^{-}$, $\hat{p}_{d,II}^{+}$ and $\hat{p}_{d,II}^{-}$. With knowledge of the acoustic waves in case of upstream and downstream excitation, the definition of the scattering matrix (3.44) is recast into a system of linear equations, which collects the reflection and transmission coefficients in the vector of unknowns. The solution of these linear equations yields the four scattering matrix coefficients. Further details on the numerical implementation of the two-source location method in the context of LNSE simulations are given by Gikadi [2014].

3.8.4 Determination of Entropy Transmission and Reflection Coefficient

The indirect noise generation inside a certain element, described by entropy transmission and reflection coefficients in eq. (3.49), can be determined in a single step. Exciting entropy waves upstream of the examined system, which is terminated with non-reflecting boundaries, acoustic waves solely occur as a result of the indirect noise generation inside the system. The excitation of an entropy wave with defined amplitude $\hat{s}_u$ is realized for instance using the boundary condition (3.39). After excitation, the acoustic pressure, entropy and mean flow variables are recorded upstream and downstream of the system in numerous monitor planes. These variables are area-averaged in each monitor plane to get quasi one-dimensional quantities. The upstream and downstream traveling acoustic waves are retrieved using eq. (3.50). The entropy wave is obtained from the solution of the following optimization problem based on the analytical solution (3.26)

$$\min_{S}\left\{\sum_{m=1}^{n_{mon}}\left(\hat{s}\left(x_m\right)-Se^{-\mathrm{i}k_s x_m}\right)^2\right\}. \tag{3.51}$$

Once the outgoing acoustic waves $\hat{p}_u^-$ and $\hat{p}_d^+$ arising from the accelerated entropy wave $\hat{s}_u$ are computed, the entropy transmission and reflection coefficients can be calculated by the defining eqs. (3.46) and (3.47).

4 Combustion Noise Models

This chapter is focused on the modeling of combustion noise sources and their spectral content. First a theoretical description of combustion noise and its sources is provided, as well as a review of the most important experimental and numerical studies on combustion noise. Based on this a new semi-analytical model is proposed comprising non-linear source terms due to chemical reactions embedded in a linear propagation model for non-reactive acoustics such as the LNSE. The consistency of the model with previous work on combustion noise is demonstrated. In this context it is shown that all major features of combustion noise sources are incorporated in the model. The model is capable to represent essential differences in the physics of turbulent perfectly premixed and non-premixed flames with respect to the generation of entropy waves and therefore indirect combustion noise. The chapter is completed by a review of spectral modeling approaches for the combustion noise source terms.

4.1 Theoretical and Phenomenological Description

In the following subsections the physics of combustion noise generation and the main experimental and numerical findings are reviewed. These results found the basis for the development of a new combustion noise source term model proposed in this thesis.

4.1.1 Extended Inhomogeneous Wave Equation

Most of the theoretical investigations of aerodynamic and combustion noise sources rely on the famous *Lighthill equation* [Lighthill, 1954, Lighthill and Newman, 1952]

$$\frac{1}{\bar{c}^2}\frac{\partial^2 p'}{\partial t^2} - \frac{\partial^2 p'}{\partial x_k \partial x_k} = \underbrace{\frac{\partial^2}{\partial x_i \partial x_j}\left(\rho u_i u_j - \tau_{ij}\right)}_{\text{I}} - \underbrace{\frac{\partial^2 \rho_e}{\partial t^2}}_{\text{II}}. \tag{4.1}$$

The left hand side represents the classical isentropic wave propagation operator as introduced by eq. (3.22) in sec. 3.5. The Lighthill theory belongs to the area of acoustic analogies [Goldstein, 2003]. Only in a small portion of the acoustic propagation domain, non-linear effects due to turbulent fluctuations are relevant. These non-linear fluctuations result in non-negligible terms on the right hand side of eq. (4.1) and act as sound sources to the wave operator on the left hand side of eq. (4.1). In the remaining domain the contributions of the source terms on wave propagation are small if not zero [Ehrenfried, 2002].

The source terms in the Lighthill eq. (4.1) are originating from two different phenomena: The first term I is a quadrupole term due to aerodynamic sound sources. The second term II is characterized by the excess density $\rho_e := \rho' - p'/\bar{c}^2$, which is defined as the difference between the real density-fluctuation including entropy waves and the density fluctuation in the isentropic case. The excess density is different from zero in areas with irreversible processes like heat conduction or combustion [Dowling and Mahmoudi, 2015]. Term II represents a thermoacoustic source term. Rienstra and Hirschberg [2012] demonstrated that this term is equivalent to a mass source term. Based on the Lighthill eq. (4.1), Dowling derived an extended inhomogeneous wave equation for reacting flows to further investigate combustion noise sources

$$\frac{1}{\bar{c}^2}\frac{\partial^2 p'}{\partial t^2} - \frac{\partial^2 p'}{\partial x_k \partial x_k} = -\underbrace{\frac{\partial}{\partial t}\left[\frac{\alpha\bar{\rho}}{c_p\rho}\left(\sum_{k=1}^{n}\left(\frac{\partial h}{\partial Y_k}\right)_{\rho,p,Y_m}\rho\frac{\mathrm{D}Y_k}{\mathrm{D}t} + \frac{\partial\dot{q}_i}{\partial x_i} - \tau_{ij}\frac{\partial u_i}{\partial x_j}\right)\right]}_{\mathrm{I}} +$$

$$+ \underbrace{\frac{\partial^2}{\partial x_i \partial x_j}\left(\rho u_i u_j - \tau_{ij}\right)}_{\mathrm{II}} + \underbrace{\frac{1}{\bar{c}^2}\frac{\partial}{\partial t}\left[\left(1 - \frac{\bar{\rho}\bar{c}^2}{\rho c^2}\right)\frac{\mathrm{D}p'}{\mathrm{D}t} - \frac{p'}{\rho}\frac{\mathrm{D}\rho}{\mathrm{D}t}\right]}_{\mathrm{III}} + \underbrace{\frac{\partial^2}{\partial t\partial x_i}\left(u_i\rho_e\right)}_{\mathrm{IV}}, \quad (4.2)$$

The derivation of eq. (4.2) is documented by Crighton et al. [1992]. Its main advantage in comparison to the Lighthill eq. (4.1) is that it offers insight into additional mechanisms of noise generation in reactive flows. Following the argumentation of Dowling, the term I constitutes a monopole sound source by unsteady combustion with order $\mathcal{O}(\bar{\mathrm{M}}^{2-3})$ in the Mach number. Pressure fluctuations arising from this term are called *direct combustion noise*. Term II stands for the quadrupole jet-noise source term in the Lighthill theory with order $\mathcal{O}(\bar{\mathrm{M}}^8)$. Deviations from isentropic conditions are accounted for by the term III with order $\mathcal{O}(\bar{\mathrm{M}}^8)$. Finally term IV is of dipole nature and represents the *indirect noise* generation by accelerated excess density fluctuations or entropy waves. This term is of order $\mathcal{O}(\bar{\mathrm{M}}^6)$ in the Mach number and will be further discussed in subsec. 4.1.4. As demonstrated by Crighton et al. [1992] the monopole source term I due to unsteady heat release dominates all remaining terms in the low Mach number limit $\bar{\mathrm{M}} \to 0$, so that eq. (4.2) simplifies to

$$\frac{1}{\bar{c}^2}\frac{\partial^2 p'}{\partial t^2} - \frac{\partial^2 p'}{\partial x_k \partial x_k} = \frac{\partial}{\partial t}\left[\frac{\bar{\rho}\left(\kappa - 1\right)}{\rho c^2}\dot{\omega}_T\right], \quad (4.3)$$

using the identities $\alpha/c_p = (\kappa - 1)/\bar{c}^2$ and $\dot{\omega}_T = -\sum_{k=1}^{n}(\partial h/\partial Y_k)_{\rho,p,Y_m}\rho\mathrm{D}Y_k/\mathrm{D}t$. The diffusive terms $\partial\dot{q}_i/\partial x_i$ and $-\tau_{ij}\partial u_i/\partial x_j$ in eq. (4.2) are mainly dipole sources with order $\mathcal{O}(\bar{\mathrm{M}}^6)$, which were neglected as well for low Mach numbers. The identification of the heat release fluctuations as the main driver for combustion noise in low Mach number flames is of vital importance for the development of adequate source terms in this thesis. In the next subsection the different mechanisms leading to the generation of entropy waves in perfectly premixed and non-premixed flames are reviewed. These fundamental differences need to be included when modeling source terms for both flame types.
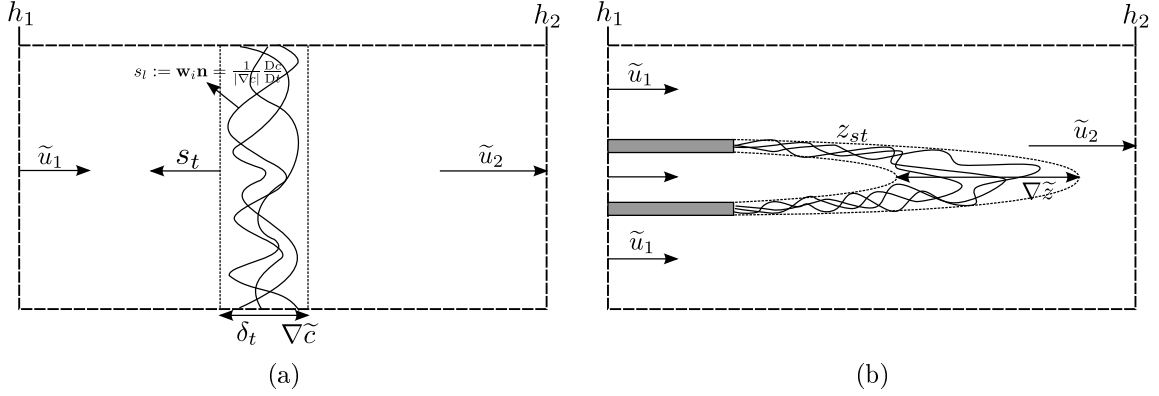
Figure 4.1: Control volume for the total enthalpy in case of a (a) perfectly premixed flame and (b) non-premixed flame.

4.1.2 Entropy Wave Generation

The following analysis of the entropy wave generation in perfectly premixed and non-premixed flames relies on the assumption of high Reynolds and Damköhler numbers, so that the flame constitutes an ensemble of laminar flamelets [Peters, 2010].

The entropy wave generation in perfectly premixed and non-premixed flames is derived by the integral balance of the total enthalpy for a fixed control volume in which a flame is enclosed. As sketched in fig. 4.1 the boundaries of the control volume on the side of the reactants and products are chosen in such a manner that they are far upstream and downstream of the flame. As a consequence the boundaries do not interact with the flame at any time, implying the absence of apparent fluctuations due to flame intermittency on the control volume boundaries. Still the fluctuation of the flame will change the amount of reactants and products in the control volume, and create velocity fluctuations, which lead to combustion noise. Under the assumption of an adiabatic control volume with negligible flow velocities (isobaric low Mach number flame) the enthalpy h in eq. (2.6) is conserved across the flame, i.e. $h_2 - h_1 = 0$. According to Sattelmayer [2008] this leads in conjunction with mean averaged heat capacities $\sum_{k=1}^{n} \int_{T^0}^{T} c_{p,k}(T) Y_k \mathrm{d}T \approx \sum_{k=1}^{n} Y_k \bar{c}_{p,k}(T - T^0)$ to the following expression:

$$\left[\sum_{k=1}^{n} Y_k \bar{c}_{p,k} \Big|_0^2 (T_2 - T^0) \right]_P + \Delta h_R - \left[\sum_{k=1}^{n} Y_k \bar{c}_{p,k} \Big|_0^1 (T_1 - T^0) \right]_R = 0. \qquad (4.4)$$

Therein the enthalpy of reaction is defined by the difference of the sum of the standard formation enthalpies $h_{f,k}^0$ between the products and reactants:

$$\Delta h_R = (h_P^0 - h_R^0) = \left[\sum_{k=1}^{n} Y_k h_{f,k}^0 \right]_P - \left[\sum_{k=1}^{n} Y_k h_{f,k}^0 \right]_R. \qquad (4.5)$$

The linearization of eq. (4.4) offers insight into the generation mechanisms of entropy waves, which yields after rearrangement

$$\sum_{k=1}^{n}\left[\left(\bar{Y}_k\bar{c}_{p,k}\big|_0^2 T_2'\right)_P - \left(\bar{Y}_k\bar{c}_{p,k}\big|_1^0 T_1'\right)_R\right] = -\left(\left[\sum_{k=1}^{n} Y_k'\bar{c}_{p,k}\big|_0^2 (\bar{T}_2-\bar{T}^0)\right]_P - \left[\sum_{k=1}^{n} Y_k'\bar{c}_{p,k}\big|_0^1 (\bar{T}_1-\bar{T}^0)\right]_R\right)$$
$$- \Delta h_R'(Y_k'). \quad (4.6)$$

This equation describes the production of sensible enthalpy or temperature fluctuations by mass fraction fluctuations. Recalling that entropy waves are predominantly associated with temperature fluctuations, eq. (4.6) can be interpreted as the production of entropy waves by mass fraction fluctuations. It is important to notice that eq. (4.6) is an exclusive function of the mass fraction fluctuations because $(\bar{c}_{p,2}T_2')_P - (\bar{c}_{p,1}T_1')_R = f(Y_k')$. Under the assumption of negligible initial temperature fluctuations $(T_1' = 0)$ eq. (4.6) simplifies to

$$(\bar{c}_{p,2}T_2')_P = -\left(\left[\sum_{k=1}^{n} Y_k'\bar{c}_{p,k}\big|_0^2 (\bar{T}_2 - \bar{T}^0)\right]_P - \left[\sum_{k=1}^{n} Y_k'\bar{c}_{p,k}\big|_0^1 (\bar{T}_1 - \bar{T}^0)\right]_R\right) - \Delta h_R'(Y_k'). \quad (4.7)$$

This equation holds for a non-premixed flame, which is characterized by strong mixture fraction fluctuations. As a consequence the turbulent combustion of a non-premixed flame is inherently accompanied by the production of entropy waves. Mixture inhomogeneities are partially converted into inhomogeneities of the sensible enthalpy and therefore temperature oscillations appearing in form of entropy waves. In a perfectly premixed flame no fluctuations of the mixture fraction of the reactants are present $(Y_k'|_R = 0)$. A homogeneous mixture of the reactants results in a homogeneous mixture of the products $(Y_k'|_P = 0)$, so that eq. (4.6) reduces in case of a perfectly premixed flame to

$$\sum_{k=1}^{n}\left[\left(\bar{Y}_k\bar{c}_{p,k}\big|_0^2 T_2'\right)_P - \left(\bar{Y}_k\bar{c}_{p,k}\big|_0^1 T_1'\right)_R\right] \approx (\bar{c}_{p,2}T_2')_P - (\bar{c}_{p,1}T_1')_R = 0. \quad (4.8)$$

In words, temperature fluctuations generated by a premixed flame behave according to the change in the mean specific heat capacities, i.e. $T_2' = \bar{c}_{p,1}/\bar{c}_{p,2}T_1'$. The entropy difference across the flame is determined by $s_2' - s_1' = \bar{c}_{p,1}T_1'(1/\bar{T}_2 - 1/\bar{T}_1)$. If no entropy fluctuations are traveling upstream of the flame $(s_1' = 0)$, the upstream temperature fluctuation T_1' exclusively stems from acoustic fluctuations. But the acoustic temperature fluctuation is negligible because $T_1' = T_{1,a}' = T_a' = \bar{T}_1\frac{p_1'}{\bar{p}}\frac{R}{c_p} \ll p_1'$. This justifies to assume $T_1' = 0$, which directly yields $T_2' = 0$ and $s_2' = s_1' = 0$. This result is consistent with the study by Strobio Chen et al. [2016], who found that the entropy production due to interactions of acoustics and mean temperature gradients is negligible.

The enthalpy balance (4.6) over the combustion volume is visualized in fig. 4.2 for premixed (left) and non-premixed flames (right). The enthalpy of the reactants and products consists of the enthalpy of formation and the sensible enthalpy, cf. eq. (2.6). In fig. 4.2 the enthalpy of formation is represented by the difference between the reference state and

Perfectly premixed flame
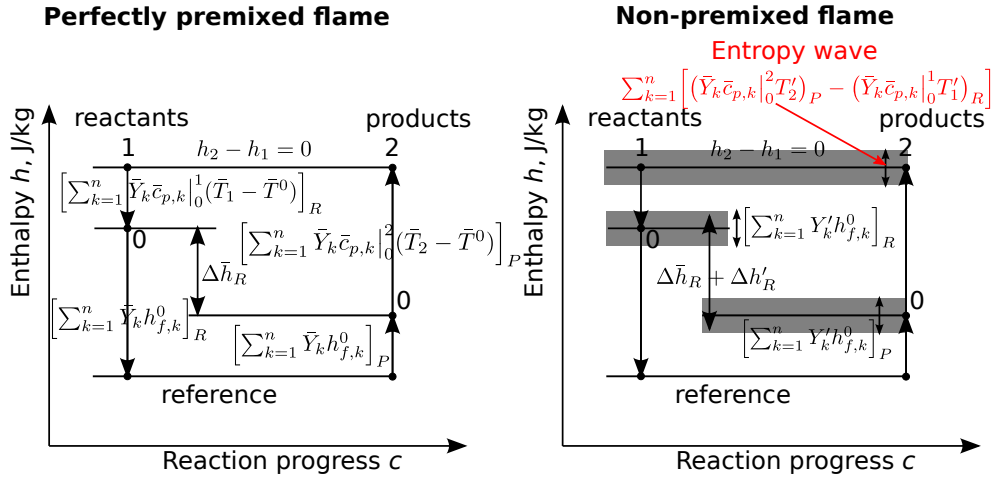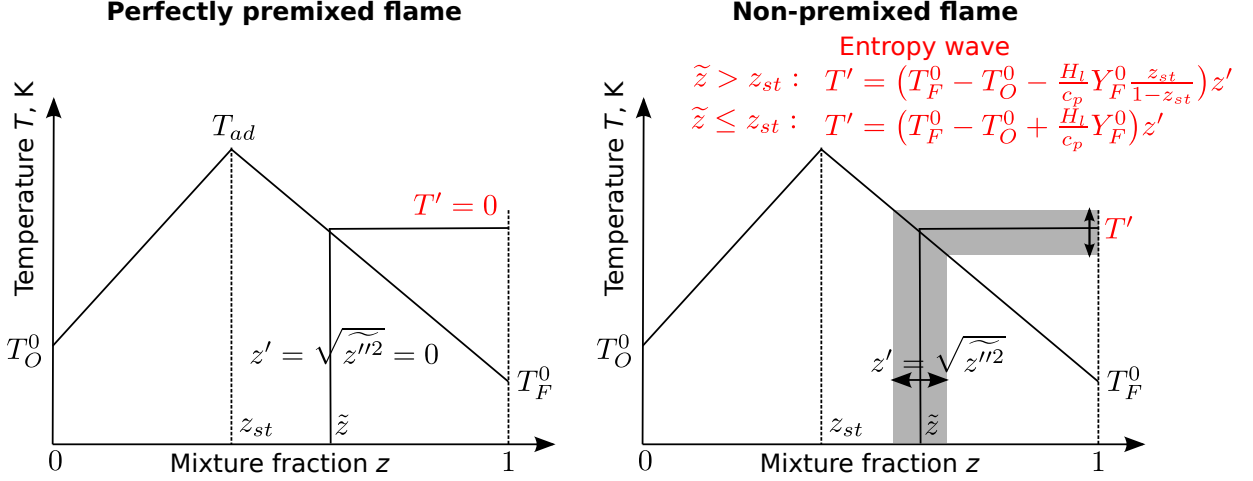
Non-premixed flame

Figure 4.2: Visualization of the conversion of mass fraction fluctuations into sensible enthalpy fluctuations in case of non-premixed flames (right). For perfectly premixed flames the picture is "frozen" (left).

state 0 at a certain temperature T^0. The sensible enthalpy describes the amount of energy, which is necessary to rise the temperature from reference temperature T^0 to the temperatures T_1 and T_2 of the reactants and products. Due to the combustion process the enthalpy of formation of the reactants is partially converted into sensible enthalpy of the products. In case of perfectly premixed flames shown on the left of fig. 4.2 no fluctuations of the reactant composition occur. As a consequence the composition of the exhaust gases is also fixed. Therefore no fluctuations of the enthalpy of formation and sensible enthalpy exist on the reactant and product side, so that the picture on the left in fig. 4.2 is frozen. Since the sensible enthalpy represents a measure of the temperature, the perfectly premixed flame leads to a mean temperature rise, whereas no fluctuations of the product's temperature and entropy occur. The right of fig. 4.2 shows the conversion process in case of non-premixed flames. Inhomogeneities in the reactant composition result in fluctuations of the product composition. These variations in the mixture fractions, indicated by the gray bars around the average values, lead to fluctuations of the sensible enthalpy and temperature of the products. These temperature fluctuations are proportional to entropy fluctuations and can be imagined as the entropy wave created by the non-premixed flame.

In fig. 4.3 the adiabatic flame temperature is given as a function of the mixture fraction for the infinitely fast chemistry limit, known as the Burke-Schumann flame structure [Poinsot and Veynante, 2005]. The left of fig. 4.3 shows the perfectly premixed case, where no fluctuations around the mean mixture fraction occur. As a consequence the adiabatic flame temperature is constant, implying the absence of entropy waves. The non-premixed flame is characterized by variations of the mixture fraction around its mean values, which are indicated by the gray bars on the right of fig. 4.3. These mixture fraction variations result in temperature fluctuations and therefore the formation of entropy waves. The for-

35

mulas for the temperature fluctuations given in fig. 4.3 are deduced from the eqs. (4.71) and (4.72) by computing the total differential of the temperature with respect to the mixture fraction, i.e. $T' = (\partial T/\partial z)z'$.

Perfectly premixed flame

Non-premixed flame

Figure 4.3: Visualization of the conversion of mixture fraction fluctuations into temperature fluctuations in case of non-premixed flames (right), assuming irreversible infinitely fast chemistry (Burke-Schumann flame structure) [Poinsot and Veynante, 2005]. Again for perfectly premixed flames the picture is "frozen" (left).

Summary

The analysis above leads to the most important conclusions of this subsection:

- Perfectly premixed flames do not generate entropy waves. Apparent entropy and mass fraction fluctuations due to flame intermittency do not propagate, instead they are given by a level set approach (G-equation, cf. Peters [2000] or Pope [1988]) like all other thermodynamic variables in a perfectly-premixed flame.

- Entropy fluctuations in non-premixed flames arise from the partial conversion of mixture fraction fluctuation into oscillations of the sensible enthalpy and temperature.

4.1.3 Direct Noise

In the previous subsections 4.1.1 and 4.1.2 the sources of combustion noise and entropy waves were investigated. The following paragraphs are focused on the phenomenological description of the environmental impact of the combustion noise sources.

Combustion noise of turbulent flames arises from the unsteady flame-turbulence interactions, which are responsible for local heat release fluctuations. These lead to an unsteady gas expansion and finally to the release of pressure fluctuations, which are noticeable as

the direct sound emissions. The flame-turbulence interactions involve a wide range of length and time scales so that direct combustion noise exhibits a broadband character [Dowling and Mahmoudi, 2015]. This represents a fundamental difference to tonal combustion instabilities occurring under certain circumstances at discrete frequencies due to the feedback from acoustics on the heat release oscillations of the flame [Dowling, 1995, Dowling and Stow, 2003]. Typical combustion noise spectra in sound power level (PWL) vs. frequency of turbulent flames are sketched in fig. 4.4. The maximum amplitudes are typically found in the low frequency range between approximately 200 to 1000 Hz [Kotake, 1990, Rajaram and Lieuwen, 2009]. The low frequency acoustic power of combustion noise and its monopole source character represent the most important differences to high frequency aerodynamic noise, which has a significant directionality (quadrupole source). In fig. 4.4 the typical combustion noise spectrum is characterized in the low and high frequency regime by the polynomial dependencies on the frequency f^{β} and $f^{-\alpha}$ with $\alpha, \beta > 0$. The spectrum reaches its maximum amplitude at the peak frequency f_p located in-between these two regions [Rajaram and Lieuwen, 2009].
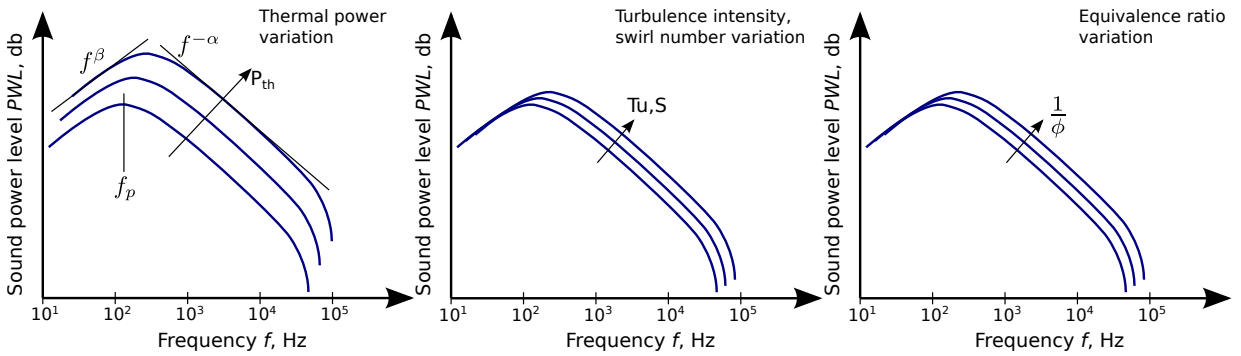
Figure 4.4: Typical sound power level spectra of direct combustion noise of a non-premixed turbulent swirling flame [Jörg, 2015], and qualitative influence of the thermal power (left), turbulence intensity and swirl number (center) and equivalence ratio (right).

According to fig. 4.4, the most important parameters controlling the combustion noise emissions are the following:

- Thermal power P_{th} (fig. 4.4 left): When keeping the equivalence ratio ϕ constant, the PWL increases as the thermal power P_{th} increases, whereas the peak frequency is shifted towards higher frequencies. This result holds for premixed and non-premixed flames [Jörg, 2015, Wäsle, 2007, Winkler, 2007]. In these studies the thermal power was varied through the total mass flow of fuel and oxidizer.

- Incoming turbulence intensity Tu: It affects the higher frequency components of the PWL (fig. 4.4 middle) in such a way that higher turbulence levels create higher PWLs [Kotake and Takamoto, 1990]. This behavior also applies to the swirl num-

ber S dependence when holding the equivalence ratio and the total mass flow rate constant. An enhanced swirl level is always accompanied by intensified turbulence, which results in an increase of the PWL [Jörg, 2015].

- Equivalence ratio ϕ (fig. 4.4 right): The acoustic power of a non-premixed flame increases as the equivalence ratio is decreased [Jörg, 2015].

Although not explicitly shown in fig. 4.4 further important dependencies of the combustion noise are:

- The formation of large coherent periodic vortex structures (vorticity waves), which alter the flame surface and considerably influence the characteristic frequency f_p of combustion noise.

- The spatial and temporal coherence of the heat sources, which affect the acoustic power levels. The coherence between the sources can be accounted for by the concept of the coherence volume [Wäsle et al., 2005, Winkler et al., 2005].

- The nozzle burner geometry: For fixed equivalence ratio and thermal power an increase of the nozzle diameter d results in higher PWLs while the peak frequency decreases according to the proportionality $1/d$ [Kotake and Takamoto, 1987].

In several studies scaling laws for the acoustic power released by turbulent flames were developed [Candel et al., 2009, Clavin and Siggia, 1991, Strahle, 1971, 1985]. Most of them are based on the far-field solution of the inhomogeneous wave eq. (4.3) for acoustical compact, isobaric ($\rho c^2 = \bar{\rho}\bar{c}^2 = \kappa\bar{p}$) and low Mach number flames [Crighton et al., 1992], which reads

$$p'(\boldsymbol{x}, t) = \frac{1}{4\pi r} \frac{(\kappa - 1)}{\bar{c}^2} \frac{\partial}{\partial t} \int_V \dot{\omega}'_T(\boldsymbol{x}_s, t - \tau_s) \mathrm{d}V. \qquad (4.9)$$

τ_s describes the retarded time for the propagation of an acoustic wave from the source location $\boldsymbol{x}_s$ to the observer location $\boldsymbol{x}$ over a distance $r = |(\boldsymbol{x} - \boldsymbol{x}_s)|$. The total flame volume is termed by V. The total acoustic power P_a emitted by the flame is obtained by integration of the time-averaged acoustic intensity over the surface S of a spherical with radius R and surface normal n_i [Wäsle, 2007, Winkler, 2007]. This yields together with eq. (4.9) the following expression for the acoustic power

$$P_a = \frac{1}{\bar{\rho}\bar{c}} \int_S \overline{p'(\boldsymbol{x}, t)p'(\boldsymbol{x}, t)} \mathrm{d}S = \frac{1}{4\pi\bar{\rho}} \frac{(\kappa - 1)^2}{\bar{c}^5} \int_{V'} \int_V \overline{\frac{\partial}{\partial t}\dot{\omega}'_T(\boldsymbol{x}_s, t)\frac{\partial}{\partial t}\dot{\omega}'_T(\boldsymbol{x}_s + \boldsymbol{r}, t + \tau)} \mathrm{d}V \mathrm{d}V'. \qquad (4.10)$$

This analytical solution is the starting point for the statistical noise model developed by Hirsch et al. [2007], which is presented in sec. 4.3. Further overviews about the topic of combustion noise are given by Candel et al. [2009] or Dowling and Mahmoudi [2015].

4.1.4 Indirect Noise

In context of the inhomogeneous wave eq. (4.2) the dipole source term IV represents the source of indirect combustion noise due to accelerated inhomogeneities in the flow. Howe [2010] derived an extended wave equation for the total sensible enthalpy $h_t = h_s + u^2/2$, which explicitly shows the indirect noise generation by accelerated vorticity, i.e.

$$\rho \frac{\mathrm{D}}{\mathrm{D}t} \left(\frac{1}{\bar{c}^2} \frac{\mathrm{D}h_t}{\mathrm{D}t} \right) - \frac{\partial}{\partial x_k} \left(\rho \frac{\partial h_t}{\partial x_k} \right) = \underbrace{\frac{\partial}{\partial x_i} \left(\rho \epsilon_{ijk} \Omega_j u_k - \rho T \frac{\partial s}{\partial x_i} \right)}_{\text{I}} + \underbrace{\rho \frac{\mathrm{D}}{\mathrm{D}t} \left(\frac{\alpha T}{c_p} \frac{\partial s}{\partial t} \right)}_{\text{II}}. \quad (4.11)$$

The first term I represents all dipole sound sources due to vortex acceleration and entropy gradients (refraction of sound), while the last term II constitutes a monopole source due to heat addition. As explained by Lieuwen [2012] the major coupling term for the indirect noise generation by entropy waves is the term $\rho' \bar{u}_j \partial \bar{u}_i / \partial x_j$ in the linearized momentum eq. (3.3). Thus indirect noise generation by entropy waves is an effect of inertia forces due to varying density.

Experimental evidence of the indirect noise arising from entropy waves was provided by the entropy wave generator (EWG) experiment [Bake et al., 2008, 2009]. They measured the acoustic response of a convergent-divergent nozzle exposed to entropy waves. Entropy waves were generated by heating wires located upstream of the nozzle, while the acoustic response was recorded by several microphones installed downstream of the nozzle. Indirect noise was investigated by several theoretical and numerical studies [Duran and Moreau, 2011, 2013, Howe, 2010, Leyko et al., 2011, Marble and Candel, 1977], all of which could be validated with the EWG. Only a few studies are available addressing the vorticity as the second source of indirect noise. For instance in the frame of the vorticity wave generator (VWG) experiment by Kings and Bake [2010] and Kings et al. [2012], vorticity waves were excited by the pulsed injection of a circumferential mass flow upstream of a convergent-divergent nozzle. Similar to the EWG experiment, four microphones were installed downstream of the nozzle to measure the acoustic response to the vortical excitation. Recent analytical studies by Mahmoudi et al. [2015] showed that the contribution of the vorticity to the indirect noise generation is negligible as it possesses amplitudes one order of magnitude smaller than the entropy contribution.

Entropy waves are excited as a consequence of mixing processes, heat conduction and chemical reactions. Mixing is described by the first four terms in the entropy eq. (3.8). Laminar heat conduction is represented by the fifth term in eq. (3.8). As later shown in subsec. 4.2.1 this term can be extended to include turbulent heat fluxes using a triple-decomposition approach. These turbulent heat fluxes are in particular relevant at the air-cooled combustor walls. As shown by Sattelmayer [2003] and Eckstein et al. [2006] entropy waves generated by the flame are significantly damped due to aerodynamic shear dispersion [Goh and Morgans, 2011]. But the impact of the entropy wave generation by secondary air injections and dilution air in RQL combustors has not been assessed yet.

When only considering the entropy wave generation by the flame itself and taking into account the findings of the subsec. 4.1.2 the following statements can be made:

- A perfectly premixed flame excludes the generation of indirect noise as it does not support the production of entropy waves.

- A non-premixed flame may feature indirect noise, unless the entropy waves are dissipated by aerodynamic flow shearing and mixing before reaching the nozzle downstream of the combustion chamber.

4.2 Source Term Modeling

In hybrid CFD/CAA methods, such as the RANS/LNSE approach applied in this thesis, the large differences between the time and length scales of the reacting flow and acoustics are exploited [Bui et al., 2007a, Ewert, 2008]. As sketched in fig. 4.5 the combustion source region solely occupies a very small region of the combustor geometry. In the combustion region intense turbulent fluctuations of the density, temperature, reaction progress, mixture fraction and entropy are observed. In the remaining combustion chamber only small-amplitude acoustic, vorticity and entropy modes propagate and no chemical reactions occur. In this thesis the idea by Lighthill and Newman [1952], Strahle [1972] and Crighton et al. [1992] is followed, who proposed a two step procedure, where aerodynamic or combustion noise sources are separately determined in the first step. These sources are then included into an acoustic model to solve the sound propagation problem. For the latter the extended linear wave equation [Crighton et al., 1992], the acoustic perturbation equations for reacting flows (APE-RF) [Bui et al., 2006] or LEE [Mühlbauer et al., 2010] were proposed. Since the goal of this thesis is to determine direct as well as indirect noise, the transport of vorticity and entropy must be captured by the model. Accordingly either the LNSE or LEE can be used to model the acoustic and entropy propagation in the acoustical domain. Due to the importance of heat conduction at the combustor walls for the propagation of entropy waves, all acoustic simulations done in the present thesis are based on the LNSE.

All previous attempts to use combustion noise source terms have introduced them into the non-reactive linearized equations via the energy equation and treating the release of the reaction enthalpy as a fluctuating heat source. While this is without consequence in the inhomogeneous wave equation (3.22), it generates entropy waves in the LNSE (3.2)-(3.4) and the LEE (3.17)-(3.19). Furthermore it models the wrong physics as shown in the case of perfectly premixed turbulent combustion, which must not produce entropy waves. To the best of the authors knowledge only the theoretical studies by Strobio Chen et al. [2014, 2016] address the issue of entropy wave generation in perfectly premixed and diffusion flames. The formulation of adequate combustion source terms for linearized partial differential equations such as LEE or LNSE is still pending. This is the major purpose of

Source region: Turbulence effects, incompressible, but non-isentropic flow, strong apparent turb. density/entropy fluctuations

$$\frac{\mathrm{D}\rho''}{\mathrm{D}t} \gg 0, \frac{\mathrm{D}p''}{\mathrm{D}t} \approx 0$$
$$\rho'' \gg 0, p'' \approx 0$$

$\langle \phi''\phi'' \rangle \neq 0$

Coherent turbulent fluctuations

Propagation region (LNSE): linear acoustics, compressible, isentropic

$$\bar{\rho}\bar{T}\frac{\mathrm{D}s'}{\mathrm{D}t} = \frac{\mathrm{D}p'}{\mathrm{D}t} - \bar{c}^2\frac{\mathrm{D}\rho'}{\mathrm{D}t} = 0$$
$$\rho' = \frac{p'}{\bar{c}^2} \approx 0$$

$\frac{\partial}{\partial x_j}\tau'_{ij,L}$ $Y''_k = 0$ $\bar{\rho}s'_V$

P_u^+ $S_u = 0$ P_u^-

(a)

Source region: Turbulence effects, incompressible, but non-isentropic flow, strong turb. density/entropy fluctuations

$$\frac{\mathrm{D}\rho''}{\mathrm{D}t} \gg 0, \frac{\mathrm{D}p''}{\mathrm{D}t} \approx 0$$
$$\rho'' \gg 0, p'' \approx 0$$

$\langle \phi''\phi'' \rangle \neq 0$

Coherent turbulent fluctuations

Propagation region (LNSE): linear acoustics, compressible, non-isentropic

$$\bar{\rho}\bar{T}\frac{\mathrm{D}s'}{\mathrm{D}t} = \frac{\mathrm{D}p'}{\mathrm{D}t} - \bar{c}^2\frac{\mathrm{D}\rho'}{\mathrm{D}t}$$
$$\bar{\rho}\bar{T}\frac{\mathrm{D}s'}{\mathrm{D}t} = (\kappa - 1)\dot{\omega}'_z$$

Y''_k $\dot{\omega}'_z$

P_u^+ S_u P_u^-

(b)

Figure 4.5: LNSE including stochastic sound sources for two cases: (a) perfectly premixed flame, and (b) non-premixed flame.

the following paragraphs.

In summary the theoretical considerations and the review of the experimental and numerical studies on combustion noise in this chapter lead to the following requirements to be fulfilled by the source term formalism for linearized non-reactive equations:

- The propagation model should be based on non-reacting linearized acoustic equations, in which the interaction to low Mach number reacting flows is expressed by monopole source terms (since combustion is limited to a small source region within the large acoustic propagation domain) [Crighton et al., 1992].

- Heat release oscillations should be caused by turbulent [Strahle, 1972], non-linear and stochastic fluctuations [Rajaram and Lieuwen, 2009].

- A certain level of coherence between stochastic turbulent fluctuations should represent a necessary criterion for the release of combustion noise [Wäsle et al., 2005].

- The feedback from acoustics on the reacting flow [Lieuwen, 2003] should be excluded since the model is focused on broadband combustion noise but not on tonal combustion instabilities.

- The entropy wave generation in perfectly-premixed and non-premixed flames should be correctly represented, cf. subsec. 4.1.2 or Strobio Chen et al. [2016].

- The source terms should include power spectra / autocorrelation spectra of the fluctuating heat release rate [Lieuwen, 2012].

- The source term model should provide a relation to the statistical model by Hirsch et al. [2006, 2007].

- Finally a formalism to include source terms obtained from incompressible URANS or LES simulations should be given.

As explained above the broadband combustion noise is inherently coupled to stochastic turbulent fluctuations, which represent a fundamental difference to the tonal combustion instabilities [Dowling and Mahmoudi, 2015]. These turbulent quantities need to be kept when modeling combustion noise, while they can be neglected when considering combustion instabilities. Although the model equations are not solved for the turbulent stochastic and non-linear fluctuations, they can be treated as given source terms in the acoustic propagation problem. A technique to include linear acoustic and turbulent fluctuations in the model is the so-called triple-decomposition approach [Lieuwen, 2012].

In the following paragraphs stochastic combustion noise sources due to low-speed reacting flows are incorporated in the LNSE using a triple-decomposition approach, initially proposed by Hussain and Reynolds [1970, 1972]. By this means a semi-analytical model is derived, which fulfills the requirements stated above. A triple decomposition approach was

also proposed by Bechara et al. [1994], Bailly et al. [1996] and by Bailly and Juve [1999] to include stochastic aerodynamic sources in the LEEs for aeroacoustic problems based on isentropic wave propagation. A further overview about the different modeling approaches for combustion noise is given by Bailly et al. [2010].

4.2.1 LNSE Including Stochastic Sound Sources

As sketched in fig. 4.5, in the following a model is proposed, which splits up the domain into the following parts:

- A source region, governed by reactive non-linear flow equations along with the assumption of an isobaric low Mach number flame [Poinsot and Veynante, 2005].

- A propagation domain, described by non-reactive linearized equations including stochastic source terms due to unsteady combustion. These source terms are complex non-linear functions of the turbulent combustion process and are treated as fixed and given frequency-dependent terms in the linear acoustic propagation problem.

The model is derived by introducing a triple-decomposition approach. It separates any unsteady flow quantity $\phi(\boldsymbol{x}, t)$ into a time-averaged mean part $\bar{\phi}(\boldsymbol{x})$, a coherent part $\phi'(\boldsymbol{x}, t)$ with small-amplitude and time-harmonic oscillations, and a stochastic turbulent and non-linear part $\phi''(\boldsymbol{x}, t)$. This splitting technique can be interpreted as a combination of the Reynolds-decomposition [Adams, 2008] and the linearization approach (3.1). Then the unsteady fields of the density, velocities, pressure and species mass fraction are given by

$$\rho\left(\boldsymbol{x}, t\right) = \bar{\rho}\left(\boldsymbol{x}\right) + \rho'\left(\boldsymbol{x}, t\right) + \rho''\left(\boldsymbol{x}, t\right), \qquad \rho' \ll \bar{\rho}, \qquad (4.12)$$

$$u_i\left(\boldsymbol{x}, t\right) = \bar{u}_i\left(\boldsymbol{x}\right) + u_i'\left(\boldsymbol{x}, t\right) + u_i''\left(\boldsymbol{x}, t\right), \qquad u_i' \ll \bar{c}, \qquad (4.13)$$

$$p\left(\boldsymbol{x}, t\right) = \bar{p}\left(\boldsymbol{x}\right) + p'\left(\boldsymbol{x}, t\right), \qquad p' \ll \bar{p}, \qquad (4.14)$$

$$Y_k\left(\boldsymbol{x}, t\right) = \bar{Y}_k\left(\boldsymbol{x}\right) + Y_k''\left(\boldsymbol{x}, t\right). \qquad (4.15)$$

Important assumptions are already included in this decomposition: First eq. (4.14) implies an incompressible low Mach number flame where turbulent pressure fluctuations are negligible, i.e. $p'' \to 0$. Eq. (4.15) also leads to a set of non-reacting acoustic equations ($Y_k' = 0$), which is sufficiently fulfilled under the assumption of complete combustion in the propagation domain. Then the species eq. (2.2) is dropped for the linearized problem, but still valid for the non-linear source terms. No linearization can and needs to be performed for the species equation which accounts for the highly non-linear characteristics of combustion [Poinsot and Veynante, 2005]. The turbulent density fluctuation ρ'' will turn out to be the dominant quantity of the turbulent combustion on the linearized continuity equation. This is is also reflected by the excess density in the extended linear wave eq. (4.2) and Lighthill eq. (4.1), so that it is reasonable to assume a close relation between the turbulent density fluctuation and the excess density [Strahle, 1972].

Based on the assumptions of constant heat capacities for all species ($c_p = c_{p,k} = $ const.), a unit Lewis number (Le = 1) and a negligible change of the gas constant ($\mathrm{D}R/\mathrm{D}t = 0$), the procedure by Hussain and Reynolds [1970, 1972] is followed: The starting point is the substitution of the triple-decomposition (4.12) - (4.15) into the conservation eqs. (2.1), (2.2), (2.3) and (2.11) for reactive flows, which are simplified using the assumptions above. Products of the coherent quantities are neglected ($\phi'\phi' = 0$), whereas higher order stochastic quantities are kept ($\phi''\phi'' \neq 0$). Due to the large length and time scale differences between turbulent and acoustic fluctuations, interaction terms of the form $\phi'\phi'' = 0$ are assumed to be zero. Then phase or ensemble-averaging eliminates all terms including solely first moments of stochastic quantities ($\langle\phi''\rangle = 0$), while coherent periodic waves are retained ($\langle\phi'\rangle = \phi'$). The mean flow field is subsequently separated by time-averaging ($\overline{\phi'} = 0$). Finally the linearized equations for the fluctuating density, velocities and pressure are obtained by the subtraction of the time-averaged equations from the phase-averaged equations to give

$$\frac{\mathrm{D}\rho'}{\mathrm{D}t} = -u_i'\frac{\partial\bar{\rho}}{\partial x_i} - \bar{\rho}\frac{\partial u_i'}{\partial x_i} - \rho'\frac{\partial\bar{u}_i}{\partial x_i} - \frac{\partial}{\partial x_i}\Big[\langle\rho''u_i''\rangle - \overline{\rho''u_i''}\Big], \tag{4.16}$$

$$\bar{\rho}\frac{\mathrm{D}u_i'}{\mathrm{D}t} = -\bar{\rho}u_j'\frac{\partial\bar{u}_i}{\partial x_j} - \rho'\bar{u}_j\frac{\partial\bar{u}_i}{\partial x_j} - \frac{\partial p'}{\partial x_i} + \frac{\partial\tau_{ij}'}{\partial x_j} + \bar{\rho}f_i' - \frac{\partial}{\partial x_j}\Big[\bar{\rho}\langle u_i''u_j''\rangle - \bar{\rho}\overline{u_i''u_j''}\Big], \tag{4.17}$$

$$\frac{\mathrm{D}p'}{\mathrm{D}t} = -u_i'\frac{\partial\bar{p}}{\partial x_i} - \kappa\bar{p}\frac{\partial u_k'}{\partial x_k} - \kappa p'\frac{\partial\bar{u}_k}{\partial x_k} + (\kappa-1)\bigg\{\Phi' + \big[\langle\Phi''\rangle - \overline{\Phi''}\big] + \lambda\frac{\partial^2 T'}{\partial x_i\partial x_i} -$$
$$- \frac{\partial}{\partial x_i}\big[\langle\dot{q}_i''\rangle - \overline{\dot{q}_i''}\big] + \dot{q}_V'\bigg\} + (\kappa-1)\big[\langle\dot{\omega}_T\rangle - \overline{\dot{\omega}_T}\big]. \tag{4.18}$$

In comparison to the classical LNSE (3.2)-(3.4) for non-reacting flows, several source terms due to stochastic turbulent fluctuations arise in form of ensemble-averaged quantities. The different terms are discussed in the next paragraphs: Gikadi et al. [2014] and Hussain and Reynolds [1972] interpreted the source terms in the linearized momentum eq. (4.17) as an additional eddy viscosity acting on the acoustic wave propagation. They also can be understood as the classical aerodynamic noise sources or Lighthill stresses $\tau_{ij,L}' = \bar{\rho}\langle u_i''u_j''\rangle - \bar{\rho}\overline{u_i''u_j''}$ as proposed by Lighthill and Newman [1952] or Bechara et al. [1994]. The source term in the linearized continuity eq. (4.16) was also derived by Bui et al. [2007b] but not utilized to implement combustion noise sources. In the following it is expressed in terms of a time derivative of the turbulent density fluctuation $\rho_t' = \langle\rho\rangle - \bar{\rho}$ using the Reynolds-averaged (not Favre-averaged) continuity equation [Poinsot and Veynante, 2005, cf. chapter 4.5.1, p. 141] along with the assumption of a low-speed flame ($\langle u_i\rangle \to 0$), yielding

$$\frac{\partial\rho_t'}{\partial t} = \frac{\partial\langle\rho\rangle}{\partial t} \approx -\frac{\partial}{\partial x_i}\Big[\langle\rho''u_i''\rangle - \overline{\rho''u_i''}\Big]. \tag{4.19}$$

The time derivative of the density highlights that this term represents a monopole source [Ehrenfried, 2002, Rienstra and Hirschberg, 2012]. The source term in the linearized energy

eq. (4.18), expressed by the difference between the ensemble and time averaged heat rate of combustion, is defined as $\dot{\omega}_T' = \langle \dot{\omega}_T \rangle - \overline{\dot{\omega}_T}$ in the following. When neglecting the dissipation function due to stochastic fluctuations $\Phi'' = \tau_{ij}'' \partial u_i'' / \partial x_j$ and turbulent heat fluxes $\dot{q}_i'' = -\lambda (\partial T'' / \partial x_i)$, the linearized set of eqs. (4.16) - (4.18) simplifies to

$$\frac{\mathrm{D}\rho'}{\mathrm{D}t} = -u_i' \frac{\partial \bar{\rho}}{\partial x_i} - \bar{\rho} \frac{\partial u_i'}{\partial x_i} - \rho' \frac{\partial \bar{u}_i}{\partial x_i} + \frac{\partial \rho_t'}{\partial t}, \tag{4.20}$$

$$\bar{\rho} \frac{\mathrm{D}u_i'}{\mathrm{D}t} = -\bar{\rho} u_j' \frac{\partial \bar{u}_i}{\partial x_j} - \rho' \bar{u}_j \frac{\partial \bar{u}_i}{\partial x_j} - \frac{\partial p'}{\partial x_i} + \frac{\partial \tau_{ij}'}{\partial x_j} + \bar{\rho} f_i' - \frac{\partial}{\partial x_j} \tau_{ij,L}', \tag{4.21}$$

$$\frac{\mathrm{D}p'}{\mathrm{D}t} = -u_i' \frac{\partial \bar{p}}{\partial x_i} - \kappa \bar{p} \frac{\partial u_k'}{\partial x_k} - \kappa p' \frac{\partial \bar{u}_k}{\partial x_k} + (\kappa - 1) \left\{ \Phi' + \lambda \frac{\partial^2 T'}{\partial x_i \partial x_i} + \dot{q}_V' \right\} + (\kappa - 1)\dot{\omega}_T'. \tag{4.22}$$

In these modeling equations the noise generation by the turbulent combustion process is represented by the monopole source terms $\partial \rho_t' / \partial t$ and $\dot{\omega}_T'$ in the linearized continuity eq. (4.20) and energy eq. (4.22). These source terms are a result of the turbulent non-linear combustion process, so that they represent non-linear functions of the turbulence quantities. These terms act as fixed and given sources in the linear propagation problem, where only the linear fluctuations of the density ρ', velocities u_i' and pressure p' are solved. The dipole source term f_i' and the quadrupole sources due to aerodynamic noise $\tau_{ij,L}'$ are incorporated in the linearized momentum eq. (4.21). The source term due to electrical heat input is represented by $\dot{q}_V'$. Apart from the noise generation by viscous, thermal and species diffusion, this model contains all main noise sources as given by the Lighthill eq. (4.1) or the extended linear wave eq. (4.2). No assumptions concerning premixed or non-premixed flames were made so far, so that this set of linearized equations holds for both types of flames. A differentiation is introduced in the following subsection.

The source terms in the linearized continuity eq. (4.20) and energy eq. (4.22) are not independent from each other. They are coupled through the non-linear pressure-density relation (2.14) for reacting flows as derived by Crighton et al. [1992]. Also the relation between both source terms determines the entropy wave generation, which is demonstrated in the subsections for perfectly-premixed and non-premixed flames. When assuming an isobaric ($\mathrm{D}p/\mathrm{D}t \to 0$), incompressible and small Mach number flame ($\langle u_i \rangle \to 0$, i.e. $\mathrm{D}/\mathrm{D}t \approx \partial/\partial t$), followed by ensemble and time-averaging, the pressure-density relation (2.14) simplifies to

$$\frac{\partial \langle \rho \rangle}{\partial t} + \left\langle u_i'' \frac{\partial \rho''}{\partial x_i} \right\rangle - \overline{u_i'' \frac{\partial \rho''}{\partial x_i}} = -\frac{\kappa - 1}{c^2} \left[\langle \dot{\omega}_T \rangle - \overline{\dot{\omega}_T} \right]. \tag{4.23}$$

Replacing the left side of eq. (4.23) with the Reynolds-averaged continuity equation [Poinsot and Veynante, 2005, cf. chapter 4.5.1, p. 141] yields

$$\left\langle \rho'' \frac{\partial u_i''}{\partial x_i} \right\rangle - \overline{\rho'' \frac{\partial u_i''}{\partial x_i}} = -\frac{\kappa - 1}{c^2} \left[\langle \dot{\omega}_T \rangle - \overline{\dot{\omega}_T} \right]. \tag{4.24}$$

This equation states that heat release fluctuations caused by unsteady combustion are converted into turbulent velocity and density fluctuations. The unsteady combustion pro-

cess leads to an unsteady volume generation and is therefore a monopole source, which is reflected in the divergence of the velocity.

4.2.2 Source Models For Perfectly-Premixed and Non-premixed Flames

A comparison between the non-reacting LNSE (3.2)-(3.4) and the LNSE including stochastic sound sources (4.20) - (4.22) reveals that one major difference is the source term in the linearized continuity equation. Some studies showed that this term can increase the local volume flow rate up to 20% [Muniz and Mungal, 2001]. As stated by eq. (4.19) this term represents the ensemble averaged coherence between turbulent density and velocity fluctuations, i.e. the covariance $\langle \rho'' u_i'' \rangle$, which is closely related to the turbulent combustion process [Gulati and Driscoll, 1986]. Beyond this the heat of combustion source term in the linearized energy eq. (4.22) contains highly non-linear correlations of the turbulent species and temperature fluctuations [Poinsot and Veynante, 2005]. The natural way to proceed is to retain the LNSE in the form of eqs. (4.20) - (4.22) and to determine the spectral content of both source terms including the amplitude and phase information by performing URANS, LES or even DNS. As the entropy wave generation is controlled by the relation between both source terms this approach automatically includes the differences of perfectly premixed and non-premixed flames.

In this thesis different statistical combustion noise models based on stationary RANS simulations are applied, which can not provide the phase information of any source term. Therefore also the relation and phase difference between the source terms in the continuity eq. (4.20) and energy eq. (4.22) are unknown when using statistical noise models. For this reason a model is needed to further simplify the pressure-density relation (4.23), which connects the source terms in the continuity and energy equation. For the special cases of perfectly premixed and non-premixed flames such a model is derived in the next paragraphs.

LNSE For Perfectly Premixed Flames

In the following the relation between the source terms in the linearized continuity eq. (4.20) and energy eq. (4.22) is modeled to derive the LNSE with stochastic sound sources for perfectly premixed flames. This is achieved by evaluating the covariances $\langle \rho'' u_i'' \rangle$ and $\langle \rho'' c'' \rangle$. The density-velocity covariance $\langle \rho'' u_i'' \rangle$ represents the source term in the continuity equation, cf. eq. (4.19). The heat of combustion can be expressed by a covariance between the density and reaction progress variable $\langle \rho'' c'' \rangle$, because in case of a low-Mach number flame with negligible mass diffusion $\dot\omega_T = -\Delta h_R \dot\omega_c = -\Delta h_R \rho \mathrm{D}c/\mathrm{D}t$ simplifies to

$$\dot\omega_T = -\Delta h_R \frac{\partial \rho c}{\partial t}, \tag{4.25}$$

so that $\dot\omega_T'$ depends on $\langle \rho'' c'' \rangle$. The apparent turbulent fluctuations are strictly coupled through the flame surface movement in perfectly premixed flames. This represents a re-

duction of the degrees of freedom as compared to the non-premixed flame, where not only apparent turbulent fluctuations are observed, but also "true" mixture fraction fluctuations. In a perfectly premixed flame all turbulent fluctuations are functions of the reaction progress variable, which presumably leads to the high coherence levels of the density-velocity correlation, among others. Based on the work of Bray and Moss [1977] the covariances $\langle \rho'' u_i'' \rangle$ and $\langle \rho'' c'' \rangle$ can be explicitly given in terms of the mean variance of the reaction progress variable $\widetilde{c''^2}$ and the heat release parameter $\tau := \rho_u / \rho_b$ [Poinsot and Veynante, 2005], i.e.

$$\langle \rho'' c'' \rangle = -\langle \rho \rangle \frac{\tau \widetilde{c}(1 - \widetilde{c})}{1 + \tau \widetilde{c}} = -\langle \rho \rangle \frac{\tau \widetilde{c''^2}}{1 + \tau \widetilde{c}}, \tag{4.26}$$

$$\langle \rho'' u_i'' \rangle = -\langle \rho \rangle \frac{\tau \widetilde{c}(1 - \widetilde{c})}{1 + \tau \widetilde{c}} \left(\bar{u}_i^b - \bar{u}_i^u \right) = -\langle \rho \rangle \frac{\tau \widetilde{c''^2}}{1 + \tau \widetilde{c}} \left(\bar{u}_i^b - \bar{u}_i^u \right) = \langle \rho'' c'' \rangle \left(\bar{u}_i^b - \bar{u}_i^u \right). \tag{4.27}$$

The underlying Bray Moss Libby (BML) analysis [Bray et al., 1988] assumes a discrete double-delta PDF for all thermodynamic variables. This implies an infinitely fast chemistry, where either unburnt gases (index u) or burnt gases (index b) exist, but no intermediate species are present. The covariances are directly proportional to each other and in phase because $\langle \rho'' u_i'' \rangle \sim \langle \rho'' c'' \rangle < 0$. The negative sign of the density-velocity correlation is also in line with experimental measurements by Gulati and Driscoll [1986]. The covariances may be expressed by the autocovariance of the reaction progress variable, i.e. $\langle \rho'' c'' \rangle = f(\widetilde{c''^2})$ and $\langle \rho'' u_i'' \rangle = f(\widetilde{c''^2})$. Based on this phenomenological analysis it is reasonable to assume that the source terms in the linearized continuity eq. (4.20) and energy eq. (4.22) are in phase for perfectly-premixed flames. Taking this into account and neglecting the correlation between the turbulent velocity and density gradients, the pressure-density relation (4.23) simplifies to

$$\bar{\rho} s_V' = \frac{\partial \rho_t'}{\partial t} = \frac{(\kappa - 1)}{\bar{c}^2} \dot{\omega}_T' = -\frac{(\kappa - 1)}{\bar{c}^2} \Delta \bar{h}_R \dot{\omega}_c'. \tag{4.28}$$

This equation connects the source terms in the linearized continuity eq. (4.20) and energy eq. (4.22) for perfectly premixed flames. As shown below the eq. (4.28) is equal to imposing a volume source without any entropy production. In order to highlight the volume source character of the source terms they are formally expressed by $\bar{\rho} s_V' = \partial \rho_t' / \partial t$, in which s_V' can be interpreted as a divergence of the velocity. This represents one major effect as stated by Strahle [1972]: Turbulent density fluctuations ρ_t' inside the flame volume caused by unsteady combustion are converted into velocity fluctuations leading to the release of acoustic waves. Pierce [1994] initially derived a relation between arbitrary energy and mass sources, which leads to the same results as given by eq. (4.28). Inserting the source term relation (4.28) into the eqs. (4.20) - (4.22) yields the LNSE including turbulent stochastic

sources for perfectly-premixed flames

$$\frac{\mathrm{D}\rho'}{\mathrm{D}t} = -u'_i\frac{\partial\bar{\rho}}{\partial x_i} - \bar{\rho}\frac{\partial u'_i}{\partial x_i} - \rho'\frac{\partial\bar{u}_i}{\partial x_i} + \bar{\rho}s'_V(\widetilde{c''^2}), \tag{4.29}$$

$$\bar{\rho}\frac{\mathrm{D}u'_i}{\mathrm{D}t} = -\bar{\rho}u'_j\frac{\partial\bar{u}_i}{\partial x_j} - \rho'\bar{u}_j\frac{\partial\bar{u}_i}{\partial x_j} - \frac{\partial p'}{\partial x_i} + \frac{\partial\tau'_{ij}}{\partial x_j} + \bar{\rho}f'_i - \frac{\partial}{\partial x_j}\tau'_{ij,L}, \tag{4.30}$$

$$\frac{\mathrm{D}p'}{\mathrm{D}t} = -u'_i\frac{\partial\bar{p}}{\partial x_i} - \kappa\bar{p}\frac{\partial u'_k}{\partial x_k} - \kappa p'\frac{\partial\bar{u}_k}{\partial x_k} + (\kappa-1)\left\{\Phi' + \lambda\frac{\partial^2 T'}{\partial x_i\partial x_i} + \dot{q}'_V\right\} + \bar{\rho}\bar{c}^2 s'_V(\widetilde{c''^2}). \tag{4.31}$$

The volume source term s'_V is a function of the variance of the reaction progress variable, which was shown in context of the BML analysis above, cf. eqs. (4.26) and (4.27). Linearization of the entropy eq. (2.13) and injecting the material derivative of the pressure (4.31) and density (4.29) leads to the linearized energy equation in entropy form

$$\bar{\rho}\bar{T}\frac{\mathrm{D}s'}{\mathrm{D}t} = \frac{\mathrm{D}p'}{\mathrm{D}t} - \bar{c}^2\frac{\mathrm{D}\rho'}{\mathrm{D}t} = -\left(\bar{\rho}\bar{T}u'_i + \bar{\rho}T'\bar{u}_i + \rho'\bar{T}\bar{u}_i\right)\frac{\partial\bar{s}}{\partial x_i} -$$
$$-\frac{\kappa p' - \bar{c}^2\rho'}{\kappa-1}\frac{\partial\bar{u}_k}{\partial x_k} + \left\{\Phi' + \lambda\frac{\partial^2 T'}{\partial x_i\partial x_i} + \dot{q}'_V\right\}. \tag{4.32}$$

The volume source terms s'_V do not appear on the right side of eq. (4.32), where sources and interaction terms of entropy waves are found. Consequently the volume source term modeling approach for perfectly-premixed flames as proposed in this thesis does not lead to any entropy wave generation. This is the most important finding of the current subsection. It should be emphasized that the presented volume source term approach for premixed flames is consistent with the source term filtering technique developed by Ewert and Schröder [2003]. As shown for instance by Delfs [2016] the volume source approach can also be arrived at by introducing a volume source term in the linearized continuity equation, which then appears in the linearized energy equation after a rigorous derivation.

However when it comes to the propagation of acoustic waves released by the volume source terms, the entropy eq. (4.32) reveals an inherent limitation of the non-reacting LNSE (4.29) - (4.31). As indicated by the first term $-u'_i\partial\bar{s}/\partial x_i$ in eq. (4.32), the interaction of acoustic and vorticity waves with mean entropy gradients always leads to an excitation of entropy waves, which is independent from the source model. Therefore the LNSE do not support an isentropic wave propagation in a non-isentropic mean flow.

LNSE For Non-Premixed Flames

In non-premixed flames not only apparent turbulent fluctuations due to flame intermittency are observed but also fluctuations resulting from variations in the mixture fraction composition. Therefore the turbulent fluctuations are no more exclusive functions of one primary variable like the reaction progress variable in the premixed case. They are also functions of the turbulent mixture fraction fluctuations, which can be understood as an

additional degree of freedom with regard to the generation of heat release oscillations. The measurements by Dibble et al. [1984] support the idea that the additional degree of freedom leads to lower coherence between the source terms in the continuity eq. (4.20) and energy eq. (4.22). As measured by Jörg [2015] this does not necessarily mean that the acoustic power radiated by a non-premixed flame is lower than the acoustic power emitted by a premixed flame with the same mean thermal power.

Since the relation between the source terms in the continuity eq. (4.20) and energy eq. (4.22) cannot be analytically given as done before in context of the perfectly premixed flame, the heat release fluctuations are imposed in the conventional way by setting [Poinsot and Veynante, 2005]

$$\dot{\omega}_T = \dot{\omega}_z = -\rho D (\nabla z)^2 \frac{\partial^2 Y_k}{\partial z^2} = -\frac{1}{2} \rho \chi \frac{\partial^2 Y_k}{\partial z^2}. \tag{4.33}$$

This implies that the fluctuating heat release is a function of the variance of the mixture fraction $\dot{\omega}_z' = f(\widetilde{z''^2})$, cf. (2.22). The source term in the linearized continuity eq. (4.20) is assumed to be zero in this case. Then the LNSE (4.20) - (4.22) including turbulent stochastic sources for non-premixed flames read

$$\frac{\mathrm{D}\rho'}{\mathrm{D}t} = -u_i' \frac{\partial \bar{\rho}}{\partial x_i} - \bar{\rho} \frac{\partial u_i'}{\partial x_i} - \rho' \frac{\partial \bar{u}_i}{\partial x_i}, \tag{4.34}$$

$$\bar{\rho} \frac{\mathrm{D}u_i'}{\mathrm{D}t} = -\bar{\rho} u_j' \frac{\partial \bar{u}_i}{\partial x_j} - \rho' \bar{u}_j \frac{\partial \bar{u}_i}{\partial x_j} - \frac{\partial p'}{\partial x_i} + \frac{\partial \tau_{ij}'}{\partial x_j} + \bar{\rho} f_i' - \frac{\partial}{\partial x_j} \tau_{ij,L}', \tag{4.35}$$

$$\frac{\mathrm{D}p'}{\mathrm{D}t} = -u_i' \frac{\partial \bar{p}}{\partial x_i} - \kappa \bar{p} \frac{\partial u_k'}{\partial x_k} - \kappa p' \frac{\partial \bar{u}_k}{\partial x_k} + (\kappa - 1) \left\{ \Phi' + \lambda \frac{\partial^2 T'}{\partial x_i \partial x_i} + \dot{q}_V' \right\} + (\kappa - 1) \dot{\omega}_z'(\widetilde{z''^2}). \tag{4.36}$$

In linear acoustics a monopole source can be either prescribed in the continuity or energy equation. Because of that, imposing the combustion noise source term solely in the continuity or energy equation has no influence on the acoustic amplitudes produced by it. But as the additional source term controls the generation of entropy waves the conventional model (4.33) is inherently accompanied by an entropy wave generation, which is desirable for non-premixed flames. This is demonstrated by a derivation of the entropy equation based on the linearized continuity eq. (4.34) and energy eq. (4.36) for non-premixed flames to finally obtain

$$\bar{\rho} \bar{T} \frac{\mathrm{D}s'}{\mathrm{D}t} = \frac{\mathrm{D}p'}{\mathrm{D}t} - \bar{c}^2 \frac{\mathrm{D}\rho'}{\mathrm{D}t} = -\left(\bar{\rho} \bar{T} u_i' + \bar{\rho} T' \bar{u}_i + \rho' \bar{T} \bar{u}_i \right) \frac{\partial \bar{s}}{\partial x_i} -$$
$$- \frac{\kappa p' - \bar{c}^2 \rho'}{\kappa - 1} \frac{\partial \bar{u}_k}{\partial x_k} + \left\{ \Phi' + \lambda \frac{\partial^2 T'}{\partial x_i \partial x_i} + \dot{q}_V' \right\} + \dot{\omega}_z'(\widetilde{z''^2}). \tag{4.37}$$

This equation contains the heat rate of combustion $\dot{\omega}_z'(\widetilde{z''^2})$ as a source term for entropy waves on the right hand side. As already mentioned in context of premixed flames the interaction of acoustic waves with mean entropy gradients, identified as the first term in eq. (4.37), produces entropy waves.

Transformation Into Frequency Domain

For the sake of completeness the LNSE with stochastic sound sources are transformed into frequency domain using eq. (3.11). This delivers in case of perfectly premixed flames:

$$i\omega\hat{\rho} + \bar{u}_i\frac{\partial\hat{\rho}}{\partial x_i} = -\hat{u}_i\frac{\partial\bar{\rho}}{\partial x_i} - \bar{\rho}\frac{\partial\hat{u}_i}{\partial x_i} - \hat{\rho}\frac{\partial\bar{u}_i}{\partial x_i} + \bar{\rho}\hat{s}_V, \tag{4.38}$$

$$i\omega\bar{\rho}\hat{u}_i + \bar{\rho}\bar{u}_j\frac{\partial\hat{u}_i}{\partial x_j} = -\bar{\rho}\hat{u}_j\frac{\partial\bar{u}_i}{\partial x_j} - \hat{\rho}\bar{u}_j\frac{\partial\bar{u}_i}{\partial x_j} - \frac{\partial\hat{p}}{\partial x_i} + \frac{\partial\hat{\tau}_{ij}}{\partial x_j} + \bar{\rho}\hat{f}_i - \frac{\partial}{\partial x_j}\hat{\tau}_{ij,L}, \tag{4.39}$$

$$i\omega\hat{p} + \bar{u}_i\frac{\partial\hat{p}}{\partial x_i} = -\hat{u}_i\frac{\partial\bar{p}}{\partial x_i} - \kappa\bar{p}\frac{\partial\hat{u}_k}{\partial x_k} - \kappa\hat{p}\frac{\partial\bar{u}_k}{\partial x_k} + (\kappa-1)\left\{\hat{\Phi} + \lambda\frac{\partial^2\hat{T}}{\partial x_k\partial x_k} + \hat{q}_V\right\} + \bar{\rho}\bar{c}^2\hat{s}_V. \tag{4.40}$$

In case of non-premixed flames the frequency-transformed LNSE with stochastic sound sources read:

$$i\omega\hat{\rho} + \bar{u}_i\frac{\partial\hat{\rho}}{\partial x_i} = -\hat{u}_i\frac{\partial\bar{\rho}}{\partial x_i} - \bar{\rho}\frac{\partial\hat{u}_i}{\partial x_i} - \hat{\rho}\frac{\partial\bar{u}_i}{\partial x_i}, \tag{4.41}$$

$$i\omega\bar{\rho}\hat{u}_i + \bar{\rho}\bar{u}_j\frac{\partial\hat{u}_i}{\partial x_j} = -\bar{\rho}\hat{u}_j\frac{\partial\bar{u}_i}{\partial x_j} - \hat{\rho}\bar{u}_j\frac{\partial\bar{u}_i}{\partial x_j} - \frac{\partial\hat{p}}{\partial x_i} + \frac{\partial\hat{\tau}_{ij}}{\partial x_j} + \bar{\rho}\hat{f}_i - \frac{\partial}{\partial x_j}\hat{\tau}_{ij,L}, \tag{4.42}$$

$$i\omega\hat{p} + \bar{u}_i\frac{\partial\hat{p}}{\partial x_i} = -\hat{u}_i\frac{\partial\bar{p}}{\partial x_i} - \kappa\bar{p}\frac{\partial\hat{u}_k}{\partial x_k} - \kappa\hat{p}\frac{\partial\bar{u}_k}{\partial x_k} + (\kappa-1)\left\{\hat{\Phi} + \lambda\frac{\partial^2\hat{T}}{\partial x_k\partial x_k} + \hat{q}_V\right\} + (\kappa-1)\hat{\dot{\omega}}_z. \tag{4.43}$$

In summary these sets of equations contain monopole source terms related to electrical heat input $(\hat{q}_V)$, as well as the combustion of a perfectly premixed flame $(\hat{s}_V)$ or diffusive flame $(\hat{\dot{\omega}}_z)$. The momentum equation additionally contains the dipole source terms $(\hat{f}_i)$ and quadrupole sources $(\hat{\tau}_{ij,L})$, which allows to model aerodynamic noise.

Isentropic Wave Propagation

When limiting the investigation on direct noise or when neglecting the entropy wave generation downstream of the flame (due to dilution and cooling air) it is useful to apply the isentropic version of the LNSE on the regarded combustion chamber. The non-premixed flame and source model exclude isentropic wave propagation per definition, so that the isentropic assumption is only justifiable in case of premixed flames, where the effects of entropy wave generation downstream of the flame are negligible. Under the assumption of isentropic wave propagation the energy eq. (4.31) is dropped in the LNSE (4.29)-(4.31) for perfectly premixed flames, which simplify to

$$\frac{\mathrm{D}\rho'}{\mathrm{D}t} = -u_i'\frac{\partial\bar{\rho}}{\partial x_i} - \bar{\rho}\frac{\partial u_i'}{\partial x_i} - \rho'\frac{\partial\bar{u}_i}{\partial x_i} + \bar{\rho}s_V'(\widetilde{c''^2}), \tag{4.44}$$

$$\bar{\rho}\frac{\mathrm{D}u_i'}{\mathrm{D}t} = -\bar{\rho}u_j'\frac{\partial\bar{u}_i}{\partial x_j} - \rho'\bar{u}_j\frac{\partial\bar{u}_i}{\partial x_j} - \frac{\partial}{\partial x_i}(\bar{c}^2\rho') + \frac{\partial\tau_{ij}'}{\partial x_j} + \bar{\rho}f_i' - \frac{\partial}{\partial x_j}\tau_{ij,L}'. \tag{4.45}$$

In this case only the source term in the linearized continuity eq. (4.44) is kept. This is a valid approach for the simulation of direct combustion noise because the source terms in the linearized continuity eq. (4.44) and energy eq. (4.31) are equal with respect to the acoustic excitation as long as they are coupled through the relation (4.28) [van Kampen, 2006, van Kampen et al., 2003]. As demonstrated above the second source term of both controls the entropy wave generation, which can be ignored when applying the isentropic assumption.

Summary

Based on physical argumentation the following two semi-analytical submodels were derived:

- Perfectly premixed flames: The high coherence of density, velocity and reaction progress variable fluctuations lead to a perfect coupling of the source terms in the linearized continuity eq. (4.20) and energy eq. (4.22), i.e. they are exactly in phase. This behavior corresponds to a perfect volume source, which is not accompanied by entropy wave generation.

- Non-premixed flames: The higher the degree of non-premixing, the smaller the coherence between the source terms in the linearized continuity eq. (4.20) and energy eq. (4.22). Then coupling and phase relation between both source terms become less defined and distinct, which corresponds more to the behavior of a heat source. The conventional approach is applied in this case since no analytical relation between the source terms can be derived.

- Partially premixed flames are not treated in this thesis. The derivation of a source model for such flames was out of the scope with respect to time of the current project. This should be addressed in further studies.

4.2.3 Source Term Properties

In the following the main features of the presented semi-analytical model are summarized:

- **Source terms due to turbulent fluctuations**: Under the assumption of complete combustion, eqs. (4.29) - (4.31) and eqs. (4.34) - (4.36) describe the propagation of acoustic, entropy and vorticity waves in a non-reacting environment. In a small source region enclosed in the propagation domain, source terms arise in the LNSE due to intense turbulent fluctuations of the density and heat rate of combustion in a low Mach number flame. According to the eq. (4.19), these source terms are non-linear functions of the turbulent fluctuations.

- **Monopole combustion noise sources**: The LNSE with stochastic sound sources contain all major source mechanisms of the Lighthill eq. (4.1) and extended linear wave eq. (4.2). This is proven by recasting the LNSE for premixed and non-premixed flames into the corresponding linear wave equations. In case of premixed flames,

inserting the divergence of the momentum eq. (4.30) into the time derivative of the continuity eq. (4.29) and assuming no mean flow ($\bar{u}_i = 0$, $\partial \bar{u}_i / \partial x_j = 0$, $\partial \bar{\rho} / \partial x_i = \partial \bar{p} / \partial x_i = 0$) yields

$$- \frac{1}{\bar{\rho} \bar{c}^2} \frac{\partial^2 p'}{\partial t^2} + \frac{1}{\bar{\rho}} \frac{\partial^2 p'}{\partial x_i \partial x_i} = \frac{\partial f'_i}{\partial x_i} - \frac{1}{\bar{\rho}} \frac{\partial^2}{\partial x_i \partial x_j} (\tau'_{ij,L}) - \frac{1}{\bar{\rho}} \frac{\partial^2 \rho'_t}{\partial t^2}. \qquad (4.46)$$

In case of non-premixed flames the linear wave equation is deduced from the LNSE by taking the divergence of the momentum eq. (4.35) and the time derivative of the energy eq. (4.36). When neglecting the mean flow, the combination of both equations leads to the following linear wave equation:

$$- \frac{1}{\bar{\rho} \bar{c}^2} \frac{\partial^2 p'}{\partial t^2} + \frac{\partial}{\partial x_i} \left(\frac{1}{\bar{\rho}} \frac{\partial p'}{\partial x_i} \right) = \frac{\partial f'_i}{\partial x_i} - \frac{\partial}{\partial x_i} \left(\frac{1}{\bar{\rho}} \frac{\partial}{\partial x_j} \tau'_{ij,L} \right) - \frac{\kappa - 1}{\bar{\rho} \bar{c}^2} \frac{\partial \dot{\omega}'_z}{\partial t}. \qquad (4.47)$$

The time derivatives of the density in eq. (4.46) and the heat rate of combustion in eq. (4.47) indicate the monopole character of the source models for perfectly premixed and non-premixed flames, cf. Ehrenfried [2002], Rienstra and Hirschberg [2012].

- **Coherence**: The amplitude of the source terms for premixed and non-premixed flames depends on the coherence between stochastic quantities. No combustion noise is released without a certain level of coherence between the stochastic turbulent fluctuations [Wäsle et al., 2005]. For example, the source term in the linearized continuity eq. (4.20) is a function of the coherence between turbulent density and velocity fluctuations. When introducing the density-velocity coherence function $R^*_{\rho u} := \langle \rho'' u''_i \rangle / (\rho_{\mathrm{rms}} u_{\mathrm{rms}})$, the source term in the linearized continuity eq. (4.20) may be written as

$$\bar{\rho} s'_V = - \frac{\partial}{\partial x_i} \langle \rho'' u''_i \rangle = - \rho_{\mathrm{rms}} u_{\mathrm{rms}} \frac{\partial}{\partial x_i} R^*_{\rho u}. \qquad (4.48)$$

The combustion noise source term vanishes for completely uncorrelated turbulent velocity and density fluctuations, i.e. $R^*_{\rho u} = 0$ yields $\bar{\rho} s'_V = 0$. According to eq. (4.33) the source amplitude of a non-premixed flame depends on the coherence between mixture fraction fluctuations.

- **Power density source spectra**: The presented triple-decomposition approach naturally delivers power density spectra of the different combustion noise source terms for premixed and non-premixed flames, which is explained as follows: When regarding premixed flames the source term in the linearized continuity eq. (4.29) depends on the one-point covariance $R_{\rho u}(t) = \langle \rho''(\tau) u''_i(\tau + t) \rangle$ as stated by eq. (4.19). The source term in the linearized energy eq. (4.31) contains the covariance $R_{\rho c}(t) = \langle \rho''(\tau) c''(\tau + t) \rangle$. Both source terms can be expressed in terms of autocovariances $R_{\widetilde{c''^2}}(t) = \langle c''(\tau) c''(\tau + t) \rangle$ of the reaction progress variable and its variance

using the BML model eqs. (4.26) and (4.27). When performing the transformation into frequency domain this directly leads to a power density spectrum of the variance of the reaction progress variable, e.g. for the cross-spectrum of the velocity-density covariance [Pope, 2000]

$$\chi_{\rho u}(\omega) = \mathcal{F}\{R_{\rho u}(t)\} = \frac{1}{\pi}\int_{-\infty}^{\infty}\langle\rho''(\tau)u_i''(\tau+t)\rangle e^{i\omega t}\mathrm{d}t. \tag{4.49}$$

Then the power spectral density of the reaction progress variable is given by setting $t = 0$ to obtain

$$\chi_{\widetilde{c''2}}(\omega) = \mathcal{F}\{R_{\widetilde{c''2}}(t=0)\} = \mathcal{F}\{\langle c''^2\rangle\} = \frac{1}{\pi}\int_{-\infty}^{\infty}\langle c''(\tau)c''(\tau+t)\rangle e^{i\omega t}\mathrm{d}t. \tag{4.50}$$

For non-premixed flames the source term in the linearized energy eq. (4.36) is a function of the autocovariance $R_{\widetilde{z''2}}(t) = \langle z''(\tau)z''(\tau+t)\rangle$ as given by eq. (2.22). The transformation into frequency domain directly leads to the power spectral density of the mixture fraction

$$\chi_{\widetilde{z''2}}(\omega) = \mathcal{F}\{R_{\widetilde{z''2}}(t=0)\} = \mathcal{F}\{\langle z''^2\rangle\} = \frac{1}{\pi}\int_{-\infty}^{\infty}\langle z''(\tau)z''(\tau+t)\rangle e^{i\omega t}\mathrm{d}t. \tag{4.51}$$

This is a key result of the proposed model as it provides a formal derivation of the existence of power spectra as source terms due to stochastic turbulent fluctuations in the linearized equations. This can not be achieved when considering linear source terms of deterministic variables. To the best of the authors knowledge the models proposed so far for instance by Weyermann [2010] or Mühlbauer et al. [2010] give no explanation for imposing the power spectral density as source terms. Beyond this eq. (4.50) gives a formal derivation of the starting point of the spectral model by Hirsch et al. [2006, 2007], which assumes a spectrum of the mean reaction progress variable. In conclusion the model reveals that the source terms are directly related to power spectral density of the mean variance of the progress variable $\widetilde{c''2}$ and mixture fraction variance $\widetilde{z''2}$, respectively.

- **Entropy wave generation**: The different physics of the entropy wave generation in perfectly premixed flames and non-premixed flames is accurately accounted for by the model. This was demonstrated by deducing the entropy equation from the LNSE for perfectly premixed and non-premixed flames in each case. For perfectly premixed flames the entropy eq. (4.32) confirms that the volume source terms $\bar{\rho}s_V'$ do not contribute to an entropy wave generation. In case of non-premixed flames the heat rate of combustion $\dot{\omega}_z'$ appears on the right side of the entropy eq. (4.37), where sources of entropy waves are found.

  In both cases the energy equations in entropy formulation, eqs. (4.32) and (4.37), provide evidence of an inherent limitation of the linearized non-reacting equations since they do not support an isentropic solution in a non-isentropic mean flow, which is represented by the first term $-u_i'\partial\bar{s}/\partial x_i$.

- **Coupling with LES simulations**: Finally the model provides the opportunity to easily incorporate source terms obtained from ensemble-averaged/filtered equations such as LES or URANS. In case of premixed flames the volume source terms in the linearized continuity (4.29) and energy eq. (4.31) are obtained by the evaluation of the time derivative of the density

$$\bar{\rho}s'_V = \frac{\partial \rho'_t}{\partial t} = \frac{\partial \langle \rho \rangle}{\partial t}. \tag{4.52}$$

In case of non-premixed flames the ensemble averaged heat rate of combustion additionally needs to be computed to get the source term in the linearized energy eq. (4.36).

After deriving a semi-analytical model for the combustion noise source terms, the modeling of their spectral content is reviewed in the following section.

4.3 Spectral Modeling

In the present thesis different statistical combustion noise models are applied to two combustion chamber test rigs. The original version among the tested combustion noise models was developed by Hirsch et al. [2006, 2007] for premixed flames. The statistical model by Hirsch et al. [2007] is based on the far-field solution (4.10) of the wave eq. (4.3). Its key elements can be summarized as follows: As sketched in fig. 4.6 the flame is seen as an ensemble of individual virtual sources. Each has a coherence volume V_{coh} derived from the turbulent integral length scale. The integral heat release spectrum of the flame is calculated by the spatial integration of all individual sound sources, which are weighted with the mean local heat release rate. The spectrum of the heat release fluctuation inside an individual source is expressed in terms of a modeled Eulerian turbulence spectrum defined in wave number space [Tennekes and Lumley, 1972]. The assumed spectrum is transformed into the corresponding Lagrangian frequency spectrum by postulating equal energy contents in the wave number and frequency space [Tennekes and Lumley, 1972]. In the studies by Winkler [2007] and Wäsle [2007] the model was successfully applied to unconfined swirled flames. Later Jörg [2015] extended the model to non-premixed flames by introducing a generalized scaling coefficient and modifications to the length scale and frequency-wave number mapping. He demonstrated that the proposed scaling coefficient based on the variance of the temperature fluctuation delivers good agreement between the numerical predictions and measurements for turbulent swirl flames. Beyond this the generalized scaling coefficient by Jörg [2015] can be applied on premixed as well as non-premixed flames. A modified version of the model by Hirsch et al. [2007], suggested by Liu et al. [2014], was successfully validated in the frame of a network modeling approach of a demonstrator combustor operating under premixed conditions. In the following two subsections the different spectral source models for premixed and non-premixed flames are reviewed.
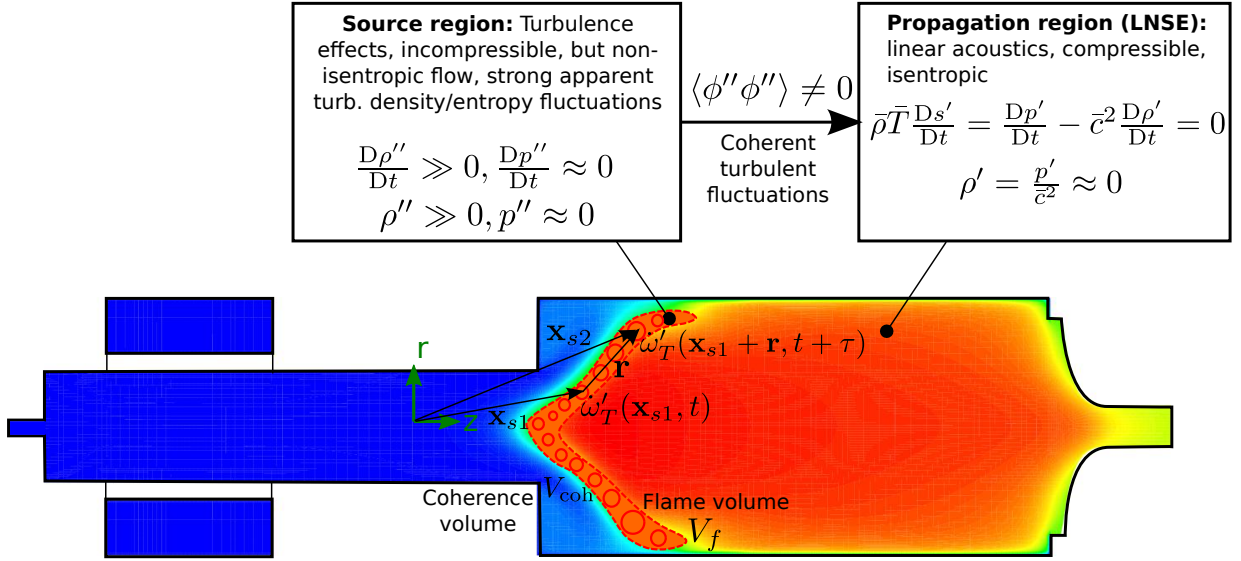
Figure 4.6: Visualization of the coherence concept of the combustion noise model for a perfectly premixed flame according to Weyermann [2010] and Jörg [2015].

Another method for modeling the spectral content of the source terms is to perform incompressible LES simulations [Bui et al., 2007a]. The source terms derived above have the opportunity to couple them to LES simulations. How this is done is shown in the last subsection.

4.3.1 Perfectly Premixed Flames

Hirsch Model (2006)

The statistical noise model proposed by Hirsch et al. [2006, 2007] provides an integral spectrum of the heat release fluctuations $\dot{\mathcal{Q}}_c(f) = |\dot{\mathcal{Q}}_c(f)^2|^{1/2}$. The subscript c indicates that the spectrum is related to a perfectly premixed flame. The spectrum is obtained by postprocessing stationary RANS simulations. As explained above the key idea of the model is to express the flame as an assembly of local sound sources. These sources with coherence volume V_{coh} are statistically independent from each other. Consequently the integral heat release spectrum is computed by the integration of all local sound sources over the total flame volume, while the spatio-temporal coherence between the different sources is accounted for by each local coherence volume to obtain [Weyermann, 2010]

$$|\dot{\mathcal{Q}}_c(f)^2| = (2\pi)^3 \int_{V_f} \left(\frac{\kappa E_q(\kappa)}{f} \right)^2 V_{\text{coh}} \mathrm{d}V. \tag{4.53}$$

Following Hirsch et al. [2007] the spectrum of the local heat release fluctuations in eq. (4.53) is modeled by an assumed Eulerian turbulence spectrum E_q, defined in wave number space κ. The heat release spectrum is in turn related to a spectrum of the fluctuations of the

mean progress variable $\widetilde{c''^2}$, which yields

$$E_q(\kappa) = \bar{\dot{\omega}}_T c_d c_s \frac{\epsilon^{\frac{2}{3}}}{k} \kappa^{-\frac{5}{3}} \exp\left[-\frac{3}{2}\left(\pi\beta\alpha^{\frac{1}{2}}(\kappa l_t)^{-\frac{4}{3}} + \alpha(\kappa\eta_c)^{\frac{4}{3}}\right)\right].\tag{4.54}$$

This spectrum is based on the modeled spectrum by Tennekes and Lumley [1972]. The empirical constants c_d, α and β and additional constants presented in the following are quantified at the end of this paragraph. The scaling function c_s in eq. (4.54) is introduced to account for varying Damköhler numbers $\mathrm{Da} = c_\mu k s_l^2/(\epsilon a c_w)$ [Hirsch et al., 2007]

$$c_s = \frac{\alpha}{c_d}\left[\frac{s_l/\sqrt{2/3k} + (1 + \mathrm{Da}^{-2})^{-0.25}}{s_l/\sqrt{2/3k} + 1}\right]^2,\tag{4.55}$$

where the laminar flame speed s_l is calculated using empirical correlations, as for instance summarized by Turns [2011]. In eq. (4.54) the integral length scale $l_t = c_l k^{\frac{3}{2}}/\epsilon$ is obtained from the turbulent kinetic energy and dissipation rate. The spectral cut-off length scale η_c is defined as the maximum of the Corrsin length scale l_c and the Gibson length scale l_g, multiplied by the empirical factor c_g, i.e.

$$\eta_c = \max\{c_g l_g, l_c\}, \qquad l_g = \frac{s_l^3}{\epsilon}, \qquad l_c = \left(\frac{a^3}{\epsilon}\right)^{1/4}.\tag{4.56}$$

A mapping rule between the wave number and frequency can be derived when postulating equal energy contents in the wave number and frequency space to give [Tennekes and Lumley, 1972]

$$\kappa = \frac{(2\pi f \tau_c)^{\frac{3}{2}}}{\delta_t \alpha^{\frac{3}{4}}}.\tag{4.57}$$

In this way the wave number spectrum of the heat release $E_q(\kappa)$ is transformed into a corresponding Lagrangian frequency spectrum $\chi_q(f)$ by [Jörg, 2015]

$$\chi_q(f) = \frac{\kappa}{\pi f}E_q(\kappa).\tag{4.58}$$

This transformation is already included in the final formula (4.53) for the integral spectrum of the heat release rate. In eq. (4.57) the chemical time scale and turbulent flame thickness are indicated by δ_t and τ_c, respectively. The chemical time scale $\tau_c = c_\tau \delta_t/s_t$ is the ratio of the turbulent flame thickness δ_t and turbulent flame speed s_t, which are in turn obtained from a Damköhler-scaling as proposed by Schmid [1995]:

$$s_t = s_l + u''(1 + \mathrm{Da}^{-2})^{-1/4},\tag{4.59}$$
$$\delta_t = \delta_l + l_t(1 + \mathrm{Da}^{-2})^{1/4}.\tag{4.60}$$

The fluctuating turbulent velocity is proportional to the turbulent kinetic energy when assuming isotropic turbulence, i.e. $u'' = u_t = \sqrt{2/3k}$. The spatial coherence is quantified

by a virtual coherence volume V_{coh}, which is deduced from the turbulent integral length scale as shown by Weyermann [2010]. In combustion noise problems the integral length scale is replaced by the turbulent flame thickness to give $V_{\text{coh}} = 8\delta_t^3$ [Jörg, 2015].

In the present thesis the following constants are chosen equally for all combustor test cases except where otherwise stated: $c_w = 1.2$, $c_l = 0.42$, $c_\mu = 0.09$, $c_\tau = 0.5$, $c_d = 2.0$, $c_g = 3.0$, $\alpha = 1.5$ and $\beta = 0.3$ [Jörg, 2015, Weyermann, 2010].

To sum up all quantities in the spectral model are exclusive functions of the turbulent kinetic energy k, the turbulent dissipation rate ϵ and the mean volumetric heat release $\bar{\dot{\omega}}_T$. Therefore the integral spectrum of the heat release of the flame is also an exclusive function of k, ϵ and $\bar{\dot{\omega}}_T$, i.e. $\dot{\mathcal{Q}}_c(f) = \dot{\mathcal{Q}}_c(f, k, \epsilon, \bar{\dot{\omega}}_T)$. These turbulent quantities are easily obtained by postprocessing a stationary RANS simulation based on the k-ϵ model, cf. sec. 2.2. The statistical model is not limited to applications based on the k-ϵ model, other turbulence models such as the k-ω or SST model can be evaluated by exploiting the relation $\omega = \epsilon/(c_\mu k)$ [Pope, 2000]. The mean heat release rate may be either reduced to a function of the turbulent quantities by utilizing simple combustion models such as the Eddy-Breakup model, or explicitly calculated by species transport models [ANSYS, 2011a, Poinsot and Veynante, 2005].

Jörg Model (2015) for Premixed Flames

The generalized scaling coefficient introduced by Jörg [2015] is valid for premixed as well as non-premixed flames. In case of high turbulent Damköhler numbers the model by Jörg [2015] converges towards the model by Hirsch et al. [2007]. The similarity of both modeling approaches with respect to the scaling coefficient was demonstrated by Jörg [2015] for a premixed flame. The model extension by Jörg [2015] to non-premixed flames contains additional modifications of the frequency-wave number mapping and the integral length scale, which are reviewed in the following subsec. 4.3.2.

When applying the model by Jörg [2015] on premixed flames, the scaling constant in the eq. (4.54) for the local heat release spectrum is replaced by the generalized scaling coefficient c_s:

$$c_s = \frac{\alpha}{c_d} \frac{\widetilde{\theta''^2}}{\widetilde{\theta}(1 - \widetilde{\theta})}. \tag{4.61}$$

It directly relates the strength of the heat release fluctuations to the mean variance of the temperature. $\widetilde{\theta}$ and $\widetilde{\theta''^2}$ represent the Gaussian pdf-weighted, dimensionless mean temperature and its variance, normalized by the local difference between the adiabatic

flame temperature $T_{ad}(z)$ and unburnt temperature T_u:

$$\widetilde{\theta} = \frac{\widetilde{T} - T_u}{\int_0^1 (T_{ad}(z) - T_u)p(z)\mathrm{d}z},\tag{4.62}$$

$$\widetilde{\theta''^2} = \frac{\widetilde{T''^2}}{\int_0^1 (T_{ad}(z) - T_u)^2 p(z)\mathrm{d}z}.\tag{4.63}$$

The Gaussian pdf is entirely defined by the mean mixture fraction $\widetilde{z}$ and its variance $\sigma_z = \sqrt{\widetilde{z''^2}}$, i.e.

$$p(z) = \frac{1}{\sigma_z \sqrt{2\pi}} \exp[-(z - \widetilde{z})^2)/(2\sigma_z^2)].\tag{4.64}$$

A transport equation for the variance of the temperature $\widetilde{T''^2}$ is solved simultaneously to the RANS equations to get its local values needed in eq. (4.63) [Gerlinger, 2005]

$$\frac{\partial \langle \rho \rangle \widetilde{T''^2}}{\partial t} + \frac{\partial \langle \rho \rangle \widetilde{u}_j \widetilde{T''^2}}{\partial x_j} = \frac{\partial}{\partial x_j}\left[\left(\nu + \frac{\nu_t}{\mathrm{Pr}_t}\right)\frac{\partial \langle \rho \rangle \widetilde{T''^2}}{\partial x_j}\right] + c_g \langle \rho \rangle \frac{\nu_t}{\mathrm{Pr}_t}\left(\frac{\partial \widetilde{T}}{\partial x_j}\right)^2 - c_d \langle \rho \rangle \frac{\epsilon}{k}\widetilde{T''^2}.\tag{4.65}$$

The empirical scaling coefficients are $c_g = 2.0$ and $c_d = 2.0$. Following the idea by Jörg [2015] the local adiabatic flame temperature in the eqs. (4.62) and (4.63) is determined by solving iteratively an enthalpy balance.

Liu Model (2014)

The modification proposed by Liu et al. [2014] introduces a prefactor $\rho_0 Y_{f,0} H_l c_d(\epsilon/k)$ in the local heat release spectrum (4.54) in comparison to the model by Hirsch et al. [2007]. Then the local heat release spectrum is computed as

$$E_q(\kappa) = \rho_0 Y_{f,0} H_l \bar{\dot{\omega}}_T c_d^2 c_s \frac{\epsilon^{\frac{5}{3}}}{k^2} \kappa^{-\frac{5}{3}} \exp\left[-\frac{3}{2}\left(\pi\beta\alpha^{\frac{1}{2}}(\kappa l_t)^{-\frac{4}{3}} + \alpha(\kappa\eta_c)^{\frac{4}{3}}\right)\right].\tag{4.66}$$

Although this prefactor is not explicitly depending on the frequency, it leads to a stronger weighting of regions with high turbulent shear. All other computations are done as before in the model by Hirsch et al. [2007].

4.3.2 Non-Premixed Flames

The basic procedure for computing the integral heat release rate is the same for perfectly premixed and non-premixed flames. The differences introduced by Jörg [2015] lie in the modeling of the scaling coefficient of the local heat release spectra and the computation of the coherence volume and frequency-wave number mapping. In the present thesis the mean

heat release rate in the modeled source spectrum is computed on basis of the mixture fraction variance. The derivation of this modeled source spectrum for non-premixed flames is given in the next paragraphs before presenting the model by Jörg [2015] for non-premixed flames.

The starting point is the flamelet approach for diffusive flames [Klein, 2000, Strahle, 1985] to express the fluctuating heat release $\dot{\omega}_z'$ in the linearized energy eq. (4.36) by help of the mean scalar dissipation rate $\widetilde{\chi}$ of the mixture fraction. Under the assumption of infinitely fast chemistry [Poinsot and Veynante, 2005] this yields

$$\bar{\dot{\omega}}_z(\widetilde{z''^2}) = \frac{Y_F^0 H_l}{2(1 - z_{st})}(\bar{\rho}\widetilde{\chi})p(z_{st}) = \frac{Y_F^0 H_l}{2(1 - z_{st})}c_d\bar{\rho}\frac{\epsilon}{k}\widetilde{z''^2}p(z_{st}). \tag{4.67}$$

Following the procedure proposed by Hirsch et al. [2006] the wave number spectrum of the heat release is then given by

$$E_\omega(\kappa) = \frac{Y_F^0 H_l}{2(1 - z_{st})}c_d\bar{\rho}\frac{\epsilon}{k}E_{\widetilde{z''^2}}(\kappa)p(z_{st}), \tag{4.68}$$

where the spectrum of the mixture fraction $E_{\widetilde{z''^2}}$ is modeled by an assumed spectrum [Tennekes and Lumley, 1972]

$$E_{\widetilde{z''^2}}(\kappa) = c_s\widetilde{\chi}\epsilon^{-1/3}\kappa^{-5/3}\exp\left[-\frac{3}{2}\left(\pi\beta\alpha^{\frac{1}{2}}(\kappa l_t)^{-\frac{4}{3}} + \alpha(\kappa\eta_k)^{\frac{4}{3}}\right)\right]. \tag{4.69}$$

The spectral cut-off length scale in eq. (4.69) is defined by the Kolmogorov length $\eta_k = (\nu^3/\epsilon)^{1/4}$. Substituting eq. (4.69) into the spectrum of the fluctuating heat of combustion (4.68) and using the mean heat release rate in eq. (4.67) finally leads to

$$E_\omega(\kappa) = c_sc_d\bar{\dot{\omega}}_z(\widetilde{z''^2})\frac{\epsilon^{2/3}}{k}\kappa^{-5/3}\exp\left[-\frac{3}{2}\left(\pi\beta\alpha^{\frac{1}{2}}(\kappa l_t)^{-\frac{4}{3}} + \alpha(\kappa\eta_k)^{\frac{4}{3}}\right)\right]. \tag{4.70}$$

As expected this is a very similar expression as the source spectrum of the premixed flame in eq. (4.54). The fundamental difference of premixed and diffusion flames lies in the heat release mechanism. In case of the non-premixed flame it is dominated by species diffusion into the flame, which is reflected in the scalar dissipation rate of the mixture fraction. In premixed flames the spectrum is controlled by fluctuations of the reaction progress variable and therefore its variance.

Jörg Model (2015) for Non-Premixed Flames

The remaining values in the local heat release spectrum (4.70) are determined following Jörg [2015]. The generalized scaling constant c_s is calculated using eq. (4.61), which was already introduced in context of premixed flames. To determine the dimensionless mean temperature and its variance, defined by the eqs. (4.62) and (4.63), the local adiabatic flame

temperature is needed. It is computed by solving iteratively the following transcendental equations

$$T_{ad}(z) = zT_F^0 + (1-z)T_O^0 + \frac{H_l Y_F^0}{c_p(T_{ad}(z))} z_{st} \frac{1-z}{1-z_{st}}, \quad z > z_{st} \quad \text{fuel side} \quad (4.71)$$

$$T_{ad}(z) = zT_F^0 + (1-z)T_O^0 + \frac{H_l Y_F^0}{c_p(T_{ad}(z))} z, \quad z \leq z_{st} \quad \text{oxidizer side.} \quad (4.72)$$

In addition to this the mean heat release rate $\bar{\dot{\omega}}_z$ in the local heat release spectrum E_ω, eq. (4.70), is determined according to the procedure given in sec. 2.2. The turbulent length scale and coherence volume in the local heat release spectrum are expressed as functions of the local gradient of the mean mixture fraction [Jörg, 2015], i.e.

$$l_t = \frac{c_l}{|\nabla \tilde{z}|}, \qquad V_{\text{coh}} = 8l_t^3 = 8\left(\frac{c_l}{|\nabla \tilde{z}|}\right)^3. \quad (4.73)$$

In the case of vanishing mixture fraction gradients the model delivers infinite values so that the following modification is proposed:

$$l_t = \min\left\{\frac{c_l}{|\nabla \tilde{z}|}, c_l \frac{k^{3/2}}{\epsilon}\right\}. \quad (4.74)$$

In the same way as for the perfectly premixed flame the integral heat release spectrum $\dot{\mathcal{Q}}_z(f) = |\dot{\mathcal{Q}}_z(f)^2|^{1/2}$ is obtained by the integration of the local sound sources over the entire flame volume

$$|\dot{\mathcal{Q}}_z(f)^2| = (2\pi)^3 \int_{V_f} \left(\frac{\kappa E_\omega(\kappa)}{f}\right)^2 V_{\text{coh}} \mathrm{d}V. \quad (4.75)$$

In contrast to the premixed noise model a different mapping rule between the Eulerian wave number and Lagrangian frequency space applies to eq. (4.75). Referring to Jörg [2015] the wave number is transformed into a corresponding frequency by

$$\kappa = \left(\frac{2}{3}\right)^{\frac{3}{2}} \frac{(2\pi f)^{\frac{3}{2}}}{\alpha^{\frac{3}{4}} \epsilon^{\frac{1}{2}}}. \quad (4.76)$$

The turbulent dissipation rate is calculated by the integral length and turbulent time, i.e. $\epsilon = l_t^2/\tau_t^3$. The turbulent time is deduced from the turbulent kinetic energy and turbulent dissipation rate to give $\tau_t = c_\tau k/\epsilon$.

4.3.3 Incompressible LES for Source Term Prediction

When applying incompressible LES simulations to predict the combustion noise source terms no submodels for perfectly premixed and non-premixed flames need to be introduced as it was done before in context of the statistical noise models. The reasons for

this different approach are twofold: First, source terms calculated by unsteady simulations are naturally complex-valued with amplitude and phase information. Second, the LES simulation model and its solution already include the relation between the source terms in the linearized continuity eq. (4.20) and energy eq. (4.22) so that it does not need to be modeled in this case. The relation between both source terms depends on the examined flame type and therefore the applied combustion model. As the relation between both source terms controls the entropy wave generation, the differences of premixed and non-premixed flames with respect to entropy waves are inherently included in the model. Then the starting point for the acoustic propagation simulations are the LNSE (4.20) - (4.22) with stochastic sound sources, which hold for all types of flames. Accordingly two source terms need to be computed, which are separately treated in the subsequent paragraphs.

The first source term is the time derivative of the density in the linearized continuity eq. (4.20). This term was also identified by Bui et al. [2007b] as a major source term for combustion noise. He coupled the LES source term computations with acoustic simulations based on the APE-RF. In the present thesis a source term in the linearized continuity eq. (4.20) is derived by means of the triple-decomposition. In subsec. 4.2.1 it is shown that the divergence of the correlation between turbulent velocity and density is equivalent to the time derivative of the density by exploiting the Reynolds-averaged continuity equation. The theoretical derivation in this thesis ends up with eq. (4.52) reproducing the result by Bui et al. [2007b]. Accordingly the spectrum of the source term is obtained by evaluating the fast Fourier transformed time derivative of the density. Then the integral spectrum of the volume source term is obtained by the volume-integration of all local sources to give

$$\bar{\rho}\mathcal{S}_V(f) = \mathcal{F}\Big\{\int_V \frac{\partial \rho}{\partial t}\mathrm{d}V\Big\}. \tag{4.77}$$

The volume is not limited to the flame itself since the source term is almost zero everywhere else so that the entire combustor is chosen as the control volume. However the evaluation of the volume integral at each time step would require tremendous computational efforts. This is avoided by reducing the volume integral in eq. (4.77) to a surface integral using the continuity equation $\partial \rho/\partial t = -\partial/\partial x_i(\rho u_i)$ and the divergence theorem to obtain

$$\bar{\rho}\mathcal{S}_V(f) = -\mathcal{F}\Big\{\Big[\int_{A_2} (\rho u_i n_i)_2\mathrm{d}A + \int_{A_1} (\rho u_i n_i)_1\mathrm{d}A\Big]\Big\}. \tag{4.78}$$

The combustor inlets are denoted by the subscript 1 and the combustor outlet is indicated by the subscript 2.

The second source term is the heat rate of combustion in the linearized energy eq. (4.22). Volume integration, followed by fast Fourier transform delivers the integral spectrum of this source term, i.e.

$$\dot{\mathcal{Q}}(f) = \mathcal{F}\Big\{\int_V \dot{\omega}_T\mathrm{d}V\Big\}. \tag{4.79}$$

Again the control volume contains the entire combustion chamber as the source term is almost zero in the complete domain apart from the small flame region.

In case of perfectly premixed flames the computationally demanding evaluation of the integral heat rate of combustion in eq. (4.79) is avoided by exploiting the relation (4.28). A further simplification of the model is achieved in cases, where the entropy wave generation due to the cooling or dilution air injections downstream of the premixed flame is negligible. Under such circumstances it is justifiable to apply the isentropic LNSE model, eqs. (4.44) and (4.45). In this way the solution of the energy equation is avoided, which leads to an additional reduction of computational resources. Such an approach is presented in sec. 8.2 in the frame of the premixed CNRS combustor.

4.4 Source Term Distribution Modeling

All spectral combustion noise models presented in sec. 4.3 provide a frequency spectrum of the integral heat release rate $\dot{\mathcal{Q}}_c(f)$ for premixed flames and $\dot{\mathcal{Q}}_z(f)$ for non-premixed flames. The LNSE with stochastic sound sources solely contain the local source terms $\bar{\rho}\hat{s}_V$ and $\hat{\omega}_z$ but no integral source terms. Therefore the integral combustion noise spectra need to be spatially redistributed in a certain way to get local source terms, which allow an LNSE implementation. How this is realized is the topic of the following paragraphs.

Weyermann [2010] demonstrated that the low-frequency range of the acoustic spectrum is independent from the shape of the combustion noise source region when only acoustic wave propagation is regarded. His result confirms the reasonable assumption of an acoustical compact source in the low frequency regime. The study of Weyermann [2010] was based on a Helmholtz equation (3.23) model, which excludes the propagation of entropy waves, so that the requirement of convectively compact flames does not need to be considered when defining the source region. In this thesis an energy-consistent model is proposed, which distributes the local sources according to the mean heat release and the time-averaged shape of the flame. The special cases of premixed and non-premixed flames are treated in the following.

Premixed Flames

The volumetric source terms $\bar{\rho}\hat{s}_V$ are modeled by redistributing the integral spectrum $\dot{\mathcal{Q}}_c(f)$ over the entire flame volume while weighting it by the local mean volumetric heat release $\bar{\dot{\omega}}_T$. This finally yields the subsequent expression for the fluctuating heat release rate

$$\hat{\dot{\omega}}_T(\boldsymbol{x}, f) = \dot{\mathcal{Q}}_c(f) \frac{\bar{\dot{\omega}}_T(\boldsymbol{x})}{\dot{m}_F H_l}. \tag{4.80}$$

Under the assumption of an isobaric low-Mach number flame the corresponding volume source term $\bar{\rho}\hat{s}_V$ in the LNSE (4.38) - (4.40) is determined by the frequency-transformed

version of eq. (4.28) to give

$$\bar{\rho}\hat{s}_V(\boldsymbol{x}, f) = \frac{\kappa - 1}{\bar{c}^2}\hat{\omega}_T(\boldsymbol{x}, f) = \frac{\kappa - 1}{\bar{c}^2}\dot{\mathcal{Q}}_c(f)\frac{\bar{\omega}_T(\boldsymbol{x})}{\dot{m}_F H_l} = \bar{\rho}\mathcal{S}_V(f)\frac{\bar{\omega}_T(\boldsymbol{x})}{\dot{m}_F H_l}. \qquad (4.81)$$

$\mathcal{S}_V(f)$ represents an equivalent spectrum of the volume source term. A comparison of the integral source spectra shows that $\bar{\rho}\mathcal{S}_V(f) = (\kappa - 1)/\bar{c}^2\dot{\mathcal{Q}}_c(f)$. The model for distributing the integral sources defined by eq. (4.81) fulfills the energy conservation by definition. The spatial integration of the volumetric sources over the entire flame volume results in the integral frequency spectrum because

$$\int_V \hat{\omega}_T(\boldsymbol{x}, f)\mathrm{d}V = \int_V \dot{\mathcal{Q}}_c(f)\frac{\bar{\omega}_T(\boldsymbol{x})}{\dot{m}_F H_l}\mathrm{d}V = \frac{\dot{\mathcal{Q}}_c(f)}{\dot{m}_F H_l}\int_V \bar{\omega}_T(\boldsymbol{x})\mathrm{d}V = \dot{\mathcal{Q}}_c(f)\frac{\bar{Q}_{th}}{\dot{m}_F H_l} = \dot{\mathcal{Q}}_c(f).$$
$$(4.82)$$

In comparison to the model by Weyermann [2010] the advantage of this model is that it does not need an additional definition of an arbitrary source volume. Later in subsec. 8.2.6 the results obtained by the source term distribution model (4.81) and an arbitrary source region are compared with each other to validate the modeling approach for direct noise computations.

Non-Premixed Flames

The same approach is used for non-premixed flames. Once the integral source spectrum is computed using eq. (4.75) it is redistributed in the LNSE for non-premixed flames (4.41) - (4.43) according to the mean heat release rate to obtain the local volumetric heat release source term $\hat{\omega}_z$ in the linearized energy eq. (4.43):

$$\hat{\omega}_z(\boldsymbol{x}, f) = \dot{\mathcal{Q}}_z(f)\frac{\bar{\omega}_z(\boldsymbol{x})}{\dot{m}_F H_l}. \qquad (4.83)$$

Model Limitations

In the modeling approach for premixed flames (4.81) the term $\bar{\rho}\hat{s}_V$ act as a completely coherent acoustic source spread over the entire flame volume. Phase differences between the local sources inside the flame volume are not considered. In the model eq. (4.83) for non-premixed flames the term $\hat{\omega}_z$ creates acoustic and entropy waves with the same phase in the entire flame volume. Therefore the models defined by the eqs. (4.81) and (4.83) lead to an increase of the coherence volume from V_{coh} to the flame volume V_f. Due to large acoustic wave lengths this has no effect on the acoustic sources. The situation is different when considering sources of entropy waves, i.e. the term $\hat{\omega}_z$. A coherent entropy wave created in the entire flame volume behaves different from an ensemble of entropy waves, each of which is created in the local coherence volumes. Due to the phase differences, the ensemble of entropy waves is exposed to a remarkably stronger dispersion effect in comparison to the coherent entropy wave. Therefore the source term distribution models,

defined by the eqs. (4.81) and (4.83), only hold for acoustical and convectively compact flames where phase differences between the local sources of acoustic and entropy waves can be neglected. The maximum frequencies, for which the assumption of compact flames are valid, are given by Dowling [1995]:

$$f_{\max} \ll \frac{\bar{c}}{\delta_f}, \qquad \text{acoustical compact flame}, \qquad (4.84)$$

$$f_{\max} \ll \frac{\bar{u}}{\delta_f}, \qquad \text{acoustical-convectively compact flame}. \qquad (4.85)$$

The assumption of acoustical compact flames (4.84) is fulfilled in the combustion chambers and the frequency range of interest considered in this thesis. The model requirement of convectively compact flames (4.85) is not met in the LNSE simulations including entropy waves. This leads to an overestimation of the entropy waves generated by the source term $\hat{\dot{\omega}}_z$ for non-premixed flames. This important model limitation needs to be kept in mind when analyzing the results for the indirect noise generated by partially-premixed and non-premixed flames presented in this thesis. As the volume source terms $\bar{\rho}\hat{s}_V$ for premixed flames do not support an entropy wave generation the distribution model (4.81) has no influence on the results for the indirect noise in case of premixed flames. The direct noise computations based on the isentropic assumption are also not affected by the source term distribution model (4.81).

Estimation of Entropy Dispersion Effect Due to Incoherent Sources

Following the modeling approach for the heat release spectrum by Hirsch et al. [2007], the temperature spectrum integrated over the flame volume may be written as:

$$|\mathcal{T}(f)^2| = \frac{1}{V_f^2} \int_{V_f} \chi_{\widetilde{T''^2}}(f) V_{\mathrm{coh}} \mathrm{d}V, \qquad (4.86)$$

where the power spectral density of the temperature is defined as:

$$\chi_{\widetilde{T''^2}}(\omega) = \mathcal{F}\{R_{\widetilde{T''^2}}(t=0)\} = \mathcal{F}\{\langle T''^2\rangle\} = \frac{1}{\pi}\int_{-\infty}^{\infty}\langle T''(\tau)T''(\tau+t)\rangle e^{\mathrm{i}\omega t}\mathrm{d}t. \qquad (4.87)$$

In the idealized source term distribution model with in-phase entropy wave generation, the coherence volume equals the total flame volume, i.e. $V_{\mathrm{coh}} = V_f$. This stands in contrast to the real incoherent entropy wave generation with $V_{\mathrm{coh}} \ll V_f$. When assuming the temperature spectrum and the coherence volume to be constant in the flame volume, the idealized and incoherent volume-integrated temperature spectra are related by:

$$|\mathcal{T}(f)^2|_{\mathrm{incoh}} = \frac{V_{\mathrm{coh}}}{V_f}|\mathcal{T}(f)^2|_{\mathrm{coh}}. \qquad (4.88)$$

Under these assumptions there is an average factor of $\sqrt{V_{\mathrm{coh}}/V_f}$ between the temperature fluctuations / entropy waves produced by the idealized coherent and realistic incoherent source term distribution model. Eq. (4.88) is applied in subsec. 8.2.7 on the CESAM-HP combustor to estimate the entropy waves generated by an incoherent source term distribution.

5   Methodology

In this chapter the methodology for the prediction of direct as well as indirect combustion noise emitted from turbulent confined flames is presented. The first section outlines the procedure for the application of the hybrid RANS/LNSE method to a combustion chamber. By combining the hybrid RANS/LNSE method and the network models a strategy to predict the ratio of direct and indirect combustion noise downstream of the combustor is provided.

5.1 The Hybrid RANS/LNSE Approach for Combustion Noise Predictions

The procedure for the computation of the combustion noise inside combustion chambers is shown by taking the example of the generic premixed CESAM-HP combustor in fig. 5.1.

RANS Simulation

In a first step a stationary and reactive RANS simulation is performed, which delivers the mean flow field inside the regarded combustor, i.e. $\bar{\rho}$, $\bar{u}_i$ and $\bar{p}$. In this thesis RANS simulations are carried out utilizing the commercial software package Ansys Fluent Release 14.0 [ANSYS, 2011a] along with the mesh creator Icem cfd. The boundary conditions, turbulence and combustion models applied in a certain test case are specified in the corresponding section.

Spectral Noise Model Postprocessor

After the numerical computation of the mean flow field the spectral noise model postprocessors of sec. 4.3 are applied to the results to determine the integral heat release spectra of turbulent premixed flames $\dot{\mathcal{Q}}_c(f)$ or non-premixed flames $\dot{\mathcal{Q}}_z(f)$. As explained in subsec. 4.3.1 the postprocessing can be applied for various turbulence and combustion models. The integral heat release spectra contain all statistical information such as the coherence volumes of the different sources in the flame. They act as frequency-dependent source terms in the following acoustic simulations.

The postprocessor both for the premixed and non-premixed noise model is implemented in form of user defined functions (udf) coupled to Ansys Fluent.
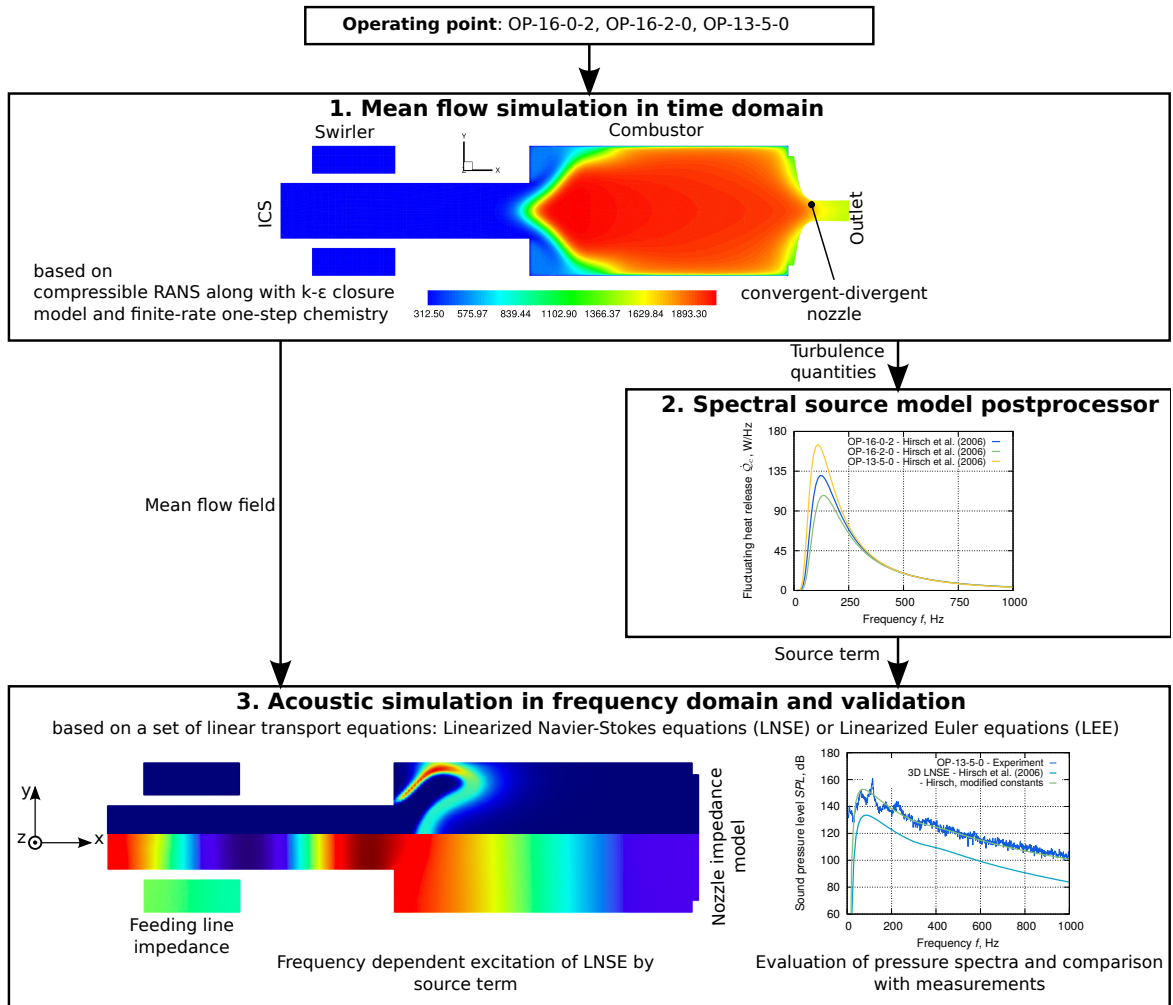
Figure 5.1: Hybrid approach for the determination of the combustion noise in the CESAM-HP combustor.

LNSE Frequency-Domain Simulation with Stochastic Sound Sources

In the final step LNSE simulations are performed, which are based on the eqs. (4.38) - (4.40) for premixed flames and on the eqs. (4.41) - (4.43) for non-premixed flames. Depending on the flame type, the LNSE are parametrically excited by the combustion noise source terms in the desired frequency range of interest situated between 10 and $1000\,\mathrm{Hz}$ for most cases. In case of a premixed flame the LNSE are excited by the volume source term $\hat{s}_V$ in the linearized continuity eq. (4.38) and energy eq. (4.40), while for the non-premixed flame the excitation is done via $\hat{\dot{\omega}}_z$ in the linearized energy eq. (4.43). The corresponding integral heat release spectra $\dot{\mathcal{Q}}_c(f)$ and $\dot{\mathcal{Q}}_z(f)$ are spatially redistributed according to the mean flame position using eqs. (4.81) and (4.83). Energy conservation of this spatial source distribution is fulfilled if the volume-integral of the local sources delivers the original integral source spectrum. The corresponding result for the statistical noise model
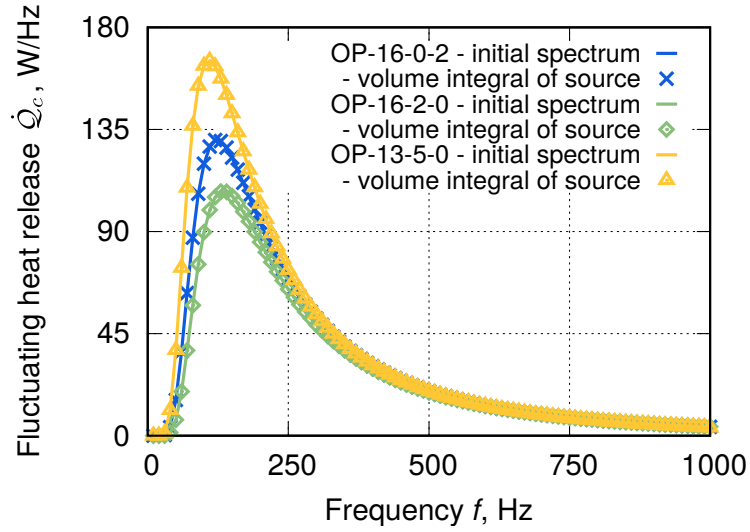
Figure 5.2: Spectra of fluctuating heat release $\dot{\mathcal{Q}}_c(f)$, [W/Hz] associated with the combustion noise for all three operating points of the CESAM-HP combustor.

by Hirsch et al. [2006, 2007] is exemplarily shown for the CESAM-HP combustor in fig. 5.2 for three different operating points. The volume-integrated values of the local sources were obtained in the postprocessing of the LNSE simulations. The original integral heat release spectrum and the volume-integral of the local source term are almost equal, which applies to all operating points. Therefore the model for the spatial source term distribution, proposed in this thesis, is energy consistent and does not need any arbitrary source volume definition. Further specifications such as boundary conditions will be given when introducing the different test cases.

The numerical solution of the LNSE yields the field of the fluctuating pressure in the combustion chamber. The resulting pressure spectra taken at the measurement positions are used for comparison with experimental data. All pressure spectra shown in this thesis are given in terms of the *sound pressure level (SPL)*, which is computed as

$$\text{SPL} = 20 \log_{10}\left(\frac{|\hat{p}|}{p_{\text{ref}}}\right) = 20 \log_{10}\left(\frac{|\mathcal{F}\{p'(t)\}|}{p_{\text{ref}}}\right). \tag{5.1}$$

The reference pressure is defined by $p_{\text{ref}} = 2 \cdot 10^{-5}\,\text{Pa}$.

5.2 Numerical Implementation of LNSE

For convenience the numerical implementation of the LNSE is only briefly outlined, see Gikadi [2014] for details. The LNSE, eqs. (4.38) - (4.40) and (4.41) - (4.43), are discretized by the finite-element method (FEM). They are written in matrix-vector formulation, where the different quantities are collected in the vector of unknowns $\hat{\boldsymbol{\phi}} = (\hat{\rho}, \hat{u}, \hat{v}, \hat{w}, \hat{p})^T$ and the

convection, coupling and diffusion matrices $\mathbf{A}_i$, $\mathbf{C}$ and $\mathbf{K}_{ij}$

$$\mathrm{i}\omega\hat{\boldsymbol{\phi}} + \mathbf{A}_i\frac{\partial\hat{\boldsymbol{\phi}}}{\partial x_i} + \mathbf{C}\hat{\boldsymbol{\phi}} = \frac{\partial}{\partial x_i}\left(\mathbf{K}_{ij}\frac{\partial\hat{\boldsymbol{\phi}}}{\partial x_j}\right) + \boldsymbol{f}. \tag{5.2}$$

The standard Galerkin-formulation or weak form of the LNSE (5.2) is obtained by the integration of its residual vector over the entire domain Ω, while weighting it by weighting functions $\boldsymbol{w} = (w_\rho, w_u, w_v, w_w, w_p)^T$ and applying Green's first identity on the diffusion terms in the momentum and energy equations to give [Codina, 1998, 2000]

$$\int_\Omega \boldsymbol{w}^T\left(\mathrm{i}\omega\hat{\boldsymbol{\phi}} + \mathbf{A}_i\frac{\partial\hat{\boldsymbol{\phi}}}{\partial x_i} + \mathbf{C}\hat{\boldsymbol{\phi}} - \boldsymbol{f}\right)\mathrm{d}\Omega + \int_\Omega \frac{\partial\boldsymbol{w}^T}{\partial x_i}\mathbf{K}_{ij}\frac{\partial\hat{\boldsymbol{\phi}}}{\partial x_j}\mathrm{d}\Omega - \int_{\Gamma_N} \boldsymbol{w}^T\mathbf{K}_{ij}\frac{\partial\hat{\boldsymbol{\phi}}}{\partial x_j}\boldsymbol{n}_i\mathrm{d}\Gamma = 0. \tag{5.3}$$

$\Gamma = \Gamma_D \cup \Gamma_N$ describes the boundary of the domain, where Dirichlet and Neumann conditions for the primitive variables and their fluxes are imposed. Eq. (5.3) is discretized by dividing the domain Ω into a total number of *nel* finite elements $\Omega^{(e)}$. The unknown variables are expressed as the sum of elementwise defined shape functions and discrete nodal values $\hat{\boldsymbol{d}}^{(e)}$. This approach is known as the Bubnov-Galerkin approach, if the weighting functions are the same as for the residual unknowns [Wall, 2010, Zienkiewicz et al., 2005a,b]

$$\hat{\boldsymbol{\phi}} = \mathbf{N}\left(\boldsymbol{\xi}\right)^{(e)}\hat{\boldsymbol{d}}^{(e)}, \qquad\qquad \boldsymbol{w} = \mathbf{N}\left(\boldsymbol{\xi}\right)^{(e)}\boldsymbol{g}^{(e)}. \tag{5.4}$$

$\mathbf{N}^{(e)} \in \mathbb{R}^{5\times 5n_p}$ is the matrix of shape functions and n_p the number of nodes on each element. The discretization of the weak form (5.3) along with the Bubnov-Galerkin approach (5.4) yields

$$\sum_{e=1}^{nel}\boldsymbol{g}^{T(e)}\bigg\{\int_{\Omega^{(e)}}\left(\mathrm{i}\omega\mathbf{N}^T\mathbf{N} + \mathbf{N}^T\mathbf{A}_i\frac{\partial\mathbf{N}}{\partial x_i} + \mathbf{N}^T\mathbf{C}\mathbf{N} + \frac{\partial\mathbf{N}^T}{\partial x_i}\mathbf{K}_{ij}\frac{\partial\mathbf{N}}{\partial x_j}\right)\mathrm{d}\Omega\hat{\boldsymbol{d}}^{(e)} -$$
$$- \int_{\Gamma_N^{(e)}}\mathbf{N}^T\mathbf{K}_{ij}\frac{\partial\mathbf{N}}{\partial x_j}\boldsymbol{n}_i\mathrm{d}\Gamma\hat{\boldsymbol{d}}^{(e)} - \int_{\Omega^{(e)}}\mathbf{N}^T\boldsymbol{f}\mathrm{d}\Omega\bigg\} = 0. \tag{5.5}$$

The shape functions are defined locally on an unitary element in the parameter space. They are transformed into real space using the isoparametric concept, i.e. the geometry $\boldsymbol{x}\left(\boldsymbol{\xi}\right)$ between the element's nodes $\bar{\boldsymbol{x}}^{(e)}$ is interpolated in the same way as the unknown variables to give

$$\boldsymbol{x}\left(\boldsymbol{\xi}\right) = \mathbf{N}\left(\boldsymbol{\xi}\right)^{(e)}\bar{\boldsymbol{x}}^{(e)}. \tag{5.6}$$

Spatial derivatives in eq. (5.5) are transformed into real space using the chain rule $\partial\mathbf{N}/\partial x_i = (\partial\mathbf{N}/\partial\boldsymbol{\xi})(\partial\boldsymbol{\xi}/\partial x_i)$, while the infinitesimal volume element is linked between parameter and real space by the Jacobian matrix, i.e. $\mathrm{d}\Omega = \det\mathbf{J}\mathrm{d}\boldsymbol{\xi}$ noting that $\mathbf{J} = \partial\boldsymbol{x}/\partial\boldsymbol{\xi}$. The following linear system of equations is obtained

$$\sum_{e=1}^{nel}\bigg\{\left(\mathrm{i}\omega\mathbf{m}^{(e)} + \mathbf{k}^{(e)}\right)\hat{\boldsymbol{d}}^{(e)} - \mathbf{k}_{NBC}^{(e)}\hat{\boldsymbol{d}}^{(e)} - \boldsymbol{b}^{(e)}\bigg\} = 0. \tag{5.7}$$

$\mathbf{m}^{(e)} \in \mathbb{R}^{5n_p \times 5n_p}$ is the element mass matrix, $\mathbf{k}^{(e)} \in \mathbb{R}^{5n_p \times 5n_p}$ is element the stiffness matrix and $\boldsymbol{b}^{(e)} \in \mathbb{R}^{1 \times 5n_p}$ is the element load vector

$$\mathbf{m}^{(e)} := \int_{\Omega^{(e)}} \mathbf{N}^T \mathbf{N} \det \mathbf{J} \mathrm{d}\boldsymbol{\xi}, \tag{5.8}$$

$$\mathbf{k}^{(e)} := \int_{\Omega^{(e)}} \left(\mathbf{N}^T \mathbf{A}_i \frac{\partial \mathbf{N}}{\partial \boldsymbol{\xi}} \frac{\partial \boldsymbol{\xi}}{\partial x_i} + \mathbf{N}^T \mathbf{C} \mathbf{N} + \frac{\partial \mathbf{N}^T}{\partial \boldsymbol{\xi}} \frac{\partial \boldsymbol{\xi}}{\partial x_i} \mathbf{K}_{ij} \frac{\partial \mathbf{N}^T}{\partial \boldsymbol{\xi}} \frac{\partial \boldsymbol{\xi}}{\partial x_j} \right) \det \mathbf{J} \mathrm{d}\boldsymbol{\xi}, \tag{5.9}$$

$$\boldsymbol{b}^{(e)} := \int_{\Omega^{(e)}} \mathbf{N}^T \boldsymbol{f} \det \mathbf{J} \mathrm{d}\boldsymbol{\xi}. \tag{5.10}$$

All local linear systems of equations (5.7) are finally assembled to obtain the global system with a total number of $ndof$ degrees of freedom (dof), i.e.

$$\left(\mathrm{i}\omega \mathbf{M} + \mathbf{K} \right) \hat{\boldsymbol{D}} = \boldsymbol{B}. \tag{5.11}$$

The global mass matrix $\mathbf{M} \in \mathbb{R}^{ndof \times ndof}$, stiffness matrix $\mathbf{K} \in \mathbb{R}^{ndof \times ndof}$, the global vector of unknowns $\hat{\boldsymbol{D}} \in \mathbb{C}^{ndof}$ and the global load vector $\boldsymbol{B} \in \mathbb{R}^{ndof}$ are given by the assembly operation.

The weak form in eq. (5.3) is prone to numerical oscillations in convection dominated problems. That is why it is stabilized by a Galerkin/least-squares (GLS) approach to give [Donea and Huerta, 2003, Hughes and Mallet, 1986, Hughes et al., 1989]

$$\text{Standard-Galerkin eq. (5.3)} + \int_{\Omega^{(e)} \setminus \partial \Omega^{(e)}} \boldsymbol{\mathcal{L}}^T(\mathbf{w}) \, \boldsymbol{\tau} \boldsymbol{\mathcal{R}}(\hat{\boldsymbol{\phi}}) \mathrm{d}\Omega = 0. \tag{5.12}$$

$\boldsymbol{\mathcal{R}}$ denotes the residual vector of the LNSE, $\boldsymbol{\mathcal{L}} = \boldsymbol{\mathcal{R}} + \boldsymbol{f}$ is the differential operator and $\boldsymbol{\tau}$ terms the stabilization matrix, cf. Donea and Huerta [2003], Zienkiewicz et al. [2005a]. The additional term in eq. (5.12) is evaluated over the interior of each element without its boundaries, indicated by operator $\Omega^{(e)} \setminus \partial \Omega^{(e)}$. In the same manner as explained above the discretized formulation of the GLS-stabilized LNSE (5.12) results in a global linear system of equations with $ndof$ degrees of freedoms

$$\left[\mathrm{i}\omega(\mathbf{M} + \mathbf{M}_{\mathrm{GLS}}) + (\mathbf{K} + \mathbf{K}_{\mathrm{GLS}}) \right] \hat{\boldsymbol{D}} = \boldsymbol{B}. \tag{5.13}$$

The diagonal of the stabilization matrix $\boldsymbol{\tau}$ in eq. (5.12) contains the stabilization parameters of each equation τ_i, which are chosen to be identical in this thesis, i.e. $\boldsymbol{\tau} = \mathrm{diag}\,(\tau_i) = \mathrm{diag}\,(\tau) = \delta_{ij}\tau_i$. As proposed by Beau et al. [1993] the stabilization parameter is derived from the spectral radius of the convection matrix $\rho\,(\mathbf{A}_k)$ and the characteristic element size h_k in the k-th direction

$$\tau_i := \max_{j=1...3} \left\{ \alpha_\tau \frac{h_j^{(e)}}{\rho\,(\mathbf{A}_j)} \right\}. \tag{5.14}$$

Unless otherwise specified the prefactor is set to $\alpha_\tau = 1.0$ in all test cases. With knowledge of the spectral radius of the convection matrices the stabilization parameter can be evaluated analytically yielding

$$\tau_i = \alpha_\tau \max_{j=1...3} \left(\frac{h_j}{|\bar{u}_j| + \bar{c}} \right). \tag{5.15}$$

To improve the condition and therefore the numerical accuracy of the linear set of equations (5.11) and (5.13), the fluctuating quantities $\hat{\rho}$, $\hat{u}_i$ and $\hat{p}$ are normalized by certain reference values to ensure that they are of the same magnitude. Therefore the LNSE are solved for non-dimensional density, velocities and pressure, i.e.

$$\hat{\rho}^* := \frac{\hat{\rho}}{\bar{\rho}_{\text{ref}}}, \qquad\qquad \hat{u}_i^* := \frac{\hat{u}_i}{\bar{c}_{\text{ref}}}, \qquad\qquad \hat{p}^* := \frac{\hat{p}}{\bar{p}_{\text{ref}}}. \tag{5.16}$$

The mean flow quantities at the inlet of each test case are chosen as reference values, i.e. $\bar{\rho}_{\text{ref}} = \bar{\rho}_1$, $\bar{c}_{\text{ref}} = \bar{c}_1$ and $\bar{p}_{\text{ref}} = \bar{p}_1$. The commercial software COMSOL MULTIPHYSICS [COMSOL, 2011] is utilized for all acoustic simulations conducted in this thesis. This finite-element based tool allows to manually implement partial differential equations (PDE) and their weak-formulations, such as the GLS-FEM discretized LNSE (5.12). Also advanced postprocessing functionalities are available due to a MATLAB interface.

5.3 Ratio Between Direct and Indirect Combustion Noise

One goal of this thesis is the determination of the ratio between direct and indirect noise for two generic combustion chambers. As explained in the following the noise ratio inside the combustor can be predicted by a variation of its outlet boundary condition, while the computation of the noise ratio downstream of the combustor requires the combination of combustor simulations and network models.

5.3.1 Inside the Combustion Chamber

In real aero engine combustors the flow through the turbine NGV reaches transonic conditions for the most operating points [Bräunling, 2009]. The combustor outlet section and turbine NGV can be therefore approximated by a choked nozzle. Under such assumptions the strategy proposed by Dowling and Mahmoudi [2015] is pursued in this thesis to determine the noise ratio inside the combustion chamber. The starting point for the LNSE combustor simulations is to substitute the nozzle by an appropriate boundary condition representing the nozzle reflection behavior, i.e. eq. (3.42) in sec. 3.7. The excitation of the LNSE along with either the volume source or heat release source term then delivers the sound field of the total noise. The resulting pressure fluctuations inside the combustor contain contributions from direct and indirect noise.
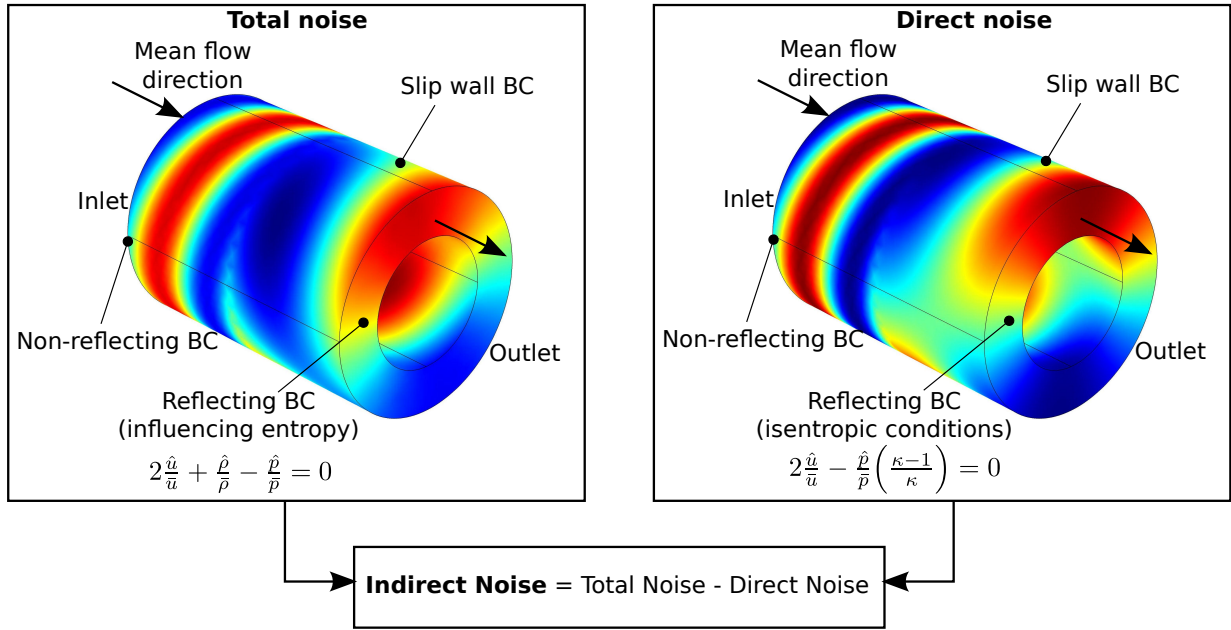
Figure 5.3: Methodology for the discrimination between direct and indirect combustion noise inside of a generic combustion chamber [Ullrich and Sattelmayer, 2015].

So far the procedure exactly corresponds to the method for the prediction of the total combustor noise as explained in sec. 5.1. To identify the different contributions of direct and indirect noise, a second simulation based on a different outlet boundary condition is performed. In this second simulation the choked mass flow condition (3.42) is modified in such a manner that it exclusively acts on the impinging acoustic waves but not on the entropy waves. In this case only direct noise is present in the combustor since no feedback of the entropy waves on the combustor acoustics is included in the model. The appropriate outlet boundary condition is derived by replacing the density in eq. (3.42) by the isentropic pressure-density relation (3.21), which yields eq. (3.43). Only the isentropic part of the density fluctuations contribute to the boundary condition (3.43), while the density fluctuation related to the entropy wave is excluded. Therefore entropy waves impinging on the outlet boundary condtion (3.43) leave the propagation domain without any acoustic feedback effect. Acoustic waves with defined pressure and isentropic density fluctuations are creating reflections at the outlet boundary condtion (3.43). In this way the second simulation provides the sound field related to the direct noise. This stands in contrast to the first simulation, where the outlet boundary condition (3.42) also acts on the density fluctuations of the entropy wave, which create an acoustic feedback in form of reflected acoustic waves, i.e. the indirect noise. Due to the linear assumption both solutions can be superimposed. The contribution of the indirect noise is retrieved by subtracting the direct sound field from the total one. The entire procedure for the prediction of the noise ratio inside the combustor is exemplarily illustrated in fig. 5.3 for the annular model combustor, which will be treated in sec. 8.1. The procedure above is based on the idea by

Dowling and Mahmoudi [2015] to separate the direct and indirect noise contributions by a variation of the choked nozzle boundary condition.

5.3.2 Downstream of the Combustion Chamber

The fully three-dimensional acoustic simulation of all components of an aero engine like combustor, turbine and exhaust nozzle is typically not feasible in an industrial design process due to limited computational resources and time. Therefore different components such as the turbine are usually modeled by network elements at least in the early design stage. The exhaust nozzle is most commonly represented by the early theoretical analytical models by Marble and Candel [1977], while the turbine is approximated by so-called actuator-disc models, established by Cumpsty and Marble [1977b]. Further details on the theoretical modeling of nozzles and turbine stages are given by Leyko et al. [2010, 2011]. In recent studies LES simulations of the generic CESAM-HP combustor [Huet et al., 2016] and even a full annular helicopter combustion chamber [Livebardon et al., 2015, 2016] were coupled with one-dimensional network tools.

The approach proposed by Huet et al. [2016] is followed to compute the noise ratio downstream of the generic CESAM-HP combustor, which will be presented in the last chapter. The general approach is exemplarily sketched in fig. 5.4 for the CESAM-HP combustor, which is connected to a convergent-divergent nozzle at the downstream side. Here the network model describing the propagation of acoustic and entropy waves downstream of the combustor is limited to the convergent-divergent nozzle. But the procedure can be applied to any other combustion chamber provided. The global transfer or scattering matrices of the complete part downstream of the combustor, e.g. a turbine, are known. The following convention is used for all presented combustor simulations: The combustor inlet and outlet plane are indicated by the subscripts 1 and 2. All variables evaluated in the section downstream of the combustor, such as the exhaust nozzle exit plane, are marked by index 3.

As sketched in fig. 5.4 first the scattering matrices related to the network model are predicted by applying the two source location method as described in sec. 3.8.3 and 3.8.4. In the second step non-isentropic combustor simulations are carried out to deliver the fields of density $\hat{\rho}$, velocities $\hat{u}_i$, pressure $\hat{p}$ and entropy $\hat{s}$, among others. In the final postprocessing of the LNSE combustor simulation, the upstream and downstream traveling acoustic waves $\hat{p}_2^+$ and $\hat{p}_2^-$ as well as the entropy waves $\hat{s}_2$ are extracted close to the combustor outlet to feed them into the network model. The procedure for the wave extraction was introduced in sec. 3.8.3. Once the upstream and downstream traveling waves at the combustor outlet are separated, they are multiplied by the acoustic and entropy transfer functions (cf. subsec. 3.8.1 and 3.8.2) to get the corresponding waves at the exhaust nozzle exit (index 3). This is demonstrated on the downstream traveling acoustic wave $\hat{p}_3^+$, which is composed of a direct part $\hat{p}_{3,p}^+$ and an indirect part $\hat{p}_{3,s}^+$. The decomposition results from the definitions

of the acoustic and entropy transmission coefficients, eqs. (3.44) and (3.46) give

$$\hat{p}_3^+ = \hat{p}_{3,p}^+ + \hat{p}_{3,s}^+ = \left(\frac{\hat{p}_{3,p}^+}{\hat{p}_2^+}\right)\hat{p}_2^+ + \left(\frac{\hat{p}_{3,s}^+}{\hat{s}_2}\right)\hat{s}_2 = T_u\hat{p}_2^+ + T_s\hat{s}_2. \tag{5.17}$$

Following Leyko et al. [2009] the noise ratio ζ at the exhaust nozzle outlet is defined by the transmitted acoustic waves related to indirect noise $\hat{p}_{3,s}^+$ and direct noise $\hat{p}_{3,p}^+$:

$$\zeta := \frac{\hat{p}_{3,s}^+}{\hat{p}_{3,p}^+} = \frac{\hat{s}_2}{\hat{p}_2^+}\frac{T_s}{T_u}. \tag{5.18}$$
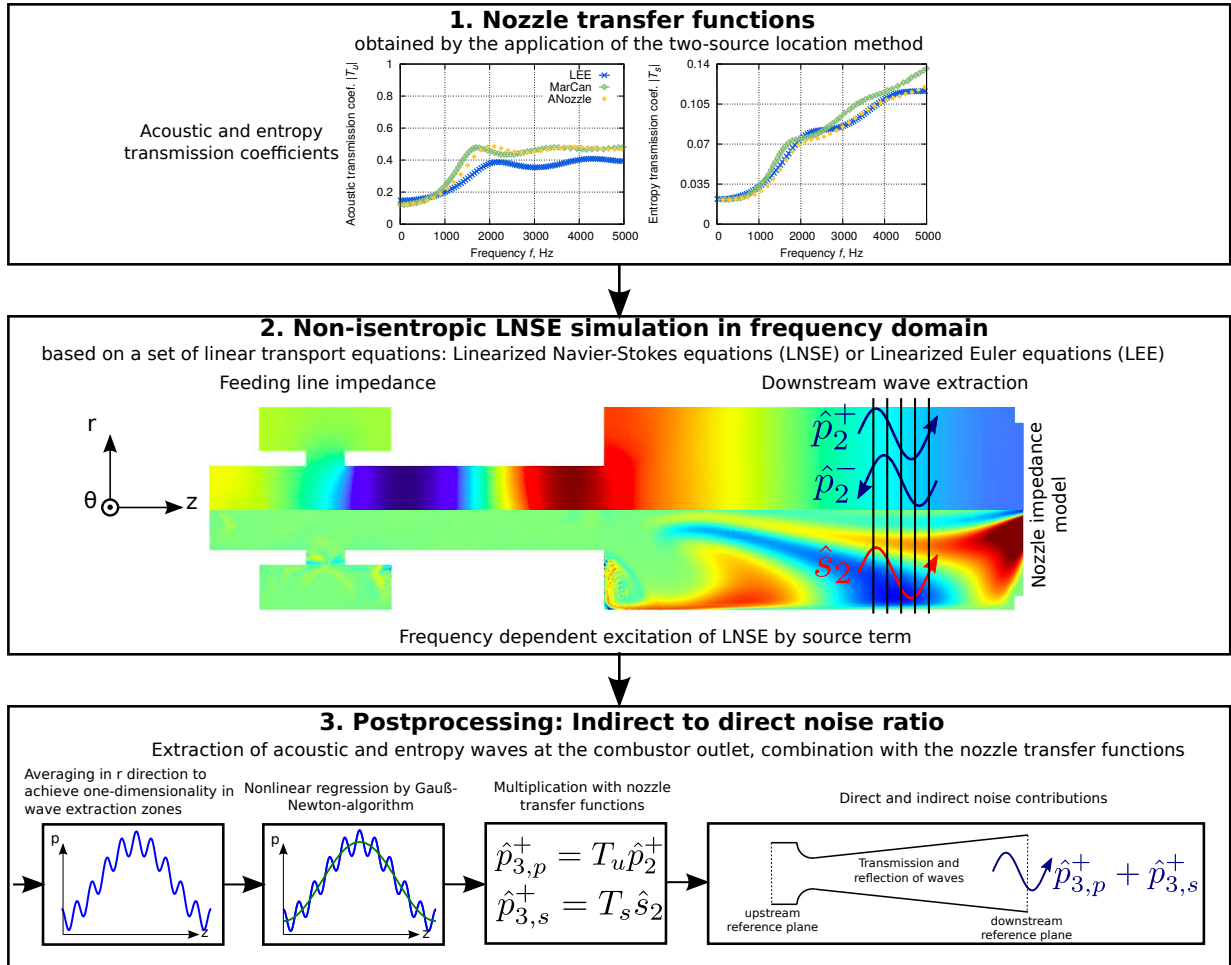
Figure 5.4: Procedure for the prediction of the direct and indirect noise contributions at the nozzle exit of the CESAM-HP combustor.

Mahmoudi et al. [2015] estimated the contribution of vorticity waves to be one order of magnitude smaller than the contribution of the entropy noise. So they concluded a minor role of vorticity waves to the production of indirect noise. For this reason the indirect noise generation by vorticity waves is not regarded in context of the noise ratio predictions done in this thesis.

6   Direct Noise Propagation

In this chapter the propagation of acoustic waves in two convergent-divergent nozzle geometries is investigated. These nozzles represent the simplest model of the complex turbine NGV flow of stationary gas turbines or aero engines. The acoustic properties are expressed in terms of scattering matrices as introduced in the sec. 3.8. The numerical results obtained by the hybrid RANS/LNSE approach are compared with analytical models and experiments.

6.1   The Entropy Wave Generator (EWG)

The Entropy Wave Generator (EWG) experiment by Bake et al. [2009] investigates the propagation of direct combustion noise through a convergent-divergent nozzle. The acoustic reflection and transmission properties are important for the propagation of the direct noise through the turbine. As later shown, the scattering properties are closely linked to the acoustic-vorticity interactions which are identified using the tools described in sec. 3.2. The simulation model and the results presented in the following are based on the study by Ullrich et al. [2014a].

6.1.1   Configuration

The EWG test rig consists of a convergent-divergent nozzle with dimensions of $l_{conv} = 0.13\,\text{m}$, $l_{div} = 0.25\,\text{m}$ and a throat radius of $r_{min} = 0.00375\,\text{m}$. A straight inlet duct of length $l_1 = 0.25\,\text{m}$ and radius $r_1 = 0.015\,\text{m}$ is mounted at the upstream end of the nozzle. The downstream end is connected to a straight exit duct with radius of $r_2 = 0.02\,\text{m}$ and length of $l_2 = 1.2\,\text{m}$. Quantities with subscript 1 represent the inlet or upstream duct, while the subscript 2 indicates the outlet or downstream duct. The aeroacoustic properties of the convergent-divergent nozzle are determined in terms of acoustic scattering matrices for subsonic and choked operating conditions. The parameters of these two operating conditions are summarized in tab. 6.1.

6.1.2   Numerical Setup

The mean flow fields are calculated by stationary compressible RANS simulations on an axis-symmetrical 2D grid. The turbulence is described by the k-ϵ model with the low-Reynolds extension [ANSYS, 2011a] resolving the boundary layers down to the viscous sublayer. Further details on the RANS are given by Ullrich et al. [2014a]. The resulting

Operating Point	Subsonic Case	Transsonic Case
Static temperature inlet (K)	293.15	296.15
Mass flow (g/s)	10.27	11.6
Nozzle throat Mach number (-)	0.7	1.0
Static pressure outlet (Pa)	101,325	100,800

Table 6.1: Operating points of the EWG test rig.

mean flow fields are shown in fig. 6.1, where a weak shock is visible nearby the nozzle throat in the transsonic case. The shock-boundary layer interaction leads to a small separation zone and further downstream to the formation of a weak jet and shear layer in the divergent nozzle part.

The frequency-domain LNSE simulations are done in cylindrical coordinates $\boldsymbol{x} = (r, \theta, z)^T$ and assuming axis symmetry (i.e. $\hat{u}_\theta = 0, \partial/\partial\theta = 0$) for the variables $\hat{\rho}, \hat{\boldsymbol{u}} = (\hat{u}_r, \hat{u}_z)^T$ and $\hat{p}$. The domain is discretized by an unstructured grid of 18,805 triangular elements with second order Lagrangian shape functions, which gives a total number of 154,560 degrees of freedom. At the inlet and outlet the acoustics are defined by non-reflecting boundaries corresponding to $Z = 1$ in the impedance boundary condition eq. (3.33). The inlet entropy is set to $S_p = 0$ in eq. (3.39).

The acoustic scattering matrix $\mathbf{S}_a$ is calculated by means of the two-source location method as introduced in sec. 3.8.3. The underlying frequency-domain simulations are carried out for both the isentropic as well as the non-isentropic formulation of the LNSE. In the isentropic case only the continuity and momentum eqs. (3.12) and (3.13) are solved. The pressure is retrieved by the isentropic pressure-density relation $\hat{p} = \bar{c}^2\hat{\rho}$. Momentum and thermal diffusion effects are neglected ($\eta = \lambda = 0$). Solving the full non-isentropic LNSE simulations the linearized energy eq. (3.14) is included. In the next section the results are presented.

6.1.3 Acoustic Scattering Matrix

In fig. 6.2 and 6.3 the absolute values of the scattering matrices are presented for throat Mach numbers of 0.7 and 1.0. At subsonic conditions the isentropic LNSE simulations and the analytical solutions of Duran and Moreau [2013] agree closely for the reflection and transmission coefficient R_u and T_u. As expected a deviation between the isentropic LNSE and the non-isentropic solution is observed over the entire frequency range. These deviations are associated with the additional acoustic damping effect included in the non-isentropic LNSE formulation. More precisely the interaction of acoustic waves with mean entropy gradients, expressed by the term $-u_i'\partial\bar{s}/\partial x_i$ in eq. (3.8), leads to a generation of entropy waves, while the acoustic waves are attenuated. This damping effect is only relevant in the boundary layers as the remaining subsonic nozzle flow is sufficiently described by an isentropic flow. As shown in the figs. 6.4 and 6.5 the pressure fields predicted by the
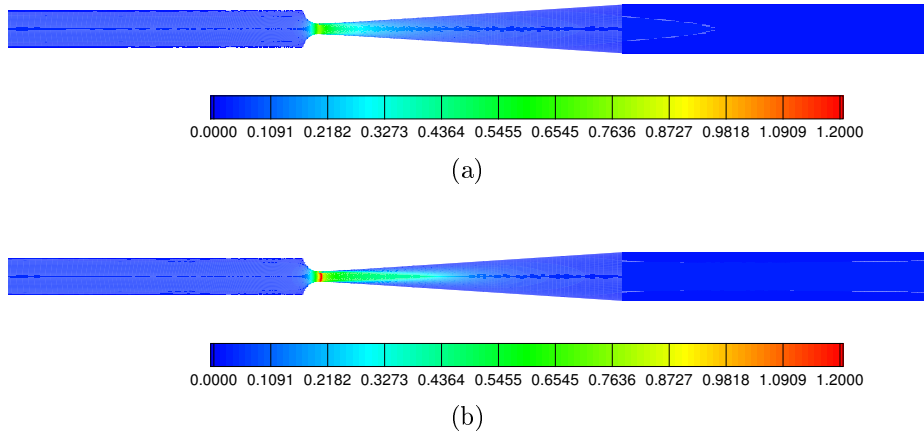
Figure 6.1: Mean Mach number $\bar{\mathrm{M}}$ at (a): subsonic conditions (throat Mach number $\bar{\mathrm{M}} = 0.7$), and (b): at transsonic conditions (throat Mach number $\bar{\mathrm{M}} = 1.0$). Results based on work by Ullrich et al. [2014a].

isentropic and non-isentropic LNSE are almost identical at subsonic conditions. Significant differences are encountered in the transsonic case, where interactions between the acoustics and the shock lead to the generation of entropy waves and therefore additional acoustic losses.

As seen in fig. 6.2 and 6.3 the magnitude of the upstream reflection coefficient (lower left) is always very close to $|R_u| \approx 1$. This is expected since the area of the throat is very small compared to the inlet cross section. In the subsonic case the isentropic LNSE start at the same level, while the non-isentropic LNSE results in slightly lower values. As a consequence acoustic waves impinging on the upstream end of the nozzle are almost fully reflected by it and the transmission of acoustic waves from the upstream to the downstream side of the nozzle remains on a low level over the entire frequency range. This process is almost independent of frequency. At transonic conditions a very similar behavior of the nozzle is found.

The downstream acoustic transmission coefficient T_d is small in the subsonic case. At choked conditions it is zero over the entire frequency range. Acoustic waves entering the nozzle at its downstream end are not able to pass the sonic line. Apart from the subsonic boundary layers no transmission of acoustic waves from the downstream to the upstream side takes place. The successive refinement of the mesh in the boundary layers has almost no influence on the transmission coefficient T_d, which remains close to zero. The transmission effect due to the subsonic boundary layers is concluded to be negligible. The convergent and divergent nozzle parts are almost perfectly decoupled with respect to acoustic transmission from the downstream end of the nozzle ($T_d = 0$). The reflection coefficient R_d for acoustic waves traveling from the downstream end in the direction of the nozzle throat significantly decreases from 0.9 at 200 Hz to 0.3 at 1000 Hz.
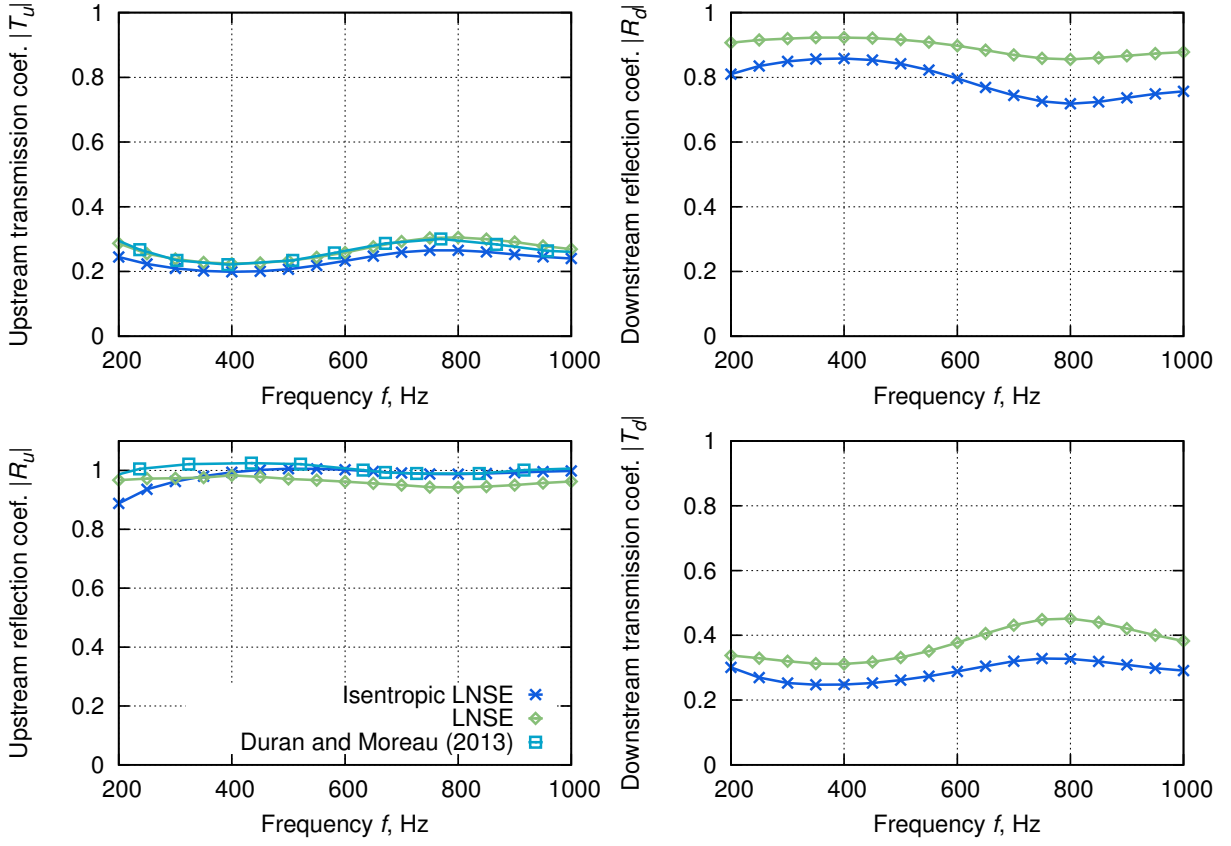
Figure 6.2: Absolute value of scattering matrix coefficients at subsonic conditions (throat Mach number $\bar{\mathrm{M}} = 0.7$) [Ullrich et al., 2014a].

In summary the analysis demonstrated that the hybrid methodology is capable to precisely predict the acoustic scattering properties of the convergent-divergent nozzle. This validation is important to ensure an accurate description of the transmission of direct as well as indirect combustion noise through nozzles. Beyond this the LNSE approach incorporates meaningful coupling mechanisms between acoustics and the mean flow field, which are presented in the following subsections.

6.1.4 Interaction Term Analysis

One advantage of the hybrid LNSE simulation in frequency domain is that all mechanisms can be analyzed during postprocessing. To clarify the acoustics-vorticity interaction, which is presumably the cause of the losses, the different source terms $S_{i,\Omega}$ in the vorticity eq. (3.10) have been calculated and integrated over the volume of the entire simulation domain. The volume integration was done to estimate the order of magnitude of the different terms. The results for the different volume-integrated terms $S_{i,\Omega}$ are given in fig. 6.6 for upstream (left) and downstream excitation (right). In case of the upstream excitation all vorticity
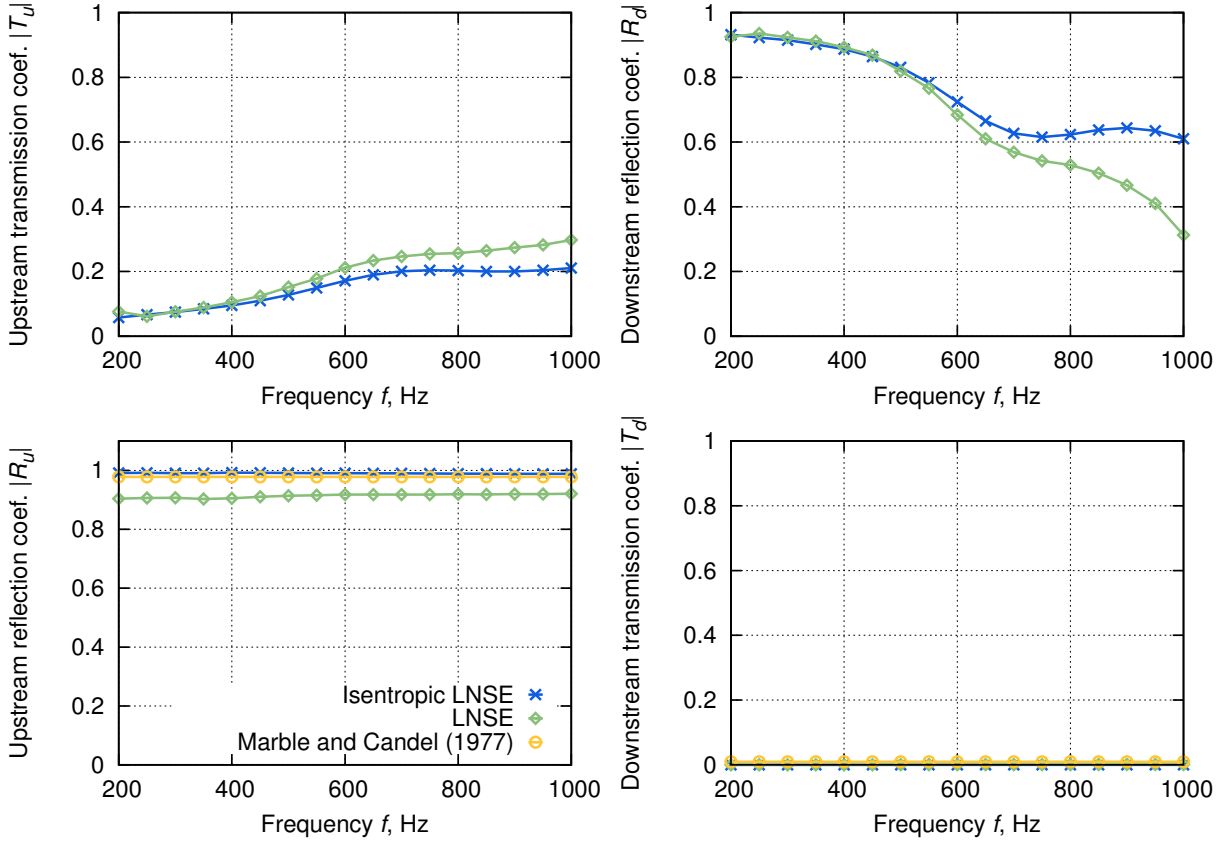
Figure 6.3: Absolute value of scattering matrix coefficients at transsonic conditions (throat Mach number $\bar{\mathrm{M}} = 1.0$) [Ullrich et al., 2014a].

source terms remain on a very low level close to zero with marginal increase with frequency. Acoustic-vorticity interactions play therefore only a minor role in the convergent nozzle part. This results in an almost perfect reflection of the acoustic waves entering the nozzle at the upstream side. A completely different evolution of the source terms is observed in case of the downstream excitation. In this case all source terms grow continuously with frequency but to different extent. The dominant damping effect in the divergent nozzle part is given by dilatation term IV in the linearized vorticity eq. (3.10). It represents the generation of vorticity as acoustic waves travel from the divergent part towards the nozzle throat, while interacting with the shear layers of the jet. Terms related to baroclinic vorticity production (term VI and VII) and acoustic shear layer interactions (term I) are another important drivers for the losses in the divergent nozzle part. All other source terms in eq. (3.10) are of minor importance. The downstream reflection coefficient is monotonically decreasing with frequency and therefore shows the opposite behavior as the vorticity source terms. In conclusion the acoustic-vorticity interaction is responsible for the different nozzle reflection properties from the upstream and downstream side. In the upstream excitation case only a small part of acoustic waves is converted into vorticity,

(a) Isentropic LNSE (200 Hz)

(b) LNSE (200 Hz)

(c) Isentropic LNSE (800 Hz)

(d) LNSE (800 Hz)
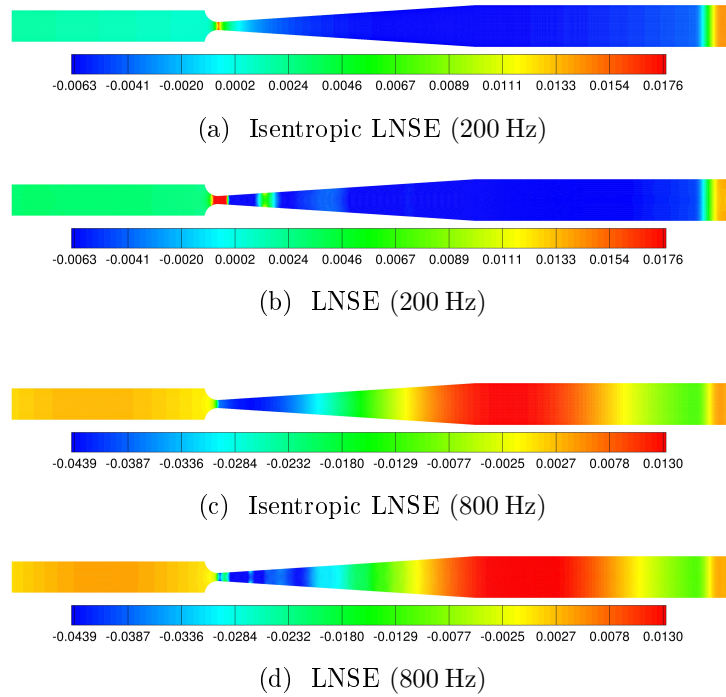
Figure 6.4: Fluctuating pressure fields $\Re\{\hat{p}\}$, Pa for downstream excitation at subsonic conditions (throat Mach number $\bar{M} = 0.7$).

(a) Isentropic LNSE (200 Hz)

(b) LNSE (200 Hz)

(c) Isentropic LNSE (800 Hz)

(d) LNSE (800 Hz)
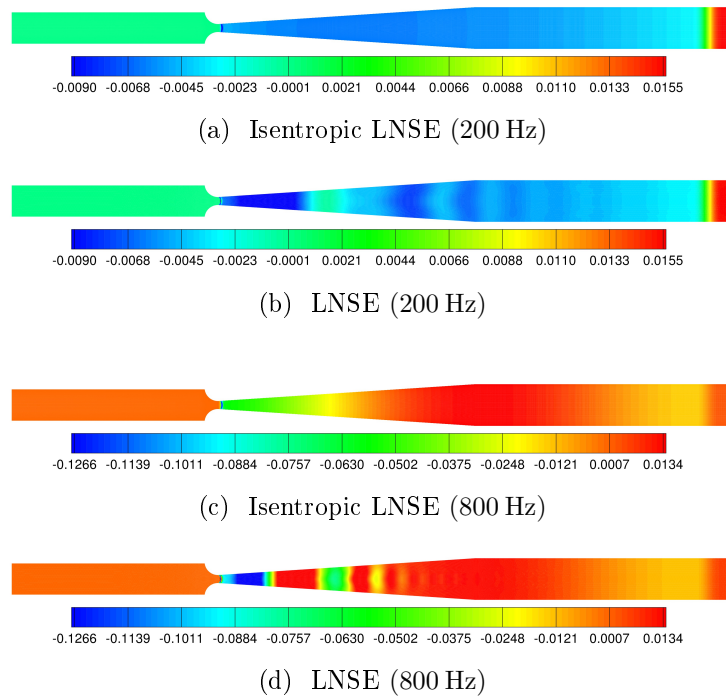
Figure 6.5: Fluctuating pressure fields $\Re\{\hat{p}\}$, [Pa] for downstream excitation at transsonic conditions (throat Mach number $\bar{M} = 1.0$)

which leads to an almost perfect reflection of acoustic waves. The downstream reflection coefficient monotonically decreases with frequency as a result of a successively increasing generation of vorticity waves due to acoustic shear layer interactions in the divergent nozzle part.
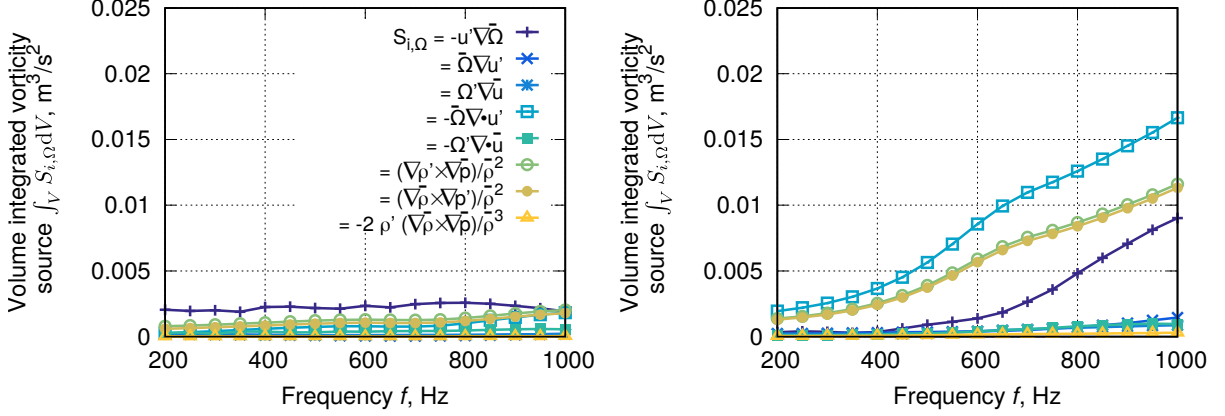
Figure 6.6: Impact (absolute value) of different interaction mechanisms, defined by eq. (3.10), on the generation of vorticity with upstream (left) and downstream excitation (right) for the transsonic case. Results from Ullrich et al. [2014b].

6.1.5 Energy Flux Analysis

In the following the analysis of the interaction terms is continued by the evaluation of the integral energy balance for all types of fluctuations. The evaluation of the energy balance provides a useful quantitative measure of the damping since the linearized vorticity eq. (3.10) does not quantify the energy content of the vorticity waves. The energy balance for linear fluctuations was initially derived by Myers [1991] and later extended to reacting flows by Giauque et al. [2006] and Brear et al. [2012]. The energy balance for a fixed control volume V, surrounded by the surface S with surface normal vector n_i, reads

$$\int_V \frac{\partial E}{\partial t} \mathrm{d}V + \int_S F_i n_i \mathrm{d}S = \int_V D \mathrm{d}V. \tag{6.1}$$

E is the phase-averaged energy density, F_i is the energy flux vector and D is the volumetric source $(D > 0)$ or sink $(D < 0)$ due to entropy and vorticity waves [Lieuwen, 2012]

$$E = \frac{1}{2}\Re\left\{\frac{\hat{p} \cdot \hat{p}^*}{2\bar{\rho}\bar{c}^2} + \frac{1}{2}\bar{\rho}\left(\hat{u}_i \cdot \hat{u}_i^*\right) + \hat{\rho}\left(\bar{u}_i \cdot \hat{u}_i^*\right) + \frac{\bar{\rho}\bar{T}\hat{s} \cdot \hat{s}^*}{2c_p}\right\}, \tag{6.2}$$

$$F_i = \frac{1}{2}\Re\left\{\hat{p}\hat{u}_i^* + \hat{p}\frac{\hat{\rho}^*}{\bar{\rho}}\bar{u}_i + \bar{\rho}\left(\bar{u}_j \cdot \hat{u}_j\right)\hat{u}_i^* + \left(\bar{u}_j \cdot \hat{u}_j\right)\hat{\rho}^*\bar{u}_i + \bar{\rho}\bar{u}_i\hat{T}\hat{s}^*\right\}, \tag{6.3}$$
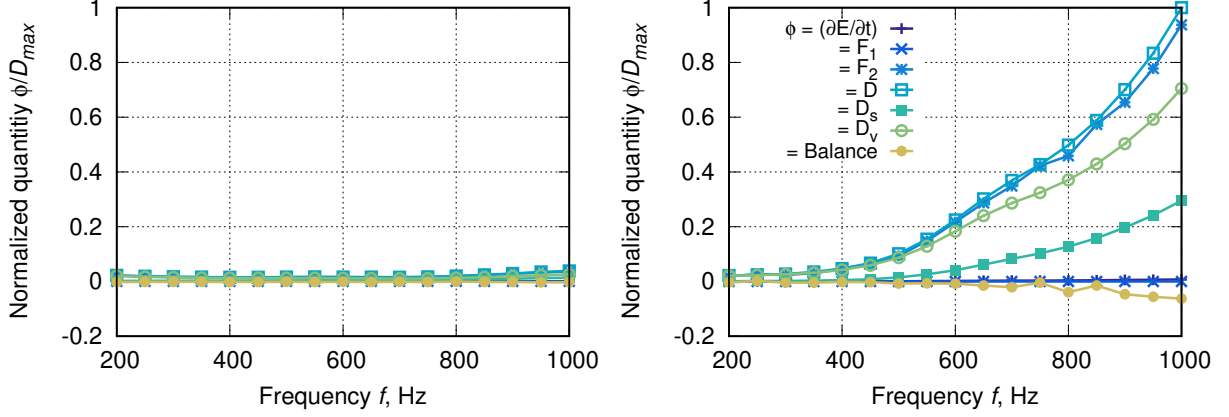
Figure 6.7: Evaluation of the disturbance energy balance (6.1) with upstream (left) and downstream excitation (right) for the transsonic case [Ullrich et al., 2014b].

$$D = \frac{1}{2} \Re \bigg\{ \bar{\rho} \bar{u}_i \cdot (\epsilon_{ijk} \hat{\Omega}_j \hat{u}_k^*) + \hat{\rho} \hat{u}_i^* \cdot (\epsilon_{ijk} \bar{\Omega}_j \bar{u}_k) - \hat{s} \left(\bar{\rho} \hat{u}_i^* + \hat{\rho}^* \bar{u}_i \right) \frac{\partial \bar{T}}{\partial x_i} +$$
$$+ \hat{s} \bar{\rho} \bar{u}_i \frac{\partial \hat{T}^*}{\partial x_i} + \bigg(\frac{\hat{\dot{q}}_V \hat{T}^*}{\bar{T}} - \frac{\bar{\dot{q}}_V \hat{T} \cdot \hat{T}^*}{\bar{T}^2} \bigg) \bigg\}. \quad (6.4)$$

The superscript $*$ denotes the conjugate complex variable in the eqs. (6.2)-(6.4), where viscous and thermal diffusion terms are neglected. When assuming phase-averaged time harmonic quantities the first term in the energy balance (6.1) is zero by definition. In the following the source term is decomposed into the first two contributions for vorticity D_v and the third and fourth term for entropy D_s.

The results for the disturbance energy balance eq. (6.1) are shown in fig. 6.7 for the transsonic case. The different terms, defined by the eqs. (6.2) - (6.4), are normalized by the maximum power of $D_{\max} = 2.87 \cdot 10^{-8}$ W. The time derivative of the phase-averaged energy density E is zero per definition under the assumption of time-harmonic fluctuations. Therefore the energy balance (6.1) is exactly fulfilled if the sum of all source terms and fluxes is zero. As indicated by the "balance" line, this is the case for the most part of the frequency range except for higher frequencies. Beyond 900 Hz slight deviations from zero are visible. Furthermore, the results for the source term D follow the same trend as observed in the frame of the interaction term analysis of the linearized vorticity eq. (3.10). A further discrimination between the different contributions to the total losses D reveals that the part due to vorticity waves D_v dominates over the contribution due to entropy waves D_s. In case of the downstream excitation the flux F_1 over the inlet is zero over the entire frequency range, whereas the flux F_2 over the outlet follows the total losses D, cf. right in fig. 6.7. The flux evaluation confirms that the acoustic waves are partially converted into vorticity waves, which lead to a decreasing downstream reflection coefficient with frequency. As the acoustic waves are not able to pass the nozzle throat from the downstream side, the inlet flux F_1 and the downstream transmission coefficient are zero.

6.2 The Hot Acoustic Testrig (HAT)

The purpose of the HAT test case is to investigate the acoustic scattering properties under more realistic engine conditions with respect to the temperature and pressure level and the nozzle geometry. The simulation model and the results presented in the following subsections are based on the work by Winter [2015].

6.2.1 Configuration

The HAT test rig represents a convergent-divergent nozzle, which is connected to straight ducts at each of its endings. The shape of the HAT nozzle possesses acceleration characteristics comparable to the turbine NGV. The nozzle has a throat radius of $r_{min} = 0.015$ m. The length of the convergent nozzle part is $l_{conv} = 0.068$ m and the length of the divergent nozzle part is $l_{div} = 0.326$ m. A straight inlet duct of length $l_1 = 0.3$ m and radius $r_1 = 0.035$ m is mounted at the upstream side of the nozzle. The divergent part of the nozzle is connected to a straight exit duct with radius of $r_2 = 0.035$ m and length of $l_2 = 0.3$ m. The inlet is preheated up to a moderate level of $\bar{T}_1 = 473.15$ K while the outlet pressure remains at ambient conditions. Choked conditions including a weak shock close to the nozzle throat are reached. The operating conditions are summarized in tab. 6.2.

6.2.2 Numerical Setup

The mean flow simulations were based on steady and compressible RANS simulations. A fairly small temperature drop over the nozzle of $\Delta\bar{T} = 12.3$ K was measured in the experiment by Knobloch et al. [2015], so adiabatic walls were assumed in the RANS simulation. For turbulence the k-ϵ model together with standard wall functions was used.

The LNSE are solved on an axis-symmetrical domain with non-reflecting boundary conditions. Assuming isentropic wave propagation, entropy waves are excluded. The domain is discretized with an unstructured mesh of quadratic Lagrangian shape functions with a total number of 31,520 elements. The two-source location method is applied to determine the acoustic scattering matrix, cf. subsec. 3.8.3.

Operating Point	Transsonic Case
Static temperature inlet (K)	473.15
Mass flow (g/s)	133.1
Nozzle throat Mach number (-)	1.0
Static pressure outlet (Pa)	100,050

Table 6.2: Operating point of the HAT test rig.

6.2.3 Acoustic Scattering Matrix

The isentropic LNSE results are compared with measurements provided by German Aerospace Center (DLR)[1] [Knobloch et al., 2015]. As seen in fig. 6.8, the numerical results are in good agreement with the experiment in the frequency range from approximately 400 Hz to 1500 Hz except for the downstream reflection coefficient R_d. Here the numerical solution remarkably differs from the experimental prediction over the whole frequency range. The upstream transmission coefficient is constantly underestimated by the LNSE simulations. The upstream reflection coefficient is overpredicted by the numerical simulations for frequencies exceeding 2250 Hz. Some numerical oscillations are observed below 400 Hz for the downstream reflection coefficient. The HAT and the EWG test rig show a similar reflection and transmission behavior. The choked conditions always lead to a zero downstream transmission coefficient for all frequencies.
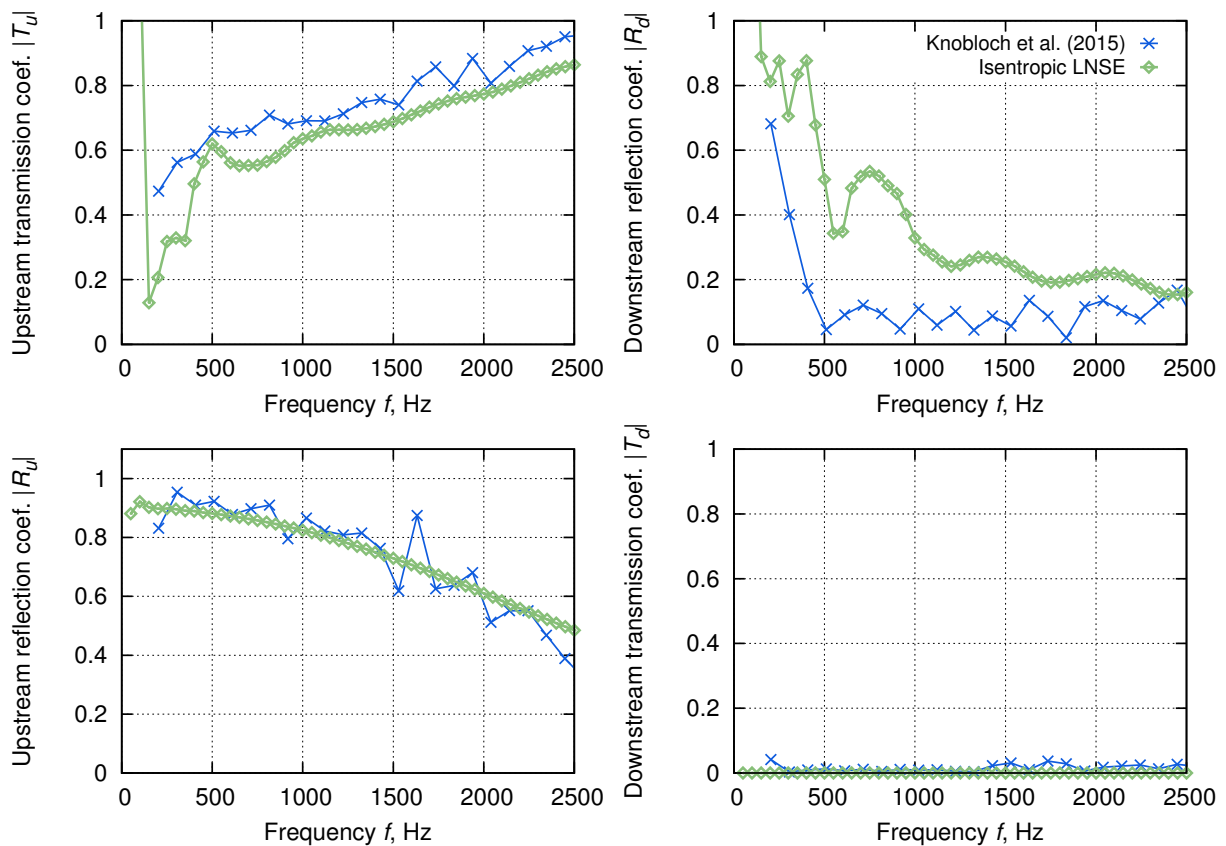
Figure 6.8: Absolute value of scattering matrix coefficients.

The scattering matrix comprises all effects of transport of the acoustic energy. In particular the acoustic flux $p'u'A$ (first and second term in eq. (6.3)) and the convective fluxes (third and fourth term in eq. (6.3)) are linear in the Mach number. The acoustic flux $p'u'A$ directly scales with the area ratio (A_{min}/A_1), which is 0.0625 for the EWG and 0.1836 for the HAT. For given inlet Mach numbers the ratio of the transmission coefficient between the EWG and HAT can be computed as $T_{u,\text{EWG}}/T_{u,\text{HAT}} = (A_{min}/A_1)_{\text{EWG}}/(A_{min}/A_1)_{\text{HAT}}(1 + \bar{\text{M}}_{\text{EWG}})/(1 + \bar{\text{M}}_{\text{HAT}}) = 0.32$. This scaling result is met exactly in the LNSE solution.

7   Indirect Noise Generation and Propagation

The main objective of this chapter is to validate the hybrid RANS/LNSE approach for indirect noise generation arising from entropy waves and vorticity waves on two experiments, where data is available.

7.1 The Entropy Wave Generator (EWG)

7.1.1 Numerical Setup

The experimental setup by Bake et al. [2009] is reproduced as closely as possible by the LNSE model in terms of geometry, excitation method and boundary conditions. The inlet is modeled by a fully-reflecting surface since it is connected to a large settling chamber in the experiment. Fully-reflective inlet properties are realized by defining $Z_1 \to \infty$ in eq. (3.33) together with $S_p = 0$ in eq. (3.39). Bake et al. [2009] designed an anechoic ending section, which was mounted on the outlet pipe. They tried to determine the reflection coefficient of the outlet in the range from 20 Hz to 200 Hz. Beyond 200 Hz no experimental data for the outlet reflection coefficient are available. Bake et al. [2009] proposed to apply the model by Selle et al. [2004] in this frequency range

$$ R_2 = \left[1 + \left(\frac{2\omega}{K} \right)^2 \right]^{-\frac{1}{2}} \qquad \text{with} \qquad K = \sigma \left(1 - \bar{\mathrm{M}}^2 \right) \frac{\bar{c}}{l}, \qquad (7.1) $$

where l is the domain length, $\bar{\mathrm{M}}$ is the outlet Mach number and σ is a scaling coefficient. The following values are chosen: $l = 1.2\,\mathrm{m}$, $\bar{\mathrm{M}} = 0.02$ and $\sigma = 1.8$. Below 200 Hz the experimental reflection coefficient by Bake et al. [2009] is applied, while the model in eq. (7.1) is used above 200 Hz. Given the reflection coefficient the reduced impedance is calculated using eq. (3.32) and inserted as an impedance boundary condition (3.33).

In the experiment, entropy waves are excited by thin heated wires located in the inlet duct upstream of the nozzle. The temperature signal arising from the pulsed excitation of the heated wires was measured by a fast thermocouple and a vibrometer. In the LNSE simulations the excitation of entropy waves $\hat{s}$ with complex temperature amplitude $\mathcal{T}(\omega)$ is achieved by imposing an electrical energy source $\hat{q}_V$ in the linearized energy equation

(3.14) [Ullrich et al., 2014a]

$$\hat{q}_V(z,\omega) = \bar{\rho}\bar{u}_z c_p \mathcal{T}(\omega) e^{-\mathrm{i}k_s(z-z_{ref})} \frac{\mathrm{d}}{\mathrm{d}z} F(z). \tag{7.2}$$

In eq. (7.2) z_{ref} indicates the phase reference plane of the entropy wave. The temperature spectrum $\mathcal{T}(\omega) := \mathcal{F}\{T'(t)\}$ is determined by the Fast Fourier Transform (FFT) of the time signal $T'(t)$ and controls the frequency content of the source term. The Fourier transform can be applied on non-periodic time signals [Meyberg and Vachenauer, 1997] such as the single temperature pulse in the EWG case. The source term's spatial dependence in axial direction z is modeled by the forcing function $F(z)$. It is defined in such a way that the spatial axial extension of the electrical source term coincides with the location of the heated wires. As suggested by Leyko et al. [2011] the time-signal of the pulsed temperature excitation with maximum amplitude T'_a is modeled as

$$T'(t) = \begin{cases} T'_a\big(1 - e^{-(t-t_0)/\tau}\big), & t_0 \leq t \leq t_0 + t_p, \\ T'_a e^{-(t-t_0)/\tau}, & t > t_0 + t_p. \end{cases} \tag{7.3}$$

t_0 is the initial time of excitation, t_p is the pulse duration and τ is the time delay. These parameters are specified in tab. 7.1 and are chosen in accordance with the study by Leyko et al. [2011]. The adaption of the LNSE source model (7.2) to the experimental pulse excitation is realized by the temperature spectrum $\mathcal{T}(\omega)$. The modeled time signals of the temperature as well as the corresponding power spectra are shown in fig. 7.1. The temperature spectrum is very similar to that of a rectangular pulse showing several peaks with constantly decreasing amplitude. As later shown the temperature spectrum on the right in fig. 7.1 is the main driver for the resulting acoustic pressure spectrum.

Operating Point	Subsonic Case	Transsonic Case
Temperature amplitude T'_a (K)	13.4	9.1
Initial time of excitation t_0 (s)	0.1	
Time delay τ (s)	0.003	
Pulse duration t_p (s)	0.1	

Table 7.1: Parameters for the modeled entropy excitation signal.

The frequency-domain LNSE simulations are based on the eqs. (3.12)-(3.14), which are solved numerically using the GLS-FEM approach defined by eq. (5.12). The LNSE model is solved in cylindrical coordinates with the simplifying assumption of axis symmetry (i.e. $\hat{u}_\theta = 0, \partial/\partial\theta = 0$). The domain is approximated by an unstructured grid of 47,946 triangular elements with second order Lagrangian shape functions. This results in a linear system of equations with a total number of 393,060 degrees of freedom to be solved.
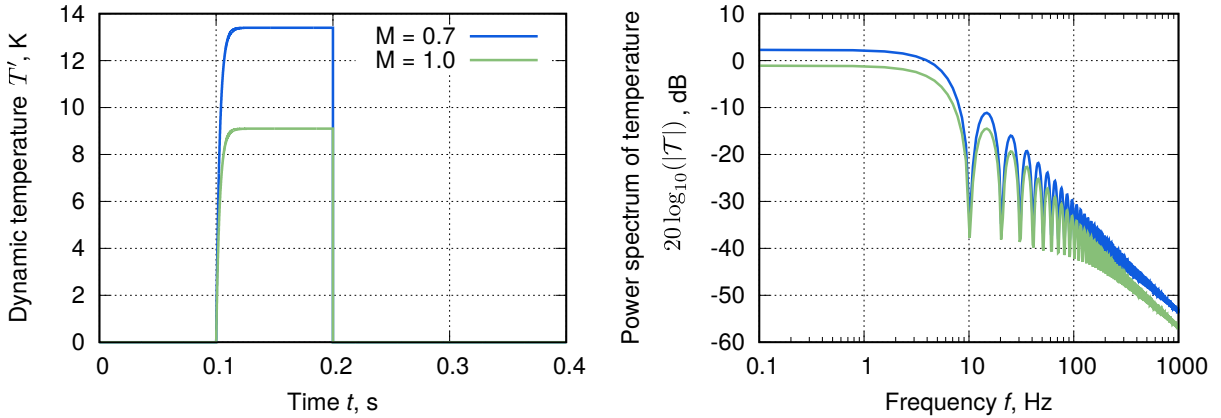
Figure 7.1: Time signal (left) and power spectrum (right), calculated by $20\log_{10}(|\mathcal{F}\{T'(t)\}|)$, [dB], of the entropy wave excitation.

7.1.2 Acoustic Simulations

In the following the measurements by Bake et al. [2009] are compared with the numerical results obtained by the hybrid RANS/LNSE approach. The experimental and numerical pressure spectra are evaluated at the fourth microphone position at $z = 1.1505\,\mathrm{m}$ and are plotted in terms of the sound pressure level (SPL) defined in eq. (5.1). The results are shown for the subsonic and the transsonic case in fig. 7.2. In general good agreement between the experiment and simulation is found for a broad frequency range from $10\,\mathrm{Hz}$ up to $200\,\mathrm{Hz}$, while increasing deviations are observed for higher frequencies. These differences are believed to be related to uncertainties of the outlet boundary condition, which may be not in line with the experiment beyond $200\,\mathrm{Hz}$. Modeling the very thin heated wires by an entropy wave excitation zone may lead to inaccuracies with respect to the shape of the entropy waves. This will result in a different acoustic response as investigated analytically in detail by Howe [2010]. Finally the spectral decay beyond $30\,\mathrm{Hz}$ is slightly overpredicted by the simulation compared to the experiment.

The comparison of the imposed temperature spectra and the resulting acoustic pressure spectra shows that there is a close relation between them. The acoustic spectrum exhibits several peaks at the same frequencies and with the same spectral fall-off around $-30\,\mathrm{dB}$ per decade in comparison to the temperature spectrum on the right in fig. 7.1. This behavior is obtained for the subsonic as well as the transsonic case. The comparison demonstrates that the indirect noise spectrum is controlled by the temperature spectrum of the entropy waves impinging on the nozzle.

In fig. 7.3 the temperature fields $\hat{T}$, corresponding to the entropy waves, and the pressure fields $\hat{p}$ are shown for different frequencies. It can be seen that the entropy waves are convectively transported from the source region into the nozzle. Once the entropy waves reach the nozzle inlet they are stretched as a consequence of the strong flow acceleration.
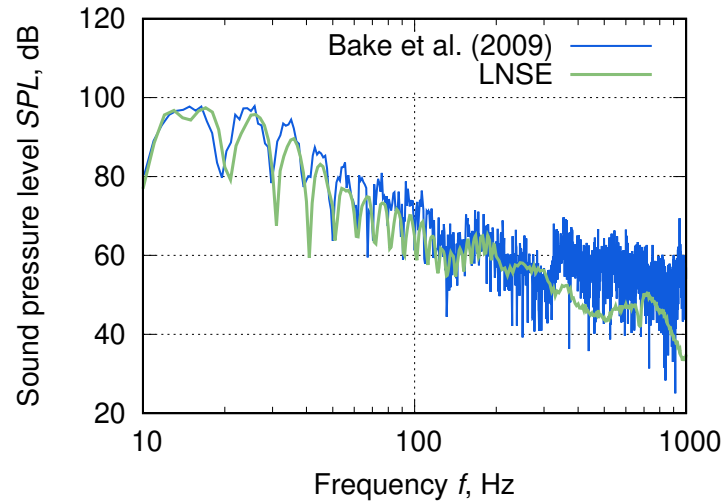
(a)
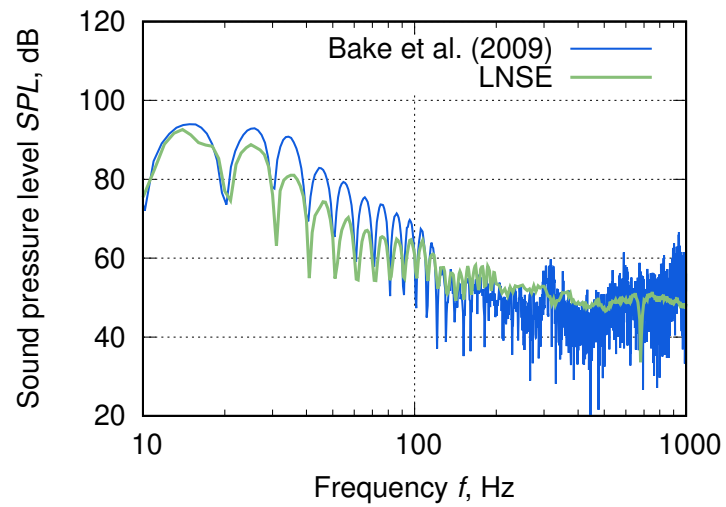
(b)

Figure 7.2: Pressure spectra given in terms of the SPL = $20 \log_{10}(|\hat{p}|/p_{ref})$, [dB] at 7.2(a): subsonic conditions (throat Mach number $\bar{M} = 0.7$), and at 7.2(b): transsonic conditions (throat Mach number $\bar{M} = 1.0$) [Ullrich et al., 2014a].

(a)   200 Hz

(b)   200 Hz

(c)   800 Hz

(d)   800 Hz
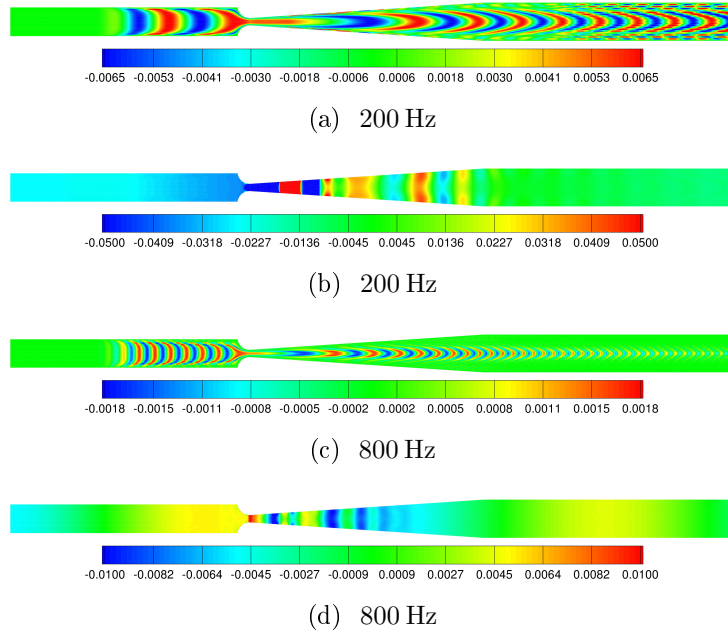
Figure 7.3: Fluctuating temperature $\Re\{\hat{T}\}$, [K] (top) and pressure fields $\Re\{\hat{p}\}$, [Pa] (bottom) at subsonic conditions (throat Mach number $\bar{M} = 0.7$) and at different frequencies [Ullrich et al., 2014a].

In this region strong pressure amplitudes arise, which marks them as indirect noise. The convective transport is reflected in the significantly smaller wave length $\lambda_s = \bar{u}_z/f$ compared to the acoustic waves. Mean flow boundary layers lead to a strong deformation of the entropy waves perpendicular to the flow direction. This dispersion effect causes a significant attenuation of the entropy waves in regions close to the walls. The dispersion effect increases with frequency. In particular at higher frequencies the attenuation of entropy waves due to dissipation already takes place upstream of the nozzle.

The same base flow and geometry but non-reflecting acoustic boundary conditions were used to determine the normalized entropy transmission and reflection coefficients. For this the impedances at the upstream and downstream end were set to $Z = 1$ in eq. (3.33) so the acoustic field would not be overlaid with reflected waves. The LNSE simulations were carried out with a quasi one-dimensional and 2D model to assess the influence of the entropy wave dispersion effect. As shown in fig. 7.4 significant deviations between the 1D and 2D results for the entropy transmission and reflection coefficient underscore the importance of the dispersion effect. The deviations between both models increase with frequency, while similar results are obtained at very low frequencies below 100 Hz. The 2D model delivers considerably lower indirect noise levels as compared to the 1D model. The 2D result indicates an enhanced attenuation of entropy waves before reaching the nozzle, which leads to a smaller release of indirect noise.
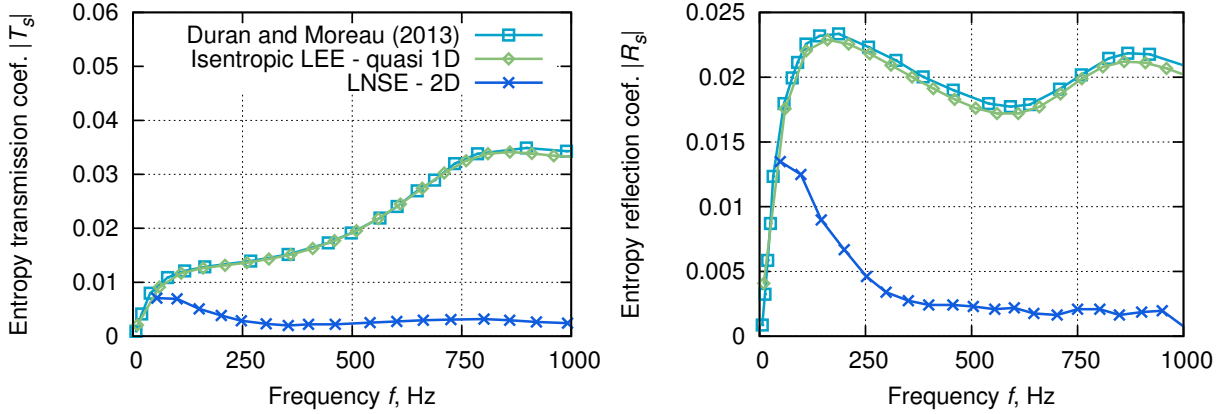
Figure 7.4: Absolute value of the entropy transmission (left) and reflection (right) coefficient at subsonic conditions (throat Mach number $\bar{\mathrm{M}} = 0.7$), comparison between the quasi one-dimensional and two-dimensional model.

7.2 The Vorticity Wave Generator (VWG)

The second case investigates the indirect noise generation by accelerated vorticity waves. The VWG test rig, which slightly differs from the EWG setup, is presented and the simulation model is explained with special emphasis on the source term modeling of vorticity waves. The LNSE model and all acoustic results shown in the following paragraphs are based on the study by Ullrich et al. [2015]. The RANS model and the mean flow simulations are based on the work by Verissimo Caschera [2014]. For brevity the RANS results discussed in detail by Ullrich et al. [2015] are not presented in this section.

7.2.1 Configuration

The VWG nozzle geometry is identical to the EWG nozzle geometry presented above. The inlet and outlet ducts are changed to the lengths of $l_1 = 0.33714\,\mathrm{m}$ and $l_2 = 0.25\,\mathrm{m}$. At the inlet, a constant, non-swirling axial mass flow is imposed. Swirl is induced by four tangential injectors, which are equally distributed over the duct perimeter at the axial location $x = -0.1365\,\mathrm{m}$ with respect to the nozzle throat. To create fluctuations of vorticity the injector mass flow is pulsed with about $10\,\%$ of the mean mass flow rate. The steady and the pulsed flow field are measured in the upstream duct using hot-wire anemometry. The experimental data were provided by DLR [Kings, 2015]. The VWG test rig is sketched in fig. 7.5 and the operating conditions are found in tab. 7.2.

7.2.2 Numerical Setup

The mean flow field is computed using RANS simulations [Verissimo Caschera, 2014]. The geometry is discretized by an unstructured grid consisting of a total number of 1,585,840 cells. In the nozzle and the injector section the mesh is refined to capture the mean
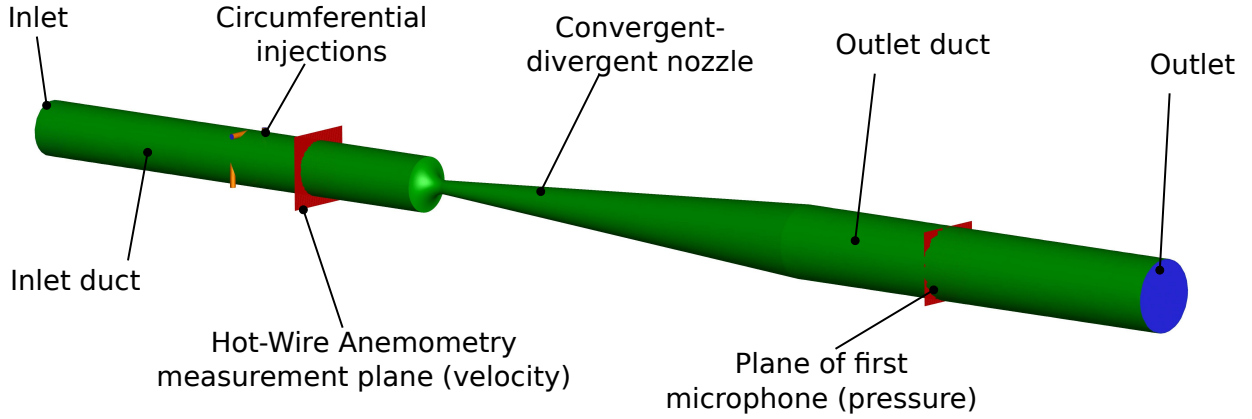
Figure 7.5: Sketch of the Vorticity Wave Generator test rig.

Operating Point	Transsonic Case
Total temperature inlet (K)	296
Main axial mass flow (g/s)	8.88
Steady circumferential mass flow (g/s)	2.77
Pulsed circumferential mass flow (g/s)	0.277
Nozzle throat Mach number (-)	1.0
Static pressure outlet (Pa)	102,200

Table 7.2: Investigated operating point of the VWG test rig.

flow gradients. Turbulence is modeled by means of the Reynolds Stress turbulence Model (RSM). The standard wall functions are applied at the walls, where prism layers are used for discretization. Total temperature and mass flow rates are specified at the inlet of the upstream duct and the circumferential injectors. The ambient pressure is prescribed at the outlet. The specific values are summarized in tab. 7.2.

The acoustic simulations are done with the isentropic formulation of the LNSE (3.12) and (3.13) since entropy wave generation due to viscous dissipation and thermal heat conduction is usually negligible in the low frequency regime. The LNSE are solved in three-dimensional cartesian coordinates with $\boldsymbol{x} = (x, y, z)^T$ for the density $\hat{\rho}$ and velocities $\hat{\boldsymbol{u}} = (\hat{u}, \hat{v}, \hat{w})^T$ using the GLS-FEM approach. A total number of 397,733 linear Lagrangian tetrahedron elements is used to discretize the entire domain, yielding approximately 0.33 million degrees of freedoms to be solved. The inlet and outlet boundary condition are exactly the same as in sec. 7.1 before.

In the experiment, the indirect noise generated by vorticity in the accelerated flow is necessarily overlaid with direct noise caused by the pulsating forcing of the swirler. In the LNSE simulation both contributions may be separated by using two different excitation methods. With the first method vorticity is excited by a fluctuating mass flow boundary condition prescribed on each of the four injectors. Below it is referred to as

"velocity excitation". The resulting pressure spectrum contains contributions from the indirect noise and from the velocity excitation itself. This excitation method corresponds to the experimental setup. In the second method, termed "vorticity excitation", vorticity is excited by means of an azimuthal body force source term, which does not induce acoustic waves. Then the resulting pressure spectrum contains only contributions from the indirect noise. The amplitudes of both excitation methods are constructed to match the frequency spectrum of the velocity signal measured by hot-wire anemometry in the inlet duct at $\boldsymbol{x}_{ex} = (-0.088\,\text{m}, 0.002\,\text{m}, 0)$. The velocity signal $u'_{v,\theta}(t)$ and its frequency spectrum $\mathcal{F}\{u'_{v,\theta}(t)\}(\omega)$ are shown in fig. 7.6. Obviously the measured signal contains a significant level of turbulence. To see the influence of the turbulence the LNSE simulations were therefore carried out for the measured velocity excitation signal and for a modeled velocity time signal removing the random noise:

$$u'_{v,\theta}(t) = \begin{cases} u'_a\left(1 - e^{-(t-t_0)/\tau}\right), & t_0 \leq t \leq t_0 + t_p, \\ u'_a e^{-(t-t_0)/\tau}, & t > t_0 + t_p. \end{cases} \tag{7.4}$$

u'_a quantifies the maximum velocity amplitude. The different parameters in eq. (7.4) were set to match the experimental data yielding: $t_0 = 0.135\,\text{s}, t_p = 0.09\,\text{s}, \tau = 0.08\,\text{s}$ and $u'_a = -3.2\,\text{m/s}$. In fig. 7.6 the measured and modeled time signal and spectrum of the dynamic velocity are compared against each other. It can be seen that the low frequency content up to $100\,\text{Hz}$ of the modeled and measured spectrum is very similar. The middle and higher frequency content of the modeled spectrum is significantly lower than the experimental spectrum as the high-frequency turbulent stochastic noise is removed by the modeled time signal. Further details on the numerical setup are given by Ullrich et al. [2015].
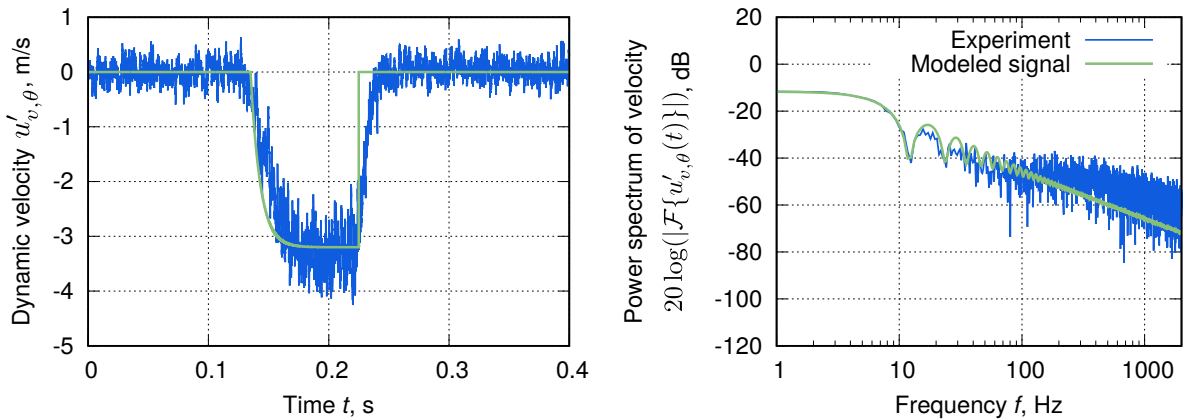
Figure 7.6: Measured and modeled velocity excitation signal in time domain $u'_{v,\theta}(t)$, [m/s] (left), measured at $\boldsymbol{x}_{ex} = (-0.088\,\text{m}, 0.002\,\text{m}, 0)$, and its power spectrum (right), calculated by $20\log(|\mathcal{F}\{u'_{v,\theta}(t)\}|)$, [dB].

7.2.3 Simulation Results

The spectra of acoustic sound pressure level (eq. (5.1)) from the LNSE and the measurements at the first microphone position at $x_m = 0.35\,\text{m}$ are compared in fig. 7.7. The upper part 7.7(a) shows the results based on the measured velocity input signal. The lower part 7.7(b) gives the results of the modeled input signal according to eq. (7.4). The green lines mark the numerical results obtained from the vorticity excitation and the orange lines stand for the simulation results with mass flow / velocity excitation.

The differences between the green and the orange curves in fig. 7.7 show the strong contribution of the direct noise to the spectrum. It can be seen that the measurements are quantitatively reproduced by the numerical simulation with velocity excitation in the low frequency regime up to 150 Hz. The SPL is overestimated by the LNSE simulations in the higher frequency range, while the curve trend is maintained quite well. Therefore the experimental spectrum is captured by the LNSE simulations when applying the velocity excitation method, which corresponds to the experimental setup, where the indirect noise is overlayed by the noise contribution from the injectors. When applying the vorticity excitation method to identify the indirect noise the experimental spectrum is significantly underpredicted above 150 Hz. The result obtained by the vorticity excitation impressively demonstrates that the indirect noise contribution is only relevant in the low frequency range up to 150 Hz. Beyond 150 Hz, the noise induced by the injectors becomes more relevant as the frequency increases. Therefore the middle and high frequency range of the experimental spectrum do not represent the indirect noise due to accelerated vorticity. This frequency range is controlled by the contribution of the noise induced by the injectors and the stochastic turbulent noise. Finally the VWG analysis demonstrated that the LNSE are also capable to capture the indirect noise generation by vorticity.
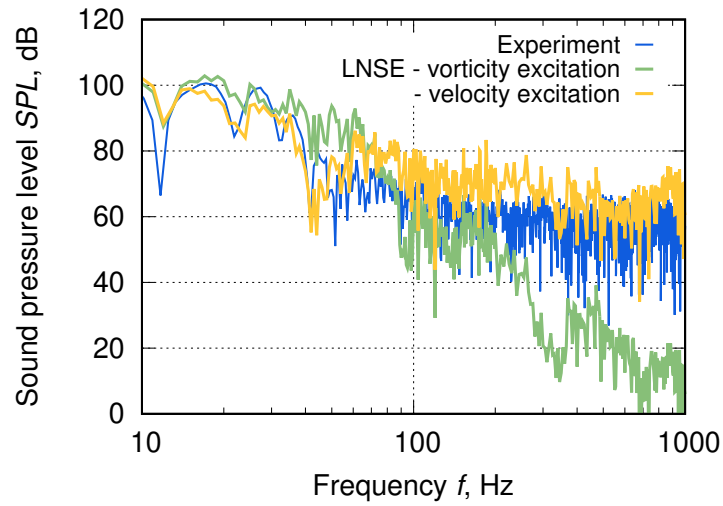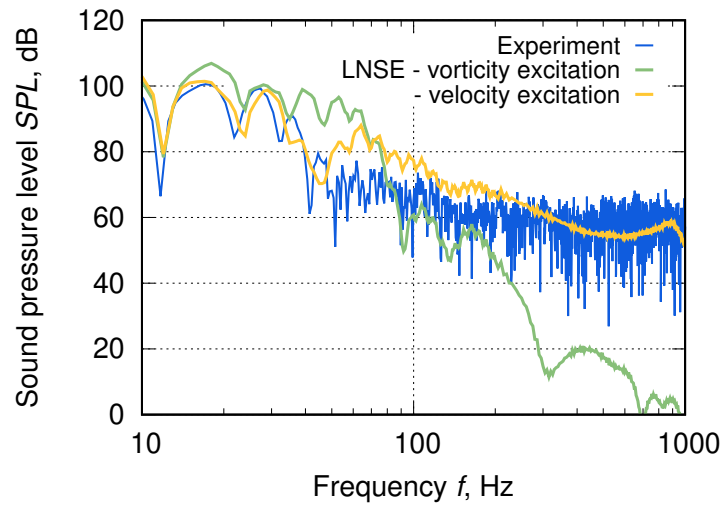
Figure 7.7: Measured and numerically calculated power spectrum of pressure, evaluated at the first microphone position at $x_m = 0.35\,\mathrm{m}$, for two excitation models: 7.7(a): excitation based on measured velocity signal, and 7.7(b): excitation based on modeled velocity signal according to eq. (7.4) [Ullrich et al., 2015].

8   Combustion Noise Generation and Propagation

In this chapter three different generic combustion systems with increasing complexity are presented. The annular model combustor represents the simplest case, which serves to validate the hybrid RANS/LNSE approach by a comparison of the results with those of the LOTAN network solver. The accuracy of the method for separating direct and indirect noise contributions is assessed. Also the impact of the source term model on the ratio between indirect and direct combustion noise is quantified. The second case is the premixed CNRS CESAM-HP combustor. Direct as well as indirect noise generation are examined. The related combustion noise source spectra are determined using different statistical noise models and LES source terms. The last test case deals with the liquid fueled combustor test rig installed at the Lehrstuhl für Thermodynamik at Technische Universität München (TUM). The hybrid approach is applied together with the statistical noise model for non-premixed flames by Jörg [2015] to compute the combustion noise spectrum emitted from a kerosene flame.

8.1 Annular Model Combustor

This section summarizes previous work by Ullrich and Sattelmayer [2015], where further details about the simulation model can be found. The main objectives of the annular model combustor case are twofold:

- First, the strategy for the separation of direct and indirect noise contributions inside of the combustor is validated. This is achieved by a detailed comparison of the numerical results obtained from the LNSE simulations and from the LOTAN solver [Dowling and Mahmoudi, 2015, Stow and Dowling, 2001].

- The second goal is to validate the different source term formulations, proposed in subsec. 4.2.2, with respect to their capability to reproduce the correct entropy wave generation of perfectly premixed and non-premixed flames. Therefore the noise ratio in an annular model combustor is evaluated for both the perfectly-premixed flame model and the conventional non-premixed flame model.

8.1.1 Mean Flow Field

The annular model combustor case was proposed by Dowling and Mahmoudi [2015]. The indirect noise generation in the turbine NGV at the combustor outlet is obtained by a suitable boundary condition representing choked flow conditions. A thin one-dimensional flame of thickness δ_f is fixed at the axial position $x_f = 0.5\,\text{m}$ in the combustor with length $l = 1.0\,\text{m}$, inner radius $r_i = 0.22\,\text{m}$, outer radius $r_o = 0.38\,\text{m}$ and mean radius $r_m = 1/2(r_o + r_i) = 0.3\,\text{m}$. At the combustor inlet a perfect and dry gas with total temperature $\bar{T}_{t1}$, total pressure $\bar{p}_{t1}$ and Mach number $\bar{\text{M}}_1$ is injected. The mean heat release of the flame is controlled by the prescription of the total temperature ratio $\bar{\Theta}_t := \bar{T}_{t2}/\bar{T}_{t1}$. The combustor inlet and outlet quantities are indicated by the subscripts 1 and 2. The local temperature is used to compute the local isobaric heat capacity of the gas [Dowling and Mahmoudi, 2015], i.e. $c_p = 973.60091 + 0.1333T$. The mean flow is assumed to be one-dimensional with axial flow changes in the flame region. In tab. 8.1 the mean flow conditions are summarized, which are representative for take-off operating conditions of a small turbojet engine with low total pressure ratio. The axial development of the mean flow temperature along the center axis is presented in fig. 8.1.

Operating Point	Value
Total inlet temperature (K)	653
Total inlet pressure (bar)	12
Inlet Mach number (-)	0.06
Ideal gas constant (J/kgK)	287
Average isobaric heat capacity (J/kgK)	1147.7
Total temperature ratio (-)	3

Table 8.1: Mean flow conditions of the annular model combustor.
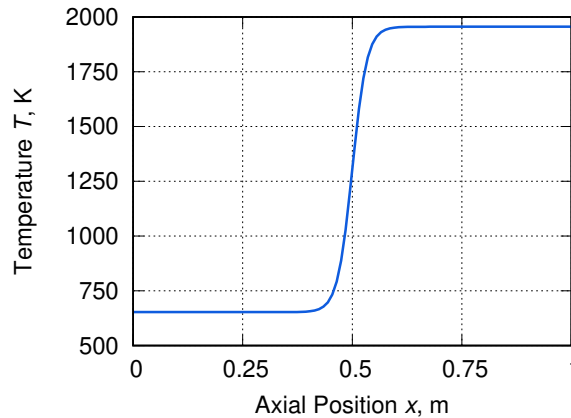
Figure 8.1: Mean temperature in the annular model combustor [Ullrich and Sattelmayer, 2015].

8.1.2 Numerical Setup

In the test case both longitudinal $n = 0$ and circumferential acoustic modes $n \geq 1$ as specified by their mode number n are considered. Longitudinal waves are investigated with a two-dimensional simulation model in cylindrical coordinates $\boldsymbol{x} = (r, \theta, z)^T$ with the assumption of axial symmetry ($\partial/\partial\theta = 0, \hat{u}_\theta = 0$). Higher circumferential modes are solved in a fully three-dimensional model in cartesian coordinates $\boldsymbol{x} = (x, y, z)^T$. While the longitudinal modes can be captured using a simplified one-dimensional model as well, a three-dimensional model is necessary to compute the circumferential modes, where the assumption of axial symmetry does not hold ($\partial/\partial\theta \neq 0$). Depending on the mode number the domain is discretized with 9000 rectangular Lagrangian elements of second order for longitudinal modes or with 70,870 tetrahedral Lagrangian second order elements, which cover the circumferential modes in the three-dimensional domain. The combustor inlet is specified by a non-reflecting boundary condition, which is obtained by imposing $Z = 1$ in eq. (3.33) for longitudinal modes. In the case of circumferential modes, the reduced impedance to be prescribed at the inlet boundary condition (3.33) reads [Evesque et al., 2003, Stow et al., 2002]

$$Z^- = \frac{\omega/\bar{c} - \bar{\text{M}}k^-}{k^-}. \tag{8.1}$$

The axial wave number k^- of the upstream propagating circumferential acoustic wave is determined by

$$k^- = \frac{-\bar{\text{M}}\omega - \sqrt{\omega^2 - \omega_{c,n}^2}}{\bar{c}\left(1 - \bar{\text{M}}^2\right)}, \tag{8.2}$$

where $\omega_{c,n}$ represents the cut-off frequency of the n-th circumferential mode propagating in an infinitely thin annular duct with mean radius r_m [Dowling and Mahmoudi, 2015, Evesque et al., 2003, Lieuwen, 2012]

$$\omega_{c,n} = \left(\frac{n\bar{c}}{r_m}\right)\sqrt{\left(1 - \bar{\text{M}}^2\right)}. \tag{8.3}$$

By setting $S_p = 0$ in eq. (3.39) no entropy waves enter the domain. In summary the combustor inlet is described by the non-reflecting impedance boundary condition (3.33), in which the reduced impedance is either set to $Z = 1$ for longitudinal modes or defined by eq. (8.1) for circumferential modes. Therefore the Mach number $\bar{\text{M}}$ and speed of sound $\bar{c}$ are evaluated at the inlet in the eqs. (8.1) - (8.3). The combustor outlet is modeled as an acoustical compact nozzle, which is defined by the boundary condition (3.42). It is varied in this test case according to the strategy presented in subsec. 5.3.1 in order to isolate the direct noise contribution from the total noise.

To determine the impact of the source model on the noise ratio, the LNSE are either excited by the conventional diffusive flame-type source term $\hat{\dot{\omega}}_z$ in the linearized energy eq.

(4.43), or the volume source term $\hat{s}_V$ in the linearized continuity eq. (4.38) and energy eq. (4.40). Therefore the difference between both source models lies in the additional source term in the linearized continuity equation. Both source terms are distributed around the mean flame position so that the volume source term is calculated by

$$\bar{\rho}\hat{s}_V(x,\theta) = -\frac{3}{2\delta_f}\left[\tanh^2\left(3\frac{x-x_f}{\delta_f}\right) - 1\right]\frac{(\kappa-1)}{\bar{c}^2}\frac{\dot{\mathcal{Q}}}{A}\mathrm{e}^{\mathrm{i}n\theta}. \tag{8.4}$$

Like in the study by Dowling and Mahmoudi [2015], the integral source spectrum $\dot{\mathcal{Q}}$ in eq. (8.4) has a constant value in the covered frequency range.

8.1.3 Noise Ratio

In fig. 8.2 the results of the total, direct and indirect sound predicted by the hybrid method and the LOTAN solver are presented for a given frequency. The pressure amplitudes are evaluated at the combustor outlet and are divided by the total volume-integrated heat release rate. The normalized results are shown in the fig. 8.2 for longitudinal ($n = 0$) and for circumferential waves ($n = 1$). The conventional source model for non-premixed flames is referred to as energy source, while the source model for perfectly premixed flames is labeled volume source in fig. 8.2. It can be seen that the amplitudes calculated by LOTAN and the LNSE method agree very well when using the LNSE energy source. This validates the 1D-hybrid LNSE simulation since LOTAN uses the same set of equations. The effect of a premixed flame source in the LNSE, denoted as volume source, is the strong reduction of entropy waves and therefore the smaller contribution of indirect noise. Ideally the indirect noise would be eliminated as the premixed flame can not produce traveling entropy waves. Therefore the remaining indirect noise obtained in this case marks the degree of imperfection of the LNSE implementation already pointed out in subsec. 4.2.3.

The noise ratio of the indirect to direct noise is plotted in fig. 8.3. Very good agreement is found between the LNSE and LOTAN solutions over the entire frequency range for the longitudinal waves. When using the volume source model the direct noise remains unchanged, whereas the indirect noise is significantly decreased over the entire frequency regime. While there shouldn't be a remaining indirect noise contribution the effect of mean entropy gradients in the flame discussed in subsec. 4.2.3 still produces entropy waves. More precisely the first term $-u_i'\partial\bar{s}/\partial x_i$ in eq. (4.32) is mainly responsible for the unphysical entropy wave generation in case of the volume source model. This is demonstrated by neglecting the mean flow gradients in the LNSE, which leads to vanishing indirect noise over the entire frequency range (see fig. 8.4, square symbols).

In fig. 8.3 it is demonstrated that the indirect noise dominates the direct noise at very low frequencies around $80\,\mathrm{Hz}$ for the energy source model. Following Dowling and Mahmoudi [2015] this can be explained by considering the different characteristic transport velocities of the entropy and acoustic waves. The dominant frequencies of indirect noise $f_i = 2\bar{u}_2/l$

are related to the mean flow convection velocity and the half combustor length resulting in a significant contribution to the low frequency content. Direct noise is associated with the speed of sound leading to much higher eigenfrequencies of about $f_d = \bar{c}_2/l \approx 886\,\text{Hz}$. For this reason the indirect noise exceeds by far the direct noise at low frequencies. Not only the fundamental frequency at $80\,\text{Hz}$ related to the indirect noise is excited, but also several higher harmonics of it with a frequency shift of about $f_i = 2\bar{u}_2/l \approx 180\,\text{Hz}$. As shown in fig. 8.3 the fundamental mode and its higher harmonics cause several peaks in the frequency spectra of the total and indirect noise.

In conclusion the analysis of the annular model test case along with the different source models of sec. 4.2.2 showed that:

- The proposed source terms for perfectly premixed and diffusive flames fulfill the constraints concerning the entropy wave generation.

- The ratio between indirect and direct noise crucially depends on an accurate source model, which accounts for the different physics of premixed and diffusion flames.

- The remaining indirect noise contribution obtained with the volume source model is a spurious effect of the LNSE propagation model but not the source model. Interactions between acoustic waves and mean entropy gradients result in an unphysical entropy wave generation, which should not be present in the idealized model combustor.

- In realistic applications the indirect noise is not only arising from the flame source, but is also related - presumably to a lesser extent - to mean gradients.

- The LNSE results based on the energy source are in excellent agreement with the LOTAN network solver results, which validates the numerical implementation.

- The direct and indirect noise contributions can be practically separated by varying the combustor outlet condition, cf. fig. 5.3.

(a) Total noise

(b) Direct noise
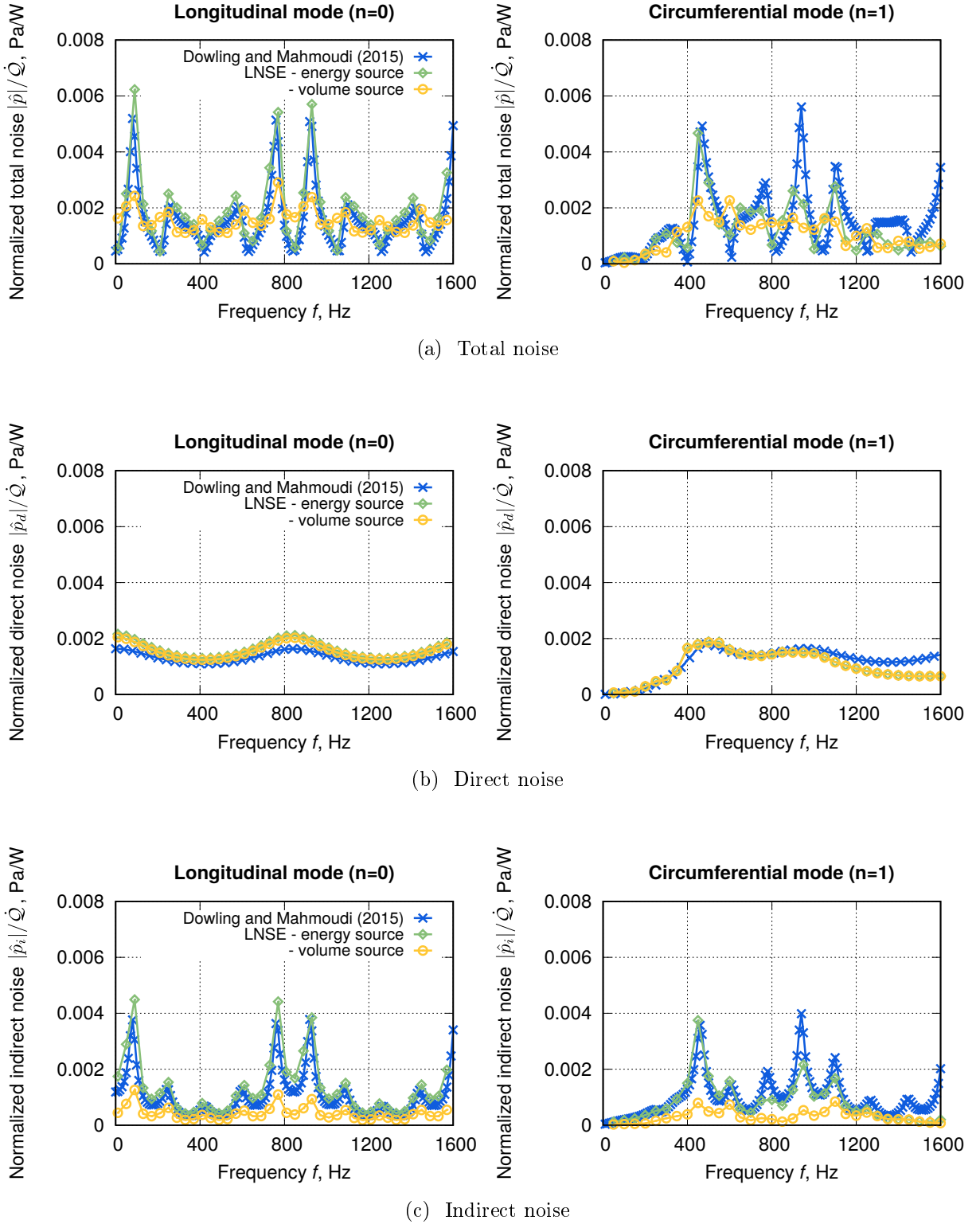
(c) Indirect noise

Figure 8.2: Different noise contributions, normalized by the total heat release rate, of the annular model combustor for longitudinal waves $n = 0$ (left) and circumferential waves with mode number $n = 1$ (right).

Longitudinal mode (n=0)

Circumferential mode (n=1)
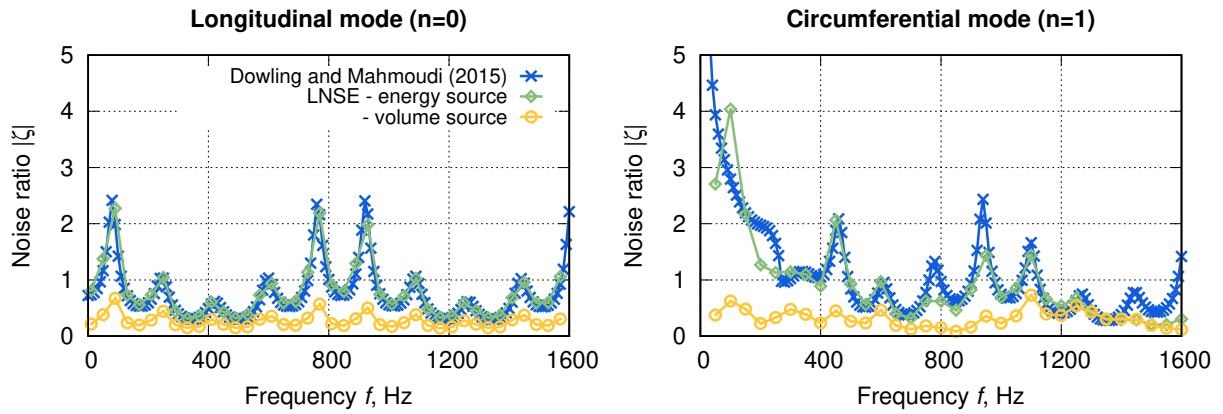
Figure 8.3: Ratio of indirect to direct noise of the annular model combustor for longitudinal waves $n = 0$ (left) and circumferential waves with mode number $n = 1$ (right).

Longitudinal mode (n=0)

Circumferential mode (n=1)
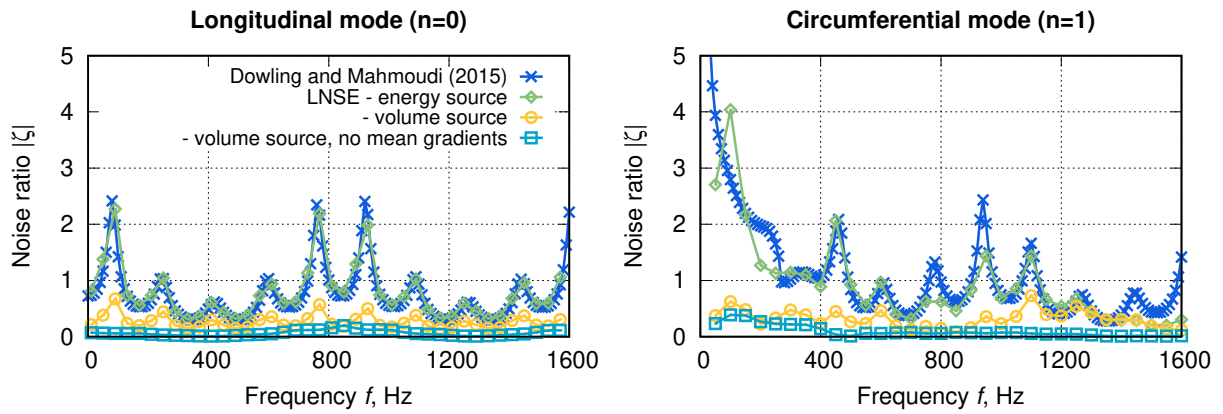
Figure 8.4: Ratio of indirect to direct noise of the annular model combustor for longitudinal waves $n = 0$ (left) and circumferential waves with mode number $n = 1$ (right).

103

8.2 CESAM-HP Combustor

The objective of the second test case was the assessment of the hybrid RANS/ LNSE based combustion noise modeling on the experimental data from the CESAM-HP combustor installed at the EM2C laboratory at the Centre National de la Recherche Scientifique (CNRS). After the description of the test rig, the simulation model both for the mean flow and acoustics are introduced. The direct noise spectrum was calculated with the statistical noise model by Hirsch et al. [2006, 2007] and by Liu et al. [2014]. Also LNSE simulations based on incompressible LES source terms are shown. Finally, non-isentropic LNSE simulations are conducted to include the effect of entropy wave propagation and to predict the indirect combustion noise. The combustion noise at the exhaust nozzle outlet is determined by coupling the three-dimensional combustor simulations to a one-dimensional network model of the exhaust nozzle. The results shown are based on previously presented work by Ullrich et al. [2016].

8.2.1 Configuration and Operating Conditions

The CESAM-HP test rig consists of a square combustion chamber with axial length of $l_c = 0.14\,\mathrm{m}$ and lateral side wall length of $b = 0.07\,\mathrm{m}$ connected to a convergent-divergent exhaust nozzle at the downstream end of the combustor [Mazur et al., 2015b]. A tangential swirler is mounted upstream of the combustion chamber on a straight premixing duct with length of $l_d = 0.1345\,\mathrm{m}$. An adjustable resonator (Impedance Control System (ICS)) is connected to the premixing duct through a perforated plate, which may be purged with air. The vortex dynamics of the swirler can be modified by introducing an air jet in the center of the perforated screen. The CESAM-HP test rig and the different air inlets are sketched in fig. 8.5. The combustor face plate, i.e. the area jump between premixing duct and combustor, defines the point of origin $x = 0\,\mathrm{m}$ in axial direction x for all simulations.

Three different operating points were realized in the tests running non-preheated propane-air flames of 45 kW at an overall equivalence ratio of 0.85 . They are referred to as OP-16-0-2, OP-16-2-0 and OP-13-5-0, where the following nomenclature is used:

`OP-[swirler_mass_flow(g/s)]-[axial_jet_mass_flow(g/s)]-[ICS_mass_flow(g/s)]`.

Details on these operating points are summarized in tab. 8.2. It can be seen that the combustor is operated under lean and pressurized conditions for all three operating points.

8.2.2 Numerical Setup

RANS Simulations

Compressible reactive RANS equations were used with the k-ϵ turbulence model closure. Combustion was modeled by a global reversible one-step finite-rate/Eddy-Dissipation

104
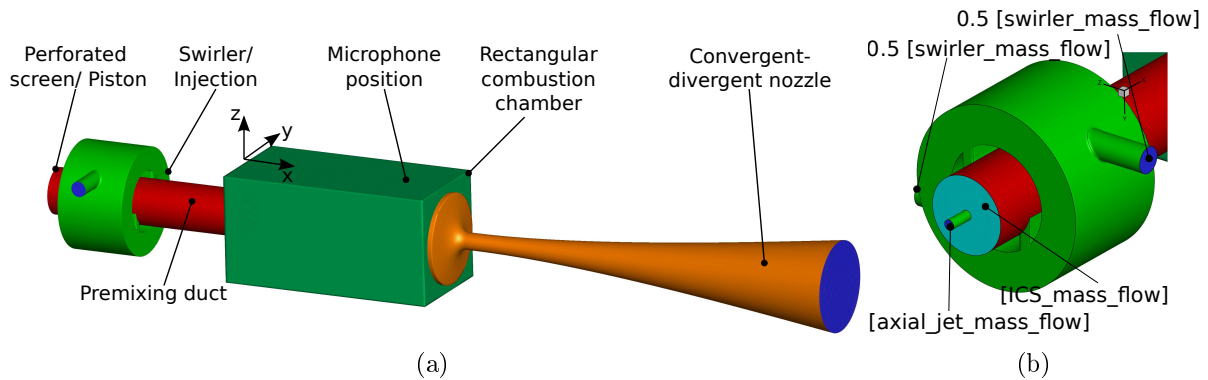
Figure 8.5: Sketches of the (a): CNRS CESAM-HP test rig, and (b): different inlets related to the nomenclature for the different operating points [Ullrich et al., 2016].

Operating Point	OP-16-0-2	OP-16-2-0	OP-13-5-0
Swirler air mass flow (g/s)	16	16	13
Axial ICS air mass flow (g/s)	2	0	0
Axial jet air mass flow (g/s)	0	2	5
Mean static pressure (bar)	2.44	2.43	2.39
Total temperature inlet (K)	296.5		
Total mass flow (g/s)	18		
Swirler fuel mass flow (g/s)	0.983		
Equivalence ratio (-)	0.85		
Thermal power (W)	45,522.46		

Table 8.2: Operating points of the CESAM-HP combustor.

(EDM) model [ANSYS, 2011a] as described in sec. 2.2. Second order upwind discretization schemes were applied for all equations except for turbulence equations, where first order upwind schemes were used. The SIMPLE algorithm was applied to compute the pressure-velocity coupling. The test rig is discretized by a fully structured grid of 1.12 million cells. Mesh-independence of the solution for cold and reacting conditions was insured. As presented in fig. 8.6(b) the simulation was split up into two separate steps: A three-dimensional reactive combustor simulation, which encompasses the combustion chamber, the convergent nozzle section and a small part of the divergent nozzle. This is followed by a quasi two-dimensional, axis-symmetrical and non-reactive simulation of the divergent nozzle section. Both RANS models are connected to each other at the interface plane at $x = 0.173\,\text{m}$, which is located in the divergent nozzle section close to its throat. The simulation strategy explained above was chosen to avoid convergence problems due to the high unsteadiness in the divergent nozzle section.

In the 3D combustor simulation the mass flow rate and total temperature are imposed at the swirler, the perforated screen and the axial air injection. At the nozzle cut plane at

(a)   (b)
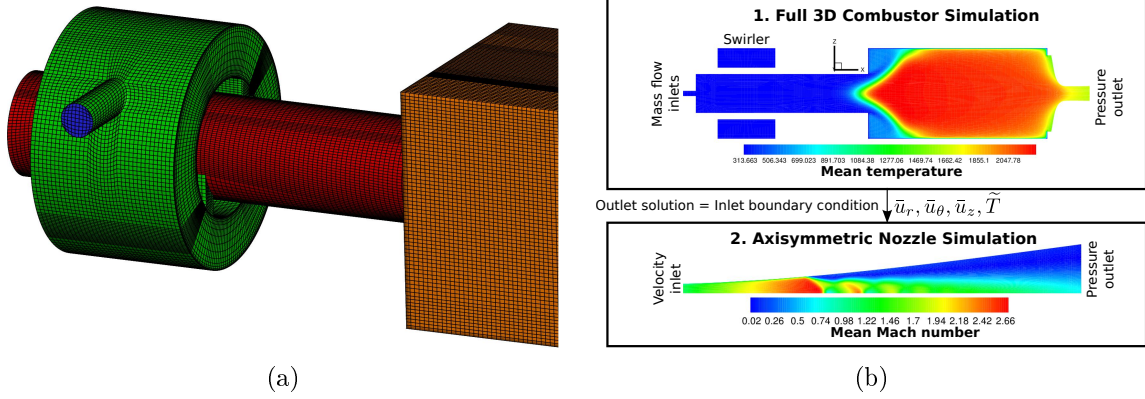
Figure 8.6: (a): Structured mesh of the CNRS CESAM-HP test rig, and (b): solution strategy RANS simulation for reacting flow [Ullrich et al., 2016].

$x = 0.173$ m a static pressure of 1.07721 bar was set to reach transonic conditions. All walls are smooth and adiabatic, but for the cooled combustor walls $\widetilde{T} = 303$ K was assumed. Near wall turbulence was modeled with standard wall functions. From the 3D simulation the velocity components in r, θ, z-direction and the static temperature profile were extracted at the outlet at $x = 0.173$ m. These profiles were then used as inlet conditions for the quasi 2D nozzle simulation. At the nozzle outlet an ambient pressure of 1.01325 bar was imposed.

In order to get a better understanding of the flame characteristics, three additional transport equations for the mixture fraction, its variance, and the temperature variance (4.65) were implemented in form of USER DEFINED FUNCTIONS (UDF) and were solved on the fixed mean flow field from the previous RANS solution. The corresponding additional boundary conditions are specified in tab. 8.3.

Operating Point	OP-16-0-2	OP-16-2-0	OP-13-5-0
Oxygen per fuel (kg O_2/kg F)	3.628447		
Fuel mass fraction (kg F/kg tot)	0.057855		0.070268
Oxygen mass fraction (kg O_2/kg tot)	0.219529		0.216637
Mixture fraction (-)	0.488818		0.540636
Stoichiometric mixture fraction (-)	0.511182		0.459364
Mixture fraction variance (-)	0		
Temperature variance (K^2)	0		

Table 8.3: Parameters and boundary conditions at the swirler inlet for additional transport equations for the reacting flow simulations.

Statistical Noise Model Postprocessor

Different combustion noise models were applied on the RANS results to deliver integral heat release spectra. These are the models for premixed flames by Hirsch et al. [2006, 2007] and by Liu et al. [2014], all of which were introduced in the subsec. 4.3.1. It is important to emphasize that for the current analysis the spectra by Hirsch et al. [2006, 2007] and Liu et al. [2014] are based on the same mean RANS field so the differences between the models directly show in the results.

LNSE Simulations

Similar to the variation of the spectral source models a number of acoustic models were applied to study their influence on the combustion noise spectra. Below the most important acoustic models are presented, while more detailed investigations are given by Ullrich et al. [2016].

All direct noise predictions are based on the isentropic formulation of the LNSE (4.38) - (4.40). Turbulence-acoustic interactions in the combustor and premixing duct are taken into account by the Lighthill stresses in the linearized momentum eq. (4.39). As proposed by Hussain and Reynolds [1972] and Gikadi et al. [2014] they are treated as an additional damping term characterized by the turbulent viscosity, i.e. $\hat{\tau}_{ij,L} := -\eta_t(\partial \hat{u}_i/\partial x_j + \partial \hat{u}_j/\partial x_i - 2/3\delta_{ij}\partial \hat{u}_k/\partial x_k)$. In the study by Gikadi et al. [2014] this approach was theoretically derived and successfully applied. The combustion noise sources are imposed by the volume source term $\hat{s}_V$ in the linearized continuity eq. (4.38) [Ullrich et al., 2016]. The integral heat release source spectra obtained from the statistical noise models are rewritten in terms of integral volume source spectra, which are spatially redistributed according to the mean heat release using eq. (4.81). The isentropic assumption is sufficiently fulfilled in this test case since the flame is almost perfectly-premixed so that entropy fluctuations are negligible. This assumption is justified by recent experimental studies by Kings et al. [2016] and Mazur [2017] as well as the numerical study by Huet et al. [2016]. As explained in sec. 3.3 viscosity can be neglected in the low frequency range implying that all walls are treated by slip boundary conditions defined in eq. (3.37). Due to the very low porosity of 0.05 of the perforated screen it is modeled by the hard wall boundary condition (3.37). In most of the acoustic simulations the nozzle at the combustor outlet is approximated by the simplified BC (3.43) to save computational effort. Its validity was proven by Ullrich et al. [2016] by doing a full simulation including the entire nozzle with a fully reflecting outlet condition (3.41) at its end.

A quasi two-dimensional and a fully three-dimensional model of the combustor were implemented to investigate the influence of the model dimension and to assess options for saving computational resources. In the quasi two-dimensional model the LNSE (4.38) - (4.40) are implemented in cylindrical coordinates $\boldsymbol{x} = (r, \theta, z)^T$ and solved for the unknown variables $\hat{\rho}$ and $\hat{\boldsymbol{u}} = (\hat{u}_r, \hat{u}_\theta, \hat{u}_z)^T$ while assuming axis-symmetry $\partial/\partial\theta = 0$. The domain

is discretized by 5423 quadratic Lagrangian elements, giving a linear system of equations with 44,928 degrees of freedom. Additional modeling approximations are required in the quasi 2D model for the swirler, where the assumption of the axis-symmetry is not valid. A method to represent the swirler in a quasi 2D modeling framework was used as proposed by Weyermann [2010]. The annular cavity of the swirler and the mixing duct were connected by a radial slot. The axial and radial dimensions of this slot are chosen in such a way that the same eigenfrequencies are obtained in the quasi 2D and the 3D case. The quasi 2D LNSE simulation model along with the combustion noise source term distribution is sketched in fig. 8.7 for OP-16-2-0.
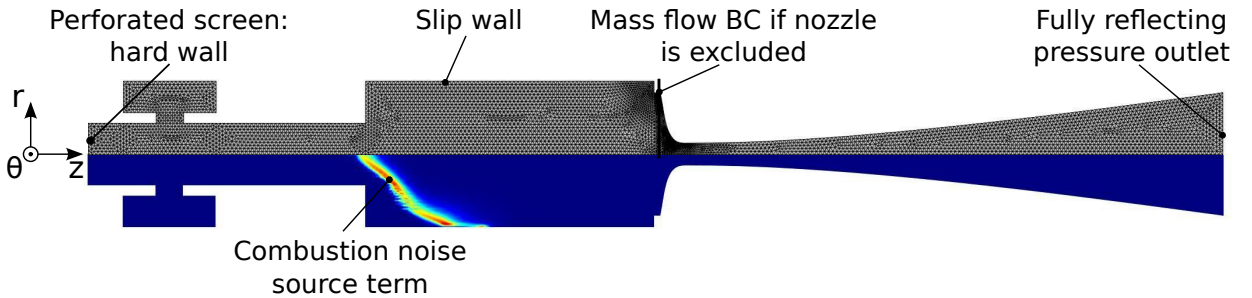
Figure 8.7: Quasi two-dimensional, isentropic acoustic model and mesh of the CNRS CESAM-HP test rig. The plot on the bottom represents the distribution of the combustion noise source term $\bar{\rho}\hat{s}_V$, [kg/(m³s)] calculated by the model by Hirsch et al. [2006, 2007] for the first operating point OP-16-2-0.

In the 3D case the LNSE are solved in cartesian coordinates $\boldsymbol{x} = (x, y, z)^T$ with the dependent variables $\hat{\rho}$ and $\hat{\boldsymbol{u}} = (\hat{u}, \hat{v}, \hat{w})^T$. The domain is discretized using an unstructured mesh with 312,613 linear tetrahedron elements (230,952 dof), which is shown in fig. 8.8. In Ullrich et al. [2018] the influence of the shape function order, iterative solver and mesh resolution on the direct noise was identified by performing additional simulations on a highly refined mesh with roughly 2.7 million dofs and second order Lagrangian shape functions. It was shown that the coarse mesh is already sufficient to predict the direct noise spectrum in the combustor.

The influence of the mean flow field on the acoustic model was further assessed in two ways: One set of LNSE simulations was based on the time averages of LES simulations to see the influence of the turbulence model. Another set eliminated the effect of the aerodynamic mean flow field and flow shearing on the resulting combustion noise spectrum by simulations based on the Helmholtz eq. (3.23). In this case all boundary conditions are kept but they were reformulated in terms of the acoustic pressure according to the eqs. (3.35) and (3.38). The source spectrum of the volume source term was rewritten in form of an equivalent heat release spectrum by means of the relation (4.28).

Predictions of the total combustion noise at the exhaust nozzle outlet were carried out
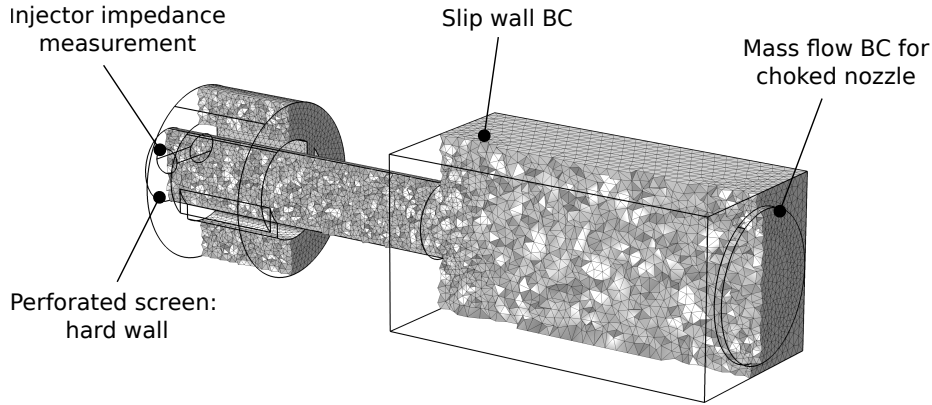
Figure 8.8: Three-dimensional acoustic model and mesh of the CESAM-HP test rig.

by applying the procedure of subsec. 5.3.2. In the first step the nozzle transfer functions were computed. Then combustor simulations based on the non-isentropic formulation of the LNSE (4.38) - (4.40) were done, which included the solution of the energy eq. (4.40) and therefore the propagation of entropy waves. Interactions between the entropy waves and turbulent heat fluxes are incorporated in the model by introducing a turbulent heat conductivity $\lambda_t = \eta_t/\mathrm{Pr}_t$ in the linearized energy eq. (4.40)[1]. The turbulent viscosity is obtained from RANS simulations, while the turbulent Prandtl number is set to $\mathrm{Pr}_t = 0.8$, which is a typical value for most CFD codes. The quasi 2D domain is discretized by a total number of 5088 quadratic Lagrangian elements, yielding 52,785 degrees of freedom (dof) to be solved. The mesh and the simulation model are sketched in fig. 8.9. Since the combustion noise source terms are distributed according to the mean flame shape, the qualitative source term distribution in fig. 8.9 for OP-13-5-0 looks very different from the one shown in fig. 8.7 for OP-16-2-0.

To determine the influence of the source term modeling on the noise ratio, mean flow gradients are neglected in the LNSE (4.38) - (4.40), so that the entropy wave generation is dominated by the source term model. Since the entropy wave dispersion was suppressed by this to a certain extent, the amount of indirect noise caused by the source term generated entropy waves was expected to be overpredicted. All boundary conditions were the same as in the isentropic LNSE model for the direct noise predictions. In the final postprocessing step the acoustic and entropy waves were extracted close to the combustor outlet and were multiplied by the nozzle transfer functions. This delivered the noise contributions related to indirect and direct noise at the exhaust nozzle outlet.

---

[1]This approach is based on the triple-decomposition approach, which yields turbulent heat fluxes of the form $-\partial/\partial x_i[\langle \dot{q}_i'' \rangle - \overline{\dot{q}_i''}]$ in the linearized energy equation eq. (4.18). Similar to the turbulent Lighthill stresses [Hussain and Reynolds, 1970] these heat fluxes $\dot{q}_i'' = -\lambda(\partial T''/\partial x_i)$ may be interpreted as an additional heat conduction term acting on the entropy waves, i.e. postulating $\dot{q}_i'' = -\lambda_t(\partial T'/\partial x_i)$.
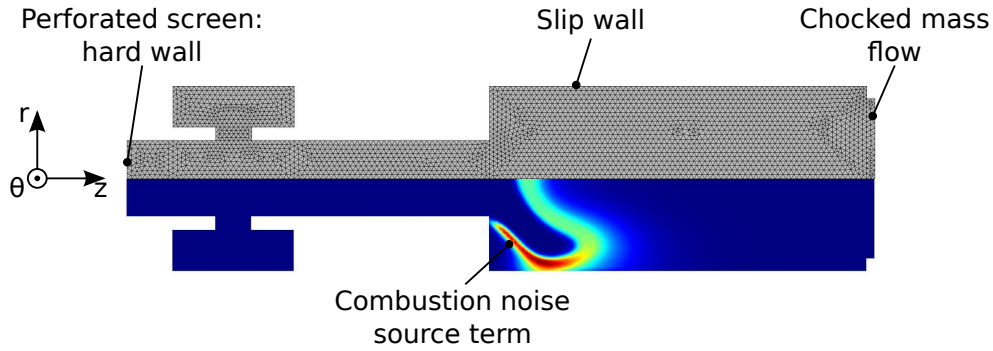
Figure 8.9: Quasi two-dimensional, non-isentropic acoustic model and mesh of the CNRS CESAM-HP test rig. The plot on the bottom represents the distribution of the combustion noise source term $\bar{\rho}\hat{s}_V$, [kg/(m^{3}s)] calculated by the model by Hirsch et al. [2006, 2007] for the last operating point OP-13-5-0.

8.2.3 Mean Flow Simulations

The mean axial velocity and mean temperature distribution obtained from the RANS simulations are shown in fig. 8.10 for the combustor (x, y)-center plane. The flow pattern is symmetrical with respect to the centerline axis for the first operating point OP-16-0-2, which has only purge air flow through the ICS. With increasing jet flow from the centered nozzle an asymmetrical pattern develops at OP-16-0-2 and increases for OP-13-5-0, where it affects the shape of the combustion zone.

The RANS results are compared quantitatively to the particle-image velocimetry (PIV) measurements provided by CNRS [Kings et al., 2015, Mazur et al., 2015a] in fig. 8.11 for the mean velocities and in fig. 8.12 for the turbulence velocities obtained at OP-16-0-2 and in figs. 8.13 and 8.14 for OP-13-5-0. For comparison with the PIV measurements of the rms-velocities, the turbulent kinetic energy k from the RANS results was post-processed by evaluating

$$u'_{\mathrm{rms}} = \sqrt{\frac{2}{3}k}, \tag{8.5}$$

which implies isotropic turbulence. As later shown for the interpretation of the comparison between simulated and measured combustion noise spectra, the influence of the turbulent length and time scales is dominant when using the spectral combustion noise models. Therefore it would be desirable to have a direct comparison of them from simulation and experiment. Since turbulent length scales were not provided by CNRS [Kings et al., 2015, Mazur et al., 2015a] they are estimated following the derivation by Hirsch [2018]. The estimation for the turbulent length and time scale is based on the k-ϵ theory in conjunction with the assumption of equilibrium shear layers, where the turbulent production P_k equals the turbulent dissipation $\rho\epsilon$, i.e. $P_k = -\langle\rho\rangle\widetilde{u''_i u''_j}\partial\widetilde{u}_i/\partial x_j = \rho\epsilon$. Inserting the Boussinesq approach (2.17) and the turbulent viscosity (2.18) into the equilibrium assumption and

OP-16-0-2

(a) Mean axial velocity [m/s]

(b) Mean temperature [K]

OP-16-2-0

(c) Mean axial velocity [m/s]

(d) Mean temperature [K]

OP-13-5-0

(e) Mean axial velocity [m/s]

(f) Mean temperature [K]
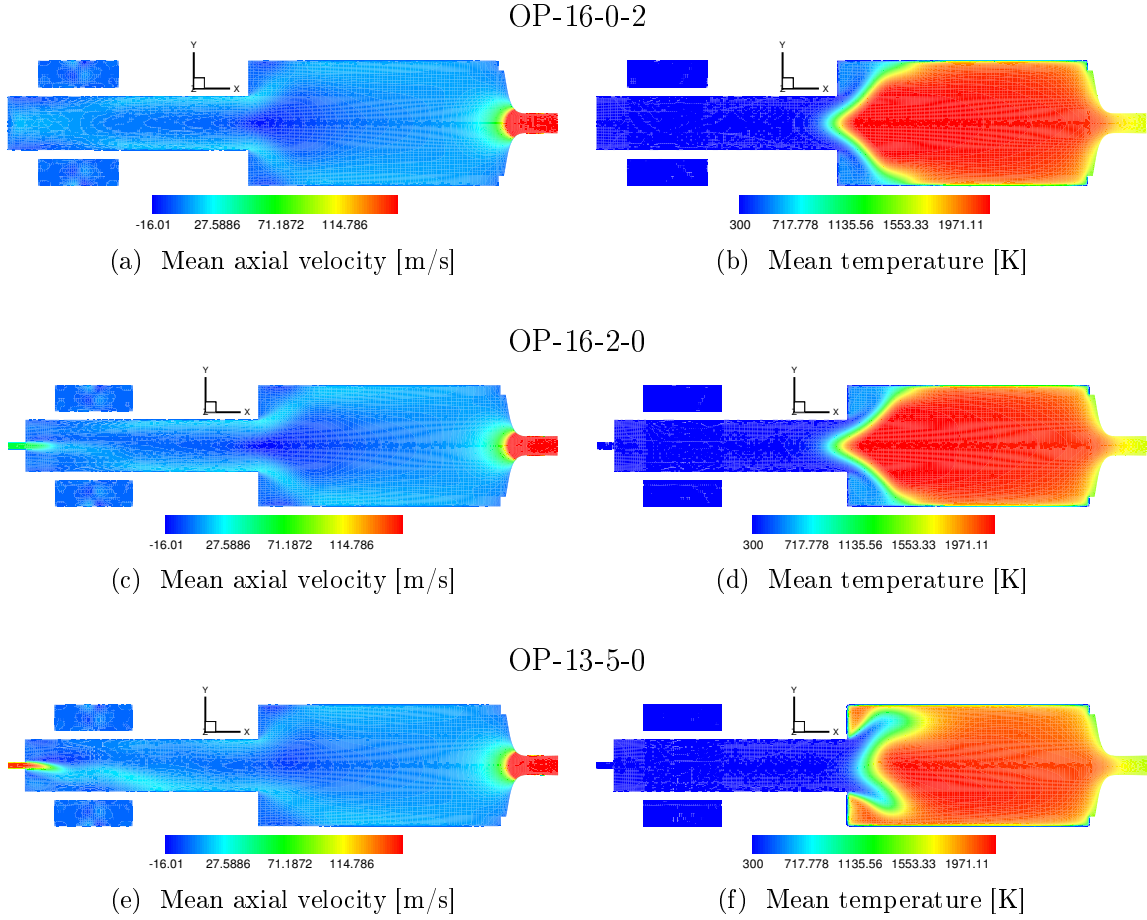
Figure 8.10: Distribution of the mean axial velocity $\widetilde{u}$, [m/s] (left) and mean temperature $\widetilde{T}$, [K] (right) in the (x,y)-center plane.

expressing the turbulent kinetic energy $k = 3/2u_{\mathrm{rms}}'^2$ and dissipation $\epsilon = u_{\mathrm{rms}}'^3/l_t$ in terms of the rms-velocity yields for the turbulent length and time scale [Hirsch, 2018]:

$$l_t = c_{lt}\frac{u_{\mathrm{rms}}'}{|\partial\bar{\boldsymbol{u}}/\partial\boldsymbol{x}|}, \tag{8.6}$$

$$\tau_t = c_{lt}\frac{1}{|\partial\bar{\boldsymbol{u}}/\partial\boldsymbol{x}|}. \tag{8.7}$$

Then the turbulent length and time scale are connected by the relation $\tau_t = l_t/u_{\mathrm{rms}}'$. In the eqs. (8.6) and (8.7) the constant of proportionality $c_{lt} = 4/(9c_\mu) \approx 4.94$ was introduced. Applying the same length scale estimation for both the experimental and the RANS data the ratios of the turbulent length and time scales between experiment and simulation are estimated below. Based on the turbulent length and time scale ratios together with the scaling $f_p \sim 1/\tau_t$ and $P_a(f) \sim (f\tau_t)^{-2} \cdot u'^7|\partial\bar{\boldsymbol{u}}/\partial\boldsymbol{x}|^{-5}$, the ratio between the simulated and experimental peak frequency, the acoustic power and the spectral fall-off can be estimated

as [Hirsch, 2018]

$$\frac{(f_p)_{\text{RANS}}}{(f_p)_{\text{exp}}} = \frac{(\tau_t)_{\text{exp}}}{(\tau_t)_{\text{RANS}}}, \tag{8.8}$$

$$\frac{(P_a)_{\text{RANS}}}{(P_a)_{\text{exp}}} = \left(\frac{(u'_{\text{rms}})_{\text{RANS}}}{(u'_{\text{rms}})_{\text{exp}}}\right)^7 \cdot \left(\frac{(\partial\bar{u}/\partial y)_{\text{exp}}}{(\partial\bar{u}/\partial y)_{\text{RANS}}}\right)^5, \tag{8.9}$$

$$\frac{(\text{dSPL}/\text{d}f)_{\text{RANS}}}{(\text{dSPL}/\text{d}f)_{\text{exp}}} = \frac{(f_p)_{\text{exp}}}{(f_p)_{\text{RANS}}} = \frac{(\tau_t)_{\text{RANS}}}{(\tau_t)_{\text{exp}}}. \tag{8.10}$$

These scaling rules provide a good basis for the interpretation of the spectral comparison, which is given later in subsec. 8.2.5.

In general the mean axial velocities are not correctly predicted by the RANS simulation in the core region and the annular jet, cf. fig. 8.11. The agreement between the simulation and experiment is far better for the radial velocities. The deviations observed between the RANS and PIV results increase in downstream direction. In conclusion the RANS is not capable to accurately predict the axial velocities in the core of the inner recirculation zone. The rms-velocities shown in fig. 8.12 are overpredicted by the RANS in the inner core region, while the rms-velocities in the jet are underestimated in comparison to the experiment. The differences between the rms-velocities obtained from RANS simulations and PIV measurements are even larger for the operating point OP-13-5-0 but the mean profiles match reasonably well, cf. figs. 8.13 and 8.14. This operating condition results in the highest broadband noise levels which is directly linked to the highest rms-values. The large deviations between the RANS results and PIV measurements are most probably to be explained by the high unsteadiness of the flow in the combustor, which cannot be captured by steady RANS simulations. These deviations directly affect the accuracy of the combustion noise source spectra, which in turn influence the quality of the final acoustic results, which is estimated in the subsequent paragraph.

To estimate the turbulent length and time scales, the rms-values and mean flow gradients are compared with each other. In the shear layer region $10\,\text{mm} \leq r \leq 15\,\text{mm}$, where the reaction takes place in fig. 8.11, the gradient of the experimental mean velocity profile is approximately twice that of the RANS simulation, i.e. $(\partial\bar{u}/\partial y)_{\text{RANS}}/(\partial\bar{u}/\partial y)_{\text{exp}} \approx 0.5$. In fig. 8.12 the simulated rms-velocity is approximately $75\,\%$ of the experimental values so that $(u'_{\text{rms}})_{\text{RANS}}/(u'_{\text{rms}})_{\text{exp}} \approx 0.75$. According to the eqs. (8.6) and (8.7) this delivers $(l_t)_{\text{RANS}}/(l_t)_{\text{exp}} \approx 1.0$ and $(\tau_t)_{\text{RANS}}/(\tau_t)_{\text{exp}} \approx 2.0$ for the ratios of the length and time scales between the simulation and experiment in case of operating point OP-16-0-2 [Hirsch, 2018]. Concerning OP-13-5-0 the gradient values of the mean axial velocity in the shear layer region $7\,\text{mm} \leq r \leq 15\,\text{mm}$ in fig. 8.13 are approximately the same as in the RANS simulation $(\partial\bar{u}/\partial y)_{\text{RANS}}/(\partial\bar{u}/\partial y)_{\text{exp}} \approx 1$. The mean level of the simulated turbulence intensity in this zone in fig. 8.14 is approximately 0.56 of the experimental value $(u'_{\text{rms}})_{\text{RANS}}/(u'_{\text{rms}})_{\text{exp}} \approx 0.56$. Then the ratios of the length and time scales between the experiment and simulation for OP-13-5-0 are $(l_t)_{\text{RANS}}/(l_t)_{\text{exp}} \approx 0.56$ and
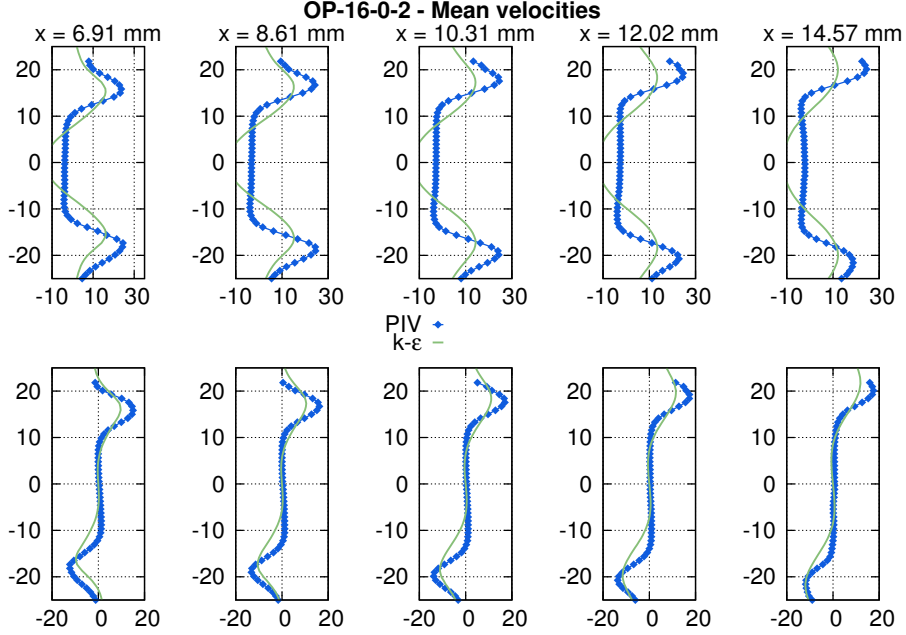
Figure 8.11: Reacting Flow OP-16-0-2: Comparison PIV and RANS results in several axial evaluation planes. Top: mean axial velocity $\widetilde{u}$, [m/s], bottom: mean radial velocity $\widetilde{v}$, [m/s].

$(\tau_t)_{\mathrm{RANS}}/(\tau_t)_{\mathrm{exp}} \approx 1.0$. The ratios for OP-16-2-0 and the other operating points are summarized in tab. 8.4.

The ratios of the length and time scales between the experiment and simulation are used to estimate the deviation between the predicted and measured peak frequency, peak amplitude and spectral fall-off according to the eqs. (8.8) - (8.10). For operating point OP-16-0-2 the evaluation of eq. (8.8) delivers a ratio of the peak frequencies of $(f_p)_{\mathrm{RANS}}/(f_p)_{\mathrm{exp}} = 0.5$, implying an underprediction of the peak frequency by the LNSE. The estimation based on eq. (8.9) yields an approximately 6 dB higher peak amplitude of the simulation in comparison to the experiment. Using eq. (8.10) the predicted spectral decay is twice as the experiment. For OP-13-5-0 the evaluation of the eqs. (8.8) - (8.10) yields the following ratios between the simulation and experiment: $(f_p)_{\mathrm{RANS}}/(f_p)_{\mathrm{exp}} = 1.0$, $(P_a)_{\mathrm{RANS}}/(P_a)_{\mathrm{exp}} = -17\,\mathrm{dB}$, $(\mathrm{dSPL}/\mathrm{d}f)_{\mathrm{RANS}}/(\mathrm{dSPL}/\mathrm{d}f)_{\mathrm{exp}} = 1.0$. In this case the deficiency of the simulated turbulence data results in a length scale, which is about 0.5 that of the experiment. As the simulated turbulence intensity is also about 50 % of the experimental value, the characteristic time scale and with it the predicted peak frequency and spectral fall-off are expected to fit the experimental data. Due to the erroneous rms-prediction a significant underprediction of the acoustic amplitudes is expected. The ratios of the peak frequency, acoustic power and spectral decay of operating point OP-16-2-0 are not explicitly given here. They are summarized in tab. 8.4 together with the data for the other two operating points. In subsec. 8.2.5 these estimations are compared to the real values obtained from the LNSE
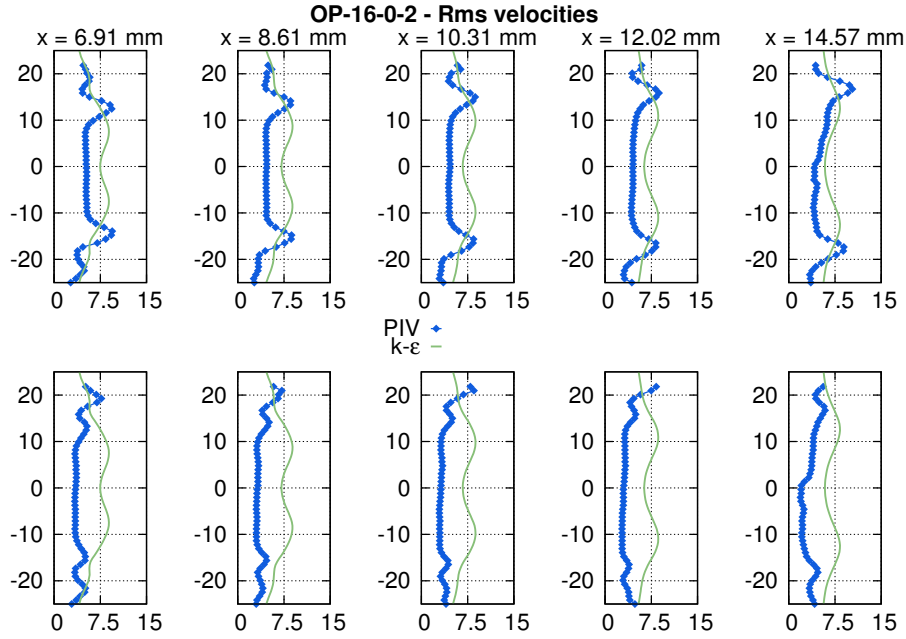
Figure 8.12: Reacting Flow OP-16-0-2. Turbulence Statistics: Comparison PIV and RANS results in several axial evaluation planes. Top: axial rms-velocity u'_{rms}, [m/s], bottom: radial rms-velocity v'_{rms}, [m/s].

simulations and measurements.

Finally, the variances of the temperature and mixture fraction are analyzed for the operating point OP-13-5-0. As shown in fig. 8.15(b) significant temperature variations are observed in the core region of the flame. This indicates a strong axial fluctuation of the flamefront, since the mixture fraction fluctuations are zero there, cf. 8.15(d). Mixture fraction fluctuations are seen in the swirler region in the premixing duct and quickly disappear further downstream before reaching the flame. This finding confirms that the considered flame behaves like an almost perfectly premixed flame regardless of the additional air injection of the axial center jet. This implies that entropy waves should not be present in the combustor downstream of the flame. The comparison between the mean temperature variance and mean mixture fraction variance revealed that temperature variations are no suitable criterion to distinguish between perfectly premixed and non-premixed flames as they are present in both cases. The analysis of the mixture fraction and its variance also provided support for the idea to define the source term $\hat{\dot{\omega}}_z$ of non-premixed flames as a function of the mean mixture fraction variance as proposed in eq. (4.70) in the present thesis.
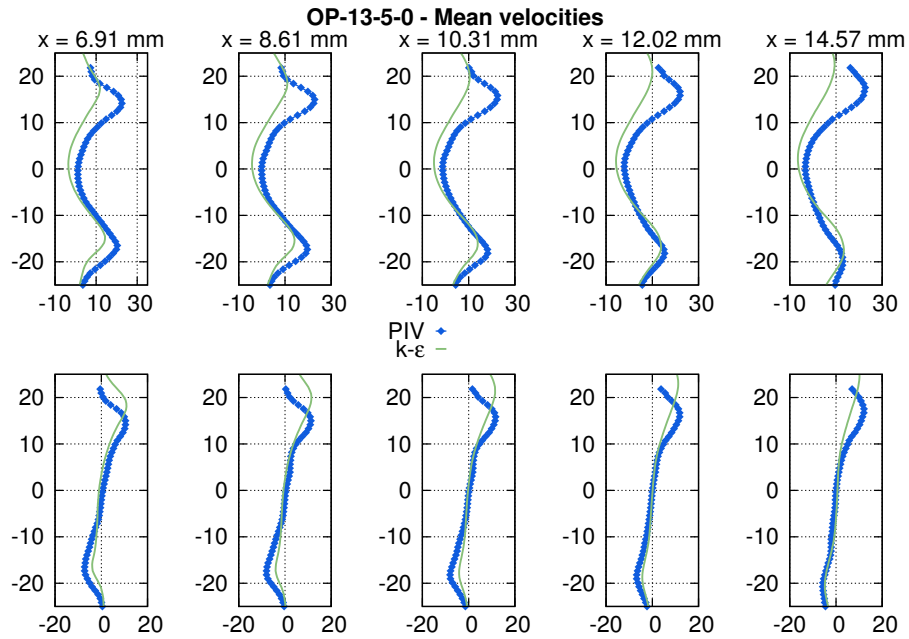
Figure 8.13: Reacting Flow OP-13-5-0: Comparison PIV and RANS results in several axial evaluation planes. Top: mean axial velocity $\widetilde{u}$, [m/s], bottom: mean radial velocity $\widetilde{v}$, [m/s].
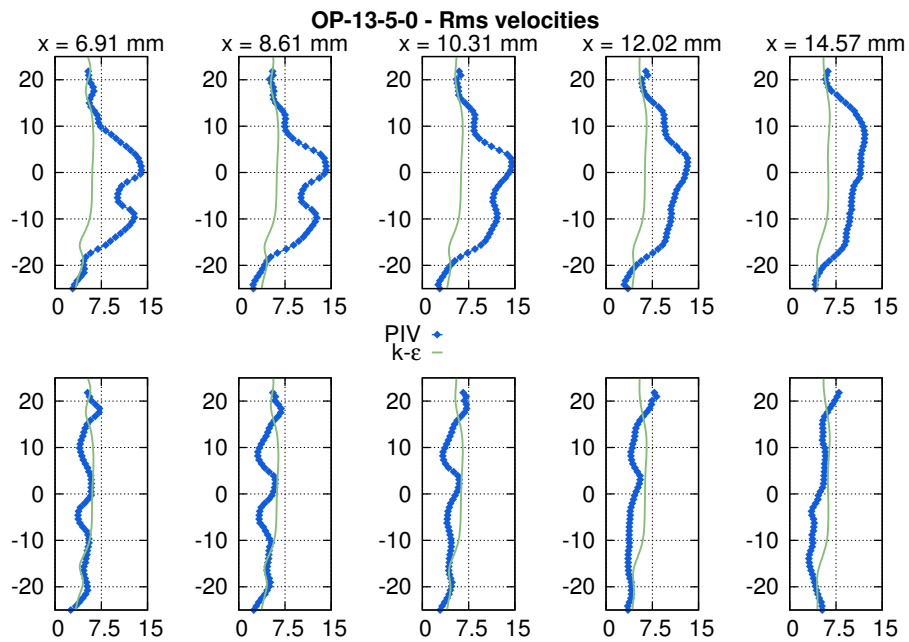
Figure 8.14: Reacting Flow OP-13-5-0. Turbulence Statistics: Comparison PIV and RANS results in several axial evaluation planes. Top: axial rms-velocity u'_{rms}, [m/s], bottom: radial rms-velocity v'_{rms}, [m/s].

Ratio Simulation/Experiment	OP-16-0-2	OP-16-2-0	OP-13-5-0
Mean velocity gradient $\frac{(\partial \bar{u}/\partial y)_{\mathrm{RANS}}}{(\partial \bar{u}/\partial y)_{\mathrm{exp}}}$ (-)	0.5	0.5	1.0
Rms-velocity $\frac{(u'_{\mathrm{rms}})_{\mathrm{RANS}}}{(u'_{\mathrm{rms}})_{\mathrm{exp}}}$ (-)	0.75	1.0	0.56
Turbulent time scale $\frac{(\tau_t)_{\mathrm{RANS}}}{(\tau_t)_{\mathrm{exp}}}$ (-)	2.0	2.0	1.0
Turbulent length scale $\frac{(l_t)_{\mathrm{RANS}}}{(l_t)_{\mathrm{exp}}}$ (-)	1.5	2.0	0.56
Peak frequency $\frac{(f_p)_{\mathrm{RANS}}}{(f_p)_{\mathrm{exp}}}$ (-)	0.5	0.5	1.0
Acoustic power $\frac{(P_a)_{\mathrm{RANS}}}{(P_a)_{\mathrm{exp}}}$ (dB)	6.9	5.5	-17.6
Spectral fall-off $\frac{(\mathrm{dSPL}/\mathrm{d}f)_{\mathrm{RANS}}}{(\mathrm{dSPL}/\mathrm{d}f)_{\mathrm{exp}}}$ (-)	2.0	2.0	1.0

Table 8.4: Estimation of turbulent length scale, time scale as well as the peak frequency, peak amplitude and spectral decay based on the rms-velocity and mean velocity gradient.

(a) Mean temperature [K]

(b) Mean temperature variance [K^2]

(c) Mean mixture fraction [-]

(d) Mean mixture fraction variance [-]
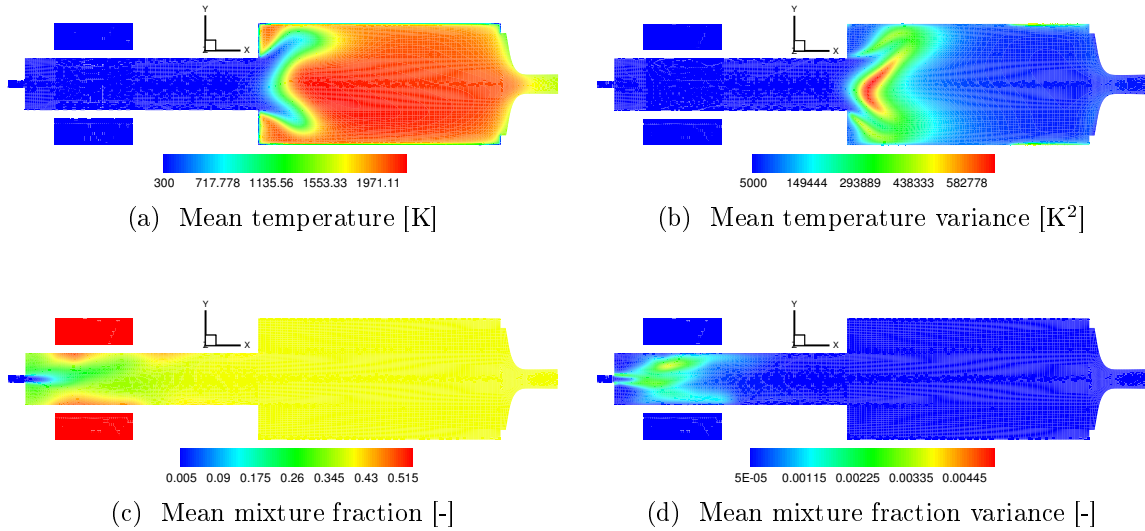
Figure 8.15: OP-13-5-0: Distribution of the mean temperature $\widetilde{T}$, [K], and its variance $\widetilde{T''^2}$, [K^2], on the left column. The right column shows the mean mixture fraction $\widetilde{z}$ and its variance $\widetilde{z''^2}$ in the (x, y)-center plane.

8.2.4 Combustion Noise Source Spectra

The postprocessing of the RANS simulations using the statistical noise model by Hirsch et al. [2006, 2007] delivers integral heat release spectra as shown in fig. 8.16(a). It can be seen that the model by Hirsch et al. [2006, 2007] predicts similar peak frequencies of the fluctuating heat release spectra, which are between 110 Hz and 130 Hz for the three different operating points. The highest peak amplitudes of the source spectrum are obtained for the operating point OP-13-5-0, which is in line with the rms-values predicted by the RANS. The spectral decay rates of the different operating points converge towards each other and are equal beyond 400 Hz.

In the following modifications to the statistical noise model by Hirsch et al. [2006, 2007] are introduced in order to estimate how the noise model would perform if it was based on more accurate RANS predictions. As shown above the steady RANS cannot fully capture the highly unsteady behavior of the flow in the CESAM-HP combustor, which is reflected in an underprediction of the rms-values in particular for operating point OP-13-5-0, cf. fig. 8.14. Among others the lower turbulence intensity results in lower amplitudes of the heat release source spectra and so of the combustion noise spectra. As already indicated in subsec. 8.2.3 using the estimations (8.8) - (8.10) and as shown in the next subsection, these deficiencies in the simulation of the underlying turbulence will result in deviations of the acoustic spectra obtained from LNSE and experiment. These deviations are especially relevant for OP-13-5-0. The quality of the combustion noise source spectra and the resulting acoustic spectra significantly depends on the quality of the turbulence quantities obtained from RANS. To show this the model constants of operating point OP-13-5-0 were modified as explained in the following to compensate the errors of the RANS mean flow simulation. The ratios of the predicted and experimental turbulence intensities and turbulent length scales are $(u'_\mathrm{rms})_\mathrm{RANS}/(u'_\mathrm{rms})_\mathrm{exp} \approx 0.5$ and $(l_t)_\mathrm{RANS}/(l_t)_\mathrm{exp} \approx 0.5$. As demonstrated by Jörg [2015] the peak frequency of the combustion noise spectrum scales with $f_p \sim c_\tau/\tau_t = (c_\tau/c_l)(u'_\mathrm{rms}/l_t)$. Then the ratio between the simulated and experimental peak frequency becomes $(f_p)_\mathrm{RANS}/(f_p)_\mathrm{exp} = (c_\tau/c_l) \cdot [(u'_\mathrm{rms})_\mathrm{RANS}/(u'_\mathrm{rms})_\mathrm{exp}] \cdot [(l_t)_\mathrm{exp}/(l_t)_\mathrm{RANS}]$. The requirement $(l_t)_\mathrm{RANS} = (l_t)_\mathrm{exp}$ yields for the modified length scale constant $c_l^* = 2c_l$ to compensate the erroneous RANS length scale prediction. Equal peak frequencies $(f_p)_\mathrm{RANS} = (f_p)_\mathrm{exp}$ are realized by the modified constant for the turbulent time scale $c_\tau^* = 1/2c_\tau$. The integrated spectrum obtained from these modified constants with $c_l^* = 1.0$ and $c_\tau^* = 0.25$ is plotted in fig. 8.16(b) and is referred to as "modified constants". In this figure the heat release spectrum obtained form the "standard-constants" is based on the constants as introduced by Hirsch et al. [2006, 2007] in subsec. 4.3.1. The modification of the scaling constants results in an increase of the turbulent Damköhler number by a factor of approximately 8.

Finally the RANS data was postprocessed at the University of Cambridge (UCAM) with the model by Liu et al. [2014] who kindly provided the integral heat release spectrum plotted in fig. 8.17. The Liu et al. [2014] model delivers higher peak frequencies, higher peak amplitudes and a smaller spectral decay rate compared with the model by Hirsch et al.
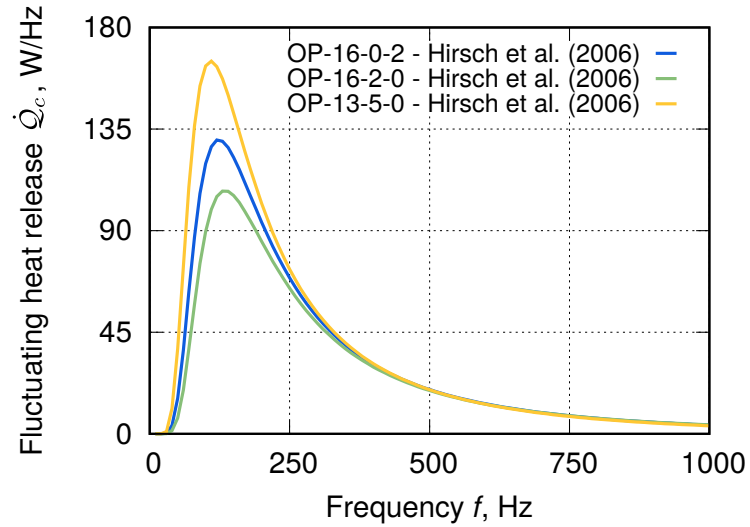
(a) All operating points
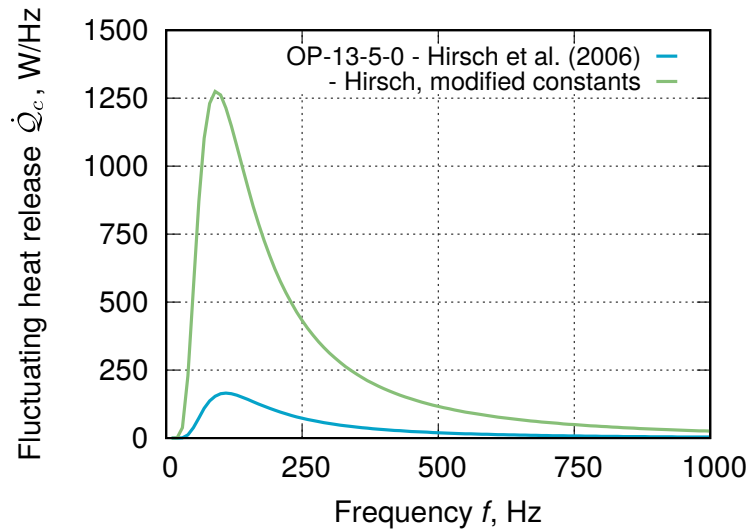
(b) OP-13-5-0

Figure 8.16: Spectra of fluctuating heat release $\dot{\mathcal{Q}}_c(f)$, [W/Hz] associated with the combustion noise for all three operating points, obtained from the statistical noise models by Hirsch et al. [2006, 2007].

[2006, 2007]. The model by Liu et al. [2014] deviates from the Hirsch et al. [2006, 2007] model by a prefactor $\rho_0 Y_{f,0} H_l c_d(\epsilon/k)$ as defined in eq. (4.66). Although the additional factor ϵ/k does not contain an explicit dependence on frequency, regions of high turbulent shear are weighted much stronger. As a consequence the modified model by Liu et al. [2014] delivers larger amplitudes for higher frequencies and therefore a smaller spectral decay.
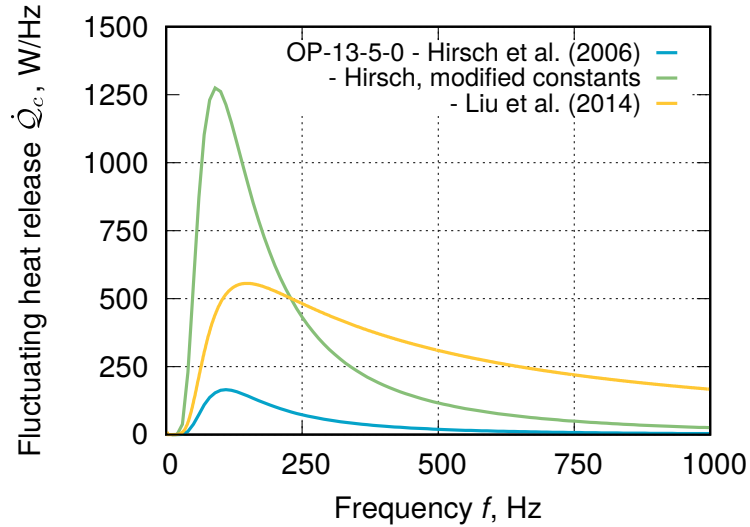
Figure 8.17: Spectra of fluctuating heat release $\dot{\mathcal{Q}}_c(f)$, [W/Hz] associated with the combustion noise for operating point OP-13-5-0, obtained from statistical noise model by Hirsch et al. [2006, 2007] and the modified version by Liu et al. [2014].

8.2.5 Direct Noise Prediction Using Statistical Noise Modeling

The acoustic pressure predicted by the LNSE simulation is evaluated at the wall at an axial location of $x = 122.5$ mm and compared with the measurements from CNRS [Kings et al., 2015, Mazur, 2017, Mazur et al., 2015a]. The position of the evaluation in the simulation model and experiment is visualized in fig. 8.5(a). The time-series data of the dynamic pressure measurements provided by CNRS are postprocessed in MATLAB using the `pwelch`-algorithm [Welch, 1967] in conjunction with a Hanning window with 50% overlap [MathWorks, 2017]. The power spectral density of the pressure signal is normalized by the reference pressure to obtain the spectrum of the Sound Pressure Level (SPL), defined by eq. (5.1).

In the following discussion only the broadband contributions to the noise spectra of the different operating points are regarded. As later shown several eigenfrequencies at 130 Hz, 260 Hz, 390 Hz and 520 Hz are observed in the experimental pressure spectrum of OP-16-0-2, while slightly higher eigenfrequencies are obtained for the OP-16-2-0. Also the

spectrum of OP-13-5-0 contains some eigenfrequencies, which are covered to a significant extend by a much higher broadband noise contribution in comparison to the first two operating points. The studies by Mazur [2017] and by Lapeyre et al. [2017] showed that these eigenfrequencies are most likely associated with thermoacoustic modes caused by instabilities of the swirling flow in the mixing duct. These thermoacoustic modes are not treated in this thesis as the simulation of them requires the introduction of a flame transfer function, which describes the feedback effect from the acoustics on the flame. The flame-acoustic interactions should be investigated in further studies. The wording "peak frequency" and "peak amplitude" used in the following paragraphs refers to the broadband noise content but not to the distinct thermoacoustic eigenfrequencies.

The results obtained by the statistical noise model by Hirsch et al. [2006, 2007] are given in fig. 8.18 for the operating points OP-16-0-2 and OP-16-2-0. The peak frequency and peak amplitude of the broadband spectra are captured by the simulation with fairly good agreement. For OP-16-0-2 a peak frequency of 86 Hz is predicted by the LNSE in comparison to approximately 129 Hz in the experiment. Therefore the ratio of $(f_p)_{\text{RANS}}/(f_p)_{\text{exp}} = 0.66$ between the predicted and experimental peak frequency matches well with the estimated ratio of $(f_p)_{\text{RANS}}/(f_p)_{\text{exp}} = 0.5$ in subsec. 8.2.3. The LNSE simulation delivers about 10 dB higher peak amplitudes in comparison to the experiment. This is in line with the scaling ratio (8.9), which yield a 6 dB higher peak amplitude of the LNSE simulation. The spectral fall-off predicted by the simulation is about twice the experimental one. This leads to an increasing deviation between the simulation and measurement beyond approximately 500 Hz. The comparison of the combustion noise spectra with the heat release source spectra of the previous subsec. 8.2.4 shows that they follow the same trend. So it can be concluded that the spectrum of the source term directly affects the pressure spectrum.
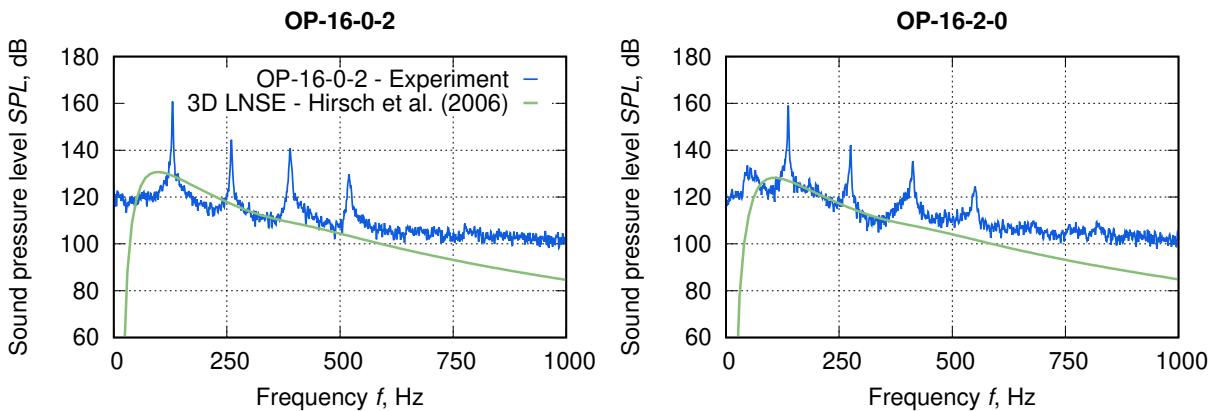
Figure 8.18: Pressure spectrum of OP-16-0-2 (left) and OP-16-2-0 (right) evaluated at fourth microphone position $x = 122.5\,\text{mm}$.

The experimental and predicted pressure spectrum of OP-13-5-0 is shown in fig. 8.19. Although the thermal power of the flame is constant for all operating points, the measured peak amplitude of OP-13-5-0 is approximately 20 dB higher in comparison to OP-16-0-2 and OP-16-2-0. This is caused by the injection of a significant amount of air in the axial jet, which leads to a highly unsteady behavior of the flame and much higher rms-values in comparison to the first two operating points. For OP-13-5-0 maximum rms-amplitudes of $u'_{\mathrm{rms}} \approx 15\,\mathrm{m/s}$ are found close to the centerline axis, while the rms-values are limited to $u'_{\mathrm{rms}} \approx 9\,\mathrm{m/s}$ for OP-16-0-2, cf. figs. 8.12 and 8.14. The impact of the rms-amplitudes on the combustion noise source amplitudes can be estimated using the volume source term $\hat{s}_V$ derived in this thesis. As stated by the eqs. (4.48) and (4.50), the local spectral amplitude depends on the squared reaction progress variable fluctuation. When assuming a direct proportionality between reaction progress variable and velocity fluctuations, the doubling of the local rms-values leads to an increase of the local source term amplitude around 12 dB for OP-13-5-0. This local estimation does not contain any summation of the different sources, which will lead to an additional increase of the integral source spectrum and the resulting pressure amplitudes.
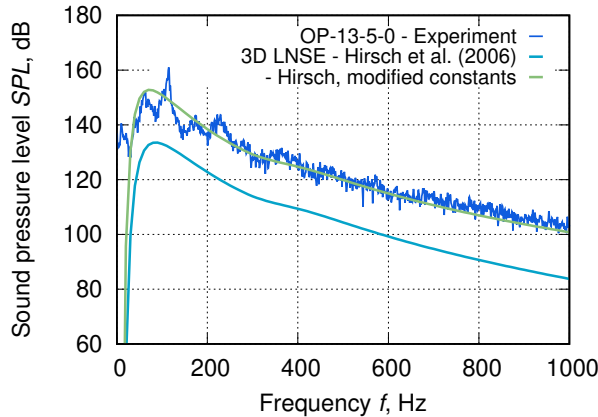
Figure 8.19: Pressure spectrum of OP-13-5-0 evaluated at fourth microphone position $x = 122.5\,\mathrm{mm}$.

In the following the LNSE simulation results are compared against the measurements in fig. 8.19 for operating point OP-13-5-0. As described in subsec. 8.2.3 the effects of the erroneous turbulent length scale and time scale prediction by the RANS cancel each other out leading to the same peak frequencies in the simulation and experiment. This estimation is confirmed by the simulation result shown in fig. 8.19, where the peak frequency and spectral fall-off predicted by the LNSE simulation together with model by Hirsch et al. [2006, 2007] match the experiment. According to the estimation in subsec. 8.2.3 the differences in the turbulence quantities between the RANS and experiment would lead to an underestimation of the SPL values of about 17 dB. This estimation corresponds well with acoustic amplitudes predicted by the LNSE, where a throughout underestima-

tion by approximately 20 dB is observed. When applying the model by Hirsch et al. [2006, 2007] with the modified constants as introduced in the previous subsec. 8.2.4 the spectrum "modified constants" is obtained, which is seen to match the measured spectrum quite well. In conclusion it can be stated that the spectral model perform only as good as the quality of the underlying simulated turbulence data. This could be demonstrated by modifying the model constants, which compensated the deficiencies of the simulated turbulence field of OP-13-5-0.

As illustrated in fig. 8.20 the predicted peak frequency and the peak amplitude matches the experimental data when applying the model by Liu et al. [2014]. The higher peak amplitude is caused by the additional prefactor $\rho_0 Y_{f,0} H_l c_d(\epsilon/k)$ in eq. (4.66) in comparison to the model by Hirsch et al. [2006, 2007]. The frequency slope is underpredicted leading to an overestimation of the noise amplitudes beyond approximately 375 Hz. As implied by the analysis above, the model by Liu et al. [2014] presumably leads to a significant overprediction of the noise amplitudes for all operating points when feeding the model with more accurate RANS simulation data.
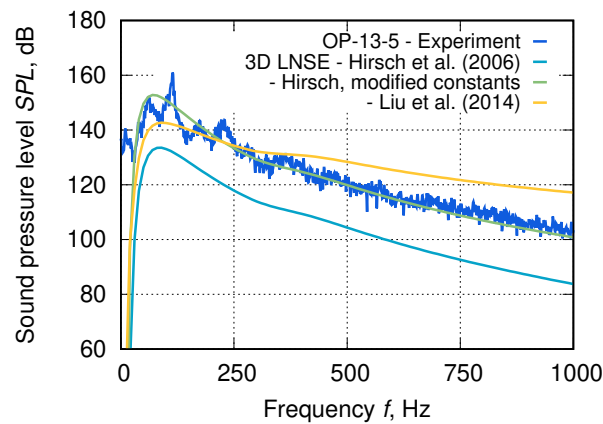
Figure 8.20: Influence of combustion noise model on the pressure spectrum of OP-13-5-0 evaluated at fourth microphone position $x = 122.5\,\mathrm{mm}$.

8.2.6 Direct Noise Prediction Using LES Source Terms

In the following LNSE results based on incompressible LES source spectra are presented. The combustor investigation is extended to the high frequency range above 1000 Hz, where the noise spectrum is controlled by the system eigenfrequencies to a significant extent. Also several additional influences on the direct combustion noise spectrum are identified.

The LES was carried out by Technische Universität Darmstadt using the LES solver PRECISE-UNS, which was developed by Rolls-Royce Deutschland. In several studies the potential of PRECISE-UNS to deliver highly accurate flow prediction was demonstrated

[Anand et al., 2013, Raynaud, 2015]. The LES was postprocessed by Rolls-Royce Deutschland to evaluate combustion noise source terms [Ullrich et al., 2018]. The time-averaged LES mean flow fields and the source terms were kindly provided by TU Darmstadt and Rolls-Royce Deutschland. The results presented in the subsequent paragraphs are based on the joint-publications by Ullrich et al. [2017, 2018]. The analysis below is restricted to the last operating point OP-13-5-0 as it provides the most stable operating conditions with respect to tonal combustion instabilities.

Heat Release Spectrum

The LES model is only briefly introduced, while it is referred to the publications by Lackhove et al. [2017] and Ullrich et al. [2018] for further details. The PRECISE-UNS solver is based on the incompressible form of the filtered Favre-averaged Navier-Stokes equations, which are solved along with transport equations for the mixture fraction and progress variable. Turbulence on the unresolved small-scales is accounted for by the dynamic Smagorinsky subgrid turbulence model. Combustion is modeled using the Flamelet Generated Manifold (FGM) method together with premixed flamelets. The flamelets are based on the GRI-3.0 mechanism and are computed and tabulated prior to the simulation.

The integral volume source spectrum is extracted from LES using the approach described in subsec. 4.3.3. After the spatial redistribution of the integral source spectrum, the local sources are imposed on the linearized continuity eq. (4.38) in the isentropic formulation of the LNSE. Using eq. (4.28) the integral volume source spectrum $\mathcal{S}_V(f)$ can be rewritten in terms of an equivalent heat release spectrum $\dot{\mathcal{Q}}_c(f)$, both of which are shown in fig. 8.21. The instantaneous spatial distribution of the local source term is visualized in fig. 8.22.
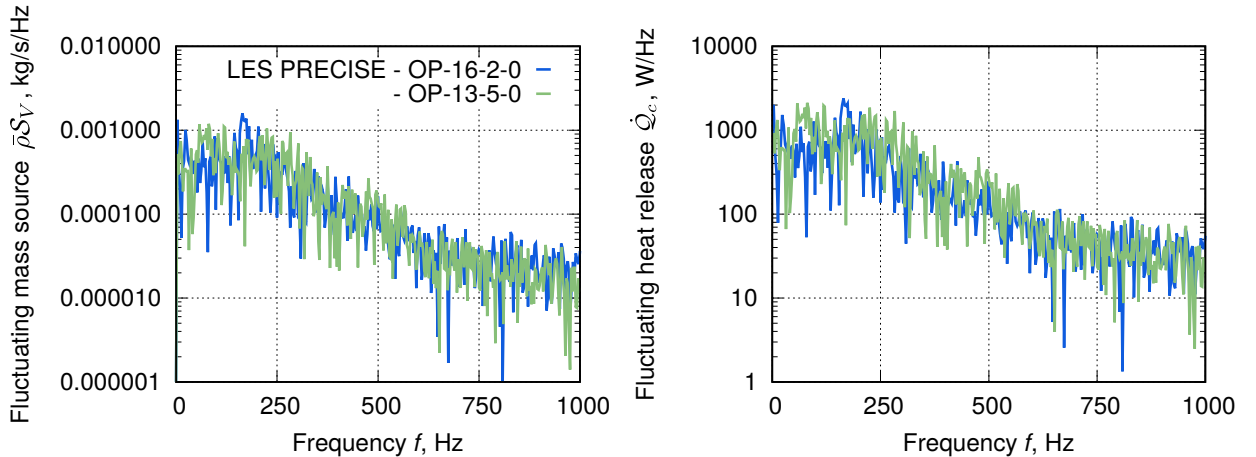
Figure 8.21: Absolute value of the integral spectra of the mass source $\bar{\rho}|\mathcal{S}_V(f)|$, [kg/s/Hz] and equivalent heat release $|\dot{\mathcal{Q}}_c(f)|$, [W/Hz] determined by incompressible LES simulations [Ullrich et al., 2018].

Since time domain LES simulations are performed the source spectrum contains both the information about the absolute value and the phase i.e. the source spectra $\mathcal{S}_V(f)$ and $\dot{\mathcal{Q}}_c(f)$ are complex valued. This allows to study the impact of the phase on the resulting combustion noise spectrum.
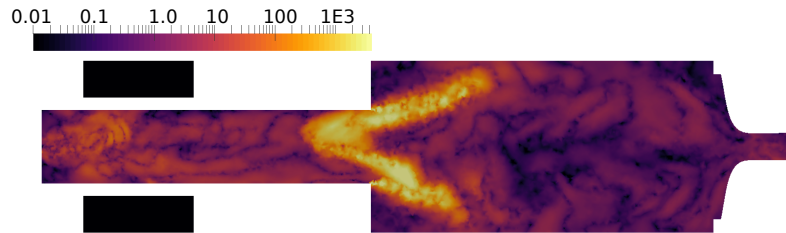
Figure 8.22: Instantaneous spatial distribution of $|\partial\rho/\partial t|$, [kg/(m³s)] for OP-13-5-0, obtained from the LES. Picture kindly provided by TU Darmstadt.

Influence of the Spectral Source Model on Direct Noise

In fig. 8.23 the results for the quasi 2D and 3D model based on the LES source term are given. For comparison the result of the 3D simulation obtained with the statistical noise model by Hirsch et al. [2006, 2007] with modified constants is also plotted. When using the statistical noise model the simulation sufficiently matches the experimental data up to a frequency of about 1200 Hz. Increasing deviations between the simulation and experiment are observed for higher frequencies. Significant improvement of the prediction of the direct noise spectrum is achieved when using the LES source term, which holds in particular for the high frequency range. In this case the numerical simulations are in good agreement with the measurements over the entire frequency range. The quasi 2D model and the 3D model deliver very similar results with high accuracy in the low frequency range up to 1000 Hz. Only for very low frequencies below 50 Hz the quasi 2D model performs much better than the 3D model, which overestimates the noise amplitudes in this frequency range.

Concerning the combustor eigenfrequencies the 3D model delivers better results as the quasi 2D model. The first eigenmode at 2960 Hz predicted by the 3D model matches the measurements. The second eigenmode at 3300 Hz is weaker and located closer to the first mode in comparison to the quasi 2D model. The first and second eigenmodes are visualized in terms of the acoustic density $\hat{\rho}$ in the fig. 8.24 for the quasi 2D and 3D model. It can be seen that the acoustic modes obtained from the quasi 2D and 3D model have a similar shape except for the swirler and perforated screen regions. In these regions the acoustic modes almost disappear in the quasi 2D model. In both models the first eigenmode represents the $\lambda/2$-mode in the combustion chamber, while the second eigenmode is related to the λ-mode in the premixing duct. In the 2D model not all coupling effects between acoustic

and vorticity waves are included due to the assumption of axis-symmetry $\partial/\partial\theta = 0$. These acoustic-vorticity interactions are in particular relevant in the strong rotational flow in the premixing duct, where the second eigenmode establishes. The neglection of some interaction effects in the 2D model might lead to a higher transmission of the acoustic waves from the premixing duct into the combustion chamber, where the noise is evaluated. Therefore the second eigenmode presumably becomes more visible in the 2D model. In conclusion the 3D model leads to a more accurate prediction of the acoustic behavior in the combustor. A more detailed discussion of the eigenmodes is given by Ullrich et al. [2018].
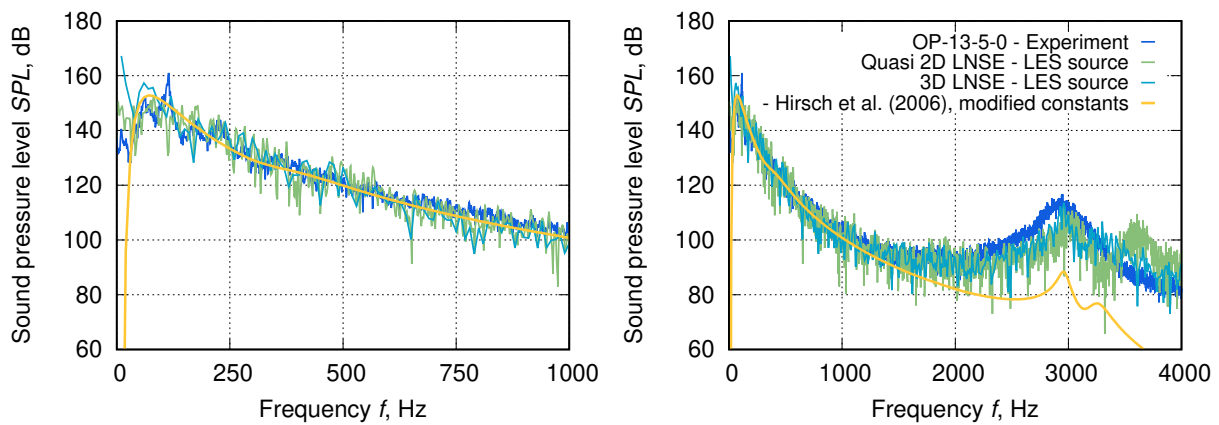
Figure 8.23: Quasi 2D vs. full 3D simulation [Ullrich et al., 2018].

(a) $f = 3001$ Hz

(b) $f = 3598$ Hz

(c) $f = 2960$ Hz

(d) $f = 3300$ Hz
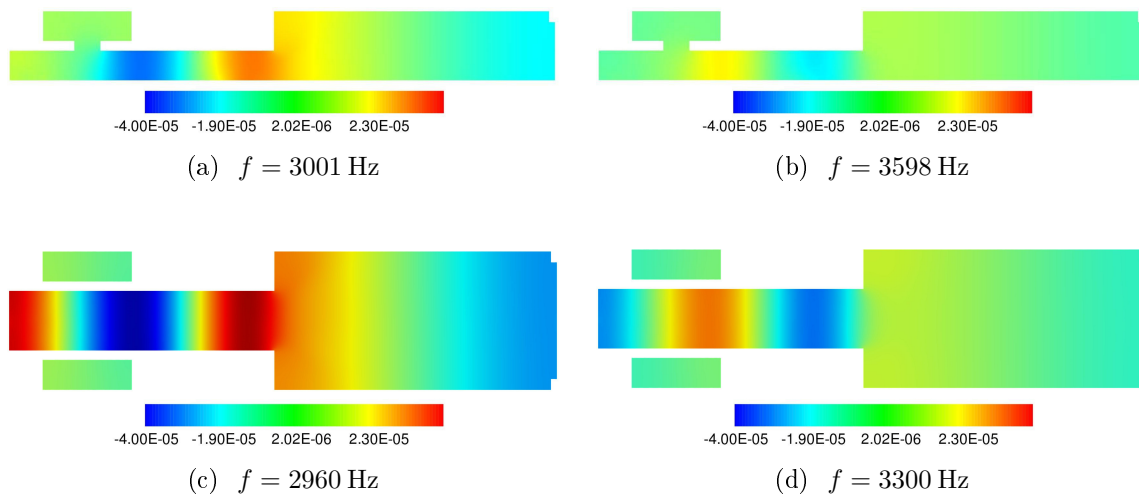
Figure 8.24: Acoustic density distribution $\Re\{\hat{\rho}\}$, [kg/(m^3)] for the quasi 2D (top) and 3D model (bottom) at their respective eigenfrequencies, based on the RANS mean flow field.

Influence of Mean Flow Field on Direct Noise

The influence of the mean flow field on the acoustic pressure spectrum is assessed by performing additional 3D simulations based on the time-averaged LES flow field. The corresponding results are compared in fig. 8.25 to the numerical solution based on the RANS mean flow field. In both mean flow cases shown in fig. 8.25 the combustion noise source term spectra were still determined from the incompressible LES. The simulations based on the LES mean flow field deliver a constantly higher amplitude of approximately $2\,\text{dB}$-$4\,\text{dB}$ in comparison to the RANS-based simulation. The shape of the spectrum is almost not affected by the mean flow field. The different acoustic amplitudes between the RANS and LES-based simulations can be explained by the different acoustic impedances. As derived theoretically by Strahle [1971] or Crighton et al. [1992] the acoustic power emitted by a flame is proportional to the inverse of the acoustic impedance ($\bar{\rho}\bar{c}$) of the surrounding medium, cf. eq. (4.10). The acoustic impedance is given by the mean temperature level $\bar{T}$ and pressure $\bar{p}$, i.e. $(\bar{\rho}\bar{c}) = \bar{p}\sqrt{\kappa/(R\bar{T})}$. Since the pressure is almost constant inside the combustor (isobaric flame with $\bar{p} = \text{const.}$) differences in the acoustic pressure amplitudes are predominantly caused by differences in the mean temperature levels. Averaging the acoustic impedance over the combustor volume delivers $(\bar{\rho}\bar{c})_{\text{LES}} = 310.81\,\text{kg}/(\text{m}^2\,\text{s})$ for the LES and $(\bar{\rho}\bar{c})_{\text{RANS}} = 390.62\,\text{kg}/(\text{m}^2\,\text{s})$ for the RANS simulation. Therefore the average factor of $20\log_{10}\big[(\bar{\rho}\bar{c})_{\text{RANS}}/((\bar{\rho}\bar{c})_{\text{LES}})\big] \approx 2\,\text{dB}$ between the acoustic impedances of the LES and RANS mean flow field presumably explains the deviations of the acoustic pressure amplitudes. The first eigenmode is predicted at a higher frequency of $3070\,\text{Hz}$ when using the time-averaged LES mean flow field. This is caused by the higher mean temperature level of $\bar{T} = 2037.6\,\text{K}$ in the combustor due to adiabatic wall boundary conditions used for the LES. Since the second eigenfrequency is related to the λ-mode in the premixing duct, it is not affected by the higher mean temperatures of the LES mean flow field. The mode shapes predicted by the LES-based 3D simulation are shown in fig. 8.26. As expected they are almost identical to the modes based on the RANS mean flow field (fig. 8.24). The pressure amplitude inside the combustor is not only controlled by the amplitude of the heat release fluctuations but also by the acoustic impedance of the surrounding mean flow. The influence of the acoustic impedance on the noise level is of minor importance in comparison to the influence of the heat release source spectrum. Excellent agreement with the experimental pressure spectrum is found over a broad frequency range, which applies to both simulation models based on the RANS and LES mean flow fields.

Also the influence of the aerodynamic mean flow convection and shearing on the direct combustion noise spectrum is identified by additional simulations based on the inhomogeneous Helmholtz eq. (3.23). The results obtained from the isentropic LNSE and Helmholtz simulations are compared with each other in fig. 8.27. Both numerical solutions rely on the LES source term spectra. As demonstrated in fig. 8.27 almost the same broadband pressure spectrum is obtained for the Helmholtz equation. Slightly lower pressure amplitudes are delivered by the LNSE simulation, which is most probably caused by the damping due to viscous and flow shearing. These effects are not incorporated by the Helmholtz equation.

126
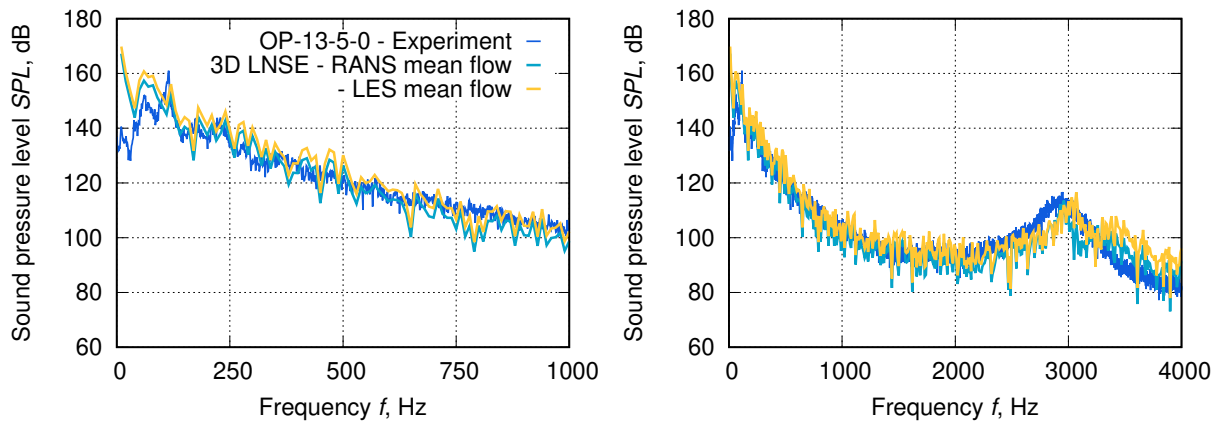
Figure 8.25: Full 3D simulation: RANS vs. LES mean flow [Ullrich et al., 2018].

(a) $f = 3070\,\text{Hz}$ (b) $f = 3420\,\text{Hz}$

Figure 8.26: Acoustic density distribution $\Re\{\hat{\rho}\}$, [kg/(m³)] for the 3D model at the eigenfrequencies, based on the LES mean flow field.

It is found that the aerodynamic flow field has a negligible effect on the combustion noise spectrum. This stands in contrast to the eigenfrequencies, which are significantly influenced by the aerodynamic mean flow. The same acoustic eigenfrequencies at approximately 3000 Hz and 3300 Hz are predicted by the Helmholtz-based simulations as compared with the LNSE simulation. But the amplitudes at the eigenfrequencies are remarkably overpredicted when using the Helmholtz equation. An additional eigenfrequency at 390 Hz is obtained for the Helmholtz equation, which is not present in the experimental pressure spectrum. A comparable low-frequency eigenmode at 550 Hz was predicted in the APE-based study by Lackhove et al. [2017]. The analytical study by Mazur et al. [2015b] and the numerical study by Lackhove et al. [2017] suggest that this eigenfrequency is related to the $\lambda/4$-mode in the premixing duct and combustion chamber. Due to the incorporation of mean flow damping effects, the LNSE simulations result in much better amplitude predictions at the different eigenfrequencies. The eigenfrequency at 390 Hz is not observed in the LNSE-based model.
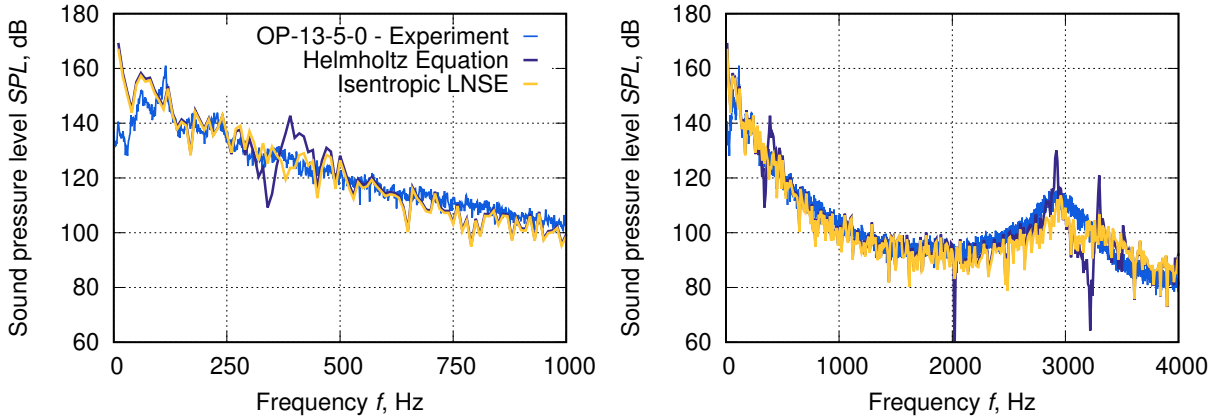
Figure 8.27: Influence of the aerodynamic mean flow on the combustion noise spectrum [Ullrich et al., 2017].

Influence of Source Term Phase on Direct Noise

The LNSE and Helmholtz simulations shown so far are based on the absolute value of the spectrum $|\dot{\mathcal{Q}}_c(f)|$, cf. fig. 8.21. The influence of the phase of the source term is assessed by performing additional simulations using the complex spectrum $\dot{\mathcal{Q}}_c(f)$ as the source term. The excitation based on the complex spectrum is equal to the excitation with the absolute spectrum apart from the phase. Therefore the same results are expected for the complex source, which are only shifted by the phase differences. As the phase differences are not included in the absolute pressure spectra, both source spectra should deliver the same results. This theoretical consideration of the phase influence on the combustion noise spectrum is proven in the following. As demonstrated in fig. 8.28 the simulations based on the absolute and complex-valued source spectrum deliver almost identical results over the entire frequency range. Therefore the phase of the combustion noise source term is unimportant for the resulting pressure spectrum in the relevant frequency range. This result justifies the usage of absolute source spectra extracted from the LES simulations. The outcome of this analysis strongly supports the validity of statistical noise models which cannot predict complex-valued source spectra as they are fed by steady state mean flow fields.

Influence of Source Term Distribution on Direct Noise

The impact of the shape of the source region on the combustion noise spectrum is quantified in the following. For this purpose another simulation is conducted, in which the source region is arbitrarily defined by a flame sheet with thickness $\delta_f = 0.01\,\mathrm{m}$ and axial extensions from $0.01\,\mathrm{m}$ to $0.02\,\mathrm{m}$. Then the local heat release source term is deduced from the integral spectrum by

$$\hat{\dot{\omega}}_T(f) = \frac{1}{A\delta_f}\dot{\mathcal{Q}}_c(f), \tag{8.11}$$
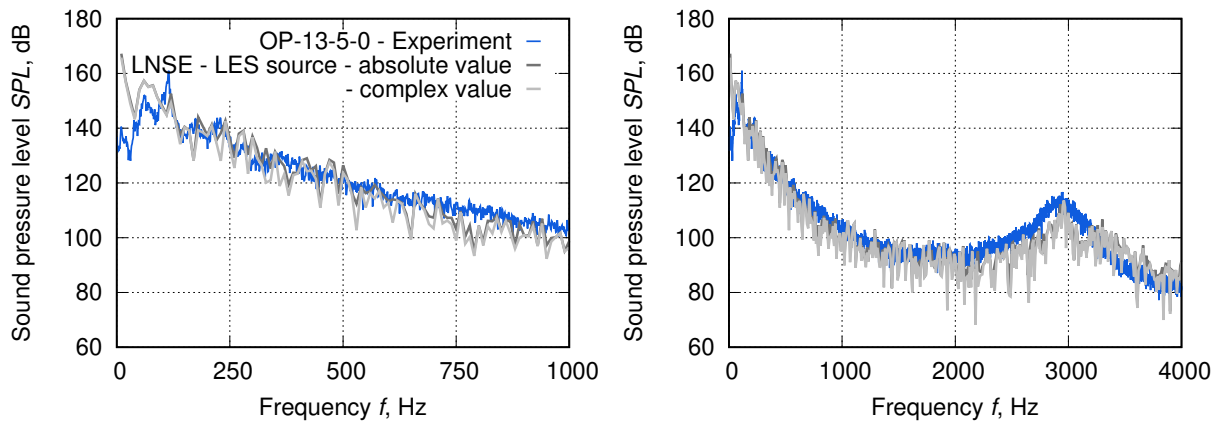
Figure 8.28: Influence of the source term phase on the combustion noise spectrum [Ullrich et al., 2017].

where A defines the cross section area of the combustor. The heat release source term is transformed to an equivalent volume source using eq. (4.28). The result obtained from the simulation model above is referred to as "rectangular source region" in fig. 8.29. The pressure spectrum is not influenced by the shape of the source region in the frequency range up to 1000 Hz. This important finding confirms the validity of the compact flame assumption for the direct noise computation in the low frequency range and is in line with previous numerical studies by Weyermann [2010]. The influence of the source region increases with frequency but remains of minor importance even at 4000 Hz. When only direct noise is considered, the shape of the combustion noise source region is arbitrary to a certain extend but must obey the integral energy conservation. This requirement is guaranteed by the model for the spatial source term distribution proposed in sec. 4.4 in this thesis.
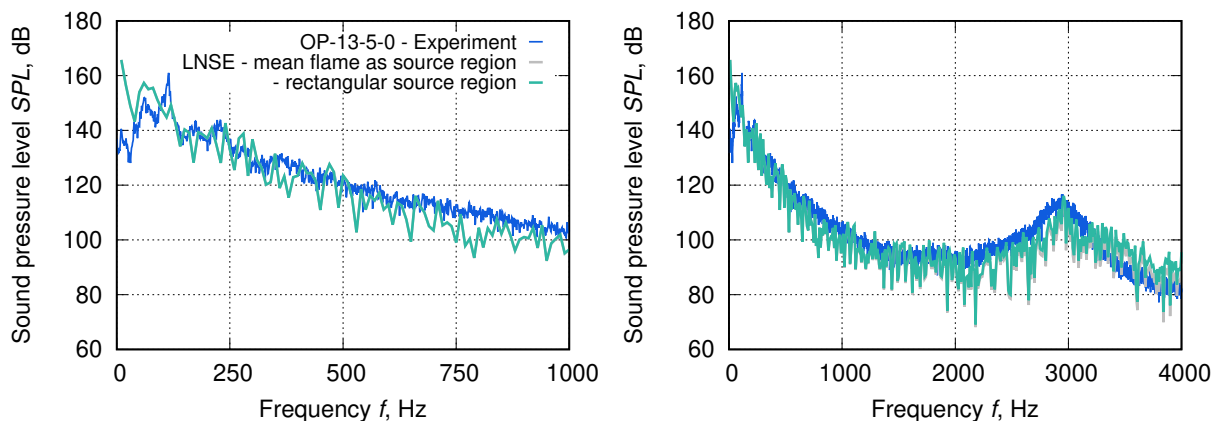
Figure 8.29: Influence of the spatial source term distribution on the combustion noise spectrum [Ullrich et al., 2017].

Influence of Source Term Model on Direct Noise

One of the most important result concerns the source term modeling, which has not been considered yet. Several numerical studies on combustion noise are based on heat release source terms $\hat{\dot{\omega}}_T$. This stands in contrast to the LNSE simulation model for the direct noise predictions presented above, which achieves acoustic excitation by means of the volume source term $\hat{s}_V$ in the linearized continuity eq. (4.38). The theoretical basis for this source model was provided in sec. 4.2 using the triple-decomposition approach. When using incompressible LES instead of statistical modeling to determine the frequency content of the source terms, the analysis above revealed that the volume source model is capable to deliver highly accurate predictions of the resulting combustion noise spectrum.

Good agreement was found by Ullrich et al. [2017] between the LNSE simulations and the simulations by UCAM using their acoustic network solver LOTAN. The LOTAN solver is based on the LEE, which are excited by the heat release source term. Although an explicit comparison is not shown here, the consistency between both solutions provides further support for the volume source term approach presented in this thesis.

Summary

In a final analysis the results of the different models above showed that:

- The accuracy of the LNSE combustion noise predictions based on the statistical noise model by Hirsch et al. [2006, 2007] depends on the quality of the underlying RANS mean flow simulations.

- For the operating points OP-16-0-2, OP-16-2-0 and OP-13-5-0 deviations between the predicted and experimental peak frequencies, peak amplitudes and spectral fall-offs can be explained by deficiencies in the underlying RANS simulations.

- A significant improvement of the prediction of the combustion noise spectrum of OP-13-5-0 is achieved when applying the LNSE model in conjunction with incompressible LES source terms.

- The shape of the resulting combustion noise spectrum is mainly driven by the heat release source spectrum, so that the quality of the simulation result crucially depends on the accuracy of the spectral model.

- The influence of the acoustic impedance of the surrounding fluid on the combustion noise spectrum plays a minor role in comparison to the source term effect.

- The mean flow convection and flow shearing only weakly influence the shape of the broadband combustion noise spectrum, whereas they have a significant effect on the damping of the eigenmodes.

- The phase and spatial distribution of the combustion noise sources have a negligible effect on the noise spectrum in the frequency range of interest.

- The volume source term approach applied in the frame of the isentropic LNSE simulation is a valid method for the prediction of direct combustion noise under the isentropic assumption.

- The model for the spatial distribution of the integral heat release source spectra, proposed in this thesis, is energy consistent and does not need any arbitrary source volume definition.

8.2.7 Total Noise Prediction Using Different Source Terms

The investigation of the CESAM-HP combustor is completed by the determination of the total noise at the exhaust nozzle exit with particular focus on the impact of the combustion noise source term modeling. For this purpose the strategy presented in subsec. 5.3.2 is applied. The study is limited to operating point OP-13-5-0.

LNSE Combustor Simulation

Two source term formulations in the non-isentropic LNSE are investigated in the following. The first one is the volume source term model $\hat{s}_V$ for perfectly-premixed flames implemented in the linearized continuity eq. (4.38) and energy eq. (4.40), cf. subsec. 4.2.2. In the second simulation the volume source term $\hat{s}_V$ is only implemented in the linearized energy eq. (4.40) to investigate its influence of the entropy wave generation and the total noise at the exhaust nozzle outlet. The second model corresponds to the commonly applied approach to model the combustion noise sources as arbitrary heat sources in the energy equation. Each of the source term model is fed by the integral spectrum $\dot{\mathcal{Q}}_c(f)$ for premixed flames, which is computed using the spectral combustion noise model by Hirsch et al. [2006, 2007] with modified constants as introduced in sec. 8.2.4.

On the left of fig. 8.30 the pressure spectrum resulting from the two source term models are compared against the measurements. The trend as well as the amplitude is well predicted by the hybrid approach. There are only marginal differences for the direct combustion noise between both source term formulations. This stands in contrast to the generation of entropy waves, which is demonstrated on the right in fig. 8.30 by considering the line-of-sight integrated temperature spectrum evaluated at $x = 122.5\,\mathrm{mm}$

$$< \hat{T} > (x) = \frac{1}{b} \int_0^b \hat{T}(x, y) \mathrm{d}y. \tag{8.12}$$

The LNSE results are compared with the line-of-sight integrated temperature spectrum obtained from Laser interferometric Vibrometer measurements by Kings et al. [2016] and Mazur [2017]. In the experiment almost no temperature fluctuations are measured, indicating the absence of entropy waves in case of the premixed flame. Some peaks are visible
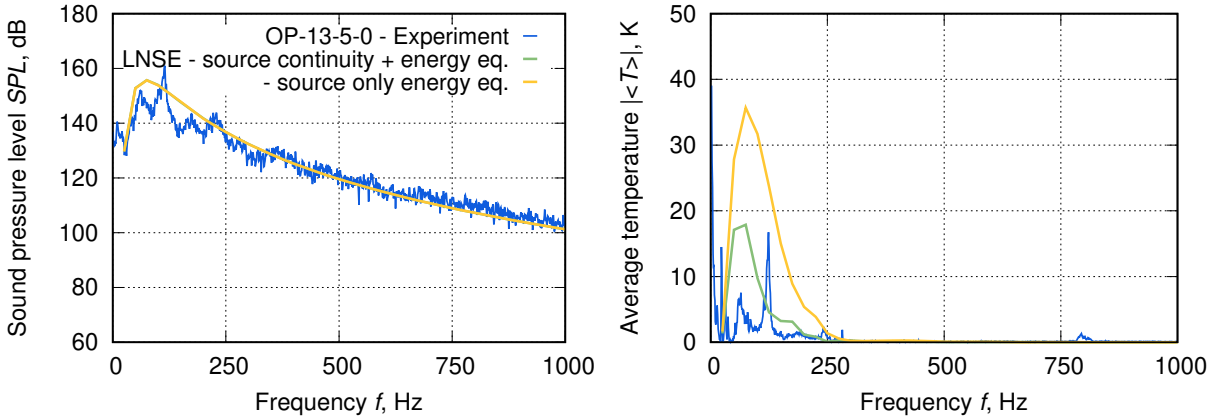
Figure 8.30: Pressure spectrum (left) and line-averaged temperature fluctuations (right), evaluated at fourth microphone position $x = 122.5\,\mathrm{mm}$.

at the eigenfrequencies, which remain on a negligible level below $20\,\mathrm{K}$ in comparison to the mean temperature level in the downstream part of the combustor. The LNSE computation based on the source term $\hat{s}_V$ in the linearized continuity eq. (4.38) and energy eq. (4.40) should ideally deliver no temperature fluctuations over the entire frequency range since mean flow gradients are neglected. As this is not the case the remaining averaged temperature fluctuations with amplitude below $20\,\mathrm{K}$ indicate numerical errors and spurious entropy wave generation. As discussed in subsec. 4.4, also the distribution of the source terms over the flame volume with constant phase might lead to an additional unphysical entropy wave generation, although the volume source term should ideally produce no entropy waves. When implementing the source term only in the energy eq. (4.40) of the LNSE, represented by the orange line on the right in fig. 8.30, significantly higher averaged temperature fluctuations and entropy waves are obtained. This becomes evident when evaluating the absolute temperature fluctuations instead of the line-averaged fluctuations, which is shown on the left in fig. 8.31 for the location $x = 17.5\,\mathrm{mm}$.

The impact of the coherence of the entropy wave sources is estimated on the right in fig. 8.31 for the model with source terms $\hat{s}_V$ in the linearized continuity eq. (4.38) and energy eq. (4.40). For fully coherent sources as given by the distribution model (4.81) the remaining temperature fluctuation is below $35\,\mathrm{K}$. The temperature fluctuations produced by an incoherent source are estimated using eq. (4.88). The coherence volume and flame volume are approximated from the RANS simulation to give $V_{\mathrm{coh}} = 3.14 \cdot 10^{-6}\mathrm{m}^3$ and $V_f = 1.12 \cdot 10^{-4}\mathrm{m}^3$. According to eq. (4.88) this yields a factor of $\sqrt{V_{\mathrm{coh}}/V_f} = 0.1676$ between the temperature fluctuations generated by a coherent and incoherent entropy source. Then the estimated temperature fluctuations due to an incoherent source term distribution model are never exceeding $6\,\mathrm{K}$, which is represented by the dark blue line on the right in fig. 8.31. This result impressively demonstrates that no entropy waves are generated by the premixed flame when applying the incoherent volume source term model.
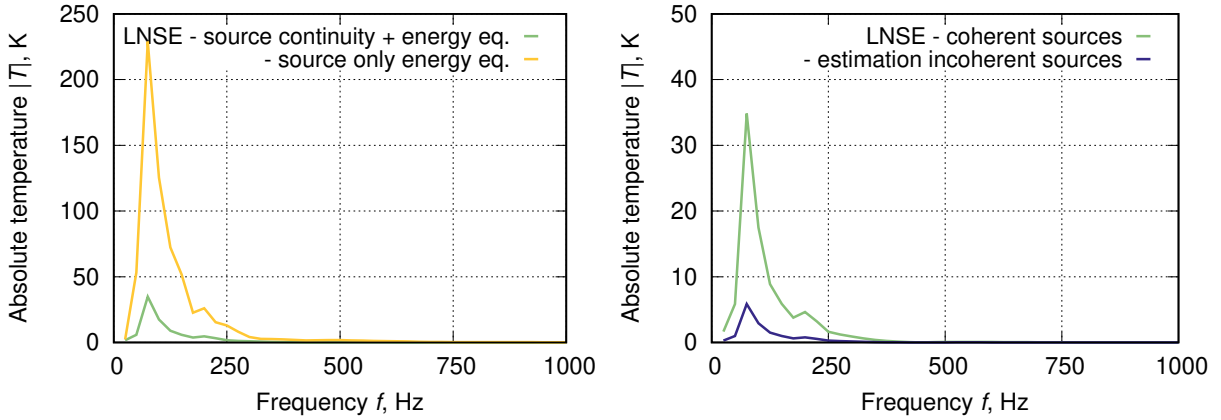
Figure 8.31: Absolute temperature fluctuations $|\hat{T}|$, [K] evaluated at the first possible microphone position $x = 17.55\,\text{mm}$ (left). Estimation of the temperature fluctuations when taking into account the incoherent entropy wave generation (right).

In conclusion none of the source term models is able to predict zero temperature fluctuations. But the implementation of the source term only in the energy equation leads to a vast overprediction of the amplitudes of the temperature fluctuations. The volume source model containing source terms in the continuity and energy equation results in quantitatively correct amplitudes apart from some remaining temperature fluctuations. Therefore an accurate estimation of the temperature amplitudes can only be realized by applying the model with source terms in the continuity and energy equation representing the perfectly premixed flame. The remaining unphysical temperature fluctuations are presumably caused by the distribution of the sources with constant phase in the entire flame volume and by numerical errors, which are growing at lower frequencies. These remaining temperature fluctuations should be investigated in detail in further studies. Another important outcome of the combustor simulation is that the source term model exclusively affects the entropy generation, while the generation of acoustic waves is equal for both models, cf. left in fig. 8.30.

The qualitative distribution of the acoustic and entropy waves predicted by the quasi 2D LNSE model including the volume source term is given in fig. 8.32 for the frequencies of 100 Hz, 400 Hz and 1000 Hz. The entropy waves are most probably caused by numerical errors in the model as the volume source term $\hat{s}_V$ in the linearized continuity eq. (4.38) and energy eq. (4.40) should ideally produce no entropy waves. None of the amplitudes of the entropy waves is higher than 17.5 K so that they are still negligible in comparison to the mean temperature level. The dispersion effect of these spurious entropy waves is clearly visible and increases significantly with frequency.
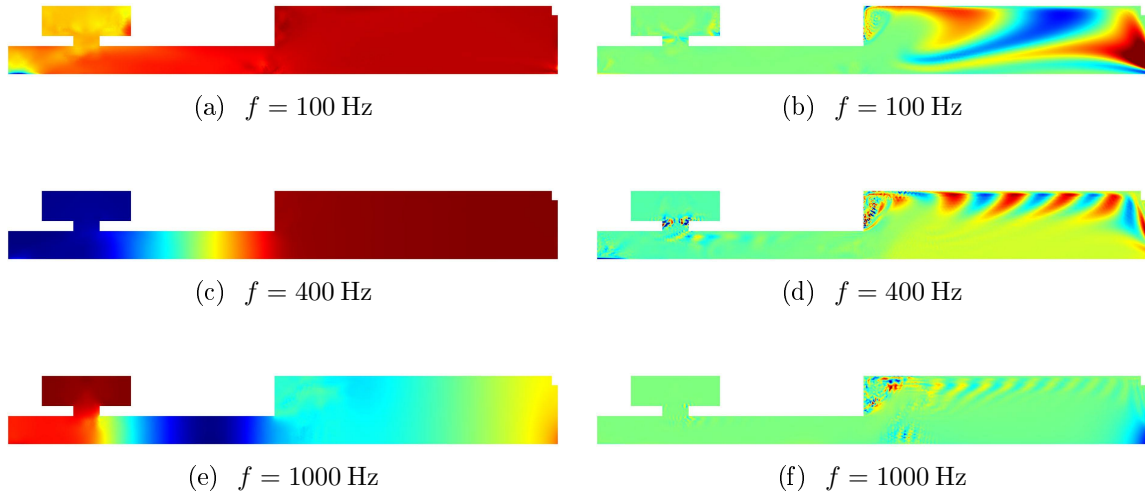
Figure 8.32: Qualitative pressure $\Re\{\hat{p}\}$, [Pa] (left) and temperature distribution $\Re\{\hat{T}\}$, [K] (right) for different frequencies and the volume source term model.

Nozzle Characterization

The nozzle is characterized in terms of the transmission and reflection coefficient for acoustic and entropy waves. As explained in detail in subsec. 3.8.3 the nozzle transfer functions are determined by the two-source location method, which utilizes the quasi one-dimensional LEE solver as implemented in the frame of the EWG test case.

The results for the acoustic and entropy transmission coefficient are given in fig. 8.33, where they are compared with results by the one-dimensional MarCan (ONERA) and ANozzle (CERFACS) solvers [Huet et al., 2016]. Good agreement is found between all solvers up to a frequency of approximately 1000 Hz, which applies to all four different coefficients. As shown in the top left of fig. 8.33 the acoustic transmission coefficient increases from approximately 0.15 at 0 Hz to 0.2 at 1000 Hz, which represents the frequency range of interest for direct and indirect combustion noise. Therefore only a small part of the incident acoustic waves is transmitted through the nozzle, while the largest part is reflected by it. The acoustic reflection coefficient stays at 1.0 over the entire frequency range. The bottom left of fig. 8.33 shows that the transmission of acoustic waves due to an accelerated entropy wave slightly increases with frequency below 1000 Hz.

Combustion Noise At Exhaust Nozzle Outlet

The LNSE combustor simulations are postprocessed and combined with the nozzle transfer functions in order to determine the combustion noise at the exhaust nozzle exit. This is achieved by the application of the procedure introduced in subsec. 5.3.2.

The numerical results for the direct, indirect and total noise at the nozzle exit are com-
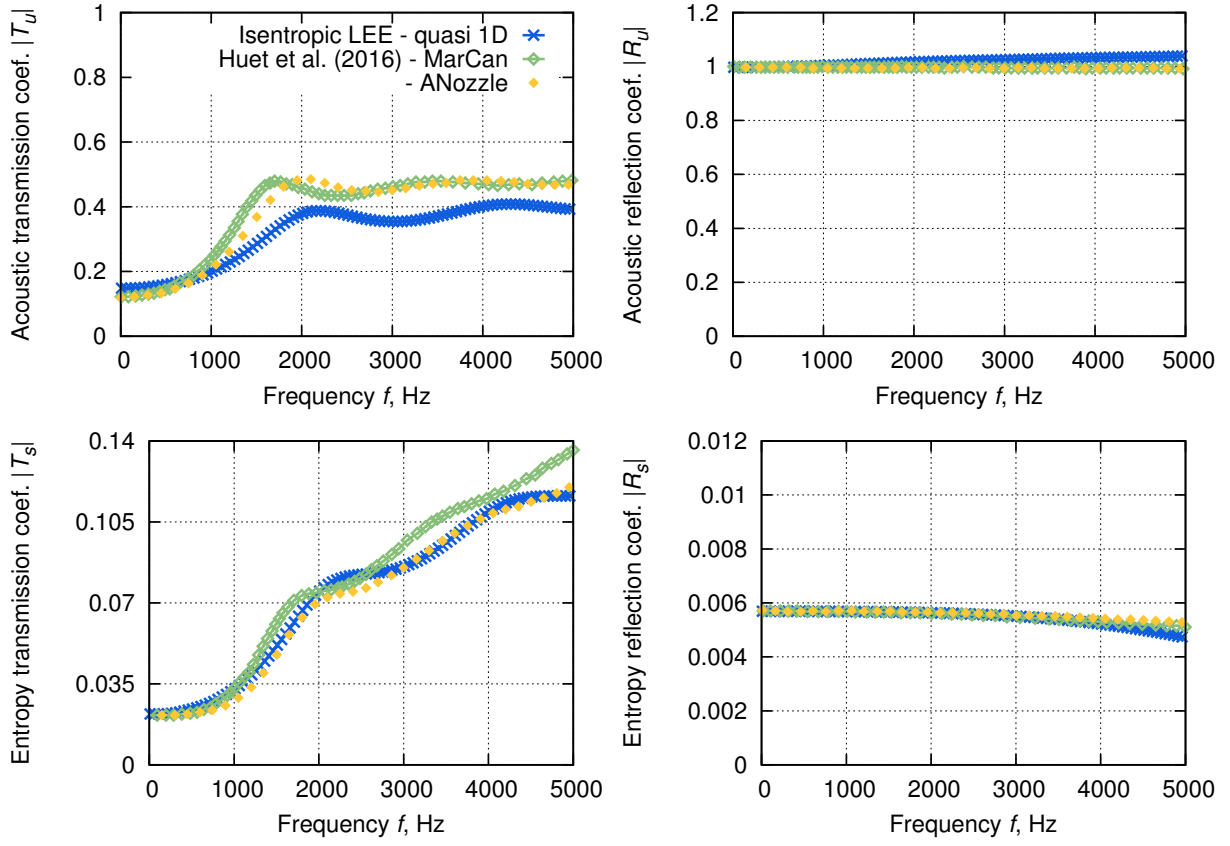
Figure 8.33: Transmission coefficients (left column) and reflection coefficients (right column) of the exhaust nozzle for operating point OP-13-5-0.

pared with the experimental pressure spectrum inside the combustion chamber in fig. 8.34 for both source models. In general it is seen that the noise amplitudes at the exhaust nozzle outlet are about 20 dB lower in comparison to the location inside the combustion chamber. This is explained by the acoustic properties of the nozzle. As indicated by the upstream reflection coefficient R_u, the incoming acoustic waves are almost fully reflected by the nozzle, while only up to 20 % are transmitted through it below 1000 Hz. The reduction of the acoustic amplitudes across the nozzle can be easily estimated by means of the upstream transmission coefficient T_u, which yields $20 \log_{10}(T_u) \approx -16.5$ dB. This is in line with the data shown in fig. 8.34.

In the following the different contributions to the total combustion noise at the exhaust nozzle outlet are discussed in detail. As presented in the left of fig. 8.34 the indirect noise never exceeds the direct noise at any frequency if the model with the source term $\hat{s}_V$ in the linearized continuity eq. (4.38) and energy eq. (4.40) is applied. The model, which only contains the source term in the energy eq. (4.40), predicts higher indirect noise levels as compared to the direct noise for frequencies up to approximately 200 Hz. In the
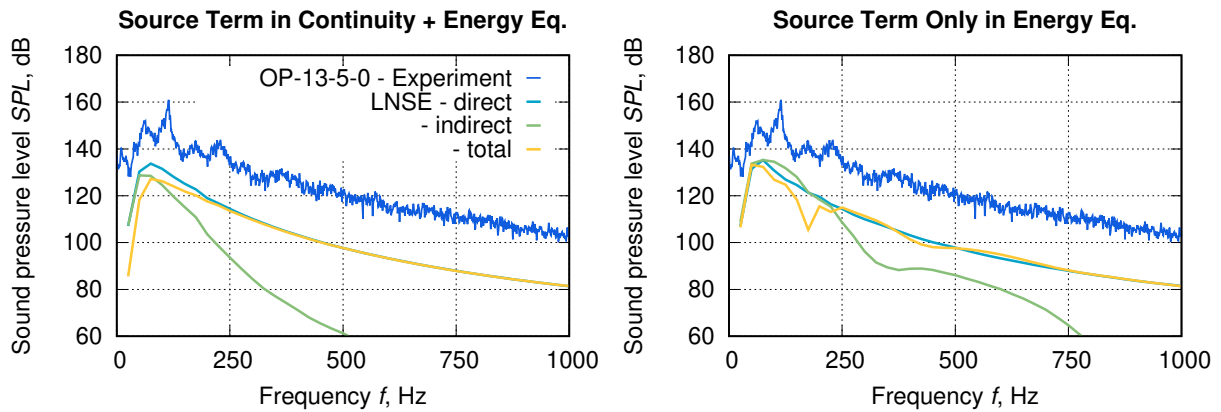
Figure 8.34: OP-13-5-0: Comparison of numerical results at the nozzle exit and the measurements inside the combustion chamber. LNSE results based on the statistical noise model by Hirsch et al. [2006, 2007] with modified constants.

recently published studies by Huet et al. [2016], Kings et al. [2016] and by Mazur [2017] it is concluded that the indirect noise is of minor importance in comparison to the direct noise in the CESAM-HP combustor. Their results can only be consistently reproduced if the model with the source term in the continuity and energy equation as proposed in this thesis is applied. Due to the almost perfectly premixed flame in this configuration only small amplitude entropy waves are generated, which lead to a dominance of the direct noise over the entire frequency range.
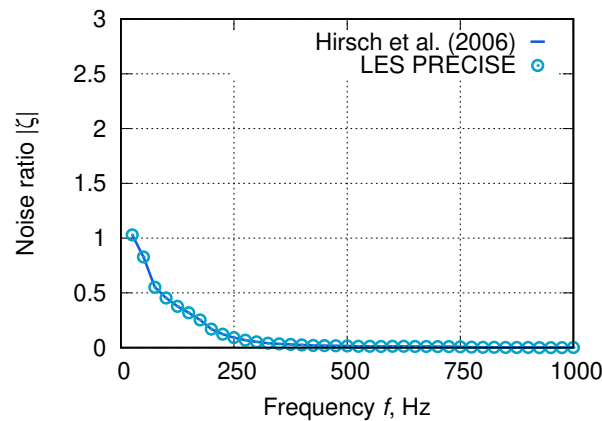
Figure 8.35: Dependence of the noise ratio on the source model, evaluated at the nozzle outlet.

The volume source model with sources in the continuity and energy equation still delivers a considerable contribution of the indirect noise to the total noise at low frequencies. This is reflected in the noise ratio at the exhaust nozzle outlet, which converges towards 1

for low frequencies as shown in fig. 8.35. The indirect noise contribution is overpredicted by the model due to the summation of errors during the simulation and postprocessing process: First, the neglection of phase differences between the source terms spread over the flame volume leads to an underestimation of the entropy shear dispersion effect, although these volume sources should theoretically produce no entropy waves. Beside of this, numerical errors might result in an overestimation of the entropy waves reaching the combustor outlet and impinging on the nozzle. The third important source of errors, which support the unphysical indirect noise contribution, is the wave extraction at the combustor outlet. As described in sec. 5.3.2 the extraction of the acoustic and entropy waves is based on area-averaged quantities and the one-dimensional solution of the LEEs. This may lead to considerable errors in retrieving the amplitudes of the acoustic and entropy waves at certain frequencies. With given nozzle properties, the noise contributions and the noise ratio at the exhaust nozzle outlet only depend on the quality of the wave extraction.

The noise ratio at the exhaust nozzle outlet was also computed for the LNSE model including the LES source term. The comparison of the numerical results based on the LES source and the statistical noise model by Hirsch et al. [2006, 2007] is given in fig. 8.35. While the amplitudes of the acoustic and entropy waves are considerably affected by the spectral source model, the noise ratio is not influenced by it. Hence the noise ratio is mainly controlled by the source term modeling approach but independent from the source spectrum.

Summary

The main findings of the total combustion noise predictions using different source terms in the non-isentropic LNSE can be summarized as follows:

- The nozzle transfer functions predicted by the quasi one-dimensional LEE are in good agreement with the results presented by Huet et al. [2016] in the frequency range of interest.

- The generation of entropy waves by combustion crucially depends on the source term model applied in the LNSE.

- The LNSE model, which only contains the source term in the energy equation leads to a vast overprediction of the temperature fluctuations. The model with source terms in the continuity and energy equation delivers more realistic results, which are, however, still overpredicted as compared to the measurements. The tendency to overpredict entropy amplitudes represents an inherent limitation of the LNSE approach, which does not feature an isentropic solution in case of non-isentropic mean flows as indicated by eq. (4.32) in subsec. 4.2.2.

- The noise ratio predictions based on the herein proposed volume source model, containing the source term in the continuity and energy equation, are consistent with the findings of the studies by Huet et al. [2016], Kings et al. [2016] or Mazur [2017].

- The simulations based on the model with the source term in the energy equation result in a dominance of the indirect noise below $200\,\mathrm{Hz}$, which is not in line with experimental observations by Kings et al. [2016] or Mazur [2017].

- The semi-analytical volume source model for perfectly premixed flames proposed in this thesis significantly improves the predictions of the flame behavior with respect to entropy wave generation. As it still produces unphysical entropy waves the model needs further improvements and calibration to allow quantitatively correct entropy predictions.

- An estimation showed that no entropy waves are generated by the premixed flame when applying the proposed volume source term model with an incoherent source term distribution model.

- The noise ratio is independent of the source spectrum as it represents a relative measure between entropy and acoustic wave generation by combustion, as long as constant nozzle properties are assumed.

8.3 Liquid Kerosene Fueled Combustor

The last test case in the current thesis deals with a liquid fueled combustor, which incorporates important characteristics of a real aero engine combustor, namely

- the non-premixed spray combustion of Jet A-1 kerosene, and

- the downstream boundary condition representing the turbine impedance.

After the introduction of the test rig and the simulation models, the results of the mean flow and the acoustics are presented. The analysis is completed by the determination of the noise ratio inside the combustor, which is discussed in detail in subsec. 8.3.5.

8.3.1 Configuration and Operating Conditions

The considered test rig represents the atmospheric single-burner test rig installed at the Lehrstuhl für Thermodynamik at TUM. The test rig can be operated under different conditions. In the present work one operating point is considered, which is referred to as *Climb* in the following. The operating point is specified in tab. 8.5.

Preheated air is supplied through a plenum duct. The combustion of Jet A-1 kerosene under lean conditions is established by the PERM injection system with a prefilming airblast atomizer nozzle [Keller et al., 2015, Kern et al., 2011, Marinov et al., 2010]. The injection system was developed by GE AVIO and the Karlsruhe Institute of Technology. The products are accelerated up to transonic conditions in the nozzle at the combustor outlet.

Operating Point	Climb
Air mass flow (g/s)	39.5
Equivalence ratio (-)	0.618
Fuel mass flow (g/s)	1.672
Adiabatic flame temperature (K)	1951.80
Thermal power (W)	72,083
Total temperature inlet (K)	598
Mean static pressure (bar)	1.0325

Table 8.5: Investigated operating point.

8.3.2 Numerical Setup

The numerical models related to the mean flow as well as the acoustic simulations are based on the work of Gikadi [2014] and Ullrich [2012]. In contrast to the CESAM-HP simulations the base flow simulation model does not contain the exit nozzle. This was done in order to apply an incompressible flow and combustion model like the assumed PDF approach. The nozzle is replaced by an appropriate boundary condition.

RANS Simulations

The RANS equations [ANSYS, 2011a] are solved in conjunction with a standard k-ϵ turbulence closure model according to the eqs. (2.20) and (2.21). Near wall turbulence is modeled using the standard wall function approach. The gaseous mean flow is assumed to be incompressible due to the low Mach numbers occurring in the combustor. Combustion is accounted for by two combustion models. The first model is a presumed PDF approach, where both the transport equations for the mixture fraction and its variance are solved [Gerlinger, 2005, Poinsot and Veynante, 2005]. Once the mixture fraction field and its variance are solved, the corresponding mean values of the species and temperature are deduced from the assumed PDF β-distribution. Non-adiabatic cooling effects are taken into account by evaluating the PDF for a number of discrete heat loss values [ANSYS, 2011a, chapter 8.2.3., page 235]. The second combustion model is the finite-rate/eddy-dissipation model (EDM), where four transport equations for kerosene $C_{12}H_{23}$, oxygen O_2, carbon dioxide CO_2 and water H_2O are solved according to the global reaction scheme: $C_{12}H_{23} + 17.75(O_2 + 79/21N_2) \leftrightarrow 12CO_2 + 11.5H_2O + 17.75 \cdot 79/21N_2$. In this way the influence of the combustion model on the resulting pressure spectrum is identified.

The continuous gas phase and discrete kerosene droplets are described in an Eulerian-Lagrangian framework, where the equations describing the particle motion are solved numerically by time integration (trapezoid rule) at each fifth iteration step. The interaction between the discrete and continuous phase is expressed in terms of source terms for the mass, energy and momentum equations. Liquid kerosene droplets are injected at the pressure swirl atomizer with prescribed temperature, mass flow rate and spray and dispersion angle. The linearized instability sheet atomization model developed by Schmidt et al. [1999]

139

is applied to describe the primary droplet breakup and atomization [ANSYS, 2011a]. The RANS equations are solved on a high quality hybrid mesh ensuring one-to-one connectivity at its interfaces.

The plenum duct is modeled by adiabatic wall boundary conditions, while a constant temperature of $\widetilde{T}_w = 673\,\mathrm{K}$ is imposed on the combustor walls. Despite of the convective cooling effect included in the model, it was found that in this setup the RANS simulation still tends to predict too high temperatures in the combustion chamber. This is likely to be caused by an underprediction of the heat losses. For this reason the effect of heat losses due to non-luminous radiation is included in the model by the implementation of an energy sink term $\dot{q}_r$ in the enthalpy equation (2.4) [Poinsot and Veynante, 2005]. The PERM injection system provides fine droplet atomization and intense mixing, which prevents the soot formation and results in blue flames at atmospheric conditions. This justifies to exclude the thermal radiation from soot particles by applying a non-luminous radiation model. Assuming a thin-optical medium of gray-gases and neglecting the turbulence-radiation interaction, the mean sink term[2] in the Reynolds-averaged form of eq. (2.4) reads according to Siegel and Howell [1971]

$$\widetilde{\dot{q}}_r := -4\sigma \bar{k}_p \big(\widetilde{T}^4 - \widetilde{T}_w^4 \big), \tag{8.13}$$

with $\sigma = 5.67 \cdot 10^{-8}\,\mathrm{W/(m^2 K^4)}$ being the Stefan-Boltzmann constant. $\bar{k}_p = \bar{k}_p(\bar{p}, \widetilde{Y}_i, \widetilde{T})$ represents the Plank mean absorption coefficient, which is determined by the gas composition (mole fractions $\widetilde{X}_i$) and the mean pressure $\bar{p}$:

$$\bar{k}_p = \bar{p} \sum_{i=1}^{n} \widetilde{X}_i k_{p,i}(\widetilde{T}) = \bar{p} \big[\widetilde{X}_{\mathrm{CO}} k_{p,\mathrm{CO}}(\widetilde{T}) + \widetilde{X}_{\mathrm{CO_2}} k_{p,\mathrm{CO_2}}(\widetilde{T}) + \widetilde{X}_{\mathrm{H_2O}} k_{p,\mathrm{H_2O}}(\widetilde{T}) \big]. \tag{8.14}$$

According to Baehr and Stephan [2006], Malalasekera et al. [2002], Viskanta and Mengüc [1987] only the thermal radiation of CO, CO_2 and H_2O are relevant in the infrared range, where ray scattering can be neglected as well. Consequently only these molecules are accounted for in eq. (8.14). The different Plank mean absorption coefficients $k_{p,i}$ are evaluated from the RADCAL database [Grosshandler, 1993] and are given in terms of temperature-dependent polynomials [Barlow, 2004]. The sink term according to eq. (8.13) was successfully applied in several numerical simulations [Barlow et al., 2001, Guo et al., 1997]. In this study a wall temperature of $\widetilde{T}_w = 673\,\mathrm{K}$ is assumed in eq. (8.13).

Statistical Noise Model Postprocessor

The RANS mean flow simulations are postprocessed in order to determine the integral heat release spectrum $\dot{\mathcal{Q}}_z(f)$ using the statistical noise model by Jörg [2015] for non-premixed

---

[2]Note that averaged values are inserted in eq. (2.4), but the exact formulation reads $\widetilde{\dot{q}}_r = -4\sigma\bar{p} \int_{-\infty}^{\infty} \sum_{i=1}^{n} X_i(z,\chi,\zeta) k_{p,i}(T(z,\chi,\zeta)) \big[T(z,\chi,\zeta)^4 - T_w^4 \big] p(z)p(\chi)p(\zeta) \mathrm{d}z \mathrm{d}\chi \mathrm{d}\zeta$ [Marracino and Lentini, 1997]. Furthermore, turbulence-radiation interactions are neglected by assuming $\overline{k_p T} \approx \bar{k}_p \bar{T}^4$ and $\overline{T^4} \approx \bar{T}^4$ to reduce the computational effort [Molina, 2015], despite of their importance [Coelho et al., 2003, Cumber, 2014, Hartick et al., 1996].

flames as introduced in detail in subsec. 4.3.2. Following the derivation of the local heat release spectrum (4.70) proposed in this thesis, the mean heat release rate is computed according to eq. (2.22) using the mean mixture fraction variance.

The resulting integral spectra of the heat release fluctuations $\dot{\mathcal{Q}}_z(f)$ obtained without and with the thermal radiation model are presented in fig. 8.36 for the presumed PDF approach and the finite rate/EDM combustion model. The presumed PDF approach and the finite rate/EDM combustion model deliver very similar peak frequencies. The latter model calculates a much lower peak amplitude of the fluctuating heat release rate. The heat release spectra obtained by these two combustion models converge towards each other for high frequencies. In conclusion the combustion model mainly affects the peak amplitude of the heat release spectrum, while it has a negligible influence on the spectral shape and peak frequency.

The application of the radiation model leads to a reduced peak amplitude, which is shifted towards higher frequencies at the same time. This behavior applies to both combustion models. To explain the impact of the thermal radiation model, different mean flow quantities were area-averaged in several combustor cross-section areas downstream of the airblast atomizer nozzle. The evaluation was done by taking the example of the finite rate/EDM combustion model. The mean volumetric heat release rate and the mean temperature are shown on the left and right in fig. 8.37. It is seen that the thermal radiation leads to a lower maximum of the volumetric heat release rate, which is shifted more upstream in comparison to the simulation without radiation. The reduced heat release rate results in a lower temperature level inside the combustor. Also the mean variance of the temperature is remarkably reduced due to the thermal radiation, which is visualized in fig. 8.38. The same applies to the generalized scaling constant c_s, which is proportional to the temperature variance according to eq. (4.61). Although not shown here, the ratio $\epsilon^{2/3}/\kappa$ between the turbulent dissipation and kinetic energy is decreased in case of thermal radiation. According to the heat release spectrum (4.70) the effects of a reduced mean heat release rate, generalized scaling coefficient and ratio of the turbulent dissipation and kinetic energy are multiplied with each other. Altogether these different effects lead to a significant decrease of the peak amplitude of the combustion noise source spectrum in the case of thermal radiation. In case of the finite rate/EDM combustion model the peak amplitude of the fluctuating heat release rate is reduced from $34\,\mathrm{W/Hz}$ to $19.5\,\mathrm{W/Hz}$. This peak amplitude reduction is in good agreement with the multiplication of the reducing factors for mean heat release of 0.84, the generalized scaling constant of about 0.79 and the ratio $\epsilon^{(2/3)}/\kappa$ of 0.96. The shift of the spectrum towards higher frequencies is caused by the upstream movement of the flame root. As shown in the right of fig. 8.39 in this case the flame is anchored in regions with higher turbulent frequencies due to stronger flow shearing in comparison to the case without thermal radiation. Also fig. 8.39 shows that main parameters of the combustion noise model are not influenced by the thermal radiation, so that the peak frequency shift is an exclusive effect of the upstream movement of the flame caused by thermal radiation. The same analysis of the mean flow quantities can be applied
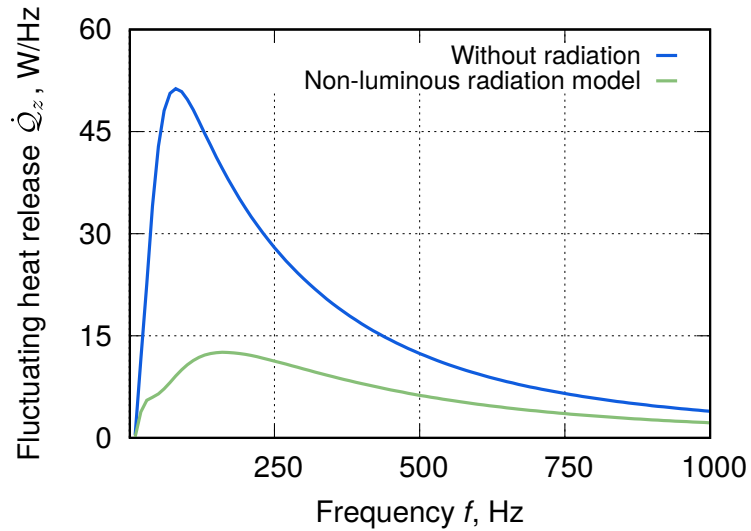
(a) Presumed PDF approach
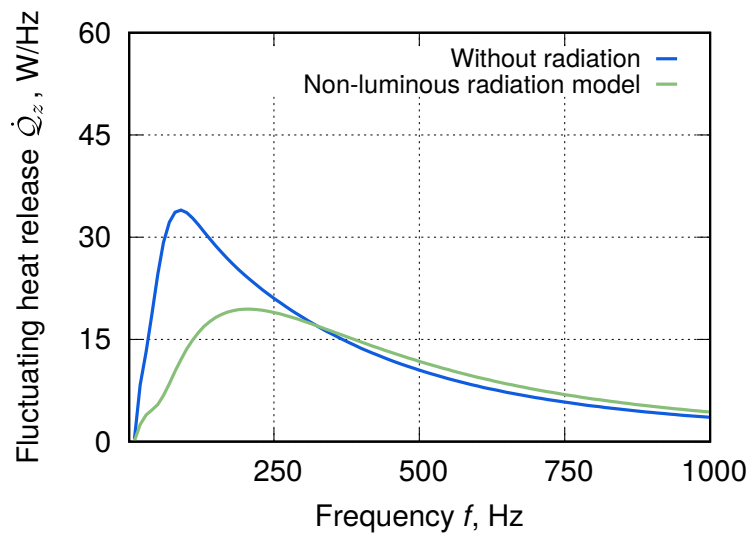
(b) Finite rate/EDM model

Figure 8.36: Influence of the thermal radiation on the spectrum of the fluctuating heat release $\dot{\mathcal{Q}}_z(f)$, [W/Hz] determined by the non-premixed combustion noise model by Jörg [2015] for the *Climb* operating point. RANS simulations based on different combustion models.
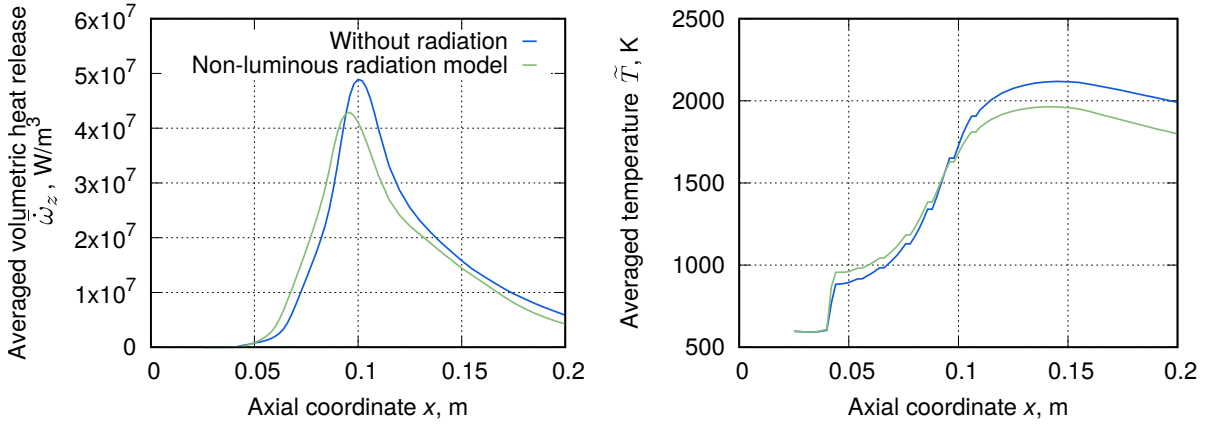
Figure 8.37: Area-averaged volumetric heat release rate (left) and temperature (right) predicted with and without thermal radiation in case of the finite rate/EDM combustion model.

on the PDF combustion model to identify the influence of the thermal radiation on the combustion noise source spectrum. The thermal radiation again leads to a reduction of the mean heat release and the temperature variance, but with greater extend in comparison to the finite rate/EDM combustion model. This in turn leads to a stronger reduction of the peak amplitude of the fluctuating heat release spectrum. Finally it is concluded that the following combustion noise model parameters were chosen independently from the combustion model applied in the RANS simulation: $c_l = 0.275$, $c_\mu = 0.09$, $c_\tau = 1.35$, $c_d = 2.0$, $\alpha = 1.5$ and $\beta = 0.3$.

LNSE Simulations

The acoustic simulations are based on a quasi two-dimensional axis-symmetrical model and a fully three-dimensional model, in which the LNSE (4.41) - (4.43) are solved by means of the GLS-FEM approach as given by eq. (5.12). Interactions between the turbulence and the acoustic, vorticity and entropy waves are incorporated in the linearized momentum eq. (4.42) and energy eq. (4.43) by the concept of the turbulent viscosity and turbulent heat conductivity. Mean density gradients $\partial \bar{\rho} / \partial x_i$ are not accounted for to improve numerical stability, which has no influence on the resulting pressure spectrum as demonstrated by Zhang et al. [2014]. The quasi 2D domain is represented by an unstructured grid of 16,540 triangle elements with second order Lagrangian shape functions, whereas the 3D model consists of 225,319 tetrahedral Lagrangian first order elements. The LNSE are excited by the energy source term $\hat{\dot{\omega}}_z$ in the linearized energy eq. (4.43) with discrete frequencies up to 1000 Hz. The different integral heat release spectra $\dot{\mathcal{Q}}_z(f)$ obtained by the statistical noise model by Jörg [2015] for non-premixed flames are redistributed to the local source term $\hat{\dot{\omega}}_z$ using the model in eq. (4.83). The simulation model is completed by the prescription of suitable boundary conditions to match the experimental conditions in the best way. All walls are described by the kinematic boundary condition (3.37). The nozzle at the
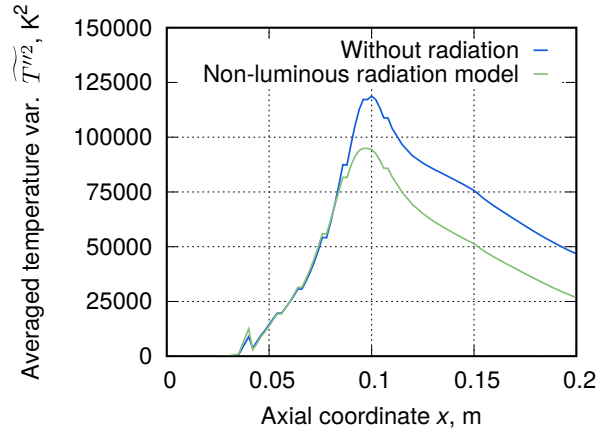
Figure 8.38: Area-averaged temperature variance (right) predicted with and without thermal radiation in case of the finite rate/EDM combustion model.

outlet is not included in the simulation model and therefore replaced by the fully-reflecting condition (3.42). It should be noted that the nozzle boundary condition (3.42) is strictly only valid for choked conditions. In the experiment the nozzle was not entirely choked but reached transonic conditions with Mach numbers from 0.9 to 0.95, so that the simulation is likely to slightly overestimate the reflections from the nozzle in the low frequency regime. The inlet is modeled by the partially reflecting impedance boundary condition (3.33), in which the reduced impedance $Z = (1 + R_{\mathrm{exp}})/(1 - R_{\mathrm{exp}})$ is obtained from measurements of the reflection coefficient by Gikadi [2014]. The reflection coefficient stays constant above $200\,\mathrm{Hz}$ at approximately 0.4.

The discretizations of the quasi 2D and full 3D domain are visualized in the figs. 8.40 and 8.41. The reasons for the application of the quasi 2D model are threefold: First, the mean flow field is almost axis-symmetrical except for the swirler channels of the PERM injector. Second, only the low frequency regime is relevant to the combustion noise, where only longitudinal modes are present. Finally, the computational time and requirements are by far lower than those of the 3D model. The quasi 2D model is numerically less stable than the 3D model, since it features no damping in circumferential direction. This might lead to unstable modes in circumferential direction. Such numerical stability issues are encountered below $100\,\mathrm{Hz}$, so that the quasi 2D model is only solved for frequencies higher than $100\,\mathrm{Hz}$.

In order to separate the direct and indirect noise contributions from the total combustion noise the procedure of subsec. 5.3.1 is applied to the combustor. A second simulation based on the isentropic nozzle boundary condition (3.43) is performed to identify the direct noise in the combustion chamber. Then subtracting the direct noise contribution from the total noise yields the indirect noise and finally the noise ratio. As discussed in sec. 4.4 the indirect noise computations are likely to be overpredicted due to the generation of fully
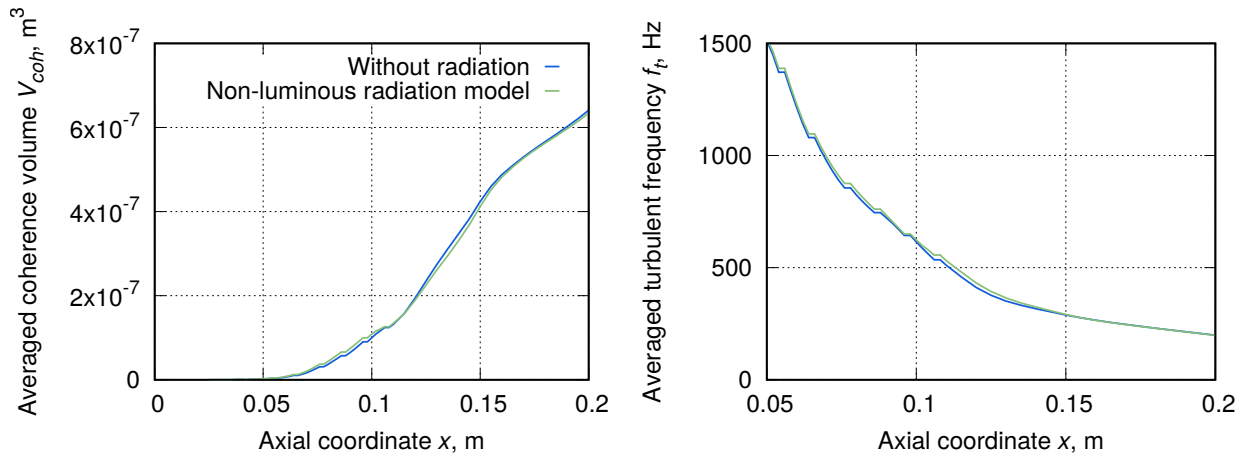
Figure 8.39: Area-averaged coherence volume (left) and turbulent frequency (right) predicted with and without thermal radiation in case of the finite rate/EDM combustion model.
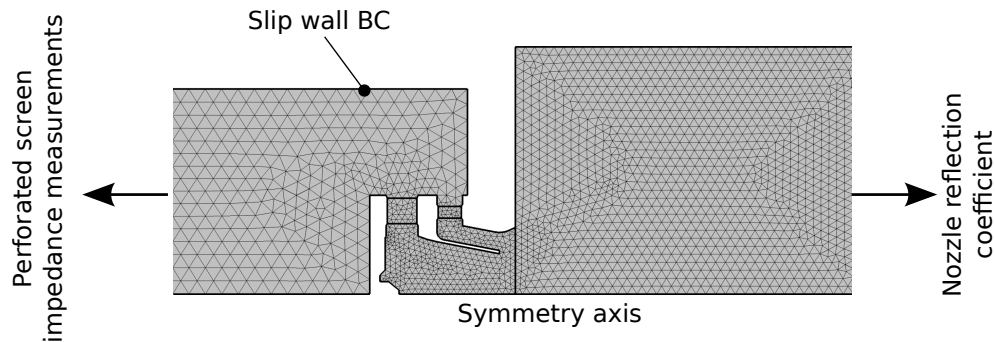
Figure 8.40: Quasi 2D LNSE model and the unstructured mesh of 16,540 elements, giving 170,520 degrees of freedom (dof).

coherent entropy waves over the flame volume by the distributed source term $\hat{\dot{\omega}}_z$.

8.3.3 Mean Flow Simulations

The mean flow simulations are carried out in a successive manner with increasing complexity for the operating point *Climb*. First the preheated non-reacting flow is computed. This is followed by the injection of the liquid kerosene Jet A-1 particles without considering an interaction between them and the gas phase. In a succeeding step the interaction between both phases is included and delivers the reacting flow fields as shown in fig. 8.42. In the current study the mean flow fields are normalized by their respective maximum values.

The application of the presumed PDF approach and the finite-rate/EDM model delivers similar high temperature levels if no radiation is considered. The latter model predicts slightly higher temperature levels as compared to the former one. When applying the
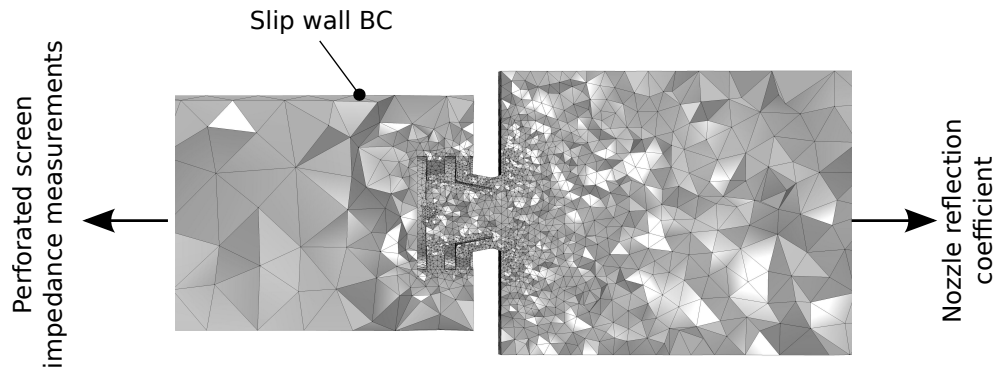
Figure 8.41: 3D LNSE model and the unstructured mesh of 225,319 elements, giving 224,665 degrees of freedom (dof).
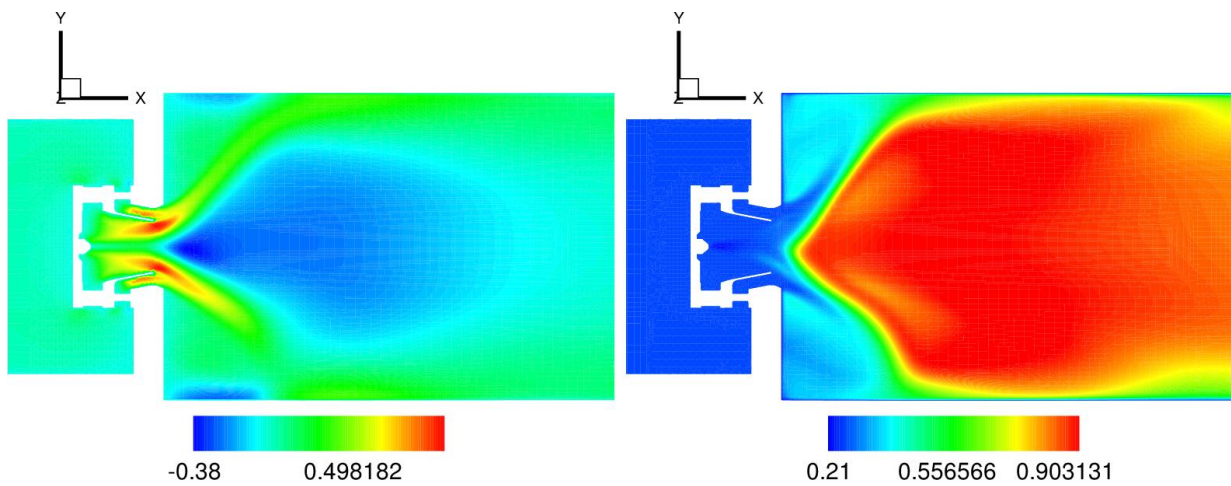
Figure 8.42: Reacting flow: Dimensionless mean axial velocity $\widetilde{u}/\widetilde{u}_{max}$ (left) and mean temperature $\widetilde{T}/\widetilde{T}_{max}$ (right) based on the PDF combustion model.

radiation model (8.13) the averaged temperature over the combustor volume is significantly reduced. These different temperature levels have a significant effect on the eigenfrequencies of the combustor as shown later in the acoustic part.

8.3.4 Total Noise

The acoustic pressure spectra obtained from the different LNSE models and underlying mean flow models are compared with the pressure measurements at the position at $x = 0.67$ m. All pressure spectra are given in terms of the SPL defined by eq. (5.1). The experimental validation data were acquired in the frame of the work by Gikadi [2014].

Influence of Combustion Model on Total Noise

In a first step the influence of the combustion model on the resulting pressure spectrum is investigated without considering thermal radiation. The corresponding results for the presumed PDF approach and the finite-rate/EDM model are compared in fig. 8.43 with each other and with the measurements by Gikadi [2014]. The acoustic simulations are based on the quasi 2D model. The trend is well represented by the numerical simulation for a broad frequency range above approximately 100 Hz, which applies to both combustion models. In general the shape of the pressure spectrum is only marginally affected by the combustion model apart from the eigenfrequencies. When using the presumed PDF model the first combustor eigenfrequency is predicted at 565 Hz, whereas the LNSE simulations based on the finite-rate/EDM model deliver 580 Hz. The first eigenfrequency is considerably overestimated for both combustion models in comparison to the experimental value of 510 Hz. As later shown the first combustor eigenfrequency corresponds to the $\lambda/2$-mode in the combustion chamber. The modeshape and the experimental and numerical eigenfrequency predictions can be used to estimate the overprediction of the mean combustor temperature by the RANS simulation, which yields about $\Delta\widetilde{T} \approx 290\,\mathrm{K}$ in comparison to the real conditions. Therefore the heat losses of the RANS model due to convective cooling appear to be too low regardless of the applied combustion model. In conclusion the application of the finite-rate/EDM model does not significantly improve the solution with respect to the first eigenfrequency.
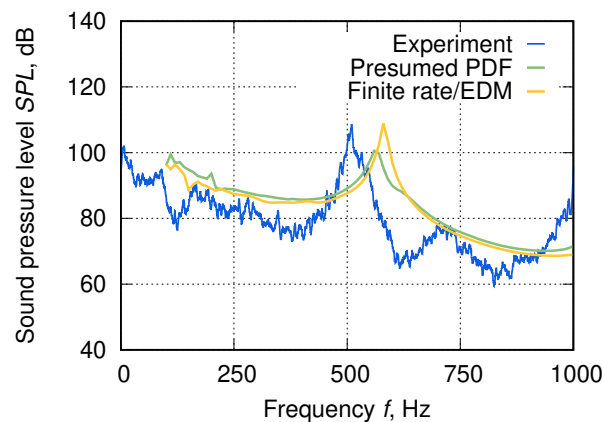
Figure 8.43: Influence of combustion modeling without radiation on the pressure spectrum, evaluated at the axial position $x = 0.67\,\mathrm{m}$ for the quasi 2D model.

Influence of Thermal Radiation on Total Noise

Remarkable improvement of the accuracy of the combustor eigenfrequency prediction is realized by the implementation of the thermal radiation model. As demonstrated in fig. 8.44 excellent agreement between the measured and predicted eigenfrequency is obtained when using the quasi 2D LNSE model in conjunction with the presumed PDF approach

including thermal radiation. Furthermore the radiation model performs better in the low frequency regime as compared to the model without radiation. In conclusion a correct representation of the heat losses and mean temperature levels in the combustor are essential for a correct prediction of the eigenfrequencies and the shape of the pressure spectrum.
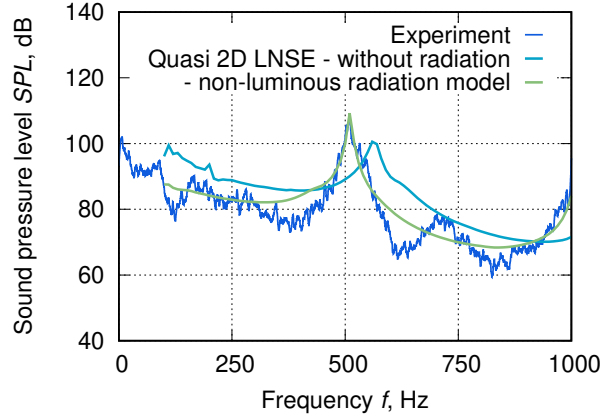
Figure 8.44: Influence of the radiation model on the pressure spectrum, evaluated at the axial position $x = 0.67$ m for the quasi 2D model.

The eigenfrequencies can be estimated prior to the acoustic simulation by considering the mean temperature levels predicted by the RANS simulation. In case of the presumed PDF approach with thermal radiation model the averaged temperature is associated with an average speed of sound in the combustor of $\bar{c}_{\mathrm{avg,rad}} = 735$ m/s. Then, the first eigenfrequency, representing the $\lambda/2$-mode of the combustor, with radiation model is estimated by

$$f_1 = \frac{\bar{c}}{2l_2} \approx 504 \, \mathrm{Hz}.$$

A combustor length of $l_2 = 0.73$ m was inserted. Without a radiation model the mean temperature level in the combustor results in an eigenfrequency of $f_1 \approx 570.86$ Hz. These values almost exactly correspond to the results obtained by the LNSE simulation.

Influence of Model Dimension on Total Noise

In fig. 8.45 it is demonstrated that the simplified quasi 2D model delivers comparable results to the full 3D model apart from the eigenfrequency. Both simulation results are based on the evaluation of the RANS with presumed PDF and thermal radiation model. The first eigenfrequency is slightly shifted towards higher frequencies and is more damped in the 3D model. The 3D model overpredicts the damping of the first combustor eigenfrequency, which might be caused by excessive acoustic vorticity interactions in the swirling flow. In general, the assumptions of the quasi 2D model are a valid approximation of the

real conditions even if they are not exactly fulfilled in the PERM injector. The quasi 2D model reduces the computational time by a factor of twelve at least.
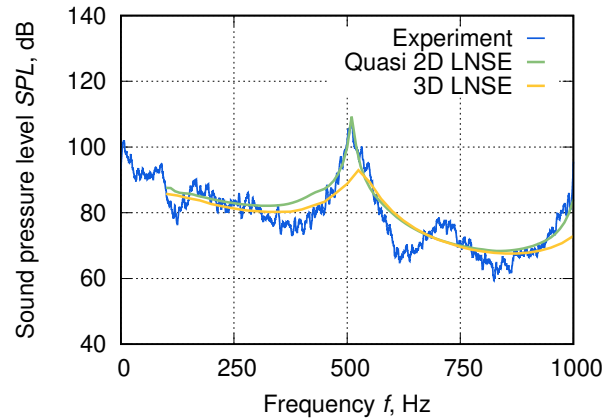
Figure 8.45: Influence of the model dimension on the pressure spectrum, evaluated at the axial position $x = 0.67\,\text{m}$ for the quasi 2D model.

8.3.5 Noise Ratio

Once entropy waves are generated in the flame, the indirect noise and therefore the noise ratio only depend on the propagation of the entropy waves from the flame zone to the combustor outlet. In fig. 8.46 the propagation of the acoustic, entropy and vorticity waves is evaluated at the first eigenfrequency at $510\,\text{Hz}$. The first eigenfrequency is caused by the $\lambda/2$-mode in the combustion chamber, which is clearly visible in fig. 8.46(a). The evolution of the entropy wave is visualized in fig. 8.46(b). Obviously the entropy wave is almost dissipated after the half length of the combustor. The behavior at this frequency is representative for a broad range of frequencies except for low frequencies below $100\,\text{Hz}$, where a small part of the initial entropy waves impinges on the combustor outlet. Apart from that, the entropy waves are not able to reach the nozzle and to release indirect noise because of the high aerodynamic damping. Therefore the indirect noise turns out to be negligible in this configuration. Then the total and direct noise are almost equal over the entire frequency range, which is not shown here.

However important modeling assumptions should be recalled when analyzing the results for the indirect noise above. First, the distribution model (4.83) for the combustion noise source term $\hat{\dot{\omega}}_z$ generates entropy waves with the same phase in the entire flame volume, which leads to an overestimation of the generated entropy waves, cf. sec. 4.4. This modeling limitation is presumably of minor importance for the regarded test case, where the indirect noise contribution is anyhow close to zero. Second, the model does not include the excitation of entropy waves due to the combustor wall cooling as density gradients are neglected in the LNSE model. This implies that the entropy waves might have a

(a)

(b)

(c)
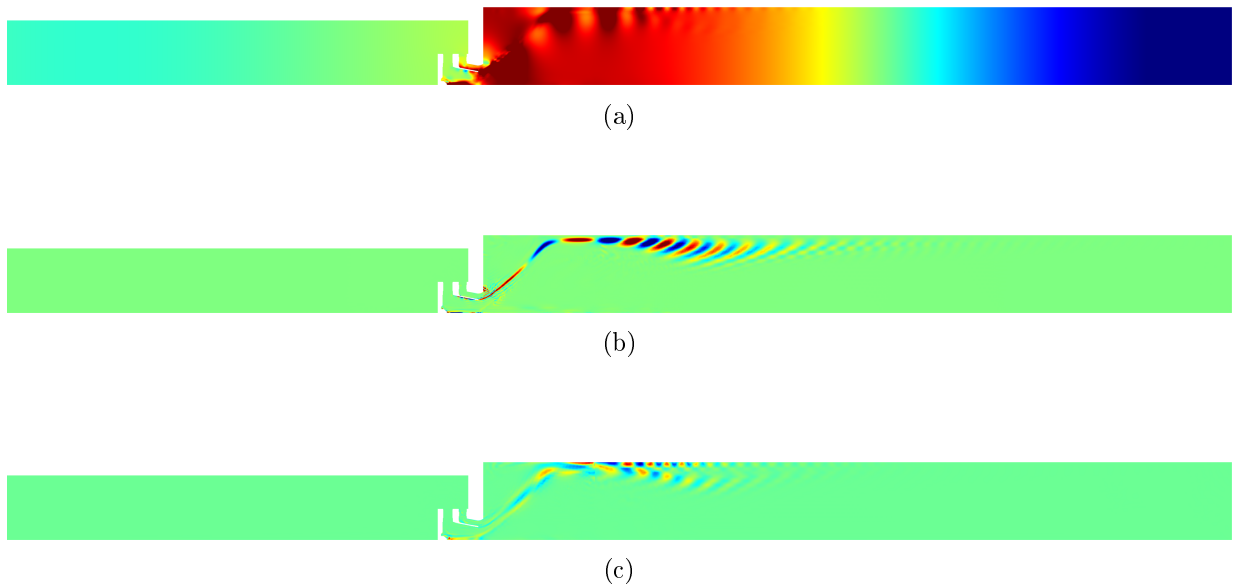
Figure 8.46: Quasi 2D model: Qualitative distribution of the fluctuating pressure $\Re\{\hat{p}\}$, [Pa] (top), entropy $\Re\{\hat{s}\}$, [J/(kgK)] (center), and circumferential vorticity $\Re\{\hat{\Omega}_\theta\}$, [1/s] (bottom) at the first eigenfrequency of 510 Hz.

stronger effect in reality. Nevertheless even in this case the contribution of indirect noise is expected to remain of minor importance. Finally, the combustor length of 0.73 m is not representative for real annular aero engine combustors, where typically ratios between the combustor length and height of $l/b = 2 \ldots 2.8$ are found [Bräunling, 2009]. With the given lateral combustor length of $b = 0.15$ m, the ratio l/b implies a realistic combustor length of $l = 0.3$ m $\ldots 0.42$ m. In this case of a shortened combustor, the indirect noise contribution is by far more relevant because a significant amount of the entropy waves is able to impinge on the nozzle. Then the error introduced by the coherent entropy wave generation might adversely influence the results, which was not the case in the considered elongated test rig. These issues should be addressed in future investigations on the indirect noise generated by liquid fueled combustion.

Summary

In conclusion the main findings of the analysis of the liquid fueled combustor test rig are as follows:

- The shape of the heat release source spectrum is only weakly influenced by the underlying combustion model when postprocessing the RANS simulation with the statistical noise model for non-premixed flames as proposed by Jörg [2015]. The combustion model mainly affects the peak amplitude, while the peak frequency remains unchanged.

- The heat release source spectrum depends on the mean temperature level and the

heat losses predicted by the RANS combustor simulations. Higher heat losses due to thermal radiation result in lower peak amplitudes and higher peak frequencies of the heat release spectrum. Therefore the quality of the heat release source spectrum obtained by the statistical noise model crucially depends on an appropriate prediction of the heat losses in the combustor.

- The trend and amplitude of the resulting pressure spectrum is well-predicted by the statistical noise model for non-premixed flames by Jörg [2015] when it is applied on the RANS simulation including the thermal radiation model.

- The quasi 2D and full 3D model deliver similar results apart from the low frequency range below 100 Hz, where the 3D model is more robust.

- The indirect noise appears to be negligible in this configuration as the entropy waves are dissipated due to the aerodynamic flow shearing before reaching the nozzle. The noise ratio of the combustor test rig is exactly or close to zero regardless of the applied combustion or radiation model.

- The considered combustion chamber length is not representative for aero engine combustors, which are much shorter in realistic applications. In this case of a shortened combustor length, the indirect noise might play a role as entropy waves are able to reach the combustor outlet.

9 Conclusion and Outlook

Reducing the pollutant and noise emissions of modern aero engines requires a thorough understanding of the underlying physics and further development and validation of numerical prediction tools. Considerable advances of the engine manufactures in reducing the jet, fan and compressor noise were achieved during the last decades. This has led to an increasing relevance of combustion noise, which holds in particular for take-off and approach conditions.

The objective of the present thesis is to contribute to the development of numerical tools for the prediction of combustion noise emitted by confined premixed and non-premixed swirling flames. This is achieved by further developing an existing hybrid approach using reactive RANS mean flow data with a frequency domain LNSE combustor simulation. In this thesis stochastic sound sources are incorporated in the LNSE following a rigorous derivation based on a triple-decomposition. The different physics of entropy wave generation in perfectly premixed and non-premixed flames are treated by a semi-analytical modeling approach. Premixed flames are modeled as a coupled volume source term in the linearized continuity and energy equation, which prevents the generation of entropy waves. Non-premixed flames are described by a fluctuating heat release term in the linearized energy equation, which acts as a source of both acoustic and entropy waves whenever mixture fraction fluctuations are present. The presented method is applied to two generic combustion chamber test rigs with stepwise increasing complexity, corresponding to a premixed pressurized gaseous flame and a non-premixed kerosene flame. Several modeling influences on the resulting combustion noise spectra are identified in each case. In a succeeding step the contributions of indirect and direct combustion noise are separated. The different sub-models are validated in the frame of a hierarchy of different test cases, beginning with the transmission of direct sound through generic nozzle configurations and ending up with the validation of the source models in an annular model combustor.

Based on the investigation of the different test cases and models the following conclusions are drawn:

- The direct combustion noise propagation through nozzles representing the turbine NGV is properly captured using the RANS/LNSE approach. The transmission of direct combustion noise increases monotonically with frequency.

- The validity of the hybrid approach for sufficiently accurate predictions of indirect noise generation due to entropy and vorticity disturbances is demonstrated in the

frame of the EWG and VWG test cases. The transmission of indirect noise arising from entropy waves is strongly dependent on the model dimension, which is related to the entropy shear dispersion effect. As a consequence the applicability of one-dimensional models for indirect noise predictions without the consideration of mean flow shearing is questionable.

- The approach by Dowling and Mahmoudi [2015] to separate the direct and indirect noise by varying the combustor outlet condition is implemented in the LNSE methodology. The procedure is validated by considering an annular model combustor, where excellent agreement is found between LNSE and LOTAN simulations.

- A semi-analytical model based on a triple-decomposition approach is proposed in this thesis in order to introduce turbulent stochastic combustion noise sources into the LNSE and to discriminate between perfectly premixed and diffusion flames with regard to the entropy wave generation. The theoretical derivations are confirmed in the annular model combustor test case, where a minor influence of indirect noise was obtained when using the model for perfectly-premixed flames.

- An energy-consistent model is proposed, which distributes the combustion noise source spectra over the entire flame volume with equal phase. While the distribution model does not affect the acoustic wave generation it leads to an overestimation of the entropy wave generation as phase differences between the local sources are neglected. Therefore the indirect noise computations for the non-premixed liquid kerosene flame are expected to be overpredicted.

- The statistical noise models by Hirsch et al. [2006, 2007] and by Liu et al. [2014] are applied conjointly with the hybrid RANS/LNSE approach on the CESAM-HP combustor. The quality of the computed combustion noise spectra based on the statistical noise models significantly depends on the quality of the underlying RANS simulations. Differences between the numerical and experimental combustion noise spectra are explained by inaccuracies of the turbulence quantities predicted by the RANS simulations. For OP-16-0-2 and OP-16-2-0 these inaccuracies of the RANS simulations lead to deviations between the predicted and experimental peak frequencies and peak amplitudes. In case of OP-13-5-0 the predicted peak frequency matches the experimental one, while the acoustic amplitudes are constantly underpredicted by the LNSE simulation. Significant improvement of the quality of the LNSE prediction is obtained when using sources extracted from incompressible LES.

- The application of the non-premixed noise model by Jörg [2015] to the liquid fueled kerosene combustor delivers good agreement with measurements. The quality of the prediction crucially depends on an appropriate modeling of heat losses in the combustor, which is realized by introducing a thermal radiation model.

- In general the combustion noise spectrum is driven by the heat release spectrum, while the spatial distribution and the phase of the combustion noise sources are of

minor importance for the direct noise.

- The comparison of the numerical results obtained by the LNSE and Helmholtz equation revealed a negligible influence of the mean flow in the combustor on the broadband direct noise spectrum.

- The application of the Helmholtz equation is sufficient for broadband direct noise predictions whenever the combustor outlet region with high Mach numbers can be replaced by appropriate boundary conditions. The prediction of the combustor eigenfrequencies can be improved by incorporating the acoustic damping effects due to mean flow interactions. Then the isentropic LNSE are the appropriate choice for the acoustic model. However, recent numerical studies by Hummel [2019] and by Hofmeister et al. [2019] have shown that exact predictions of acoustic damping rates require excessive mesh refinement to incorporate the acoustic-vorticity interactions on all different scales, which leads to a significantly increase of the computational effort in particular for 3D simulations. Non-isentropic LNSE simulations are only necessary if the indirect noise is of interest or other mechanisms of entropy wave generation like dilution air or wall cooling air injections should be taken into account.

- The quality of indirect noise predictions is essentially determined by the physics encoded in the source term model. In case of the premixed CESAM-HP combustor physically reasonable and consistent results with experimental data are only obtained when preventing the entropy wave generation by the flame. This is mainly achieved by the semi-analytical volume source model proposed in this thesis, which consists of source terms in the linearized continuity and energy equation of the non-isentropic LNSE. Both source terms are strictly coupled through the simplified pressure-density relation. The difficulties of an accurate modeling of the entropy wave generation in premixed and non-premixed flames are avoided by applying the Helmholtz equation or isentropic LNSE if only direct noise is regarded.

- In both combustor test cases the indirect combustion noise is found to play a minor role for the total noise spectrum. This is most probably explained by the premixed flame in the CESAM-HP combustor. In the liquid kerosene combustor the high damping of entropy waves due to shear dispersion and the unrealistic length of the combustor test rig itself are responsible for the negligible indirect noise contribution.

A complete methodology starting from the source term modeling and ending up with the noise propagation, is established and validated in the frame of this thesis. However there are a number of possible topics for future studies and improvements on the existing models, which are the following:

- The source term distribution model for non-premixed flames should be extended to include phase-differences between the local entropy sources. By this means the entropy shear dispersion effect is increased in the flame volume, which presumably leads to an improvement of the indirect noise predictions.

- The limitations of the LNSE regarding the propagation of entropy waves should be addressed by a deeper investigation of the effect of the linearization of convective terms, which might lead to an unphysical entropy wave production in non-isentropic mean flows.

- The theoretically derived noise source terms in the continuity and energy equation should be computed using either URANS simulations or even LES. Then the relation between the two source terms does not need to be modeled for the special cases of perfectly premixed and non-premixed flames as done in this thesis. As the relation between both source terms controls the entropy production the URANS or LES computation should directly result in the correct behavior of the different flame types with regard to entropy wave generation.

- Finally the transmission of direct noise and generation of indirect noise in the turbine blade stages was not considered so far. This can be achieved for instance by extending the models by analytical approaches such as the actuator-disc theory [Cumpsty and Marble, 1977b].

List of Figures

157

List of Tables

Bibliography

N.A. Adams. Grundlagen der numerischen Strömungsmechanik. Vorlesungsskript, Technische Univeristät München: Lehrstuhl für Aerodynamik, November 2007.

N.A. Adams. Turbulente Strömungen: Einführung in die Theorie und Berechnung. Vorlesungsskript, Technische Univeristät München: Lehrstuhl für Aerodynamik, May 2008.

N.A. Adams. Gasdynamik. Vorlesungsskript, Technische Univeristät München: Lehrstuhl für Aerodynamik, April 2010.

M. S. Anand, R. Eggels, M. Staufer, M. Zedda, and J. Zhu. An Advanced Unstructured-Grid Finite-Volume Design System for Gas Turbine Combustion Analysis. *ASME 2013 Gas Turbine India Conference, GTINDIA 2013*, D(GTINDIA2013-3537):1–12, 2013. doi: 10.1115/GTINDIA2013-3537.

ANSYS. *ANSYS FLUENT Theory Guide*. ANSYS, Inc., Southpointe 275 Technology Drive, Canonsburg, PA 15317, November 2011a. `http://www.ansys.com`.

ANSYS. *ANSYS FLUENT User's Guide*. ANSYS, Inc., Southpointe 275 Technology Drive, Canonsburg, PA 15317, November 2011b. `http://www.ansys.com`.

H.D. Baehr and K. Stephan. *Wärme- und Stoffübertragung*. Springer Verlag Berlin Heidelberg New York, 5. edition, 2006. ISBN 978-3-540-32334-1.

C. Bailly and D. Juve. A stochastic approach to compute subsonic noise using linearized euler's equations. In *5th AIAA/CEAS Aeroacoustics Conference and Exhibit*, number AIAA 99-1872, 1999. doi: 10.2514/6.1999-1872.

C. Bailly, P. Lafon, and S. Candel. Computation of noise generation and propagation for free and confined turbulent flows. In *2nd AIAA/CEAS Aeroacoustics Conference*, number AIAA 96-1732, 1996.

C. Bailly, C. Bogey, and S. Candel. Modelling of Sound Generation by Turbulent Reacting Flows. *International Journal of Aeroacoustics*, 9(4-5), June 2010. doi: 10.2514/3.12008.

F. Bake, N. Kings, and I. Röhle. Fundamental Mechanism of Entropy Noise in Aero-Engines: Experimental Investigation. *ASME Journal of Engineering for Gas Turbines and Power*, 130(1), January 2008. doi: 10.1115/1.2749286.

F. Bake, C. Richter, B. Muehlbauer, N. Kings, I. Röhle, F. Thiele, and B. Noll. The Entropy Wave Generator (EWG): A reference case on entropy noise. *Journal of Sound and Vibration*, 326(3-5):574–598, 2009. doi: 10.1016/j.jsv.2009.05.018.

R.S. Barlow. International workshop on measurement and computation of turbulent non-premixed flames, 2004. URL `http://www.ca.sandia.gov/TNF/`.

R.S. Barlow, A.N. Karpetis, and J.H. Frank. Scalar Profiles and NO Formation in Laminar Opposed-Flow Partially Premixed Methane/Air Flames. *Combustion and Flame*, 127(3): 2102–2118, 2001.

G.L. Le Beau, S.E. Ray, S.K. Aliabadi, and T.E. Tezduyar. SUPG finite element computation of compressible flow with the entropy and conservation variables formulations. *Computer Methods in Applied Mechanics and Engineering*, 104(3):397–442, 1993.

W. Bechara, C. Bailly, P. Lafon, and S. Candel. Stochastic approach to noise modeling for free turbulent flows. *AIAA Journal*, 32(3), October 1994. doi: 10.2514/3.12008.

W.J.G. Bräunling. *Flugzeugtriebwerke*. Springer Dordrecht Heidelberg London New York, 3rd edition, January 2009.

K.N.C. Bray and J.B. Moss. A unified statistical model of the premixed turbulent flame. *Acta Astronautica*, 4(3-4):291–319, March 1977.

K.N.C. Bray, M. Champion, and J.B. Moss. Mean reaction rates in premixed turbulent flames. In *Twenty-Second Symposium (International) on Combustion*, volume 22, pages 763–769, 1988.

M.J. Brear, F. Nicoud, T. Mohsen, A. Giauque, and E.R. Hawkes. Disturbance energy transport and sound production in gaseous combustion. *Journal of Fluid Mechanics*, 707:53–73, 2012. doi: 10.1017/jfm.2012.264.

T.P. Bui, W. Schröder, and M. Meinke. Source Term Evaluation of the APE-RF System. In *12th AIAA/CEAS Aeroacoustics Conference*, number AIAA 2006-2678, May 2006.

T.P. Bui, M. Ihme, M. Meinke, W. Schröder, and H. Pitsch. Numerical Investigation of Combustion Noise and Sound Source Mechanisms in a Non-premixed Flame using LES and APE-RF. In *13th AIAA/CEAS Aeroacoustics Conference*, number AIAA 2007-3406, May 2007a.

T.P. Bui, W. Schröder, and M. Meinke. Acoustic Perturbation Equations for Reacting Flows to Compute Combustion Noise. *International Journal of Aeroacoustics*, 6(4):335–355, 2007b. doi: 10.1260/147547207783359468.

S. Candel, D. Durox, S. Ducruix, A.-L. Birnaud, N. Noiray, and T. Schuller. Flame dynamics and combustion noise: Progress and challenges. *International Journal of Aeroacoustics*, 8(1):1–56, June 2009. doi: 10.1260/147547209786234984.

B.T. Chu and L.S.G. Kovásznay. Non-linear interactions in a viscous heat-conducting compressible gas. *Combustion and Flame*, 3(5):494–514, February 1958. doi: doi:10. 1017/S0022112058000148.

P. Clavin and E.D. Siggia. Turbulent Premixed Flames and Sound Generation. *Combustion Science and Technology*, 78:147–155, 1991. doi: 10.1080/00102209108951745.

R. Codina. Comparison of some finite element methods for solving the diffusion-convection-reaction equation. *Computer Methods in Applied Mechanics and Engineering*, 156(1): 185–210, 1998. doi: 10.1016/S0045-7825(97)00206-5.

R. Codina. On stabilized finite element methods for linear systems of convection-diffusion-reaction equations. *Computer Methods in Applied Mechanics and Engineering*, 188(1): 61–82, 2000. doi: 10.1016/S0045-7825(00)00177-8.

P.J. Coelho, O.J. Teerling, and D. Roekaerts. Spectral radiative effects and turbulence/radiation interaction in a non-luminous turbulent jet diffusion flame. *Combustion and Flame*, 133(1):75–91, 2003. doi: 10.1016/S0010-2180(02)00542-4.

COMSOL. *COMSOL Multiphysics Reference Guide*, May 2011.

D.G. Crighton, A.P. Dowling, J.E. Ffowcs Williams, M. Heckl, and F.G. Leppington. *Modern Methods in Analytical Acoustics: Lecture Notes*. Springer-Verlag London, 1992.

P.S. Cumber. Validation study of a turbulence radiation interaction model: Weak, intermediate and strong TRI in jet flames. *International Journal of Heat and Mass Transfer*, 79:1034–1047, December 2014. doi: 10.1016/j.ijheatmasstransfer.2014.08.073.

N.A. Cumpsty. Jet engine combustion noise: Pressure, entropy and vorticity perturbations produced by unsteady combustion or heat addition. *Journal of Sound and Vibration*, 66 (4):527–544, 1979. doi: 10.1016/0022-460X(79)90697-7.

N.A. Cumpsty and F.E. Marble. Core noise from gas turbine exhausts. *Journal of Sound and Vibration*, 54(2):297–309, 1977a. doi: 10.1016/0022-460X(77)90031-1.

N.A. Cumpsty and F.E. Marble. The interaction of entropy fluctuations with turbine blade rows; a mechanism of turbojet engine noise. *Proceedings of the Royal Society London*, 357(2):323–344, 1977b. doi: 10.1098/rspa.1977.0171.

J. Delfs. Basics of Aeroacoustics. Vorlesungsskript, DLR - Deutsches Zentrum für Luft- und Raumfahrt e.V.: Institut für Aerodynamik und Strömungstechnik, October 2016.

R.W. Dibble, W. Kollmann, and R.W. Schefer. Conserved scalar fluxes measured in a turbulent nonpremixed flame by combined laser Doppler velocimetry and laser Raman scattering. *Combustion and Flame*, 55(3):307–321, 1984. doi: 10.1016/0010-2180(84) 90170-6.

J. Donea and A. Huerta. *Finite Element Methods for Flow Problems*. Wiley, 7th edition, 2003. ISBN 0-471-49666-9.

A.P. Dowling. The calculation of thermoacoustic oscillations. *Journal of Sound and Vibration*, 180(4):557–581, 1995. doi: 10.1006/jsvi.1995.0100.

A.P. Dowling and Y. Mahmoudi. Combustion Noise. 35(1):65–100, 2015. doi: 10.1016/j.proci.2014.08.016.

A.P. Dowling and S.R. Stow. Acoustic Analysis of Gas Turbine Combustors. *Journal of Propulsion and Power*, 19(5), October 2003. doi: 10.2514/2.6192.

I. Duran and S. Moreau. Analytical and numerical study of the Entropy Wave Generator experiment on indirect combustion noise. In *17th AIAA/CEAS Aeroacoustics Conference*, number AIAA 2011-2829, June 2011. doi: 10.2514/6.2011-2829.

I. Duran and S. Moreau. Solution of the quasi-one-dimensional linearized Euler equations using flow invariants and the Magnus expansion. *Journal of Fluid Mechanics*, 723:190–231, April 2013. doi: 10.1017/jfm.2013.118.

J. Eckstein and T. Sattelmayer. Low-Order Modeling of Low-Frequency Combustion Instabilities in Aeroengines. *Journal of Propulsion and Power*, 22(2), March 2006. doi: 10.2514/1.15757.

J. Eckstein, E. Freitag, C. Hirsch, and T. Sattelmayer. Experimental Study on the Role of Entropy Waves in Low-Frequency Oscillations in a RQL Combustor. *ASME Journal of Engineering for Gas Turbines and Power*, 128:264–270, 2006. doi: 10.1115/1.2132379.

K. Ehrenfried. Strömungsakustik I. Vorlesungsskript WS2002/2003, Technische Univeristät Berlin, November 2002.

S. Evesque, W. Polifke, and C. Pankiewitz. Spinning and azimuthally standing acoustic modes in annular combustors. In *9th AIAA/CEAS Aeroacoustics Conference*, number AIAA 2003-3182, May 2003.

R. Ewert. Broadband Slat Noise Prediction Based on CAA and Stochastic Sound Sources from a Fast Random Particle-Mesh (RPM) Method. *Computers & Fluids*, 37(4):369–387, 2008. doi: 10.1016/j.compfluid.2007.02.003. URL `http://elib.dlr.de/45113/`.

R. Ewert and W. Schröder. Acoustic perturbation equations based on flow decomposition via source filtering. *Journal of Computational Physics*, 188(2):365–398, March 2003. doi: 10.1016/S0021-9991(03)00168-2.

J.H. Ferziger and M. Peric. *Numerische Strömungsmechanik*. Springer Verlag Berlin Heidelberg, 3. edition, February 2008.

A. Fischer. *Hybride, thermoakustische Charakterisierung von Drallbrennern.* PhD thesis, Technische Universität München, April 2004.

P. Gerlinger. *Numerische Verbrennungssimulation - Effiziente Numerische Simulation turbulenter Verbrennung.* Springer Verlag, 2005.

A. Giauque, T. Poinsot, M. Brear, and F. Nicoud. Budget of disturbance energy in gaseous reacting flows. In *Proceedings of the Summer Program 2006*, pages 285–297, 2006.

J. Gikadi. *Prediction of Acoustic Modes in Combustors using Linearized Navier-Stokes Equations in Frequency Space.* PhD thesis, Technische Univeristät München, 2014. https://www.td.mw.tum.de/fileadmin/w00bso/www/Forschung/Dissertationen/Gikadi2014.pdf.

J. Gikadi, T. Sattelmayer, and A. Peschiulli. Effects of the Mean Flow Field on the Thermo-Acoustic Stability of Aero-Engine Combustion Chambers. In *Proceedings of ASME Turbo Expo 2012*, volume 2, June 2012a. doi: 10.1115/GT2012-69612.

J. Gikadi, M. Schulze, J. Schwing, S. Föller, and T. Sattelmayer. Linearized Navier-Stokes and Euler equations for the determination of the acoustic scattering behaviour of an area extension. In *Proceedings of the 18th AIAA/CEAS Conference*, August 2012b. doi: 10.2514/6.2012-2292.

J. Gikadi, W.C. Ullrich, T. Sattelmayer, and F. Turrini. Prediction of the Acoustic Losses of a Swirl Atomizer Nozzle Under Non-Reactive Conditions. In *Proceedings of ASME Turbo Expo 2013*, number GT2013-95449, June 2013. doi: 10.1115/GT2013-95449.

J. Gikadi, S. Föller, and T. Sattelmayer. Impact of Turbulence on the Prediction of Linear Aeroacoustic Interactions: Acoustic Response of a Turbulent Shear Layer. *Journal of Sound and Vibration*, 333(24):6548–6559, 2014. doi: 10.1016/j.jsv.2014.06.033.

C.S. Goh and S. Morgans. The effect of entropy wave dissipation and dispersion on thermoacoustic instability in a model combustor. In *17th AIAA/CEAS Aeroacoustics Conference (32nd AIAA Aeroacoustics Conference)*, number AIAA 2011-2914, June 2011. doi: 10.2514/6.2011-2914.

M.E. Goldstein. A generalized acoustic analogy. *Journal of Fluid Mechanics*, 488:315–333, 2003. doi: 10.1017/S0022112003004890.

F. Grimm, B. Noll, M. Aigner, R. Ewert, and J. Dierke. The Fast Random Particle Method for Combustion Noise Prediction. In *20th AIAA/CEAS Aeroacoustics Conference*, June 2014. doi: 10.2514/6.2014-2451.

W.L. Grosshandler. RADCAL: A Narrow-Band Model for Radiation Calculations in a Combustion Environment, April 1993.

A. Gulati and J.F. Driscoll. Velocity-Density Correlations and Favre Averages Measured in a Premixed Turbulent Flame. *Combustion Science and Technology*, 48(5-6):285–307, 1986. doi: 10.1080/00102208608923898.

H. Guo, Y. Ju, K. Maruta, T. Niioka, and F. Liu. Radiation Extinction Limit of Counterflow Premixed Lean Methane-Air Flames. *Combustion and Flame*, 109(4):639–646, 1997. doi: 10.1016/S0010-2180(97)00050-3.

J.W. Hartick, M. Tacke, G. Flüchtel, E.P. Hassel, and J. Janicka. Interaction of Turbulence and Radiation in Confined Diffusion Flames. *Twenty-Sixth Symposium (International) on Combustion/ The Combustion Institute*, 26(1):75–82, 1996. doi: 10.1016/S0082-0784(96)80202-5.

C. Hirsch. Undisclosed notes on combustion noise model. Technische Universität München: Lehrstuhl für Thermodynamik, Garching, Germany, September 2018.

C. Hirsch, A. Winkler, J. Waesle, and T. Sattelmayer. Calculating the Turbulent Noise Source of Premixed Swirl Flames from Time Mean Reactive RANS Variables. In *13st International Congress on Sound And Vibration*, pages 588–595, 2006.

C. Hirsch, J.G. Wäsle, A. Winkler, and T. Sattelmayer. A spectral model for the sound pressure from turbulent premixed combustion. *Proceedings of the Combustion Institute*, 31(1):1435–1441, 2007. doi: 10.1016/j.proci.2006.07.154.

T. Hofmeister, T. Hummel, B. Schuermans, and T. Sattelmayer. Modeling and quantification of acoustic damping induced by vortex shedding in non-compact thermoacoustic systems. In *Proceedings of ASME Turbo Expo 2019*, number GT2019-90241, June 2019.

M.S. Howe. Indirect combustion noise. *Journal of Fluid Mechanics*, 659:267–288, 2010. doi: 10.1017/S0022112010002466.

M. Huet, F. Vuillot, N. Bertier, M. Mazur, N. Kings, W. Tao, P. Scouflaire, F. Richecoeur, S. Ducruix, L. Lapeyre, and T. Poinsot. Recent improvements in combustion noise investigation: from combustion chamber to nozzle flow. *Accepted for publication in AerospaceLab Journal*, 2016.

T.J.R. Hughes and M. Mallet. A new finite element method for computational fluid dynamics: III. The generalized streamline operator for multidimensional advective-diffusive systems. *Computer Methods in Applied Mechanics and Engineering*, 58(3):305–328, 1986. doi: 10.1016/0045-7825(86)90152-0.

T.J.R. Hughes, L.P. Franca, and G.M. Hulbert. A new finite element formulation for computational fluid dynamics: VIII. The Galerkin/least-squares method for advective-diffusive equations. *Computational Methods in Applied Mechanical Engineering*, 73(2): 173–189, 1989. doi: 10.1016/0045-7825(89)90111-4.

T. Hummel. *Modeling and Analysis of High-Frequency Thermoacoustic Oscillations in Gas Turbine Combustion Chambers*. PhD thesis, Technische Univeristät München, 2019. `http://www.td.mw.tum.de/fileadmin/w00bso/www/Forschung/Dissertationen/Hummel2019.pdf`.

A.K.M.F. Hussain and W.C. Reynolds. The mechanics of an organized wave in turbulent shear flow. *Journal of Fluid Mechanics*, 41(2), 1970. doi: 10.1017/S0022112070000605.

A.K.M.F. Hussain and W.C. Reynolds. The mechanics of an organized wave in turbulent shear flow. Part 3. Theoretical models and comparisons with experiments. *Journal of Fluid Mechanics*, 54(2), 1972. doi: 10.1017/S0022112072000679.

C. Jörg, J. Gikadi, and T. Sattelmayer. Numerical Investigation of the Plane-Wave Reflection Coefficient of an Exhaust Pipe at Elevated Temperatures Using Linearized Navier-Stokes Equations. In *Proceedings of ASME Turbo Expo 2013*, number GT2013-94843, June 2013. doi: 10.1115/GT2013-94843.

C.M. Jörg. *Experimental Investigation and Spectral Modeling of Turbulent Combustion Noise from Premixed and Non-premixed Flames*. PhD thesis, Technische Univeristät München, 2015. `https://www.td.mw.tum.de/fileadmin/w00bso/www/Forschung/Dissertationen/joerg2015.pdf`.

J. Keller, M. Gebretsadik, P. Habisreuther, F. Turrini, N. Zarzalis, and D. Trimis. Numerical and experimental investigation on droplet dynamics and dispersion of a jet engine injector. *International Journal of Multiphase Flow*, 75:144–162, May 2015. doi: 10.1016/j.ijmultiphaseflow.2015.05.004.

M. Kern, S. Marinov, P. Habisreuther, N. Zarzalis, A. Peschiulli, and F. Turrini. Characteristics of an ultra-lean swirl combustor flow by LES and comparison to measurements. In *Proceedings of ASME Turbo Expo 2011*, number GT2011-45300, June 2011. doi: 10.1115/GT2011-45300.

N. Kings. *Indirect combustion noise: Experimental investigation of the vortex sound generation in nozzle flow*. PhD thesis, Technische Universität Berlin, 2015.

N. Kings and F. Bake. Indirect combustion noise: noise generation by accelerated vorticity in a nozzle flow. *International Journal of spray and combustion dynamics*, 2(3):253–266, 2010. doi: 10.1260/1756-8277.2.3.253.

N. Kings, L. Enghardt, and F. Bake. Indirect Combustion Noise: Experimental Investigation of the Vortex Sound Generation in a Chocked Convergent-divergent Nozzle. In *Proceedings of Acoustics 2012 Nantes Conference*, April 2012.

N. Kings, M. Mazur, W. Tao, P. Scouflaire, F. Richecoeur, and S. Ducruix. Experimental and numerical investigation on combustion noise sources in a choked model gas turbine combustor. In *ANERS 2015 / XNOISE conference*, September 2015.

171

N. Kings, W. Tao, P. Scouflaire, F. Richecoeur, and S. Ducruix. Experimental and Numerical Investigation of Direct and Indirect Combustion Noise Contributions in a Lean Premixed Laboratory Swirled Combustor. In *Proceedings of ASME Turbo Expo 2016*, number GT2016-57848, June 2016. doi: 10.1115/GT2016-57848.

S.A. Klein. *On the acoustics of turbulent non-premixed flames.* PhD thesis, Universitat Twente, 2000.

K. Knobloch, T. Werner, and F. Bake. Noise Generation in Hot Nozzle Flow. In *Proceedings of ASME Turbo Expo 2015*, number GT2015-43702, June 2015. doi: 10.1115/GT2015-43702.

S. Kotake. On combustion noise related to chemical reactions. *Journal of Sound and Vibration*, 42(3):399–410, 1990.

S. Kotake and K. Takamoto. Combustion noise: Effects of the shape and size of burner nozzle. *Journal of Sound and Vibration*, 112(2):345–354, 1987. doi: 10.1016/S0022-460X(87)80201-8.

S. Kotake and K. Takamoto. Combustion noise: Effects of the velocity and turbulence of unburned mixture. *Journal of Sound and Vibration*, 139(1):9–20, 1990. doi: 10.1016/0022-460X(90)90771-Q.

L.S.G. Kovásznay. Turbulence in Supersonic Flow. *Journal of the Aeronautical Science*, 20(10):657–674, October 1953. doi: 10.2514/8.2793.

K. Lackhove, A. Sadiki, and J. Janicka. Efficient Three Dimensional Time-Domain Combustion Noise Simulation of a Premixed Flame Using Acoustic Perturbation Equations and Incompressible LES. In *Proceedings of ASME Turbo Expo 2017*, number GT2017-63050, June 2017. doi: 10.1115/GT2017-63050.

C.J. Lapeyre, M. Mazur, P. Scouflaire, F. Richecoeur, S. Ducruix, and T. Poinsot. Acoustically Induced Flashback in a Staged Swirl-Stabilized Combustor. *Flow, Turbulence and Combustion*, 98(1):265–282, January 2017. doi: 10.1007/s10494-016-9745-2.

M. Leyko, F. Nicoud, and T. Poinsot. Comparison of Direct and Indirect Combustion Noise Mechanisms in a Model Combustor. *AIAA Journal*, 47(11), November 2009. doi: 10.2514/1.43729.

M. Leyko, S. Moreau, F. Nicoud, and T. Poinsot. Waves Transmission and Generation in Turbine Stages in a Combustion-Noise Framework. In *16th AIAA/CEAS Aeroacoustics Conference*, number AIAA 2010-4032, June 2010. doi: 10.2514/6.2010-4032.

M. Leyko, S. Moreau, F. Nicoud, and T. Poinsot. Numerical and analytical modelling of entropy noise in a supersonic nozzle with a shock. *Journal of Sound and Vibration*, 330 (16):3944–3958, 2011. doi: 10.1016/j.jsv.2011.01.025.

T. Lieuwen. Modeling premixed combustion-acoustic wave interactions: A review. *Journal of Propulsion and Power*, 19(5), October 2003.

T.C. Lieuwen. *Unsteady Combustor Physics*. Cambridge University Press, 2012.

M.J. Lighthill. On sound generated aerodynamically II. Turbulence as a source of sound. *Proceedings of the Royal Society of London. Series A. Mathematical and Physical Sciences*, 222(1148):1–32, 1954. doi: 10.1098/rspa.1954.0049.

M.J. Lighthill and M.H.A. Newman. On sound generated aerodynamically I. General theory. *Proceedings of the Royal Society of London. Series A. Mathematical and Physical Sciences*, 211(1107):564–587, 1952. doi: 10.1098/rspa.1952.0060.

Y. Liu, A.P. Dowling, N. Swaminathan, R. Morvant, M.A. Macquisten, and L.F. Caracciolo. Prediction of Combustion Noise for an Aeroengine Combustor. *Journal of Propulsion and Power*, 30(1):114–122, February 2014. doi: 10.2514/1.B34857.

T. Livebardon, S. Moreau, T. Poinsot, and E. Bouty. Numerical investigation of combustion noise generation in a full annular combustion chamber. In *21th AIAA/CEAS Aeroacoustics Conference*, June 2015. doi: 10.2514/6.2015-2971.

T. Livebardon, S. Moreau, L. Gicquel, T. Poinsot, and E. Bouty. Combining les of combustion chamber and an actuator disk theory to predict combustion noise in a helicopter engine. *Combustion and Flame*, 165:272–287, March 2016.

Y. Mahmoudi, A.P. Dowling, and S.R. Stow. Direct and indirect combustion noise in an idealised combustor. In *25th International Colloquium on Dynamic of Explosions and Reactive Systems (ICDERS)*, August 2015.

W. Malalasekera, H.K. Versteeg, J.C. Henson, and J.C. Jones. Calculation of Radiative Heat Transfer in Combustion Systems. *Clean Air*, 3(1):113–143, 2002. doi: 10.1080/15614410211849.

F.E. Marble and S.M. Candel. Acoustic disturbances from gas non-uniformities convected through a nozzle. *Journal of Sound and Vibration*, 55(2):225–243, 1977. doi: 10.1016/0022-460X(77)90596-X.

S. Marinov, M. Kern, K. Merkle, N. Zarzalis, A. Peschiulli, F. Turrini, and O.N. Sara. On Swirl Stabilized Flame Characteristics Near the Weak Extinction Limit. In *Proceedings of ASME Turbo Expo 2004*, number GT2010-22335, June 2010. doi: 10.1115/GT2010-22335.

B. Marracino and D. Lentini. Radiation Modelling in Non-Luminous Nonpremixed Turbulent Flames. *Combustion Science and Technology*, 128(1-6):23–48, 1997. doi: 10.1080/00102209708935703.

The MathWorks. *MATLAB and Signal Processing Toolbox*, 2017.

M. Mazur. *Etude expérimentale du bruit de combustion dans un foyer de type aéronautique. Autre*. PhD thesis, Université Paris-Saclay, Français, 2017.

M. Mazur, P. Scouflaire, F. Richecoeur, and S. Ducruix. Combustion noise studies of a swirled combustion chamber with a choked nozzle using high-speed diagnostics. In *ANERS 2015 / XNOISE conference*, September 2015a.

M. Mazur, W. Tao, P. Scouflaire, F. Richecoeur, and S. Ducruix. Experimental and Analytical Study of the Acoustic Properties of a Gas Turbine Model Combustor With a Choked Nozzle. In *Proceedings of ASME Turbo Expo 2015*, number GT2015-43013, June 2015b. doi: 10.1115/GT2015-43013.

K. Meyberg and P. Vachenauer. *Höhere Mathematik 2*. Springer-Verlag Berlin Heidelberg New York, 2nd edition, January 1997.

J.H. Miles. Seperating Direct and Indirect Turbofan Engine Combustion Noise Using the Correlation Function. *Journal of Propulsion and Power*, 26(5):1144–1152, 2010. doi: 10.2514/1.48908.

J.H. Miles. Identification of indirect combustion noise at the exit of a gas turbine. In *Proceedings of the 49th AIAA Aerospace Sciences Meeting*, number AIAA 2011-844, January 2011.

J.V. Molina. *Numerical simulation of turbulent diffusion flames using flamelet models on unstructured meshes*. PhD thesis, Universitat Politecnica de Catalunyae (UPC), September 2015.

B. Mühlbauer, R. Ewert, O. Kornow, and B. Noll. Evaluation of the RPM Approach for the Simulation of Broadband Combustion Noise. *AIAA Journal*, 48(7):1379–1390, July 2010. doi: 10.2514/1.45535.

L. Muniz and M.G. Mungal. Effects of heat release and buoyancy on flow structure and entrainment in turbulent nonpremixed flames. *Combustion and Flame*, 126(1–2):1402–1420, 2001. doi: 10.1016/S0010-2180(01)00253-X.

M.L. Munjal and A.G. Doige. The two-microphone method incorporating the effects of mean flow and acoustic damping. *Journal of Sound and Vibration*, 137(1):135–138, 1990a.

M.L. Munjal and A.G. Doige. Theory of a two source-location method for direct experimental evaluation of the four-pole parameters of an aeroacoustics element. *Journal of Sound and Vibration*, 141(2):323–333, 1990b. doi: 10.1016/0022-460X(90)90843-O.

R.M. Munt. The interaction of sound with a subsonic jet issuing from a semi-infinite cylindrical pipe. *Journal of Fluid Mechanics*, 83(4):609–640, 1977. doi: 10.1017/S0022112077001384.

Bibliography

R.M. Munt. Acoustic transmission properties of a jet pipe with subsonic jet flow: I. The cold jet reflection coefficient. *Journal of Sound and Vibration*, 142:413–436, 1990. doi: 10.1016/0022-460X(90)90659-N.

M. Muthukrishnan, W.C. Strahle, and D.H. Neale. Seperation of Hydrodynamic, Entropy, and Combustion Noise in a Gas Turbine Combustor. *AIAA Journal*, 16(4), September 1977. doi: 10.2514/3.60895.

M.K. Myers. Transport of energy by disturbances in arbitrary steady flow. *Journal of Fluid Mechanics*, 226:383–400, 1991. doi: 10.1017/S0022112091002434.

F. Nicoud and K. Wieczorek. About the zero mach number assumption in the calculation of thermoacoustic instabilities. *International Journal of Spray and Combustion Dynamics*, 1:67–111, 2009. doi: 10.1260/175682709788083335.

N. Peters. *Turbulent Combustion*. Cambridge University Press, 2000. ISBN 0-521-66082-3.

N. Peters. Technische Verbrennung. Vorlesungsskript, RWTH Aachen: Institut für Technische Verbrennung, 2010.

A.D. Pierce. *Acoustics, An introduction to its physical principles and applications*. Acoustic Society of America, 1 edition, 1994. ISBN 0883186128, 9780883186121.

T. Poinsot and D. Veynante. *Theoretical and Numerical Combustion*. RT Edwards Inc, 0002 edition, January 2005.

W. Polifke. Combustion instabilities. *VKI Lecture Series*, 2004.

S.B. Pope. The evolution of surfaces in turbulence. *International Journal of Engineering Science*, 26(5):445–469, 1988. doi: 10.1016/0020-7225(88)90004-3.

S.B. Pope. *Turbulent Flows*. Cambridge University Press, first edition, August 2000.

R. Rajaram and T. Lieuwen. Acoustic radiation from turbulent premixed flames. *Journal of Fluid Mechanics*, 637:357–385, 2009. doi: 10.1017/S0022112009990681.

P.P. Rao and P.J. Morris. Use of Finite Element Methods in Frequency Domain Aeroacoustics. *AIAA Journal*, 44(7):1643–1652, July 2006. doi: 10.2514/1.12932.

F. Raynaud. Towards Unsteady Simulation of Combustor-Turbine Interaction Using an Integrated Approach. In *Proceedings of ASME Turbo Expo 2015*, number GT2015-42110, pages 1–11, Montréal, Canada, 2015. doi: 10.1115/GT2015-42110.

S.W Rienstra and A. Hirschberg. An Introduction to Acoustics. Technical report, Eindhoven University of Technology, May 2012. extended and revised edition of IWDE 92-06.

T. Sattelmayer. Influence of the Combustor Aerodynamics on Combustion Instabilities From Equivalence Ratio Fluctuations. *ASME Journal of Engineering for Gas Turbines and Power*, 125(11), January 2003. doi: 10.1115/1.1365159.

T. Sattelmayer. Technische Thermodynamik: Verbrennung, Gas-Dampf-Gemische und Gasdynamik. Lecture notes, Technische Univeristät München: Lehrstuhl für Thermodynamik, June 2008.

H.P. Schmid. *Ein Verbrennungsmodell zur Beschreibung der Wärmefreisetzung von vorgemischten turbulenten Flammen*. PhD thesis, Universität Karlsruhe, Dezember 1995.

D.P. Schmidt, I. Nouar, P.K. Senecal, C.J. Rutland, J.K. Martin, R.D. Reitz, and J.A. Hoffman. Pressure-Swirl Atomization in the Near Field. SAE International, 1999. doi: 10.4271/1999-01-0496.

M. Schulze. *Linaer Stability Assessment of Cryogenic Rocket Engines*. PhD thesis, Technische Univeristät München, 2016. `http://www.td.mw.tum.de/fileadmin/w00bso/www/Forschung/Dissertationen/schulze16.pdf`.

L. Selle, F. Nicoud, and T. Poinsot. Actual Impedance of Nonreflecting Boundary Conditions: Implications for Computation of Resonators. *AIAA Journal*, 42(5):958–964, May 2004. doi: 10.2514/1.1883.

R. Siegel and J.R. Howell. Thermal Radiation Heat Transfer, 1971.

J.H. Spurk and N. Aksel. *Strömungslehre: Einführung in die Theorie der Strömungen*. Springer Berlin Heidelberg New York, 7 edition, Dezember 2007.

S.R. Stow and A.P. Dowling. Thermoacoustic Oscillations in an Annular Combustor. In *Proceedings of ASME Turbo Expo 2001*, number 2001-GT-0037, June 2001. doi: 10.1115/2001-GT-0037.

S.R. Stow, A.P. Dowling, and T.P. Hynes. Reflection of circumferential modes in a choked nozzle. *Journal of Fluid Mechanics*, 467:215–239, September 2002. doi: 10.1017/S0022112002001428.

W.C. Strahle. On combustion generated noise. *Journal of Fluid Mechanics*, 49:399–414, 1971. doi: 10.1017/S0022112071002167.

W.C. Strahle. Some results in combustion generated noise. *Journal of Sound and Vibration*, 23(1):113–125, 1972. doi: 10.1016/0022-460X(72)90792-4.

W.C. Strahle. A More Modern Theory on Combustion Noise. *Recent Advances in the Aerospace Sciences*, pages 103–114, 1985. doi: 10.1007/978-1-4684-4298-4_6.

L. Strobio Chen, S. Bomberg, and W. Polifke. On the Jump Conditions for Flow Perturbations Across a Moving Heat Source. In *21st International Congress On Sound And Vibration*, July 2014.

L. Strobio Chen, S. Bomberg, and W. Polifke. Propagation and generation of acoustic and entropy waves across a moving flame front. *Combustion and Flame*, 166:170–180, April 2016. doi: https://doi.org/10.1016/j.combustflame.2016.01.015.

H. Tennekes and J.L. Lumley. *A First Course in Turbulence*. The MIT Press, 11 edition, 1972. ISBN 0-262-200198.

S.R. Turns. *An Introduction to Combustion: Concepts and Applications*. Mcgraw Hill Book Co, 0003 edition, February 2011. ISBN 0073380199.

W.C. Ullrich. Aeroacoustic characterization of the scattering behavior of a non-reactive highly-swirled combustion chamber flow. Undisclosed Diploma-thesis, Technische Universität München: Lehrstuhl für Thermodynamik, Garching, Germany, November 2012.

W.C. Ullrich and T. Sattelmayer. Transfer Functions of Acoustic, Entropy and Vorticity Waves in an Annular Model Combustor and Nozzle for the Prediction of the Ratio Between Indirect and Direct Combustion Noise. In *21th AIAA/CEAS Aeroacoustics Conference*, June 2015. doi: 10.2514/6.2015-2972.

W.C. Ullrich, J. Gikadi, C. Jörg, and T. Sattelmayer. Acoustic-entropy coupling behavior and acoustic scattering properties of a Laval nozzle. In *20th AIAA/CEAS Aeroacoustics Conference*, June 2014a. doi: 10.2514/6.2014-3193.

W.C. Ullrich, M. Schulze, and T. Sattelmayer. Fundamental Indirect Noise Generation by Interactions between Entropy, Vorticity and Acoustic Waves in the Context of Aero Engine Applications. In *43rd International Congress on Noise Control Engineering (Inter.noise)*, November 2014b.

W.C. Ullrich, F. Bake, N. Kings, and T. Sattelmayer. Numerical Investigation of Indirect Noise Generation by Accelerated Vorticity. In *21th AIAA/CEAS Aeroacoustics Conference*, June 2015. doi: 10.2514/6.2015-2382.

W.C. Ullrich, C. Hirsch, and T. Sattelmayer. Computation of Combustion Noise from a Premixed and Pressurized Propane Flame Using Statistical Noise Modeling. In *Proceedings of the AIAA Propulsion and Energy Forum and Exposition (Propulsion and Energy 2016)*, number AIAA 2005-2942, July 2016. doi: 10.2514/6.2016-4590.

W.C. Ullrich, Y. Mahmoudi, K. Lackhove, A. Fischer, C. Hirsch, T. Sattelmayer, A.P. Dowling, N. Swaminathan, A. Sadiki, and M. Staufer. Prediction of Combustion Noise in a Model Combustor Using a Network Model and a LNSE Approach. In *Proceedings of ASME Turbo Expo 2017*, number GT2017-64300, June 2017. doi: 10.1115/GT2017-64300.

W.C. Ullrich, C. Hirsch, T. Sattelmayer, K. Lackhove, A. Sadiki, A. Fischer, and M. Staufer. Combustion Noise Prediction Using Linearized Navier-Stokes Equations and Large-Eddy Simulation Sources. *Journal of Propulsion and Power*, 34(1), January 2018. doi: 10.2514/1.B36428.

177

J. van Kampen. *Acoustic pressure oscillations induced by confined turbulent premixed natural gas flames.* PhD thesis, Universiteit Twente, Netherlands, 2006.

J. van Kampen, R.A. Huls, J.B.W. Kok, and T.H. Van der Meer. One-dimensional acoustic modeling of thermoacoustic instabilities. In A. Nilsson and H. Boden, editors, *10th International Congress on Sound And Vibration*, pages 735–742. KTH Royal Institute of Technology, July 2003.

J.P. Verissimo Caschera. Numerische Untersuchung einer turbulenten axialen sowie verdrallten transsonischen Düsenströmung. Undisclosed Bachelor thesis, Technische Universität München: Lehrstuhl für Thermodynamik, Garching, Germany, Mai 2014.

R. Viskanta and M.P. Mengüc. Radiation Heat Transfer in Combustion Systems. *Progress in Energy and Combustion Science*, 13(2):97–160, 1987. doi: 10.1016/0360-1285(87) 90008-6.

W.A. Wall. Finite-Elemente. Vorlesungsskript, Technische Univeristät München: Lehrstuhl für Numerische Mechanik, 2010.

J. Wäsle, A. Winkler, and T. Sattelmayer. Spatial Coherence of Heat Release Fluctuations in Turbulent Jet and Swirl Flames. *Flow, Turbulence and Combustion*, 75(1-4):29–50, 2005. doi: 10.1007/s10494-005-8586-1.

J.G. Wäsle. *Vorhersage der Lärmemissionen turbulenter Vormischflammen.* PhD thesis, Technische Univeristät München, December 2007. `https://www.td.mw.tum.de/fileadmin/w00bso/www/Forschung/Dissertationen/waesle.pdf`.

P.D. Welch. The use of fast Fourier transform for the estimation of power spectra: A method based on time averaging over short, modified periodograms. *IEEE Transactions on Audio and Electroacoustics*, 15(2):70–73, 1967. doi: 10.1109/TAU.1967.1161901.

F. Weyermann. *Numerische Berechnung der Emission verbrennungsinduzierten Lärms automobiler Zusatzheizungen.* PhD thesis, Technische Universität München, September 2010. `https://www.td.mw.tum.de/fileadmin/w00bso/www/Forschung/Dissertationen/weyermann10.pdf`.

A. Winkler. *Validierung eines Modells zur Vorhersage turbulenten Verbrennungslärms.* PhD thesis, Technische Univeristät München, June 2007. `https://www.td.mw.tum.de/fileadmin/w00bso/www/Forschung/Dissertationen/winkler.pdf`.

A. Winkler, J. Wäsle, and T. Sattelmayer. Experimental Investigations on the Acoustic Efficiency of Premixed Swirl Stabilized Flames. In *Proceedings of the 11th AIAA/CEAS Aeroacoustics Conference (26th AIAA Aeroacoustics Conference)*, number AIAA 2005-2908, May 2005. doi: 10.2514/6.2005-2908.

Bibliography

F. Winter. Bestimmung des akustischen Verhaltens in einer vorgeheizten, tanssonischen Düsenstömung und einer Modellringbrennkammer. Undisclosed Semester-thesis, Technische Universität München: Lehrstuhl für Thermodynamik, Garching, Germany, April 2015.

X. Zhang, X. Chen, J. Gill, and X. Huang. Gradient Term Filtering for Stable Sound Propagation with Linearized Euler Equations. In *Proceedings of the 20th AIAA/CEAS Aeroacoustics Conference*, number AIAA 2014-3306, June 2014. doi: 10.2514/6.2014-3306.

O.C. Zienkiewicz, R.L. Taylor, and P. Nithiarasu. *The Finite Element Method For Fluid Dynamics*. Elsiver Ltd, Butterworth Heinemann, 6th edition, 2005a. ISBN 0 7506 6322 7.

O.C. Zienkiewicz, R.L. Taylor, and J.Z. Zhu. *The Finite Element Method: Its Basics and Fundamentals*. Elsiver Ltd, Butterworth Heinemann, 6th edition, 2005b. ISBN 978-07506-6320-5.